The Study of Thermally Activated Delayed Fluorescence Mechanism in Mono and Bimolecular Systems

PALOMA LAYS DOS-SANTOS

The Study of Thermally Activated Delayed Fluorescence Mechanism in Mono and Bimolecular Systems

Paloma Lays dos Santos

A Thesis Presented for the Degree of Doctor of Philosophy

Organic Electroactive Research Group

Department of Physics

University of Durham

2018

Abstract

After 30 years since the first organic light emitting diode (OLED) was reported by Tang and VanSlyke, devices based on thermally activated delayed fluorescence (TADF) emitters have shown to be the most promising and efficient approach to convert dark triplet states into emissive singlet states. The TADF mechanism relies on thermal energy to raise the triplet state to a vibronic sub level that is isoenergetic with the singlet state, thus enabling reverse intersystem crossing (rISC) and allowing internal quantum efficiency values up to 100%. Major challenges faced by TADF studies persist, concerning the full understanding of the mechanism, as it is strongly affected by the environment in which the emitter is dispersed and the different conformations that the molecules can access. Throughout the course of this thesis, the photophysical and chemical properties of the TADF mechanism were investigated in various organic molecules including novel D-A-D and D-A_3 molecules, bimolecular (exciplex) blends and excited state intramolecular proton transfer (ESIPT). Important new contributions towards the full elucidation of the TADF mechanism are presented, mainly regarding the current TADF vibronic coupling mechanism model, which highlights the need for three excited states (singlet charge transfer state; triplet charge transfer states; and triplet local excited state) to come into resonance to achieve high TADF efficiency. In addition, a solution to the dilemma that a TADF emitter cannot have both unity photoluminescence quantum yield and fast rISC rates is presented and high efficient OLEDs are shown. Moreover, it is discussed how different molecular conformers affect the efficiency of the TADF mechanism by studying molecules that show dual charge transfer emission. Furthermore, it is shown that the emitter and host combination must be optimized to minimize the rISC barrier and maximize the TADF in blue OLEDs. Additionally, the use of ESIPT emitters to generate TADF is discussed.

Contents

List of Abbreviations

CH_2Cl_2- Dichloromethane

CT- Intramolecular charge transfer

DF- Delayed fluorescence

EQE- External quantum efficiency

HOMO- Highest occupied molecular orbital

IC-Internal conversion

iCCD- Intensified charged coupled device

iMCT – Intermolecular charge transfer

IQE- Internal quantum efficiency

ISC- Intersystem crossing

^{1}LE- Local excited singlet state

^{3}LE- Local excited triplet state

LUMO- Lowest unoccupied molecular orbital

MCH- Methyl cyclohexane

Nd:YAG- Neodymium doped yttrium aluminum garnet

OLED- Organic light emitting diode

PF- Prompt fluorescence

PH- Phosphorescence

PL-Photoluminescence

PLQY- Photoluminescence quantum yield

RT- Room temperature

rISC- Reverse intersystem crossing

SOC- Spin-orbit coupling

SSL- Solid state lighting

TADF-Thermally activated delayed fluorescence

TCSPC- Time correlated single photon counting

TTA- Triplet-triplet annihilation

List of Published Papers

2018

(1) **dos Santos, P. L**.; Etherington, M. K.; Monkman, A. P. Chemical and Conformational Control of the Energy Gaps Involved in the Thermally Activated Delayed Fluorescence Mechanism. *J. Mater. Chem. C* **2018**, *6* (18), 4842-4853.

(2) **dos Santos, P. L**.; Ward, J. S.; Congrave, D. G.; Batsanov, A. S.; Eng, J.; Stacey, J. E.; Penfold, T. J.; Monkman, A. P.; Bryce, M. R. Triazatruxene: A Rigid Central Donor Unit for a D-A 3 Thermally Activated Delayed Fluorescence Material Exhibiting Sub-Microsecond Reverse Intersystem Crossing and Unity Quantum Yield via Multiple Singlet-Triplet State Pairs. *Adv. Sci.* **2018**, *5* (6), 1700989.

2017

(3) Etherington, M. K.; Franchello, F.; Gibson, J.; Northey, T.; Santos, J.; Ward, J. S.; Higginbotham, H. F.; Data, P.; Kurowska, A.; **dos Santos, P. L.**; et al. Regio- and Conformational Isomerization Critical to Design of Efficient Thermally-Activated Delayed Fluorescence Emitters. *Nat. Commun.* **2017**, *8*, 14987.

(4) **dos Santos, P. L**.; Ward, J. S.; Batsanov, A. S.; Bryce, M. R.; Monkman, A. P. Optical and Polarity Control of Donor-Acceptor Conformation and Their Charge-Transfer States in Thermally Activated Delayed-Fluorescence Molecules. *J. Phys. Chem. C* **2017**, *121* (30), 16462–16469.

(5) Pereira, D. de S.; **dos Santos, P. L.**; Ward, J. S.; Data, P.; Okazaki, M.; Takeda, Y.; Minakata, S.; Bryce, M. R.; Monkman, A. P. An Optical and Electrical Study of Full Thermally Activated Delayed Fluorescent White Organic Light-Emitting Diodes. *Sci. Rep.* **2017**, *7* (1), 6234.

(6) Costa, B.; Jardim, G. A. M.; **Santos, P. L**.; Calado, H.; Monkman, A. P.; Dias, F. B.; Silva Junior, E.; Cury, L. A. Indirect Consequences of Exciplex States on the Phosphorescence Lifetime of Phenazine-Based 1,2,3-Triazole Luminescent Probes. *Phys. Chem. Chem. Phys.* **2017**, *19* (19), 3417–4140.

(7) Huang, R.; Avó, J.; Northey, T.; Chaning-Pearce, E.; **dos Santos, P. L.**; Ward, J. S.; Data, P.; Etherington, M. K.; Fox, M. A.; Penfold, T. J.; et al. The Contributions of Molecular Vibrations and Higher Triplet Levels to the Intersystem Crossing Mechanism in Metal-Free Organic Emitters. *J. Mater. Chem. C* **2017**, *5* (25), 6269–6280.

(8) **dos Santos, P. L.**; Cenni, M. F. B.; Costa, B. B. A.; Cury, L. A. B-Carotene and Oleic Acid Contributions To the Optical Properties of Amazonic Oils. *J. Photochem. Photobiol. A Chem.* **2017**, *347*, 93–97.

(9) Altınölçek, N.; Aydemir, M.; Tavaslı, M.; **dos Santos, P. L.**; Monkman, A. P. Synthesis of Biscyclometalated iridium(III) Acetylacetonate Complexes via a 15 Minute Bridge-Splitting Reaction, Their Characterisations and Photophysical Properties. *J. Organomet. Chem.* **2017**, *851*, 184–188.

2016

(10) **dos Santos, P. L.**; Ward, J. S.; Bryce, M. R.; Monkman, A. P. Using Guest-Host Interactions to Optimize the Efficiency of TADF OLEDs. *J. Phys. Chem. Lett.* **2016**, *7* (17), 3341–3346.

(11) **dos Santos, P. L.**; Dias, F. B.; Monkman, A. P. Investigation of the Mechanisms Giving Rise to TADF in Exciplex States. *J. Phys. Chem. C* **2016**, *120* (32), 18259–18267.

(12) **Santos, P. L.;** Ward, J. S.; Data, P.; Batsanov, A. S.; Bryce, M. R.; Dias, F. B.; Monkman, A. P. Engineering the Singlet–triplet Energy Splitting in a TADF Molecule. *J. Mater. Chem. C* **2016**, *4*, 3815--3824.

(13) **Santos, P. L.**; Cury, L. A.; Dias, F. B.; Monkman, A. P. Spectroscopic Studies of Different poly3hexylthiophene Chain Environments in a Polyfluorene Matrix. *J. Lumin.* **2016**, *172*, 118–123.

Declaration

All material contained in this thesis is original and is the result of my own work except where explicit reference is made to the work of others. This thesis has not been submitted in whole or part for the award of a degree at this or any other university.

The Study of Thermally Activated Delayed Fluorescence Mechanism in Mono and Bimolecular Systems

Paloma Lays dos Santos

Acknowledgments

First, I would like to thank my supervisor, Prof. Andy Monkman, for the guidance, encouragement and advice he has provided throughout my studies. His enthusiasm and confidence in my research has motivated me a lot. My co-supervisor, Dr. Fernando Dias, who helped me and always responded to my questions and queries so promptly. Also, all the members of the OEM group for providing a stimulating and nice environment to learn and grow.

Thanks to all collaborators who enriched my work, in special Prof Martin Bryce's and Dr Thomas Penfold's teams.

Getting through my thesis required more than academic support, and I have many people to thank for supporting me over the past four years. Firstly, my best friend and husband Erhan, who has been a constant source of encouragement and love. Daniel, Chris, Heather, Roberto, Rongjuan and Vasco who have been unwavering in their personal and professional support during the time I spent at the university. The beautiful Dias' family (Fernanda, Fernando, Rita, Inês and Chuva), who opened their heart to me when I first arrived to Durham. In addition, all my lovely friends back home (Brazil) who never left me feeling alone and constantly showed their care to me.

I would like to thank CAPES Foundation, Ministry of Education of Brazil, Science Without Borders Program for a PhD studentship, Proc. 12027/13-8, for financial support.

Em último (e mais importante) agradeço os meus pais, Lúcia e Beto. Eles sempre me apoiaram em todas as etapas da minha vida, inclusive esta que ocorreu tão longe dos olhos deles. Muito obrigada pelos seus conselhos, força e amor. Vocês nunca deixaram que a longa distância os impedissem de estar perto de mim.

Dedicado aos meus
amados pais, Lúcia e Beto

Chapter 1: Introduction

1.1 Motivation

Artificial lighting is an essential aspect of our daily lives and improvements towards eco-friendly sources are urgently required. Organic light emitting diodes (OLEDs) tackles this issue as they can be used to produce large and efficient lighting panels using materials that are less harmful to the environment than the chemicals and processing conditions of conventional fluorescent tubes LEDs. Nowadays, many companies already offer lighting panels based on the OLED technology, including Philips, LG, Konica Minolta and others.

As its main research field, OLEDs are used to create displays in devices such as television screens, computer monitors or mobile phones. Apart from eco-friendly characteristics, they show many other advantages: OLEDs can be fabricated on flexible and transparent substrates. Thus, in the future, bendable, rollable or even transparent OLEDs displays are a possibility; They offer a better image quality because of the higher contrast ratio (true blacks), faster refresh rates and wider viewing-angles; They also consume less power than, for example, liquid crystal displays as only active pixels consume energy.

Putting together all these qualities, OLEDs promise a revolution in the smartphone and flat panel display industries. However, to be able to replace the current LED technology, all avenues for optimization of devices must be thoroughly considered. In this matter, research on the mechanisms through which triplet excitons (dark states) can be converted into emissive singlet excitons is essential to surpass the initial 25% internal quantum efficiency (IQE) barrier imposed by spin statistics.

After 30 years from the first device reported by Tang and VanSlyke[1], OLEDs have been classified into three different generations: Generation 1: OLEDs based on fluorescent materials; Generation 2: OLEDs based on phosphorescent materials and Generation 3: OLEDs based on thermally activated delayed fluorescent (TADF) materials, which is the most active area of OLEDs research today.

The TADF mechanism relies on thermal energy to raise the triplet state to a vibronic sub level that is isoenergetic with the emissive singlet states, thus enabling reverse intersystem crossing

(rISC) and allowing internal quantum efficiency (IQE) values up to 100%. The first report on delayed fluorescence (DF) was made by Perrin[2] in 1929, who observed two long-lived emissions, naming them phosphorescence and fluorescence of long duration. However, it was only in 2009 that the TADF mechanism was used to generate DF in OLEDs by Adachi *et al*.[3] They used the mechanism to harvest non-emissive triplet excited states in Sn^{4+}–porphyrin devices due to the small energy splitting between singlet and triplet states observed in these compounds. Using such a design strategy, the first TADF-based OLED without heavy-metals was reported in 2012[4]. Since then, the TADF mechanism has attracted considerable interest, mainly in the electroluminescence field, leading to OLEDs with high performance[5–7].

To help understanding the TADF mechanism, this thesis presents the experimental characterization of the physical and chemical aspects that are relevant to the development of TADF. A combination of data has been collected from the facilities available at the organic electroactive materials OEM group, which has a range of unique optical spectroscopy techniques and device production, mostly using TADF molecules designed and synthesised by Prof. Martin Bryce's group (chemistry department, Durham University) together with quantum chemical calculations from Dr. Thomas Penfold's group (University of Newcastle).

1.2 Thesis Organization

Chapter 2 gives a background on the theory within the context of this thesis. It starts with a short description about singlet and triplet states, energy splitting and intersystem crossing process. The discussion is then followed by an explanation of electronic transitions in organic molecules and their photophysical characteristics. Then, a detailed description of the mechanisms that give rise to delayed fluorescence are given, focusing on the TADF mechanism. Finally, OLED design and operation is discussed.

Chapter 3 gives information about the organic materials used and the data collection process. This covers the chemical structures of the molecules studied, sample preparation, optical measurements (steady state measurements, time resolved measurements and electrochemistry) and device production and testing.

The experimental results of this thesis constitute from Chapters 4 to 9 as follows:

Chapter 4 discusses the optical energy splitting between singlet and triplet states of a green emitter, DPO-TXO2 in different environments. The results show how the environment plays a

key role in fine tuning the energy levels of the singlet charge transfer (^{1}CT) state with respect to the local excited triplet state (^{3}LE). This study helped to initiate the current TADF vibronic coupling mechanism[8], a model which highlights the need for three excited states (^{1}CT, ^{3}CT and ^{3}LE) to come into resonance to achieve high TADF efficiency.

Chapter 5 provides an analysis of how the different molecular conformers affect the efficiency of the TADF mechanism by studying DPT-TXO2 and DMePT-TXO2 emitters, given that molecules that have the ability to form two different D-A conformers can lead to unwanted emission quenching and other possible side effects. Moreover, how the emission contribution of different conformers can be controlled by the polarity of the environment and by the excitation energy is shown.

Chapter 6 describes a study on high performance blue devices, showing that the emitter and host combination must be optimized to minimize the reverse intersystem crossing (rISC) barrier and maximize the TADF mechanism. In this chapter, the steps of how the device optimization process occurs is detailed using the *emitter DDMA-TXO2.*

Chapter 7 presents a completely new design of TADF molecule (TAT-3DBTO$_2$), which has a rigid donor core with multiple peripheral acceptors units. The results from this molecule show a significant enhancement to the rISC rate compared to usual D-A-D type TADF emitters and photoluminescence quantum yield close to 1. These two characteristics ensures that harvested triplets do not cycle back to the triplet state and avoids decay by non-radiative pathways. This was achieved through near degenerate multiple excited states arising from the multi D-A structure, verifying experimentally the TADF vibronic coupling mechanism.

Chapter 8 discusses bimolecular TADF systems, i.e., intermolecular charge transfer states (iMCT) formed between commercial charge donor and acceptor molecules. This study points out the competition between two DF mechanisms, triplet-triplet annihilation (TTA) and TADF, and highlights the importance of the local triplet excited states (^{3}LE) in the rISC process for bi-molecular systems.

Chapter 9 discusses the TADF mechanism in a completely different type of emitter molecule, through an excited state intramolecular proton transfer (ESIPT) mechanism. The planar ESIPT molecule triquinolonobenzene (TQB) shows TADF, and is a potentially promising new way to achieve high performance OLEDs. The optical ΔE_{ST} values of TQB emitter shows only a slight variation with the host, which will lead to simpler design of OLEDs structures, as the similar photophysics will be observed regardless of the host material selected.

Finally, in **Chapter 10**, the findings from the studies shown from chapter 4 to 9 are summarised.

1.3 References Chapter 1

1. Tang, C. W. & VanSlyke, S. A. Organic electroluminescent diodes. *Appl. Phys. Lett.* **51,** 913–915 (1987).
2. Perrin, F. La Fluorescence des Solutions. *Ann. Phys.* **12,** 169–275 (1929).
3. Endo, A. *et al.* Thermally Activated Delayed Fluorescence from Sn4+-Porphyrin Complexes and Their Application to Organic Light Emitting Diodes - A Novel Mechanism for Electroluminescence. *Adv. Mater.* **21,** 4802–4806 (2009).
4. Uoyama, H., Goushi, K., Shizu, K., Nomura, H. & Adachi, C. Highly efficient organic light-emitting diodes from delayed fluorescence. *Nature* **492,** 234–8 (2012).
5. Lee, C. W. & Lee, J. Y. Systematic control of photophysical properties of host materials for high quantum efficiency above 25% in green thermally activated delayed fluorescent devices. *ACS Appl. Mater. Interfaces* **7,** 2899–2904 (2015).
6. Miwa, T. *et al.* Blue organic light-emitting diodes realizing external quantum efficiency over 25% using thermally activated delayed fluorescence emitters. *Sci. Rep.* **7,** 284 (2017).
7. Pereira, D. de S. *et al.* An optical and electrical study of full thermally activated delayed fluorescent white organic light-emitting diodes. *Sci. Rep.* **7,** 6234 (2017).
8. Gibson, J., Monkman, A. & Penfold, T. The Importance of Vibronic Coupling for Efficient Reverse Intersystem Crossing. *ChemPhysChem* **17,** 2956–2961 (2016).

Chapter 2: Background Theory

The purpose of this chapter is to give a background on the theory within the context of this thesis. Initially, a brief overview of singlet and triplet states, the energy splitting and the intersystem crossing process is given. The discussion is then followed by an explanation of electronic transitions in organic molecules and their photophysical characteristics. All the mechanisms that give rise to delayed fluorescence, focusing on thermally activated delayed fluorescence (TADF), are subsequently presented. Lastly, the design and operation of OLEDs is given in the context of the devices produced in this work.

2.1 Fundamental Theory

2.1.1 Singlet and Triplet States

In quantum mechanics, spin is a manifestation of the electron's angular momentum, a fundamental property along with the electron's mass and charge. Commonly, a classical model of the angular momentum of a rotating sphere is used as a physical model to describe the electron spin, although electron spin is fundamentally a quantum mechanical phenomenon that has no classical analogue. A brief explanation for a two electron system, in which both particles have spin ½, is given below. More details on the topic can be found in Köhler and Bässler's review paper and Turro's book on Molecular Photochemistry[1,2].

Spin angular momentum is a vector quantity that couples according to the rules of quantum mechanics and it is designated by **S**. A two electron system will have four possible spin eigenstates (see Figure 1a). The first spin wavefunction has S = 0 and spin multiplicity m equal to 1, where m = 2S +1. It has only a single possible value of its z-component, i.e. eigenvalue $m_s = 0$, and is therefore called singlet. The next three spin wavefunctions have S = 1 and m = 3. They only differ in the z-component of the spin, which can take one of three eigenvalues (m_s = 1, 0, -1). This arrangement is therefore called triplet. A vectoral representation is given in the Figure 1b.

The full wavefunction of a particle can be written as the product of a spatial wavefunction, which depends only on spatial coordinates, and a spin wavefunction, which is a function of the particle's spin. In order to preserve the Pauli exclusion principle, the symmetric spin wavefunctions of the triplet state are always combined with an antisymmetric spatial wavefunction, while the converse is the case for the singlet state.

The ground state of organic molecules is generally a singlet state, i.e., two electrons occupy a single orbital and have antiparallel paired spins. In the excited state, the two electrons are in different orbitals, i.e., one electron is in the highest-energy molecular orbital (MO) that contains electrons (highest occupied molecular orbitals, HOMO), and another one in the lowest-energy MO empty in the ground state (lowest unoccupied molecular orbital, LUMO), and they can either have electron spin antiparallel (↑↓) (singlet) or electron spin parallel (↑↑) (triplet), see Figure 1c.

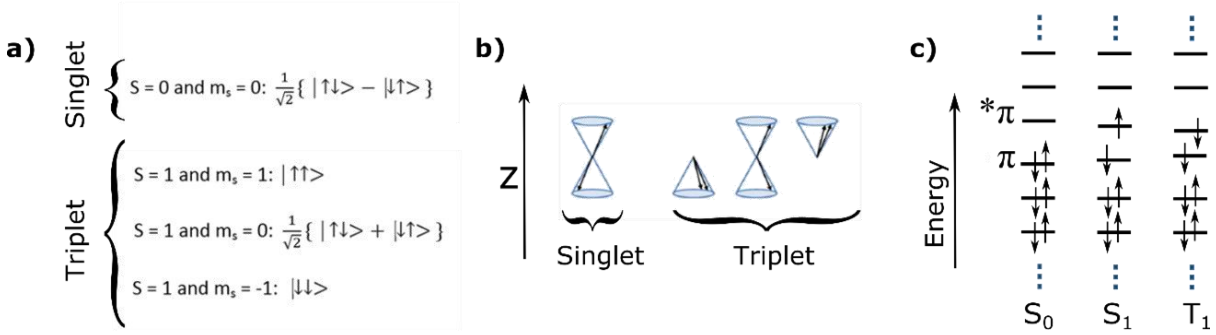

Figure 1 a) Spin wavefunctions of the four eigenstates in a two particle system b) Vector diagram illustrating the relative orientations of the two electron spins for the singlet and the triplet state. c) Singlet and triplet states in an orbital configuration scheme. Figures adapted from Köhler *et. al.*[1].

2.1.2 Singlet-Triplet Energy Splitting

The energy splitting between singlet and triplet states has an important role in the context of the thermally activated delayed fluorescence (TADF) mechanism as the rate of direct and reverse intersystem crossing processes (ISC, rISC – section 2.1.3) depends on its value. The singlet and triplet state energies, E_S and E_T, are given by equations 2.1 and 2.2, respectively:

$$E_S = E_{GAP} + K + J \tag{2.1}$$

$$E_T = E_{GAP} + K - J \tag{2.2}$$

where E_{GAP} is the energy difference between the ground and excited state, K (Coulomb interaction integral) is the first order Coulumbic correction due to classical electron-electron correlation and J (exchange interaction integral) is the first order quantum mechanical correction of the electron-electron repulsion energy due to the Pauli principle. Since the charges are the same for electron-electron electrostatic interactions that leads to repulsions, the values of both K and J are defined as positive. Coulomb repulsion increases the energy of both states, whereas the exchange interaction increases the energy of a singlet state but decreases the energy of a triplet state. Therefore, a singlet state always has higher energy than its corresponding triplet state, $E_S > E_T$. The energy splitting between singlet and triplet levels ($E_S - E_T = 2J$) depends on exchange interaction integral, which is proportional to the excited state and ground state wavefunction overlap, i.e., the overlap between the HOMO and the LUMO:

$$J = \iint \Phi(1)\Psi(2)\left(\frac{e^2}{r_1 - r_2}\right)\Phi(2)\Psi(1)dr_1 dr_2 \quad (2.3)$$

where Φ and Ψ represent the HOMO and LUMO wavefunctions, respectively, and *e* is the electron charge. Thus, J is the integral over the coordinates related to the energy exchanged when two identical particles swap their positions.

2.1.3 Intersystem Crossing

As mentioned earlier, intersystem crossing (ISC) plays a crucial role in the TADF mechanism. ISC is a non-radiative, adiabatic process that occurs between states of different multiplicity, such as singlets and triplets. Intersystem crossing from the first singlet excited state (S_1), for example, can either occur from the zero-point vibrational level of S_1 or from thermally populated higher vibrational levels of S_1. It takes place between a triplet state close in energy, either an excited vibrational level of T_1 or other higher excited states (T_n). However, the *spin rule* says that optical transitions with change in the spin multiplicity are forbidden ($\Delta S = 0$), but ISC can become allowed by coupling between the particles' spin and their orbital angular momenta (spin-orbit coupling, SOC). Figure 2 shows a schematic interpretation of ISC in terms of the energy surfaces of the states involved. In a zero-order approximation, i.e., situation for which singlet and triplet states do not interact at all, we assume there is no ISC (Figure 2a). Thus, if a molecule is initially in a singlet or triplet state, it will remain there forever, and no change in the total spin of the system will occur. However, if the system is near or at a certain critical nuclear configuration, i.e., a nuclear configuration for which two (or more) energy surfaces approach a conical intersection, and for which some sort of resonant coupling can occur between them, there may be a mixing of the singlet and triplet states at the crossing point.

Since a large SOC allows a large ISC rate, SOC in organic molecules will be effective in inducing transitions between spin states if one (or both) of the electrons involved approaches a "heavy" atom (as the process is stronger for larger nuclei, $SOC \propto Z^4$). This is because the heavy atom nucleus is capable of causing the electron to accelerate, thereby creating a strong magnetic moment as the result of increased orbital motion. Regardless of the magnitude of SOC, in order to induce a transition between states of different spin, the total angular momentum of the system (orbit plus spin), must be conserved. Thus, a transition from a singlet spin to a triplet spin is compensated by a transition from a *p* orbital of an orbital momentum 1 to a *p* orbital of angular momentum 0, i.e. $p_x \rightarrow p_y$ transition. This is known as El-Sayed's rule and it states that the rate of ISC is relatively large if the transition involves a change in the orbital type[3], i.e. , $^1(\pi,$

$\pi*)\rightarrow{}^3(n,\pi*)$ ISC is faster than $^1(\pi, \pi*)\rightarrow{}^3(\pi, \pi*)$ transitions and $^1(n,\pi*)\rightarrow{}^3(\pi, \pi*)$ faster than $^1(n,\pi*) \rightarrow{}^3(n,\pi*)$.

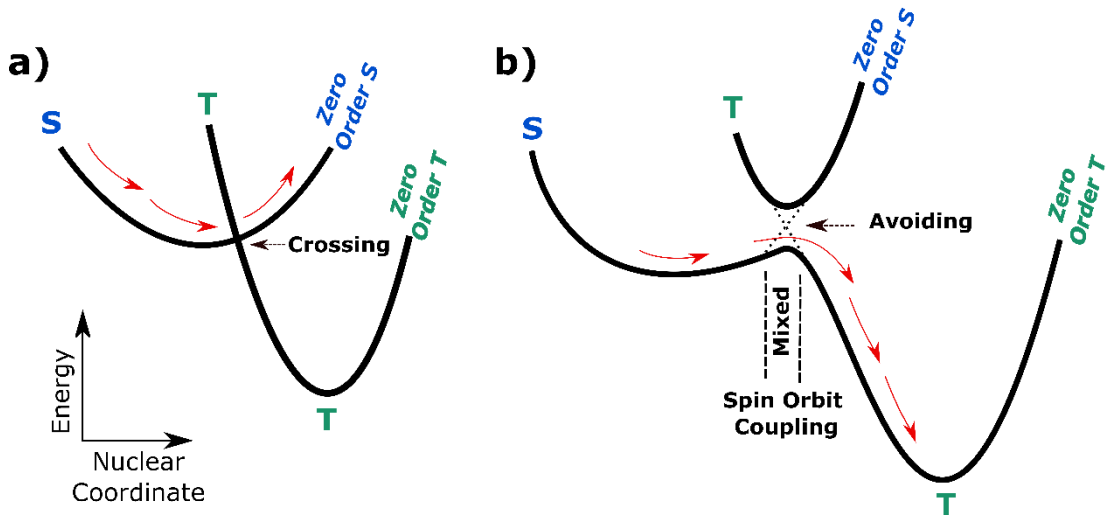

Figure 2 Intersystem crossing (ISC) scheme. a) ISC is forbidden in the zero-order approximation (no interaction between S and T states) but becomes partially allowed (b) when a spin-mixing mechanism is available near the crossing point of the energy curves for singlet and triplet states. Figures adapted from Turro[2].

Apart from SOC, the hyperfine coupling (HFC) can also contribute to ISC between singlet and triplet states. This mechanism arises from interactions between an electron's spin and nucleus' spin in the same molecule or in bi-molecular systems. Some experimental studies have proposed that hyperfine coupling induces ISC, and the interplay of SOC and HFC contributions was evaluated[4–6]. Commonly, HFC constants are small if compared to SOC, but it will have an important role in the TADF mechanism in situations where SOC is negligible.

More detailed descriptions of ISC theory and the spectroscopic methods used to investigate this process can be found on Turro's book on molecular photochemistry and Kohler and Bassler's book on the electronic processes in organic semiconductors[2,7].

2.2 Transitions Between Electronic States

For photophysical transitions, the selection rules will provide the probability (or rate) of a transition to be close to the hypothetically "strictly forbidden" (implausible) or "fully allowed" (plausible) limits. A material irradiated by an electromagnetic wave will absorb energy, and the value of the oscillator strength (f), which is a dimensionless quantity that expresses the probability of absorption or emission of electromagnetic radiation, will approach 1 if it is a

strong (allowed) transition, or zero if it is a very weak (forbidden) transition. The selection rules between electronic states can be summarized in relation to the oscillator strength f_a of a fully allowed transition through equation 2.4:

$$f = P_s * P_0 * P_P * P_m * f_a \quad (2.4)$$

Where P_s represents the electron spin, P_0 the orbital symmetry, P_P the parity and P_m the momentum factors. All these factors are detailed below:

- Electron spin, P_s

The *spin rule* says that optical transitions with change in the spin multiplicity such as phosphorescence (PH) are forbidden (ΔS = 0), however this rule is broken by spin-orbit coupling (SOC) as described in section 2.1.3.

- Orbital symmetry, P_0

The two orbitals involved in a transition must possess large amplitudes in the same region, otherwise the transitions is "overlap forbidden". For example, a transition π→ π* are allowed as their orbital lie in the same plane and have a high degree of spatial overlap. On the other hand, a transition n→ π* is forbidden, as the HOMO and LUMO are orthogonal to one another and the overlap integral is close to zero ($\langle n|\pi * \rangle = 0$).

- Parity, P_P

The *Laporte rule* states that electronic transitions that conserve parity, either symmetry or antisymmetry with respect to an inversion center, i.e., g → g (even → even) or u→ u (odd→ odd) are forbidden. Allowed transitions must involve a change in parity, either g → u or u → g. Again, the transition π→ π* is a good example, as the bonding (π) and anti-bonding (π*) orbitals do not have the same parity.

- Momentum, P_m

Transitions resulting in large scale changes in the linear or angular momentum of the molecules are momentum forbidden.

2.3 Jablonski Diagram

Figure 3 illustrates all the processes (radiative and non-radiative) that are relevant to the studies presented in this thesis. The transitions between states are depicted as vertical lines. The thicker horizontal lines represent the electronic states and the thin lines are the vibrational states, where

S_0 is the ground singlet state, S_1 is the first excited singlet state, S_n higher excited singlet states, T_1 the first excited triplet state and T_n higher excited triplet states. The spin configurations of the ground state, S_1 and T_1 are also shown in the diagram.

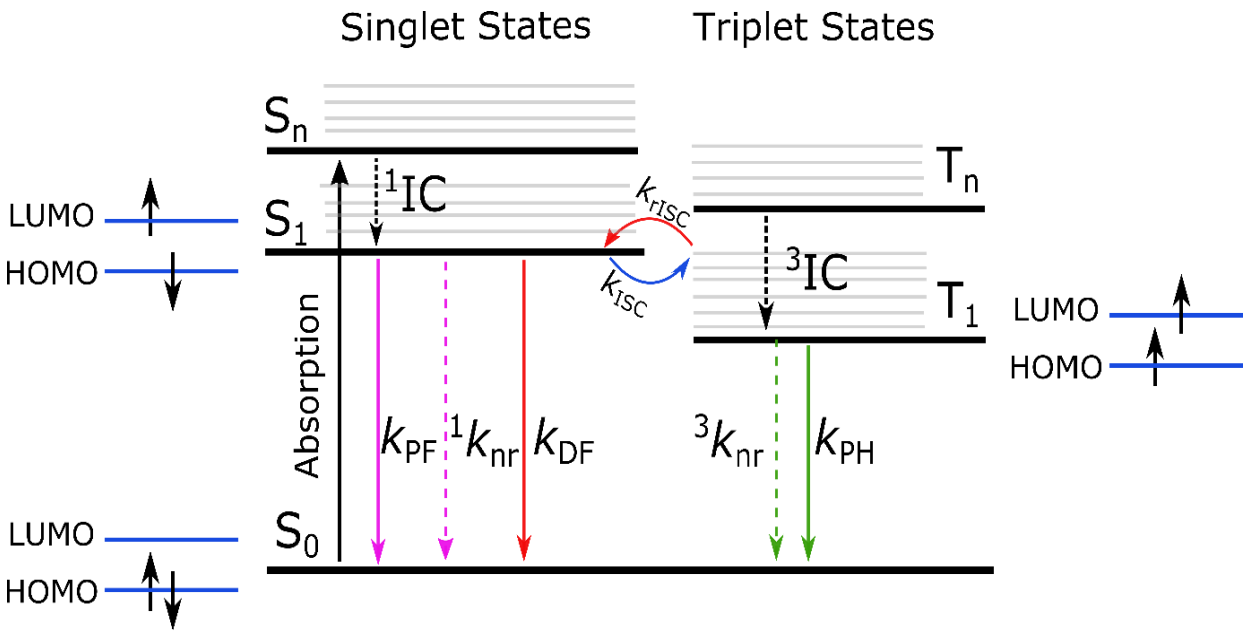

Figure 3 Jablonski diagram. Thicker horizontal lines represent the electronic states and the thin lines are the vibrational states, where S_0 is the ground singlet state, S_1 is the first excited singlet state, and S_n are higher excited singlet states, T_1 the first excited triplet state and T_n are higher excited triplet states. The spin configurations of S_0, S_1 and T_1 are also shown in the diagram.

Following light absorption (black vertical arrow), several processes can occur. When electrons are promoted to S_n, usually they relax to S_1 rapidly (10^{-12} s or less) without photon emission (non-radiative process), a transition called internal conversion (^{1}IC). This process is then followed by three distinct processes: i. radiative emission yielding prompt fluorescence (PF), a fast decay component (pico-nanosecond range) with rate constant assigned as k_{PF}; ii. non-radiative decay, $^1k_{nr}$; or iii. intersystem crossing (ISC) to the triplet states, followed by relaxation to the lowest energy triplet state (^{3}IC). Once the triplet states are reached, they can either recombine to the ground state by formally spin-forbidden radiative emission, referred to as phosphorescence (k_{PH}), non-radiative processes ($^3k_{nr}$), or by a further spin flip, back to the singlet state, reverse intersystem crossing (k_{rISC}). Phosphorescence is a formally forbidden process but takes place due to SOC; and as a result, the rate constants for triplet emission are several orders of magnitude smaller than those for

fluorescence. Molecules containing heavy atoms such as bromine and iodine are frequently phosphorescent as heavy atoms enhance intersystem crossing and thus increase phosphorescence quantum yields. Another type of radiative emission is delayed fluorescence (DF). Electrons that occupy triplet states following ISC can cross back to singlet states via three distinct processes (triplet-triplet annihilation, hot exciton and thermally activated delayed fluorescence), and the subsequent decay of S_1 to S_0 yields delayed emission (DF). The DF will then have the same spectral shape as that of the prompt fluorescence, but with a much longer lifetime. All the three mechanisms are discussed in section 2.5.

2.4 Franck-Condon Principle

The Franck-Condon principle states that the absorption of a photon is a practically instantaneous process since it involves only the rearrangement of electrons, which are inertia-free as compared to (relatively) enormously heavy nuclei. Thus, during light absorption, which occurs in femtoseconds, electrons can move but nuclei cannot. The atomic nuclei therefore have no time to readjust during absorption, but rather must move after it is over. This readjustment brings them into vibrational motion (loss of energy in the absence of light emission). Absorption and fluorescence are represented by vertical arrows in Figure 4a. For a system with almost identical equilibrium geometry in the ground and excited state, the same transitions are most favourable for both absorption and emission, with the 0-0 transition being the strongest. Therefore, the emission spectrum is a mirror image of the absorption spectrum, as shown in Figure 4b, for a hypothetical chromophore. The displacement of fluorescence bands towards longer wavelengths compared to the absorption bands is called Stokes' shift and can be seen in Figure 4b. The slight shift in equilibrium geometry of the excited states is due to the reorganization of surrounding molecules, which is much more pronounced in the case shown in Figure 4c, and is then explained in more details below.

The emitters studied in this thesis, in which charge transfer states (CT) form, have very different geometries of the ground and excited states (Figure 4c). This large change in the geometry of the excited states strongly depends on the polarity of the solvent in which the emitter is dispersed. The CT emitters have larger dipole moments in the excited state than in the ground state. After excitation, the dipoles of the solvent interact strongly with the dipole moment of the excited molecule, and the dipoles reorganize to minimize the energy, resulting in a more strongly relaxed excited state. For more polar solvents, the solvent relaxation effect

is increased, and therefore emission shifts to lower energies. The emission from CT states are also featureless, and this can be associated to the fact that there is a distribution of different solvated complexes, and all these different spectral contributions overlap resulting in a nearly Gaussian shape. The variation of distribution of different solvent reorganizational energies, also leads to the broadening of the emission spectra. Figure 4d shows the absorption and emission spectra of the TAT-3DBTO$_2$ emitter studied in Chapter 7 to illustrate the characteristics observed in most CT emitters. The difference between the peak of absorption and emission spectra (Stokes' shift) is much larger than that observed in the case shown in Figure 4a, and only the absorption spectrum shows vibronic structure, as it involves transitions from the ground state to the electronic and vibronic levels of D and A (local excited states). Importantly, when the geometries of ground and excited states are offset, excitation into a higher vibrational state is often favoured over the 0-0 transition, hence the most intense peak does necessarily correspond to the lowest energy transition. On the other hand, the emission spectra occurs from the transition between the lowest CT state to the ground state[1–3], and therefore shows a strong red shift.

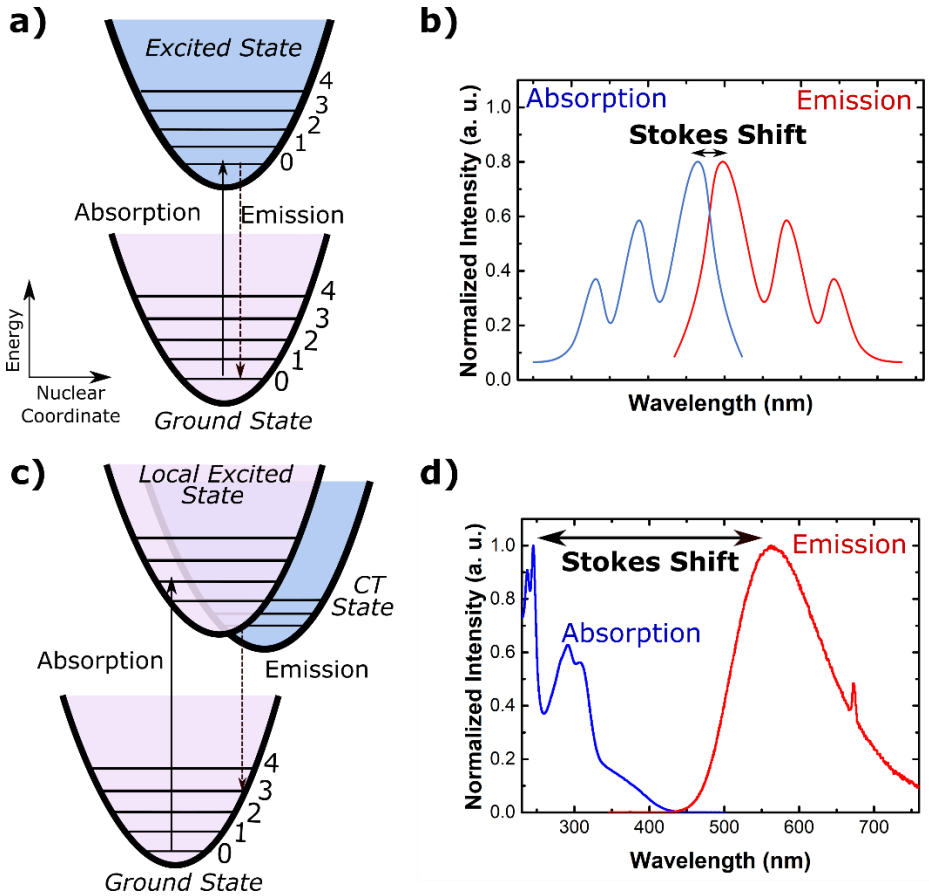

Figure 4 Schematic energy level diagram to show the Franck-Condon principle. Absorption and emission of light are indicated by vertical lines. a) System with almost identical geometry in the ground

and excited state and b) its hypothetical absorption and emission spectra. c) Charge transfer system with strong offset geometry in the ground and excited state and d) Absorption and emission spectra of TAT-3DBTO$_2$ in dichloromethane solution, as an example to highlight the CT emitters characteristics.

2.5 Delayed Fluorescence Mechanisms

As mentioned in section 2.3, three distinct mechanisms can give rise to delayed fluorescence, having the ability to harvest triplet states using metal-free organic molecules: i) triplet-triplet annihilation (TTA); ii) upper triplet crossing, also called "hot-exciton"; and iii) thermally activated delayed fluorescence (TADF). Since recombination of electrons and holes generated by electrical excitation results in a 1:3 ratio of singlet:triplets being formed, there is a 25% internal quantum efficiency limit imposed in fluorescent OLEDs. All three of these mechanisms can help to surpass this limit.

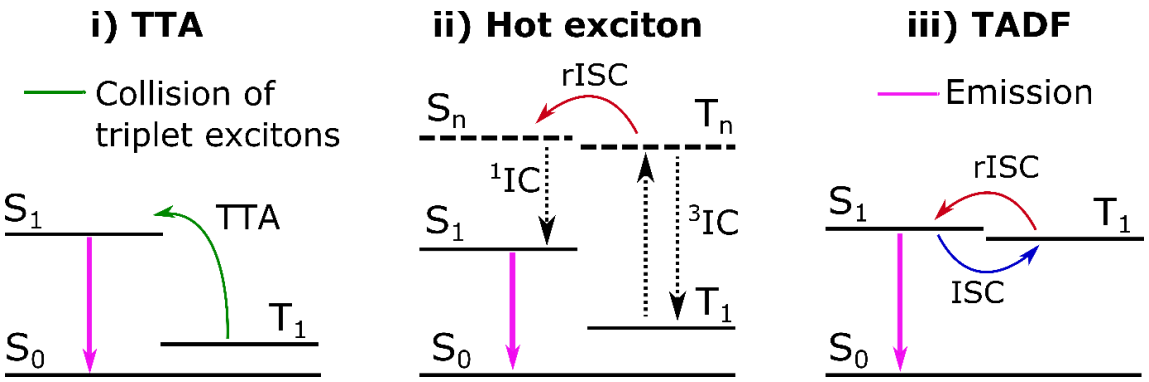

Figure 5 Simplified schematic representation of the electronic energy levels involved in i. Triplet-triplet annihilation (TTA) ii. Hot-exciton mechanism and iii. Thermally-activated delayed fluorescence (TADF).

Among these, TADF has shown to be the most efficient mechanism for triplet state harvesting. Figure 5 shows the simplified schematic representation of the electronic energy levels involved in the three mechanisms and the following sections explain each mechanism individually, with a focus on TADF.

2.5.1 Triplet-Triplet Annihilation

Triplet-triplet annihilation (Figure 5 part i) is a bimolecular process that occurs between two colliding triplet excitons. The triplets form an encounter complex which can have singlet, triplet or quintet character. If the resulting excited state is a singlet, the most desirable outcome, the TTA mechanism can result in DF and certainly increase the OLED performance[8–11]. However,

even with the best possible alignment of energy levels, TTA can only achieve IQE values up to 62.5%[12] (25% initial singlets formed plus $\frac{1}{2} * 75\% = 37.5\ \%$ excitons converted from the triplet states). The rate of triplet exciton decay can be expressed as:

$$\frac{d[T]}{dt} = G_T - \beta[T] - k_{TTA}\,[T]^2 \tag{2.5}$$

where G_T is the generation rate of triplets, β is the cumulative rate constant from radiative (k_r) and non-radiative (k_{nr}) decays, and k_{TTA} is the bimolecular annihilation constant. A common experimental method to identify TTA is by measuring the DF intensity as a function of the excitation dose. The variation depends on the competition between β and k_{TTA}. When β dominates, i.e., the triplets deactivate more quickly than the rate of triplet collisional diffusion, the intensity of DF shows a quadratic dependence on the excitation dose featuring its bimolecular character. However, when TTA dominates at higher triplet concentrations, the intensity becomes linearly dependent on the excitation dose[20].

2.5.2 Upper Triplet Crossing "hot-exciton"

Another strategy to up-convert dark triplet states involves using "hot excitons" (Figure 5 part ii). Here rISC proceeds between upper excited singlet and triplet levels ($S_n \leftarrow T_n$), followed by internal conversion (^{1}IC) to the lowest singlet states, and allowed recombination to the ground state through the emission of photons. Such upper state rISC was reported in several well-known dyes such as Rose Bengal and Erythrosin B[13,14]. More recently, Hu *et al.*[15] rediscovered this mechanism. Through this mechanism, 100% of the triplets formed by charge recombination can, potentially, be converted into emissive singlet states. However, the internal conversion (^{3}IC) between triplet states T_n and T_1, needs to be suppressed to ensure a larger production of singlet states and, in most of the organic molecules ^{3}IC is very efficient, making it difficult to achieve efficient rISC which can out compete ^{3}IC[16]. Thus, this mechanism as an approach to increase OLED performance has not yet shown significant merits.

2.5.3 Thermally Activated Delayed Fluorescence

2.5.3.1 Fundamental Concepts of the TADF Mechanism

The model of the TADF mechanism has improved considerably since the first report of harnessing the mechanism to generate DF in organic light emitting diodes (OLEDs)[17]. Initially, models either did not consider the character of the electronic states, or assumed that only charge

transfer states were involved in the ISC/rISC processes. Nowadays, the most accepted model of rISC is the vibronic coupling model, which is presented in this section.

Figure 6 shows the fundamental energy levels and the rate constants involved in the TADF mechanism. For many donor-acceptor (D-A) and donor-acceptor-donor (D-A-D) type TADF molecules there are two possible excitation channels. Firstly, the molecules may be excited via a strong local D (or A) π-π*transition, which forms a local excited singlet state (^{1}LE). Following this, the excitation can either undergo electron transfer (ET) to form a CT state, radiative decay to the ground state, or intersystem crossing (ISC) to the local triplet states (^{3}LE). Secondly, they may be excited via a weak n-π* or mixed n-π*/π-π* transition directly generating the ^{1}CT state[18]. The former is the more usual experimental situation, thus, following photoexcitation (absorption), depending on the rate of ET it is possible to detect ^{1}LE emission in the first few nanoseconds of decay. The majority of excitations, however, are transferred to the ^{1}CT manifold by very slow (on the order of 10^8 s^{-1}) ET. This ET is slow because of the decoupling between D and A units caused by near orthogonality between them even in the ground state (due to the N-C bridging bond) as discussed later in this section. Once the ^{1}CT is formed, three distinct processes follow: i. radiative emission yielding prompt ^{1}CT fluorescence (PF), k_{PF}; ii. non-radiative decay, $^1k_{nr}$; or iii. intersystem crossing (ISC) to the triplet states. Once the triplet states are reached, they can either recombine to the ground state by either radiative (k_{PH}) or non-radiative emissions ($^3k_{nr}$), or (spin) flip back to the singlet state (k_{rISC}). Normally it is assumed that the latter process only requires thermal energy to raise the triplet state to a vibronic sub-level that is isoenergetic with the emissive singlet states to enable reverse intersystem crossing (rISC) because a spin flip is an adiabatic process. These final emissive singlet states emit in the microsecond to millisecond regime due to the involvement of the longer-lived triplet states. This means that the thermally-activated delayed fluorescence that occurs as a result of rISC is sensitive to heat and oxygen. For TADF to occur, the energy splitting between singlet and triplet states, ΔE_{ST}, should be very small (less than a few hundreds of meV but ideally less than a few tens of meV for efficient rISC). Only then can most of the triplet states be up-converted back to the singlet states i.e. $k_{rISC} >> k_{PH} + {}^3k_{nr}$. A detailed description of the rate constants and quantum yields involved in the TADF mechanism can be found in the works of Berberan-Santos *et al.* and Dias[19,20].

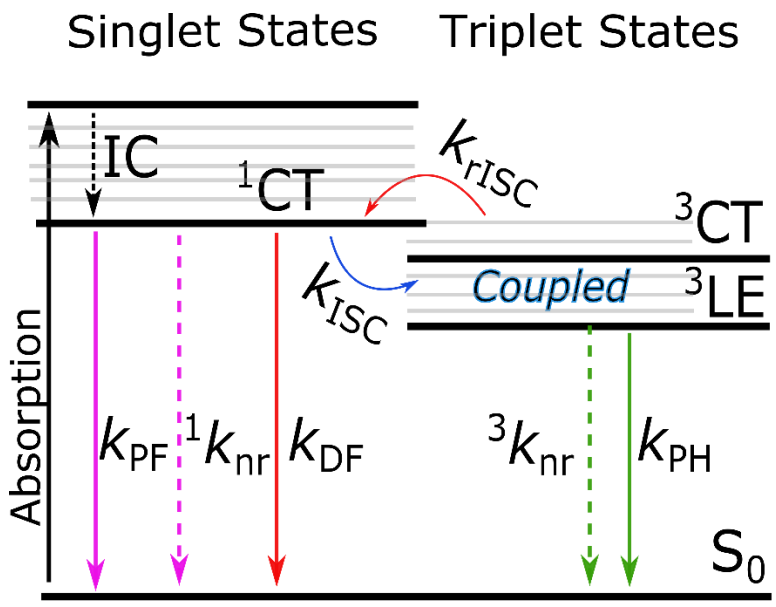

Figure 6 Schematic representation of the electronic energy levels involved in TADF according to the vibronic coupling model.

The most common strategy in the design of TADF emitters to achieve a suitably small ΔE_{ST} is to minimize the electron exchange energy (equation 2.3) in the excited state. The predominant way to achieve this so far has been through donor-acceptor (D-A) charge transfer molecules with N-C bridge. In these D-A materials excited states with strong charge-transfer character (CT) are readily formed[21]. With a N-C bridging bond[22] between the D and A units, they tend to take a perpendicular steric conformation, minimising the interaction between the electron on the D and electron on the A in the excited state, giving near zero exchange energy and thus small ΔE_{ST}. Critically, however, in this configuration the charge transfer singlet (CT^1) and triplet (CT^3) orbitals are degenerate and spin-orbit coupling is forbidden, i.e. $\langle {}^1CT|H_{SOC}|{}^3CT\rangle = 0$, as the HOMO is perpendicular to the LUMO. No change in spatial orbital would occur upon interconverting between these two states, and so no orbital angular momentum change, as required for a spin flip, could occur[23]. Monkman *et al.* pointed out that this also implies that rISC is forbidden for the same reason[18]. This is why it is also a necessary requirement for efficient rISC that another different orbital participates in the rISC process, typically one of the local excited triplet states (^{3}LE) of the D or A units mediates the spin flip mechanism via vibronic coupling to the CT states. This makes it essential to be able to differentiate between CT and LE states when studying TADF molecules.

CT states are very sensitive to their local environment, because of their large dipole moment, and the usual experimental technique used to identify CT states is to measure the

solvatochromic shift of their emission spectra. The pronounced spectral shift with increasing solvent polarity is mainly due to the shielding of the excited state dipole of the TADF molecules, by rearrangement of the solvent shell around the molecule. This reduces the Coulomb energy of the CT, causing a red shift. Occasionally, on freezing, the solvent shell can no longer reorient to relax the Coulomb energy and dramatic blue shift of the CT emission accompanies the freezing of the solvent shell[24]. LE states, on the other hand, are insensitive to changes in the environmental polarity[25–27]. The ^{3}LE energy, combined with ^{1}CT, is used to calculate the 'optical' ΔE_{ST}. Emission from ^{3}CT states has not yet been identified experimentally in the OEM group studies, which include a vast range of efficient TADF emitters[18,28,29]. This can be attributed to a few different factors, most obviously, the small energy gap between ^{1}CT-^{3}CT makes them difficult to distinguish. Additionally, the oscillator strength of CT states is already weak for the singlet state and this would be further compounded by the forbidden nature of triplet decay. Due to these difficulties extra caution should be applied when analysing the phosphorescence of TADF molecules to ensure identification of the correct state. Once the singlet and triplet states are measured in the TADF emitters, it is still not a simple task to determine those involved in the TADF (singlet-triplet) energy gap, ΔE_{ST}. In many materials, the onset of fluorescence and phosphorescence emission are difficult to estimate and in D-A molecules the phosphorescence spectra may be a superposition of both the donor and acceptor ^{3}LE phosphorescence. The need to deconvolute the energies of the two local phosphorescent states was shown in recent OEM group work[18], which allowed the correct energy gap between the ^{1}CT fluorescence and the lowest energy donor ^{3}LE phosphorescence to be obtained. A further complication that is often found is that the optical ΔE_{ST} is different to the thermal activation energy calculated from the rISC rate, k_{rISC}, using equation 2.6:

$$k_{rISC} = \mathrm{A}\, \mathrm{e}^{\frac{-\mathrm{E_a}}{\mathrm{kT}}} \tag{2.6}$$

where A is a pre-exponential factor, E_a is the activation energy for the rISC process, k is the Boltzmann constant and T is temperature. It is not just the initial and final states, ^{1}CT and ^{3}LE, that are crucial to the rISC rate, which defines more than one singlet-triplet energy splitting, as discussed below.

As said previously, spin-orbit coupling (SOC) is formally forbidden between singlet and triplet CT states for the case of near orthogonal D and A units where the exchange energy approaches zero[23], and thus other electronic states must be involved in the rISC mechanism to mediate the spin-orbit coupling spin flip. It was shown that the energetically nearest ^{3}LE state plays an

important role in the overall TADF process [18,29,30] , however, just the SOC between ^{3}LE and ^{1}CT is still not able to explain the high rates of rISC reported experimentally.

Recently, Gibson *et al.*[32] have shown that neither of these processes (SOC between ^{1}CT-^{3}LE and HFC between ^{1}CT-^{3}CT) have strong enough coupling strength to explain the measured TADF rISC rate >10^6 s^{-1}. By utilising a more rigorous quantum dynamics approach to describe the k_{rISC} that considers the vibrational density of states and implementing second-order perturbation theory they demonstrate that both ^{3}CT and ^{3}LE are pivotal to the rISC process. From this it has been identified that there are at least two energy gaps to consider when optimizing TADF molecules. TADF vibronically couple (mixing) the ^{3}LE and ^{3}CT triplet states to achieve equilibration between these states allowing adiabatic crossing between ^{1}CT and ^{3}CT, i.e., spin flip can occur between the ^{3}CT and ^{1}CT states, mediated by the ^{3}LE state. A schematic interpretation of this mix between triplet states in terms of the energy surfaces of the states involved is shown in Figure 7. In part a, it is shown a situation for which ^{3}CT and ^{3}LE do not interact at all, thus, the rISC rate will be very low. However, if the states are vibronically coupled, there may be a mixing of the ^{3}CT and ^{3}LE at the crossing point, enhancing rISC process to the singlet states.

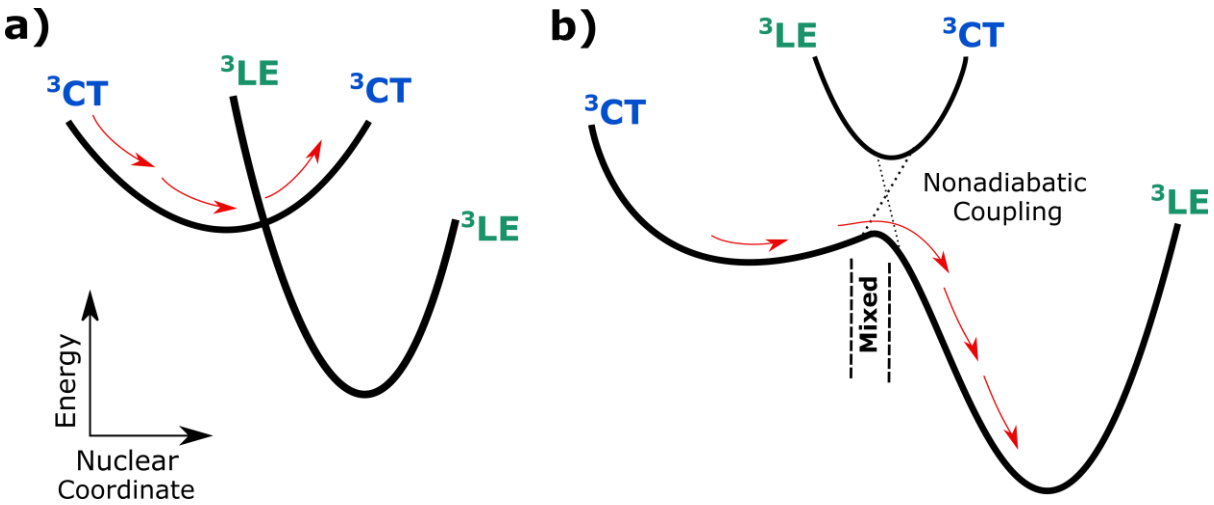

Figure 7 Scheme to illustrate the nonadiabatic coupling in the TADF model. a) rISC is supressed when no interaction occurs between ^{3}LE and ^{3}CT triplet states, but it becomes enhanced (b) when vibronic coupling (nonadiabatic coupling) is available near the crossing point of the energy curves between ^{3}LE and ^{3}CT, mixing the states.

The nonadiabatic coupling, mixing between ^{3}LE and ^{3}CT, reduces the (thermal) activation for rISC by forming an equilibrium between these two states, even without thermal activation[33]. This lowering of the energy gap occurs because, according to the second-order perturbation

theory, E_a is dominated by the ^{1}CT-^{3}CT energy gap rather than the ^{1}CT-^{3}LE energy gap. As a result, they showed the important effect of intermediate states on the E_a energy, explaining the reason for the different energy gaps associated with the TADF mechanism: the ΔE_{ST} calculated via optical energy, which commonly describes the ^{1}CT-^{3}LE gap; whereas the E_a calculated from the Arrhenius plot, which likely describes the thermal gap between ^{1}CT-^{3}CT. This is much in line with the experimental results shown in chapter 4 of this thesis, where the energy gap between ^{1}CT state and the ^3LE_D states was identified in a DPO-TXO2 toluene solution to be ΔE_{ST} = (0.07 ± 0.03) eV, whereas the activation energy required for the DF process calculated from an Arrhenius fit was found to be smaller, E_A = (0.031 ± 0.005) eV. However, the nonadiabatic coupling model still needs more study to fully explain the population transfer between the triplet states and give more insight into the dynamical mechanisms for highly efficient TADF. The mixing between ^{3}LE and ^{3}CT states also gives insights why some efficient TADF emitters do not show simple superposition of both the donor and acceptor ^{3}LE phosphorescence, and it may be because the phosphorescence spectrum also shows some ^{3}CT character, as the result triplet states is a mix of both, ^{3}LE and ^{3}CT. Finally, with consideration of vibronic coupling the rISC rate can then be defined as equation 2.7, according to second-order perturbation theory:

$$k_{rISC} = \frac{2\pi}{\hbar}\left|\frac{\langle {}^1\psi_{CT}|\hat{H}_{SOC}|{}^3\psi_{LE}\rangle\langle {}^3\psi_{LE}|\hat{H}_{vib}|{}^3\psi_{CT}\rangle}{\delta({}^3E_{LE} - {}^3E_{CT})}\right|^2 \delta({}^3E_{CT} - {}^1E_{CT}) \qquad (2.7)$$

The above equation takes into account the local excited triplet state as a mediator to the rISC and TADF process.

In line with this work, further theoretical study[34] also characterized the nature of the states involved in the rISC process. They showed that these electronic states are comprised of a mixture of LE and CT state contributions that vary with chemical structure and dynamically evolve following the changes in the molecular conformation and local dielectric environment, aspects discussed in this thesis.

2.5.3.2 Challenges of TADF Mechanism

When designing TADF molecules it is important to ensure two conditions: i. a small energy gap between the singlet and triplet states, ^{1}CT, ^{3}CT and ^{3}LE (ΔE_{ST}), to maximize the rISC process and ii. suppression of the internal conversion pathways available for the singlet and triplet excited states, to maximize emission yields. Condition i occurs by minimization of the electron exchange energy, J, and has been extensively studied in D-A and D-A-D type

molecules. However, characteristic ii is not a straightforward task, and minimizing IC to obtain a strong fluorescence yield in molecules with strong CT character has been a challenge. The desired molecule should have a photoluminescence quantum yield close to 1 with a short emissive state lifetime; this is to ensure harvested triplets do not cycle back to the triplet state and to avoid decay by non-radiative pathways. This requires strong coupling of the ^{1}CT to the ground state. However, to ensure a very small ^{1}CT–^{3}CT energy gap (which is a requirement for efficient rISC), D-A orthogonality is required which effectively decouples the ^{1}CT states from the ground state. Solving this seemingly paradoxical situation is not yet fully understood, but with TAT-3DBTO$_2$ emitter[27], work presented in chapter 7, a rISC rate > 10^7 s^{-1} whilst retaining a PLQY ~ 1 through near degenerate multiple excited states arising from the multi D-A structure was achieved.

Two other well-known challenges for TADF emitters concerning OLED performance are: efficiency roll-off with increasing current to attain high brightness; and moderate external quantum efficiency (EQE) values. Many of the TADF emitters show higher roll-off and lower EQE than those observed in devices based on phosphorescence emission (PH-OLEDs)[35], which contain costly heavy elements such as Ir and Pt. Major challenges also persist concerning the full understanding of the mechanism, mainly the rISC process, which has a rate strongly affected by the environment in which the emitter is dispersed, the regio-isomerization of the molecules and the different conformations that the molecules can access.

2.6 Organic Light Emitting Diodes

2.6.1 Design and Operation

An organic light emitting diode (OLED) is composed of a stack of organic layers with specific functions, sandwiched between two inorganic electrodes (cathode and anode) which inject opposite carriers (electrons and holes, respectively) through the organic layers. Exciton recombination occurs in the emissive layer. With this mechanism in mind, it is possible to design structures that promote carrier injection, transport, or exciton blocking in order to have recombination in the desired layer (see Figure 8). General requirements should be considered in the choice of materials for OLEDs:

- Materials should be morphologically stable and form uniform vacuum-sublimed films;

- The HOMO-LUMO energy levels of each layer should be ideally aligned according to their specific function in the device as shown in Figure 8;
- The triplet energy of the layers should be analysed in order to avoid exciton quenching, particularly in layers close to the emissive layer;
- The carrier mobility of each layer should be suitably adjusted for good charge carrier balance by means of optimising the thickness of each layer.

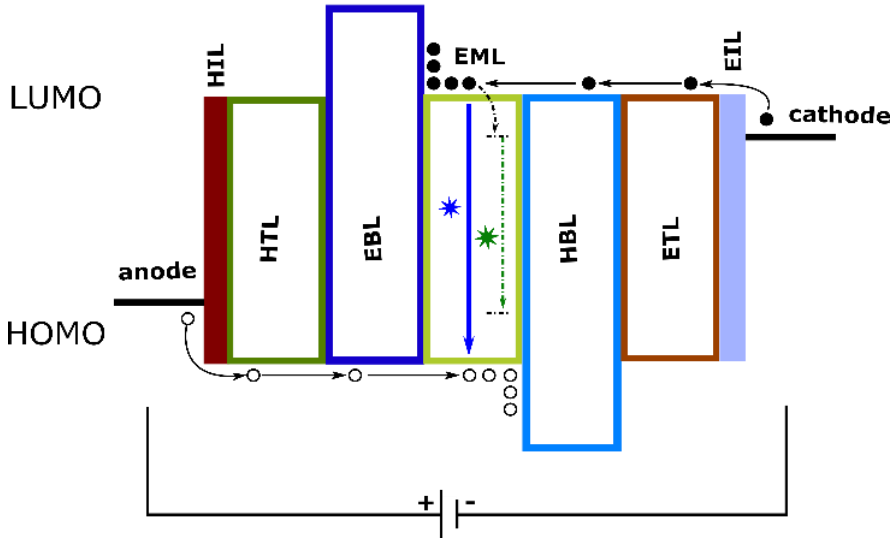

Figure 8 Ideal OLED structure. From left to right: HIL - hole injection layer; HTL- hole transport layer; EBL- electron blocking layer; EML- emissive layer; HBL- hole blocking layer; ETL- electron transport layer; EIL- Electron injection layer. Figure adapted from de Sa Pereira *et al.*[36].

The cathode is the electrode responsible for the injection of electrons into the device. Metals having a low work function, such as Li, Ca, and Mg, are desirable, as large differences in work function between the metal and organic layers limit the electron injection at the cathode-organic layer interface[37]. However, those metals are very reactive and susceptible to oxidation in air without an appropriate passivation. Therefore, more environmentally stable electrodes such as Aluminium (Al) are needed. Al was used as the cathode layer in the devices produced in this work, however, the high work function of Al results in lower luminous efficiency and higher operating voltage in OLEDs. To overcome this problem, a thin layer (1 nm) of lithium fluoride (LiF) was evaporated between the Al and the organic layer as LiF layer lowers the electron-injection barrier at the Al-organic layer interface[38].

The hole transport layer (HTL) fulfils the role of assisting the injection of holes from ITO and transporting them across the other organic layers, while the electron transport layer (ETL) has

the function of transporting the electrons from the metal cathode throughout the device. In all devices produced in this work, commercially available NPB (*N*,*N*′-bis(naphthalen-1-yl)-*N*,*N*′-bis(phenyl)-benzi dine) was used as the HTL and TPBi (1,3,5-tris(*N*-phenylbenzimidazol-2-yl)benzene) as ETL, due to their well-known high performance transport properties.

The blocking layers, either hole (HBL) or electron (EBL) are commonly introduced in the OLED design to decrease the energy barrier between the transport and emissive layers (EML), but also to confine the carriers in the EML. Therefore, what defines a good HBL is the low HOMO level and/or low hole mobility. The same can be said about EBL, but with high LUMO level and/or low electron mobility. Many studies have shown that the insertion of an blocking layer leads to both improved colour purity and higher quantum efficiencies[39,40]. In this work, TCBPA (4,4'-(Diphenylmethylene)bis(N,N -diphenylaniline)) and TCTA (Tris(4-carbazoyl-9-ylphenyl)amine) were used as EBL.

The EML is typically a host–guest layer that incorporate emitters as dopants (guests) in appropriate host matrices. This is adopted to avoid general concentration quenching and ensure high emission efficiency[41,42]. However, to simplify the device structure/fabrication and to reduce fabrication cost, it is desirable that OLEDs could be made with non-doped EML, but, to date, reports of efficient OLEDs using non-doped EML are still rare[43]. Typical commercial host materials used in this work were: CBP (4,4′-Bis(N-carbazolyl)-1,1′-biphenyl), DPEPO (Bis[2-(diphenylphosphino)phenyl]ether oxide), mCP (1,3-Bis(N-carbazolyl)benzene) and BCPO, (bis-4-(N-carbazolyl)phenyl)phenylphosphine oxide). The choice of the host material was made considering mainly their HOMO-LUMO levels, triplet levels and carrier mobility (with a preference for ambipolar hosts).

Finally, the injection of holes into the device occurs via the anode layer, and indium tin oxide (ITO) is the most common anode used in OLEDs. ITO is one of the most widely used transparent conducting oxides because of its electrical conductivity and optical transparency. However, a compromise must be made between conductivity and transparency, since increasing the thickness of ITO increases the concentration of charge carriers leading to better conductivity, but decreases its transparency. In this work, a thin film of ITO (100 nm) purchased from Ossila with a sheet resistance of 20 Ω/cm^2, previously treated by UV–ozone to decrease the potential barrier between ITO-organic layer[44], was used as the anode in all devices.

2.7 References Chapter 2

1. Köhler, A. & Bässler, H. Triplet states in organic semiconductors. *Mater. Sci. Eng. R Reports* **66,** 71–109 (2009).
2. Turro, N. J., Ramammurthy, V. & Scaiano, J. C. *Principles of Molecular Photochemistry*. (2009).
3. Marian, C. M. Spin-orbit coupling and intersystem crossing in molecules. *Wiley Interdiscip. Rev. Comput. Mol. Sci.* **2,** 187–203 (2012).
4. Ogiwara, T., Wakikawa, Y. & Ikoma, T. Mechanism of Intersystem Crossing of Thermally Activated Delayed Fluorescence Molecules. *J. Phys. Chem. A* **119,** 3415–3418 (2015).
5. Niu, L. B. *et al.* Hyperfine interaction vs. spin–orbit coupling in organic semiconductors. *RSC Adv.* **6,** 111421–111426 (2016).
6. Zimmt, M. B., Doubleday, C., Gould, I. R. & Turro, N. J. Nanosecond flash photolysis studies of intersystem crossing rate constants in biradicals: structural effects brought about by spin-orbit coupling. *J. Am. Chem. Soc.* **107,** 6724–6726 (1985).
7. Kohler, A. & Bassler, H. *Electronic Processes in Organic Semiconductors*. (Willey-VCH, 2015).
8. Luo, Y. & Aziz, H. Correlation between triplet-triplet annihilation and electroluminescence efficiency in doped fluorescent organic light-emitting devices. *Adv. Funct. Mater.* **20,** 1285–1293 (2010).
9. Wu, Z. *et al.* Management of Singlet and Triplet Excitons: A Universal Approach to High-Efficiency All Fluorescent WOLEDs with Reduced Efficiency Roll-Off Using a Conventional Fluorescent Emitter. *Adv. Opt. Mater.* **4,** 1067–1074 (2016).
10. Sinha, S. & Monkman, A. P. Delayed electroluminescence via triplet-triplet annihilation in light emitting diodes based on poly[2-methoxy-5-(2′-ethyl-hexyloxy)-1,4-phenylene vinylene]. *Appl. Phys. Lett.* **82,** 4651–4653 (2003).
11. Kondakov, D. Y. Characterization of triplet-triplet annihilation in organic light-emitting diodes based on anthracene derivatives. *J. Appl. Phys.* **102,** (2007).
12. Monkman, A. P. Singlet Generation from Triplet Excitons in Fluorescent Organic Light-Emitting Diodes. *ISRN Mater. Sci.* **2013,** 670130 (2013).
13. Reindl, S. & Penzkofer, A. Higher excited-state triplet-singlet intersystem crossing of some organic dyes. *Chem. Phys.* **211,** 431–439 (1996).
14. Larkin, J. M., Donaldson, W. R., Foster, T. H. & Knox, R. S. Reverse intersystem crossing from a triplet state of rose bengal populated by sequential 532- +1064-nm laser excitation. *Chem. Phys.* **244,** 319–330 (1999).
15. Hu, D., Yao, L., Yang, B. & Ma, Y. Reverse intersystem crossing from upper triplet levels to excited singlet: a 'hot excition' path for organic light-emitting diodes. *Philos. Trans. R. Soc. A Math. Phys. Eng. Sci.* **373,** 20140318–20140318 (2015).
16. Torres Ziegenbein, C. *et al.* Triplet Harvesting with a Simple Aromatic Carbonyl.

ChemPhysChem **18,** 2305 (2017).

17. Endo, A. *et al.* Thermally Activated Delayed Fluorescence from Sn4+-Porphyrin Complexes and Their Application to Organic Light Emitting Diodes - A Novel Mechanism for Electroluminescence. *Adv. Mater.* **21,** 4802–4806 (2009).

18. Dias, F. B. *et al.* The Role of Local Triplet Excited States in Thermally-Activated Delayed Fluorescence: Photophysics and Devices. *Adv. Sci.* **3,** 1–10 (2016).

19. Palmeira, T. & Berberan-Santos, M. N. Kinetic Criteria for Optimal Thermally Activated Delayed Fluorescence in Photoluminescence and in Electroluminescence. *J. Phys. Chem. C* **121,** 701–708 (2017).

20. Dias, F. B. Kinetics of thermal-assisted delayed fluorescence in blue organic emitters with large singlet-triplet energy gap. *Philos. Trans. R. Soc. A Math. Phys. Eng. Sci.* **373,** 20140447–20140447 (2015).

21. Grabowski, Z. R., Rotkiewicz, K. & Siemiarczuk, A. Dual fluorescence of donor-acceptor molecules and the Twisted Intramolecular Charge Transfer (TICT) states. *J. Lumin.* **18–19,** 420–424 (1979).

22. Dias, F. B. *et al.* Intramolecular charge transfer assisted by conformational changes in the excited state of fluorene-dibenzothiophene-S,S-dioxide co-oligomers. *J. Phys. Chem. B* **110,** 19329–19339 (2006).

23. Lim, B. T., Okajima, S., Chandra, A. K. & Lim, E. C. Radiationless transitions in electron donor-acceptor complexes: selection rules for S1 → T intersystem crossing and efficiency of S1 → S0 internal conversion. *Chem. Phys. Lett.* **79,** 22–27 (1981).

24. Aydemir, M. *et al.* Synthesis and investigation of intra-molecular charge transfer state properties of novel donor–acceptor–donor pyridine derivatives: the effects of temperature and environment on molecular configurations and the origin of delayed fluorescence. *Phys. Chem. Chem. Phys.* **17,** 25572–25582 (2015).

25. dos Santos, P. L. *et al.* Engineering the singlet-triplet energy splitting in a TADF molecule. *J. Mater. Chem. C* **4,** 3815–3824 (2016).

26. Haseyama, S. *et al.* Control of the Singlet–Triplet Energy Gap in a Thermally Activated Delayed Fluorescence Emitter by Using a Polar Host Matrix. *Nanoscale Res. Lett.* **12,** 1–5 (2017).

27. dos Santos, P. L. *et al.* Triazatruxene: A Rigid Central Donor Unit for a D-A 3 Thermally Activated Delayed Fluorescence Material Exhibiting Sub-Microsecond Reverse Intersystem Crossing and Unity Quantum Yield via Multiple Singlet-Triplet State Pairs. *Adv. Sci.* **5,** 1700989 (2018).

28. Huang, R. *et al.* The contributions of molecular vibrations and higher triplet levels to the intersystem crossing mechanism in metal-free organic emitters. *J. Mater. Chem. C* **5,** 6269–6280 (2017).

29. Nobuyasu, R. S. *et al.* Rational Design of TADF Polymers Using a Donor-Acceptor Monomer with Enhanced TADF Efficiency Induced by the Energy Alignment of Charge Transfer and Local Triplet Excited States. *Adv. Opt. Mater.* **4,** 597–607 (2016).

30. Santos, P. L. *et al.* Engineering the singlet–triplet energy splitting in a TADF molecule. *J. Mater. Chem. C* **4,** 3815–3824 (2016).

31. Ogiwara, T., Wakikawa, Y. & Ikoma, T. Mechanism of Intersystem Crossing of Thermally Activated Delayed Fluorescence Molecules. *J. Phys. Chem. A* **119,** 3415–3418 (2015).

32. Gibson, J., Monkman, A. & Penfold, T. The Importance of Vibronic Coupling for Efficient Reverse Intersystem Crossing. *ChemPhysChem* **17,** 2956–2961 (2016).

33. Gibson, J. & Penfold, T. J. Nonadiabatic coupling reduces the activation energy in thermally activated delayed fluorescence. *Phys. Chem. Chem. Phys.* **19,** 8428–8434 (2017).

34. Olivier, Y., Moral, M., Muccioli, L. & Sancho-García, J.-C. Dynamic nature of excited states of donor–acceptor TADF materials for OLEDs: how theory can reveal structure–property relationships. *J. Mater. Chem. C* **5,** 5718–5729 (2017).

35. Minaev, B., Baryshnikov, G. & Agren, H. Principles of phosphorescent organic light emitting devices. *Phys. Chem. Chem. Phys.* **16,** 1719–1758 (2014).

36. de Sa Pereira, D., Data, P. & Monkman, A. P. Methods of Analysis of Organic Light. *Disp. Imaging* **2,** 323–337 (2017).

37. Sheats, J. R. *et al.* Organic Electroluminescent Devices. *Science (80-.).* **273,** 884–888 (1996).

38. Hung, L. S., Tang, C. W. & Mason, M. G. Enhanced electron injection in organic light-emitting devices using Al/LiF electrodes. *Appl. Phys. Lett.* **70,** 152–154 (1997).

39. Weichsel, C., Reineke, S., Lüssem, B. & Leo, K. Influence of the Electron Blocking Layer on the Performance of Multilayer White Organic Light-Emitting Diodes. *MRS Proc.* **1402,** mrsf11-1402-u08-40 (2012).

40. Adamovich, V. I. *et al.* New charge-carrier blocking materials for high efficiency OLEDs. **4,** 77–87 (2003).

41. Park, Y. H., Kim, Y., Sohn, H. & An, K.-S. Concentration quenching effect of organic light-emitting devices using DCM1-doped tetraphenylgermole. *J. Phys. Org. Chem.* **25,** 207–210 (2012).

42. Zhang, Y. Q., Zhong, G. Y. & Cao, X. A. Concentration quenching of electroluminescence in neat Ir(ppy)3 organic light-emitting diodes. *J. Appl. Phys.* **108,** 083107 (2010).

43. Tsai, W.-L. *et al.* A versatile thermally activated delayed fluorescence emitter for both highly efficient doped and non-doped organic light emitting devices. *Chem. Commun.* **51,** 13662–13665 (2015).

44. Kim, S. Y., Lee, J.-L., Kim, K.-B. & Tak, Y.-H. Effect of ultraviolet–ozone treatment of indium–tin–oxide on electrical properties of organic light emitting diodes. *J. Appl. Phys.* **95,** 2560–2563 (2004).

Chapter 3: Materials and Experimental Methods

The aim of this chapter is to give the background information behind the data collection process. This covers the organic materials used, sample preparation, optical measurements and device production and testing. The samples used in this work are solutions and solid state films. The experimental techniques used are classified into three groups: i. steady state measurements (absorption, photoluminescence and photoluminescence quantum yield), ii. time resolved measurements (time gated acquisition and time correlated single photon counting) and iii. electrochemistry (cyclic voltammetry). The time resolved techniques provide more information than those available from the steady state data, however the steady state techniques were used as the first step to investigate all molecules studied here. At the end of this chapter, the fabrication and testing of organic light emitting diodes is discussed.

3.1 Organic Materials Studied

In this thesis, a large number of emitters, host compounds and transport layer materials for devices production were studied. The D-A-D and D-A_3 type molecules as well as there donor (D) and acceptor (A) units were synthesized in the chemistry department at Durham University. The emitter that shows excited-state intramolecular proton transfer (ESIPT) TQB was synthesised at OPERA, Kyushu University, Japan. The commercial D and A compounds used in the exciplex systems and the host materials were purchased from Sigma Aldrich and Lumtec. Table 1 summarize all chemical structures of the compounds studied, their names, commercial names and the chapter where their optical and electrical properties were investigated in this thesis.

For photophysical study, the compounds were used as purchased from the companies. For devices fabrication, all compounds were previously purified by vacuum sublimation under a temperature gradient[1], which is a method known to be most effective for separation of impurities from an organic solid as the impurities show a vapor pressure sufficiently different from the desired product.

Chemical Structure	Name	Commercial Name	Chapter
Donor and Acceptor units			
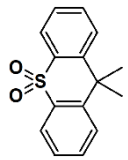	9,9-dimethylthioxanthene-*S*,*S*-dioxide	**TXO2**	**4**
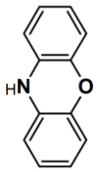	Phenoxazine	**Phenoxazine**	**4**

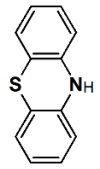	Phenothiazine	**Phenothiazine**	**5**
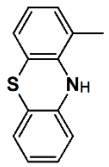	Methyl-Phenothiazine	**Methyl-Phenothiazine**	**5**
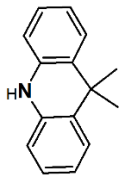	9,9-dimethyl-10H-acridine	**Acridine**	**6**
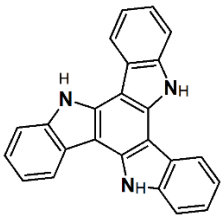	Triazatruxene	**Triazatruxene**	**7**
D-A-D Type molecules			
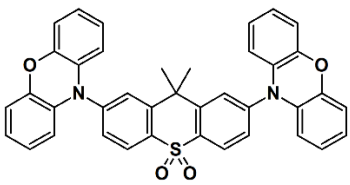	2,7-bis(phenoxazin-10-yl)-9,9-dimethylthioxanthene-*S*,*S*-dioxide	**DPO-TXO2**	**4**

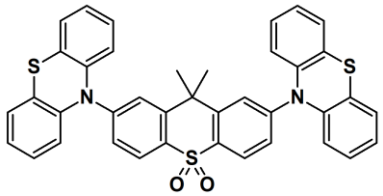	2,7- bis(phenothiazin-10-yl)-9,9-dimethylthioxanthene-*S*,*S*-dioxide	**DPT-TXO2**	**5**
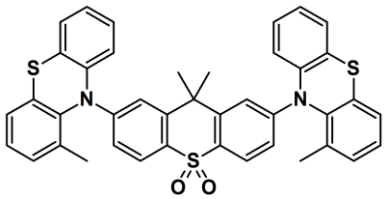	2,7-bis(1-methylphenothiazin-10-yl)-9,9-dimethylthioxan-thene-*S*,*S*-dioxide	**DMePT-TXO2**	**5**
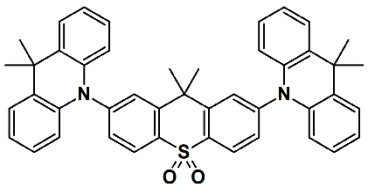	2,7-bis(9,9-dimethyl-acridin-10-yl)-9,9-dimethylthioxan-thene-*S*,*S*-dioxide	**DDMA-TXO2**	**6**
D-A$_3$ Type Molecules			
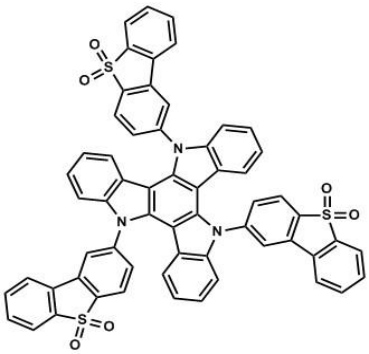	5,10,15-tris(5,5-dioxido-dibenzo[b,d]thiophen-2-yl)-10,15-dihydro-5H-diindolo[3,2-a:3',2' c]carbazole	**TAT-3DBTO$_2$**	**7**

Excited-state intramolecular proton transfer (ESIPT) molecule			
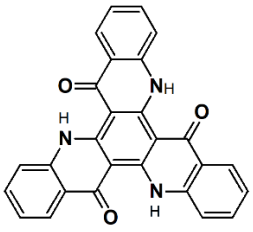	Triquinolonobenzene	**TQB**	**9**
D and A compounds used in exiplex systems			
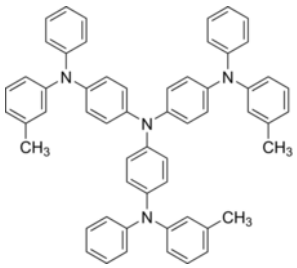	4,4′,4″-Tris[phenyl(m-tolyl)amino]triphenylamine	**m-MTDATA**	**8**
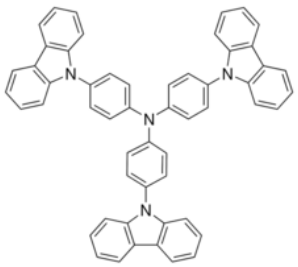	Tris(4-carbazoyl-9-ylphenyl)amine	**TCTA**	**8**
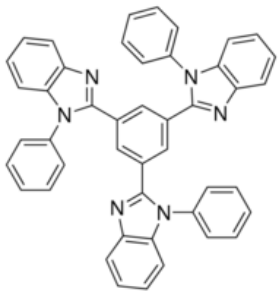	2,2′,2"-(1,3,5-Benzinetriyl)-tris(1-phenyl-1-H-benzimidazole)	**TPBi**	**8**
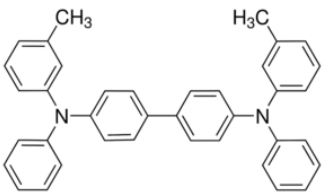	N,N′-Bis(3-methylphenyl)-N,N′-diphenylbenzidine	**TPD**	**8**

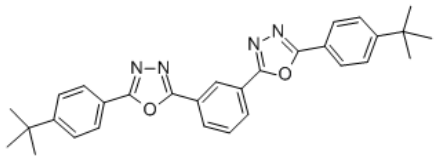	1,3-Bis[2-(4-tert -butylphenyl)-1,3,4-oxadiazo-5-yl]benzene	**OXD-7**	**8**
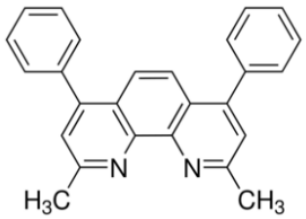	Bathocuproine	**BCP**	**8**
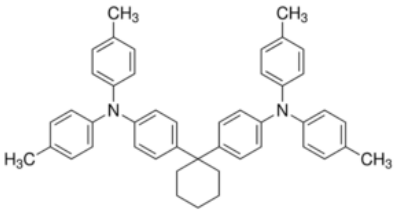	4,4′-Cyclohexylidenebis[N,N bis(4-methylphenyl) benzenamine]	**TAPC**	**8**
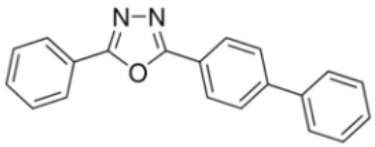	2-Phenyl-5-(4-biphenylyl)-1,3,4-oxadiazole	**PBD**	**8**
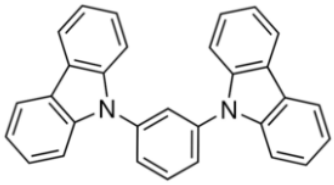	1,3-Bis(*N*-carbazolyl)benzene	**mCP** *****also used as host material	**8**
Host compounds			
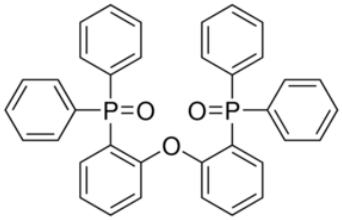	Bis[2-(diphenylphosphino)phenyl] ether oxide	**DPEPO**	**4**

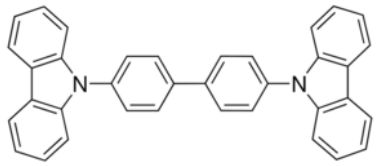	4,4′-Bis(*N*-carbazolyl)-1,1′-biphenyl	**CBP**	**4**
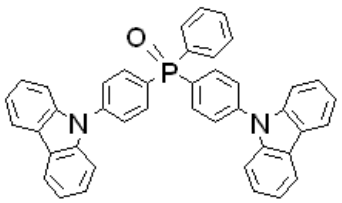	Bis-4-(*N*-carbazolyl)phenyl)phenylphosphine oxide	**BCPO**	**7**
Compounds used as transport layers in OLEDs			
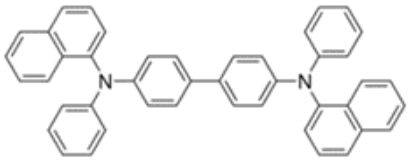	N,N' -Bis(naphthalen-1-yl)-N,N' -bis(phenyl)-benzidine	**NPB**	**4,6,7**
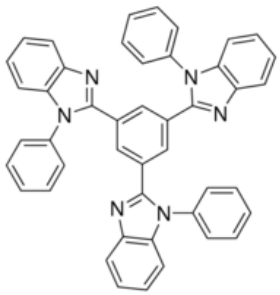	2,2′,2"-(1,3,5-Benzinetriyl)-tris(1-phenyl-1-H-benzimidazole)	**TPBi**	**4,6,7**
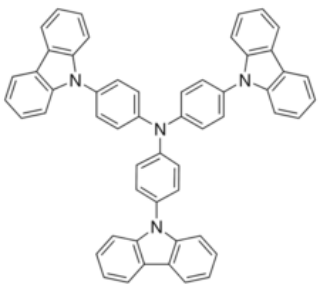	Tris(4-carbazoyl-9-ylphenyl)amine	**TCTA**	**7**

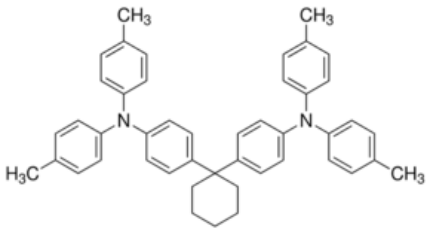	4,4′-Cyclohexylidenebis[*N*,*N*-bis(4-methylphenyl)benzenamine]	**TAPC**	**6**

Table 1 Chemical structure of the compounds studied in this thesis, their name, commercial name and chapter that they are presented.

3.2 Sample Preparation

3.2.1 Solution

In order to prepare solution samples, the materials were dissolved in solvents with different polarities and stirred for several hours to ensure fully dissolved solutions and avoid aggregation at room temperature. Some molecules showed poor solubility in nonpolar solvents, and in those cases the solution was stirred at higher temperature (between 50 and 100℃ according to the evaporation temperature of the solvent used). Concentrations were typically in the range of 10^{-3} M to 10^{-6} M and measurements were taken both in air and degassed environments using quartz cuvettes and degassing cells with a path length of 1 cm. Solutions were degassed to remove all the oxygen dissolved in it by 4 pump freezing-thawing cycles. This is a crucial step in the analysis of emission which involves triplet states as oxygen is efficient quencher because its ground state is triplet. The quenching mechanism results in an oxygen molecule in an excited singlet state and the emitting molecule in the ground state. The measurements in solutions were performed at room temperature or low temperature using a liquid nitrogen cryostat. The lowest temperature available was 78 K, which is the boiling point of the nitrogen, however for each solution the lowest temperature was chosen depending on the freezing point of the solvent used.

3.2.2 Solid State

Three types of solid state samples were studied: i. spin coated films, ii. drop casted films and iii. evaporated films.

For the fabrication of spin-coated films, solutions with different concentrations were dropped onto sapphire or quartz substrates. The substrate and solution were then spun at a controlled speed for a fixed time, with controlled acceleration up to the required spinning speed. Typical parameters are: Spinning Time = 60 seconds and speed = 500 rpm. This method results in uniform films. For drop-cast films, solutions with different concentrations were dropped onto substrates and left for a few hours under vacuum to dry. Although it is hard to control the thickness and uniformity of films using this method, it is quite simple to produce samples and the films can be prepared using a very small amount of material. The specific concentration of each solution is given in the end of each result chapter. Evaporated films were produced by thermal evaporation (single or co-evaporation) using a commercial Kurt-Lesker Spectros II deposition system (described in detail in session 3.6.1). This method results in very homogeneous thin films with controlled thickness monitored by quartz crystal sensors. However, for this method a large amount of compound is required to produce films with thicknesses of approximately 200 nm. The thickness of the films were measured using an Ellipsometer (J Woollam, JAW5964), which is a known accurate technique used to measure thickness and refractive indexes of thin films on solid surfaces[2].

3.3 Steady State Measurements

3.3.1 Optical Absorption

The absorption spectra of the molecules show the probability of absorption of a photon by a molecule and its variation with wavelength. The light intensity, which is a measure of the flux of photons in the optical beam, decreases through the sample as the photons are absorbed. There is a uniform probability of absorption throughout the sample, and the intensity reaching any distance *x* into the sample is given by the Beer-Lambert law[3]:

$$I = I_0 e^{-\varepsilon x c} \tag{3.1}$$

where I is the intensity of the transmitted light, I_0 the intensity of the incident light, ε is the molar extinction coefficient, which is a strong function of wavelength, and c the concentration of the sample.

Absorption spectra were collected using a Shimadzu model UV3600 double beam spectrophotometer, which has a reference beam and a sampling beam that passes through the sample. All spectra were collected in atmosphere at room temperature. The absorption

spectrum shows the relation between optical density (OD) as a function of wavelength. OD is defined by the equation below:

$$OD = \log \frac{I_0}{I} \tag{3.2}$$

The most intense peaks in a spectrum are often associated with $\pi \rightarrow \pi^*$ transitions. For these transitions, a red shift is observed when the polarity of the solvent is increased. Weak transitions can be associated with $n \rightarrow \pi^*$ transitions, and show a blue shift when increasing the polarity of the solvent. The observation of $\sigma \rightarrow \sigma^*$ transitions requires high energy (typically below 150 nm), which is below the cut-off wavelength of the solvents, being difficult to detect.

3.3.2 Photoluminescence

After photoexcitation the molecules may emit light through a transition back to the ground state. This process is named photoluminescence (PL). Through measurement of the PL, we are able to detect any type of radiative emission from the sample (from 250 to 750 nm) after the absorption of photons. The choice of wavelength used to excite the sample is based on the analysis of the absorption spectrum. Steady state PL measurements were performed using Jobin Yvon Horiba Fluoromax 3 or Fluorolog spectrometer, both equipped with a xenon lamp as the excitation source. Measurements could be conducted both at room and low temperatures (using liquid nitrogen). The latter spectrometer has double grating monochromators and, consequently, the highest spectral resolution.

3.3.3 Photoluminescence Quantum Yield

Photoluminescence quantum yield (PLQY) is an intrinsic property of organic light emitting material which can be defined by the ratio of absorbed photons to emitted photons:

$$\Phi_{PLQY} = \frac{Emitted\ Photons}{Absorbed\ Photons} \tag{3.3}$$

PLQY were acquired using a PLQY Quantaurus (QY Hamamatsu), which was kindly loaned from Hamamatsu UK, or using a Horiba Jobin Yvon SPEX Fluorolog 3, which is based in the Chemistry Department at Durham University. Both set up are equipped with a calibrated integrating sphere. The PLQY values were calculated according to the literature method, which consider the direct and secondary excitation of the films[4].

3.4 Time Resolved Spectroscopy

3.4.1 Time Correlated Single Photon Counting

Time-correlated single photon counting (TCSPC) is used to give estimates of excited state lifetimes with a temporal resolution of 5 picoseconds. This technique relies on detection of single photons using low excitation intensities, and by measuring a large number of excitation-decay events high resolution decay curves can be obtained. The time between excitation pulse and the detection of photon emitted by the sample is counted as one event. Part of the excitation pulse reaches a fast photodiode, and gives a signal pulse "start or stop" in the timer. The other part of the excitation pulse reaches the sample, and then the photons emitted by the sample are detected giving a second signal pulse "stop or start" to the timer. TCSPC setup using forward mode has the signal collected by the photodiode as "start" and the signal detected by the sample as "stop". Because the vast majority of TAC circles (Time-to-Amplitude Converter, which is a fast clock), will be started by the "start" pulse, but never stopped by a "stop" signal, it needs to be reset at overflow. The electronics is kept busy much more than the amount actually needed and, to avoid this, TCSPC electronics can be operated in *reverse mode*, which is the mode used in the OEM group. In this case, the signal cable carrying the high count rate from the light source is connected to the "stop" input and the low rate is connected to the "start". In the reverse mode, the time axis of the memory histogram is internally reversed in order to see photon events with long retardation times demonstrated at the right part of the time axis. The scheme of the TCSPC setup is shown in Figure 9.

During the data acquisition process, initially the decay curve representing the instrument response function (IRF) is collected, which is the signal collected in the wavelength of the laser emission. The full width at half-maximum height (FWHM) of this curve corresponds to the temporal response of the system. Then, the emission from the sample is collected, and each event (delta time between start + stop) is stored in a histogram (see right bottom of Figure 9), which will represent the waveform of the curve decay. The excited-state population decays with a rate $K_r + K_{nr}$ according to[5]:

$$dn(t)/dt = -(K_r + K_{nr})n(t) \tag{3.4}$$

where $n(t)$ is the number of excited molecules at time *t* following excitation, K_r is the emissive rate, and K_{nr} is the non-radiative decay rate. Emission is a random event, and each excited

fluorophore has the same probability of emitting in a given period of time. This results in an exponential decay of the excited state population[5]:

$$n(t) = n_0 \ \exp(-{}^{t}/_{\tau}) \tag{3.5}$$

where n_0 is the number of excited molecules at time zero and τ is lifetime, the inverse of the total decay rate, $\tau = (K_r + K_{nr})^{-1}$. In a fluorescence experiment we do not observe the number of excited molecules, but rather the fluorescence intensity, which is proportional to (t). Hence, equation 3.5 can also be written in terms of the time-dependent intensity $I(t)$. Thus, we have the usual expression for a single exponential decay[5]:

$$I(t) = I_0 \exp\left(-{}^{t}/_{\tau}\right) \tag{3.6}$$

where I_0 is the intensity at time 0. In general, the inverse of the lifetime is the sum of the rates, which depopulate the excited state. The fluorescence lifetime can be determined from the slope of a plot of log $I(t)$ versus t, but more commonly by fitting the data to assumed decay models. Equation 3.6 represents the case where the decay is mono-exponential, it means that just one radiative process is responsible for the emission, however, many cases have multiple exponential decay components. A multi-exponential decay with n components of emission is given by:

$$I(t) = \sum_{i=1}^{n} I_{0i} \exp\left(-{}^{t}/_{\tau_i}\right). \tag{3.7}$$

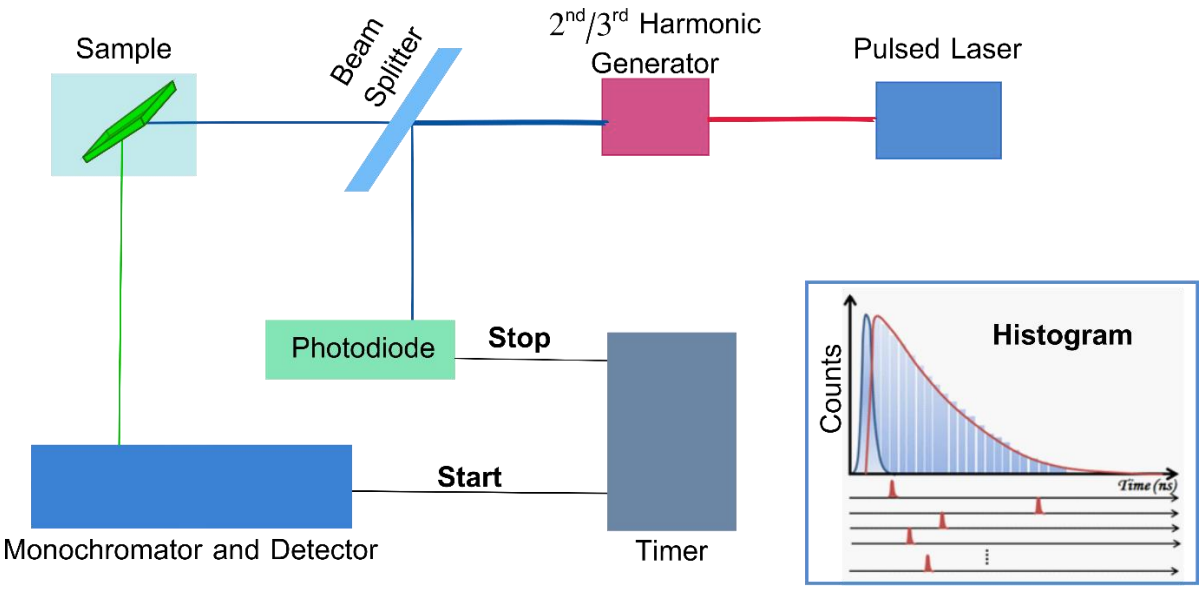

Figure 9 Time-correlated single photon counting (TCSPC) setup using a reserve mode. The TCSPC has other optics, such as filters, lenses and polarizers, which are not shown in the diagram. The figure on the bottom right shows an example of a histogram obtained from the

technique, where the blue curve is the instrument response function (IRF) of the system and the red curve is the decay curve of the emitter.

The TCSPC system used here consists of a Ti: Sapphire (Coherent Mira 900) pulsed laser tuned to 864 nm that pumps a commercial harmonic generator (Harmonixx, Photonic solutions) from which the 2nd or 3rd harmonic can be generated producing 432 nm and 288 nm, respectively. Part of the excitation beam then goes to a fast photodiode (Becker & Hickl GmbH) and part excites the sample. The emission from the samples is focused onto the entrance slits of a subtractive double monochromator (Acton Research Corporation 2400s) which has a ~4 nm spectral resolution. The monochromator gratings and slit sizes can be automatically controlled by Labview software. The instrument response function (IRF) of the system is ~27 ps, which is the resolution of the system, however deconvolution techniques can be used to obtain lifetimes faster than this value. In the results presented in this thesis, the lifetime of the species were in the *nanosecond* timeframe; thus, deconvolution techniques were not applied and the decay times were estimated simply by fitting the data using multi-exponentials on OriginPro9.

3.4.2 Time Gated Acquisition – iCCD

Time resolved emission spectra were collected using a system equipped with a pulsed Nd:YAG laser emitting at 355/266 nm (150 ps FWHM) or nitrogen laser emitting at 337 nm (3 ns FWHM) as the excitation source. The photons emitted by the sample are focused into a spectrograph equipped with a 300 lines/mm grating and imaged onto a sensitive gated intensified charge coupled device (iCCD) camera (Stanford Computer Optics) with 200 ps resolution. The iCCD camera and laser are synchronized in two different ways according to the laser used. For the Nd:YAG laser, the trigger is an electrical [TTL] pulse sent from the laser to the iCCD. For the nitrogen laser, part of the excitation beam is sent into a photodiode which sends electrical pulses to the iCCD. To obtain the spectra we use the camera control software (4 Picos software) where time delays (TD, time that the collection of photons emitted by the sample starts) and integration time (IT, how long the photons are collected) can be controlled with 0.1 ns accuracy.

As the camera is synchronized with the laser by the electrical pulse coming from the Nd:YAG laser, the zero time, i.e., time when the pulse arrives to excite the sample, needs to be determined. For this, many spectra of the laser were collected with short integration times and

delay times that covers the whole jitter (deviation of the periodic signal) region. Figure 10b gives an example of this measurement. The zero time was then established as the peak of the Gaussian curve (975.5 ns). The resolution of the technique is also determined from Figure 10b as the full width at half maximum obtain in the curve, as the resolution is given by the slowest component of the system which is the electrical trigger jitter (for Nd:YAG laser).

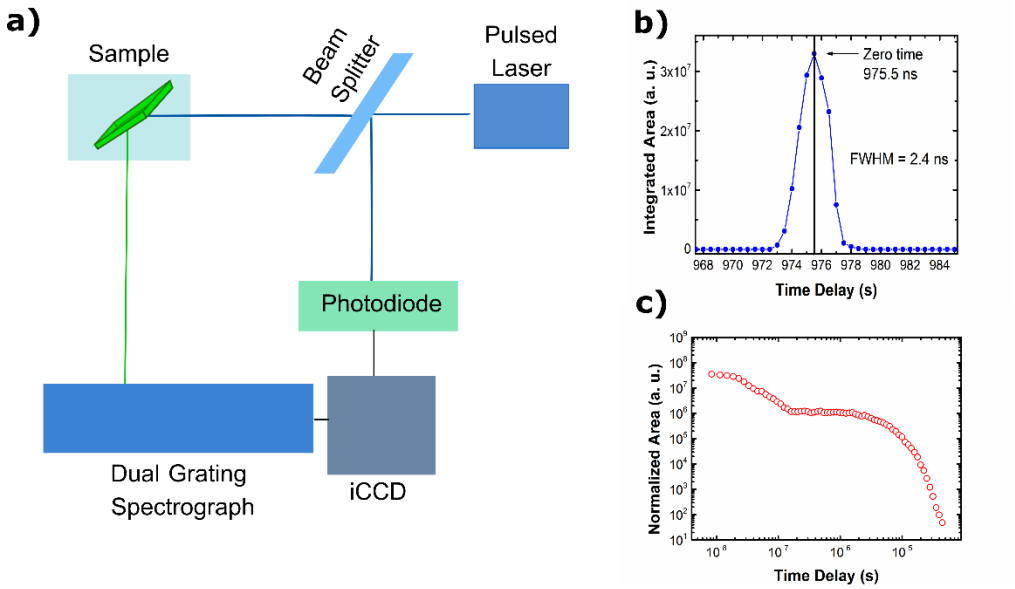

Figure 10 a) Time Gated Acquisition setup. The Pulsed laser can be trigged to the iCCD by an optical trigger as shown in the figure or by an electrical trigger. The setup has other optics, such as filters, irises and lenses, which are not shown in the diagram. b) Integrated time resolved spectra of the Nd:YAG laser beam collected using 0.5 ns integration time. c) Example of a decay curve that can be built from the data obtained using this technique.

Apart from the individual spectra measured with specified delay and integration times, this technique allows us to build a decay curve by collecting several spectra with logarithmically increasing TD and IT (self-written program). This guarantees that the TD are equally spaced on a logarithmic scale and do not overlap. The area of each spectrum can be plotted *versus* the TD and then decay curves as shown in Figure 10c are built. Sample temperature is controlled (from 80 to 320 K) using liquid nitrogen as cooling system.

3.5 Electrochemistry

3.5.1 Cyclic Voltammetry

Cyclic voltammetry was used in this work mainly to identify the HOMO and LUMO energy levels of organic compounds for the design of OLEDs. The energy of the LUMO can be approximated by the electron affinity, which is the energy required to add an electron to an atom or molecule in the gas phase. On the other hand, the energy of the HOMO is approximated by the minimum energy required to remove an electron from an atom or molecule.

In the cyclic voltammetry technique, the measurement is performed in non-reactive electrolyte solution using three electrodes: i. working electrode (platinum), ii. reference electrode (Ag/AgCl) and iii. counter electrode (platinum). The potential is measured between the working electrode and the reference electrode, while the current is measured between the working electrode and the counter electrode. Figure 11a shows a schematic of the apparatus used in this experiment.

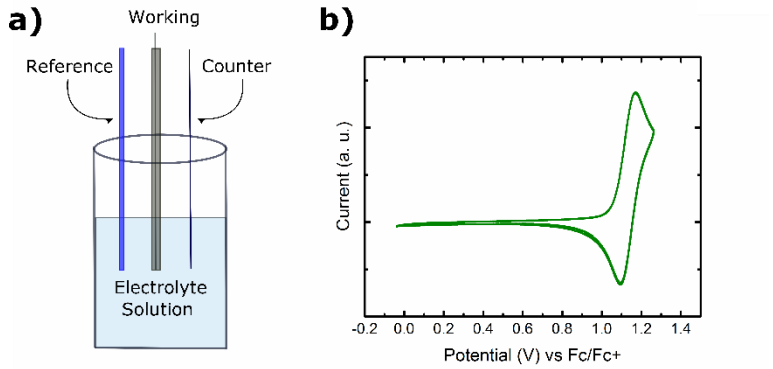

Figure 11 a) Cyclic voltammetry apparatus and b) cyclic voltammogram curve.

HOMO and LUMO energies are calculated from measure potentials using the following equations[6]:

$$HOMO = -5.1 + (-E_{onset}^{oxi}) \quad (3.8)$$

$$LUMO = -5.1 + (-E_{onset}^{red}) \quad (3.9)$$

where E_{onset}^{oxi} and E_{onset}^{red} are calculated from CV potential by using ferrocene as a standard. The ferrocene potential is used as a standard as this potential is assumed to show little variation, because the iron centre is relatively well shielded from environmental effects by the two

surrounding cyclopentadienyl ligands. The value 5.1 eV shown in the equations 3.10 and 3.11 is the approximation made to the Fermi scale, as the reduction and oxidation potentials are measured in solution and the HOMO/LUMO energies are estimated in vacuum.

The experiments were recorded using a BioLogic potentiostat SP-300 at a scan rate of 50 mV s^{-1}. Experiments were conducted in dry and deoxygenated (by bubbling N_2) solutions, as the presence of moisture and oxygen may lead to new oxidation and/or reduction peaks. Tetrahydrofuran or dichloromethane solutions with Bu_4NBF_4 (0.1 M) were used as the supporting electrolyte. The choice of the solvent was made considering the potential window required as different solvents have different voltage limits. The more reversible the redox couple is, the more similar the oxidation peak will be in shape to the reduction peak. Figure 11b shows an example of reversible couple.

3.6 Organic Light Emitting Diodes Production

3.6.1 Fabrication of Organic Light Emitting Diodes

OLEDs were produced by vacuum thermal evaporation (VTE) of organic materials, previously purified by vacuum sublimation, and inorganic layers. A Kurt-Lesker Spectros II deposition system was used, which has 6 organic and 3 inorganic evaporation sources. The evaporation activity (deposition rate) as well as the thickness of the films were controlled using 4 sensors, allowing the evaporation of two different materials at once (co-evaporation). The sensors use a quartz crystal microbalance (QCM) to measure the mass variation per unit area by measuring the change in frequency of a quartz crystal resonator, giving an accuracy of less than one nanometre in the thickness of the evaporated layers. The rate at which the material is deposited on the sensor is not equal the rate at which it is deposited on the substrate. The ratio of the two rates is called tooling factor. The tooling factor (TF) of each material was calculated by measuring the thickness (T) of material deposited on SiO_2 substrates using the Ellipsometer (J Woollam, JAW5964) and comparing it to the thickness (T') measured by the monitor system. The tooling factor value was then obtained using the equation:

$$TF = T\frac{TF'}{T'} \tag{3.10}$$

where TF' is the initial tooling factor used. The evaporation activity was monitored by a software program called SQS-242 (Inficon Inc.). Heating and shutter control, used to achieve to acquired the desired deposition rates, were controlled using a company supplied software.

During the deposition process, the chamber was kept under high vacuum ~ 10^{-6} mbar, which is maintained by a primary roughing vacuum pump (SCROLLVAC, Leybold Ltd), 10^{-2} mbar, and a turbo molecular vacuum pump (TMU521P, Pfeiffer Ltd), 10^{-6} mbar. To guarantee the uniformity of the layers, the substrates were rotated (10 RPM) and the target materials were heated continuously. A schematic of the chamber layout is shown in Figure 12.

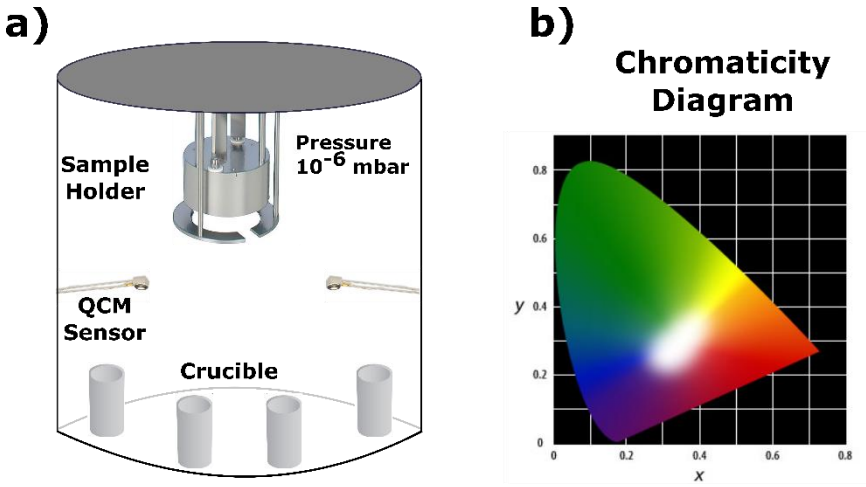

Figure 12 a) Scheme of Kurt-Lesker Spectros II deposition system used for OLED production. b) Chromaticity diagram obtained in the OLEDs testing.

The ITO anode substrates used were purchased from Ossila with a sheet resistance of 20 Ω/cm^2 and indium tin oxide (ITO) thickness of 100 nm. Each substrate had two pixels sized 4 mm × 2 mm and two pixels sized 4 mm × 4 mm pre patterned. The substrates were cleaned by sonication in acetone and isopropanol bath (15 minutes each) and finally in a UV Ozone cleaner (Femto, Diener electronic) for 6 minutes. The ozone cleaner uses a high-power UV light source to generate ozone which breaks down surface contaminants into volatile compounds. These volatile compounds evaporate from the surface leaving no trace.

The latest step in the OLED production after deposition is encapsulation. It consists in gluing a thin glass cover plate on the top of the device to prevent exposure to the air, as OLEDs are very sensitive to oxygen and moisture. However, the devices produced in this thesis were tested straight after production, and the exposure to the air was less than 10 minutes, making the encapsulation process unnecessary.

3.6.2 Testing of Organic Light Emitting Diodes

In order to evaluate the performance of an OLED, both electrical and optical characterizations are required. This gives information on parameters such as the overall device efficiency, power consumption and colour. The optoelectrical performance of OLEDs is measured with an integrating sphere (Labsphere) coated with a highly reflective material (Spectralon). The integrating sphere is previously calibrated to determine the correct and standardized device efficiency by taking account of the response of the measurement system as a whole. The calibration lamp (with a known power spectrum output, Pcal (λ) in W/nm) is positioned in the same sample position used for the devices testing[7]. Considering the emitting area of the device, a home written computer program (LabView) performs all the calculations necessary for its characterization, producing all the typical parameters of OLED devices: applied voltage (V), current (mA), current density (mA/cm^2), luminous flux (lm), brightness or luminance (cd/m^2), current efficiency (cd/A), power efficiency (lm/W), external quantum efficiency (%), commission internationale de l'eclairage (CIE) and electroluminescence spectra (EL).

The flow of electrical charge carriers through the device is given by the current observed at different applied voltages. This parameter can also be analysed per unit of area, i.e. current density. The luminous flux is defined as the amount of light capable of sensitizing the human eye per unit of time, which is standardized with the eye's maximum sensitivity at 555 nm (under normal lighting conditions as the eye response can change significantly by changing the light levels). The luminous intensity, measured in candela (cd), takes into account the colour of the light and its direction, i.e., the luminous flux emitted in to a specific solid angle. The brightness or luminance is the luminous intensity per unit of area. In application, typical brightness levels of mobile displays are between 100-400 cd/m^2 while for general illumination, higher values of around 5000 cd/m^2 are required.

The current efficiency (n_C) can be calculated as the amount of current flowing through the device (I) with an emissive area (A) necessary to produce a certain luminance (L), given by[7]:

$$n_C = \frac{LA}{I} = \frac{L}{J} \tag{3.11}$$

The power efficiency (n_P) is given by the ratio of the optical flux to the electrical input. Considering the current efficiency at an applied voltage (V_i) it is given by[7]:

$$n_P = n_C \frac{f_D \pi}{V_i} \tag{3.12}$$

where f_D is the angular distribution of the emitted light in the forward hemisphere considering its two angles (θ, φ) and the light intensity measured (I) in the forward direction[7]:

$$f_D = \frac{1}{I_0 \pi} \int_0^{\pi/2} \int_{-\pi}^{+\pi} I(\theta, \varphi) \sin(\theta) d\varphi d\theta \quad (3.13)$$

The external quantum efficiency (EQE) of an OLED is described as the product between the charge balance factor (γ), the fraction of spin-allowed excitons (η_{ST}), the photoluminescence quantum yield (Φ_{PL}) and the outcoupling efficiency (η_{out}) which is usually estimated between 20 - 30 %[7–9]:

$$EQE = \gamma \cdot \eta_{ST} \cdot \Phi_{PL} \cdot \eta_{out} \quad (3.14)$$

Finally, the colour emitted by the device is analysed by the CIE chromaticity coordinates[10] and by the electroluminescence spectrum. The CIE links the distributions of wavelengths in the electromagnetic visible spectrum with the physiological perceived colours in human colour vision, and represents this link graphically in a chromaticity diagram with coordinates X and Y (see Figure 12b).

3.7 Data Analyses

3.7.1 Determination of Onset Energy

The energy associated with each state, i.e., singlet and triplet states, was estimated using the onset of their emission spectra. The choice of the onset energy over the peak position comes from the fact that, in many of the cases studied in this thesis, the phosphorescence spectrum shows vibronic resolution, thus the energy associated with the triplet states was determined as the onset of the electronic transition (0-0 transition). For consistency, the energy of the singlet states was also determined using the same method, even though transitions involving charge transfer states are featureless and therefore not possible to clearly identify the 0-0 transition. Figure 13 gives an example of the determination of the energy associated with a $^1CT \rightarrow S_0$ transition and also how the error (± 0.2 eV) related with it was estimated. Moreover, due to error propagation, the error on the energy splitting between two states was increased and calculated to be (± 0.3 eV).

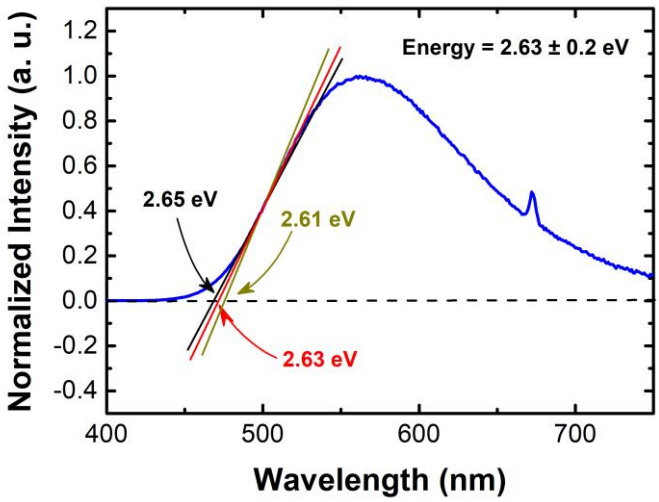

Figure 13 Determination of the energy associated to the $^1CT \rightarrow S_0$ transition. The same method was used to determine all energies associated to different transitions throughout this thesis.

3.7.2 Determination of Chromophore Lifetime

The lifetimes of the emitters were estimated by fitting the decay curves using OriginPro9 software. Typically, a *Reduced Chi-Sqr* value close to 1 indicates a good fit, and it implies that the difference between observed data and fitted data is consistent with the error variance. Commonly, the decay curves show the best fitting using multi-exponential decays, which is usually associated with emission of different conformations of the molecules:

$$y = \Sigma\, I_i.e^{(-(x-x0)/\boldsymbol{\tau}_i)} \tag{3.15}$$

and the average decay times were calculated using the following equation:

$$\boldsymbol{\tau}_{Average} = (\Sigma\, I_i\boldsymbol{\tau}_i^2) / (\Sigma\, I_i\boldsymbol{\tau}_i). \tag{3.16}$$

3.7.3 Determination of rISC Rate

One of the methods used to estimate the rISC rate was based on the equation 3.10:

$$k_{RISC} = \frac{\int I_{DF}(t)dt}{\int I_{PF}(t)dt}.\frac{1}{\tau_{DF}} \tag{3.17}$$

where the integral of DF and PF regions were calculated from the area below the prompt fluorescence and delayed fluorescence decay curves, respectively (see Figure 14), and τ_{DF} is the lifetime of the DF component.

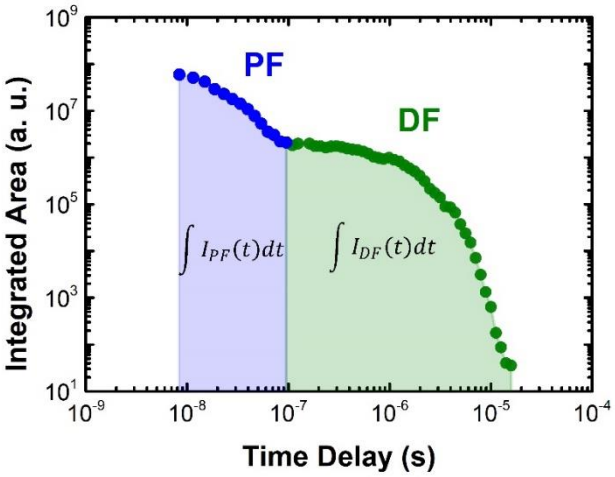

Figure 14 Integral of PF (blue) and DF (green) regions used to estimate the rate of rISC. The same method was used to determine the integrals for all decay curves throughout this thesis.

3.7.4 Contribution of Triplet States to the Overall Emission

The contribution of triplet excited states to the overall emission was determined by comparing the emission intensity in non-degassed (aerated) and degassed solutions. The emission spectra obtained in degassed and non-degassed solutions commonly match each other, showing that DF and PF come from the same ^{1}CT state. Figure 15 shows an example of this analyses. In this case, the CT emission increases by a factor of 5.8 when oxygen is removed, thus the contribution of DF is 82%, considering that only the triplet states are quenched by oxygen and therefore the degassed emission spectrum has contribution from both, PF + DF, whereas non-degassed emission spectrum has only PF contribution.

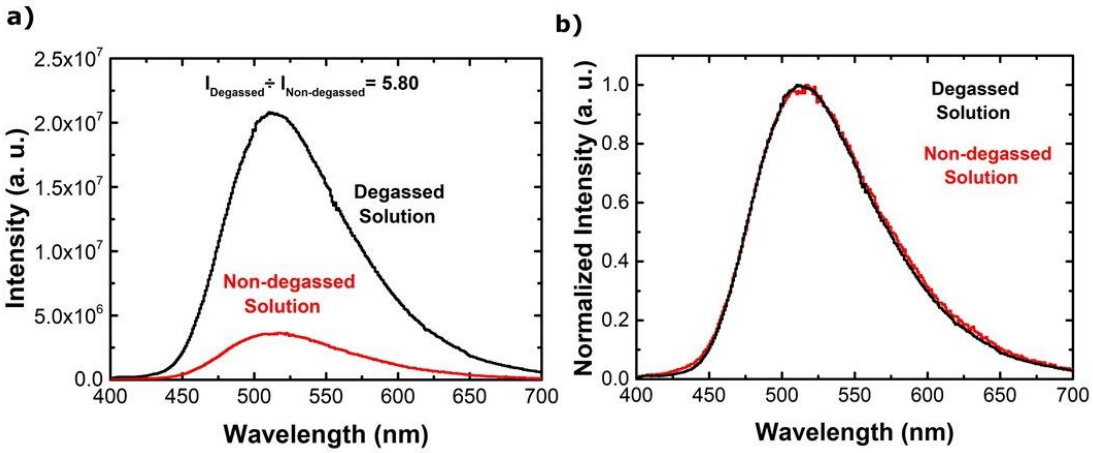

Figure 15 Analyses of the contribution from the triplet states to the overall emission. The same method was used to estimate the triplet states contribution throughout this thesis in solutions

and solid state. a) the emission spectra in a degassed solution and in non-degassed (aerated) solution and b) their normalized spectra.

3.8 References Chapter 3

1. Drechsel, J. *et al.* Influence of Material Purification by Vacuum Sublimation on Organic Optoelectronic Device Performance. *SID Symp. Dig. Tech. Pap.* **37,** 1692 (2006).
2. McCrackin, F. L., Passaglia, E., Stromberg, R. R. & Steinberg, H. L. Measurement of the thickness and refractive index of very thin films and the optical properties of surfaces by ellipsometry. *J. Res. Natl. Bur. Stand. (1934).* **67,** 4 (1963).
3. Lakowicz, J. R. *Principles of Fluorescence Spectroscopy Principles*. (1999).
4. Pålsson, B. L. & Monkman, A. P. Measurements of Solid-State Photoluminescence Quantum Yields of Films Using a Fluorimeter. *Adv. Mater.* **14,** 933–935 (2002).
5. Hirvonen, L. M. & Suhling, K. Wide-field TCSPC: Methods and applications. *Meas. Sci. Technol.* **28,** (2017).
6. Cardona, C. M., Li, W., Kaifer, A. E., Stockdale, D. & Bazan, G. C. Electrochemical considerations for determining absolute frontier orbital energy levels of conjugated polymers for solar cell applications. *Adv. Mater.* **23,** 2367–2371 (2011).
7. de Sa Pereira, D., Data, P. & Monkman, A. P. Methods of Analysis of Organic Light. *Disp. Imaging* **2,** 323–337 (2017).
8. Gather, M. C. & Reineke, S. Recent advances in light outcoupling from white organic light-emitting diodes. *J. Photon. Energy* **5,** 057607 (2015).
9. Patel, N. K., Cina, S. & Burroughes, J. H. High-efficiency organic light-emitting diodes. *Ieee J Sel Top Quant* **8,** 346-361-- (2002).
10. Cowan, W. B. An inexpensive scheme for calibration of a colour monitor in terms of CIE standard coordinates. *ACM SIGGRAPH Comput. Graph.* **17,** 315–321 (1983).

Chapter 4: Engineering the Optical Singlet-Triplet Energy Gap in TADF Emitter

The key to engineering an efficient TADF emitter is to achieve a small energy splitting between a pair of molecular singlet and triplet states. This chapter makes important contributions towards achieving this goal. By studying the new TADF emitter 2,7-bis(phenoxazin-10-yl)-9,9-dimethylthioxanthene-*S*,*S*-dioxide (DPO-TXO2) and the donor and acceptor units separately, the available radiative and non-radiative pathways of DPO-TXO2 is identified. The optical energy splitting between singlet and triplet states is identified in four different environments, in solutions and solid state. It is further shown how the environment plays a key role in the fine tuning of the energy levels of the ^{1}CT state with respect to the donor ^3LE_D triplet state, which can then be used to control the optical ΔE_{ST} energy value. This study emphasizes the importance of the ^{3}LE states in TADF, which was crucial in laying out the requirements of a model to describe the TADF vibronic coupling mechanism, in terms of three excited states (^{1}CT, ^{3}CT and ^{3}LE) that need to come into resonance to achieve high TADF efficiency.

The work presented in this chapter was published in *Journal of Materials Chemistry C* (P. L. dos Santos, J. S. Ward, P. Data, A. Batsanov, M. R. Bryce, F. Dias, A. P. Monkman, *J. Mater. Chem. C* 2016, *4*, 3815). It was a collaborative work between the OEM group and the chemistry department, both at Durham University. P. L. dos Santos performed all steady state and time resolved photophysics measurements, the device fabrication, and device testing. Dr. J. S. Ward devised and performed the synthesis, purification and chemical characterization. Dr. P. Data performed the electrochemical measurements. X-ray measurements and their analysis were performed by Dr. A. Batsanov.

4.1 Introduction

This chapter describes the study of a D-A-D material, 2,7-bis(phenoxazin-10-yl)-9,9-dimethylthioxanthene-*S*,*S*-dioxide (DPO-TXO2), a TADF emitter formed from phenoxazine donors (D) and the 9,9-dimethylthioxanthene-*S*,*S*-dioxide (TXO2) acceptor (A) (see reference [1] for details on synthesis). Phenoxazine was chosen because of its strong electron donor character, due to its low ionization potential, and because it assumes a near orthogonal D-A structure. Moreover, phenoxazine has been less extensively explored when compared with carbazole and fluorene in OLED materials[2–6]. The dimethyl TXO2 acceptor unit was introduced because this A unit has a strongly folded and constrained structure which is in contrast to the very flexible diphenylsulfone[7] and the planar and rigid dibenzothiophene-*S*,*S*-dioxide units (previously studied by the OEM group[8,9]), which are both well-established in TADF molecules. In comparison with dibenzothiophene-*S*,*S*-dioxide[9], the conjugation between the two phenyl rings of TXO2 is disrupted by the dimethylmethylene bridge. The dimethyl groups were added to prevent any deprotonation at the bridging carbon. The folded TXO2 acceptor yields a high triplet energy and a shallow LUMO level, which affects the electron transport and injection into the emitter molecules in an OLED device requiting special attention to the device architecture.

Detailed studies of the photophysical properties of DPO-TXO2 together with its subunits and the device performance using different host materials are described in this chapter. The results show that DPO-TXO2 is a promising TADF emitter, having a small optical ΔE_{ST} in different environments, both in solutions and solid state. It is shown that the environment can be used to control the optical ΔE_{ST} energy gap and, also, the dynamics of the TADF mechanism when the ^{1}CT state is located below the ^{3}LE triplet state is elucidated. Moreover, OLED performance of DPO-TXO2 in DPEPO host is analysed.

4.2 Results and Discussion

4.2.1 Chemical Characterization

The chemical structure and the single-crystal X-ray molecular structure of DPO-TXO2 are shown in Figure 16a and b, respectively. The molecule has no crystallographic symmetry, but an approximate non-crystallographic mirror plane through S(1), O(1), O(2), C(7), C(14) and

C(15). The arene rings *A* and *B* of the acceptor form a dihedral angle of 137.8°. The twists around the N(1)-C(4) and N(2)-C(10) bonds, 89.9° and 73.2°, preclude significant intramolecular conjugation. The phenoxazine substituent at C(10) is folded along the N(2)…O(4) vector, while the phenoxazine substituent at C(4) is twisted. The dihedral angle between arene rings *C* and *D* equals 173.3°, that between *E* and *F* is 162.2°. The bonds N(1)-C(16) and N(1)-C(22) in the more planarized phenoxazine unit average 1.400(2) Å, bonds N(2)-C(28) and N(2)-C(34) in the more puckered one average 1.415(2) Å, while the non-conjugated bond distances N(1)-C(16) and N(1)-C(22) average 1.434(2) Å (see reference [1] for details on X-ray study).

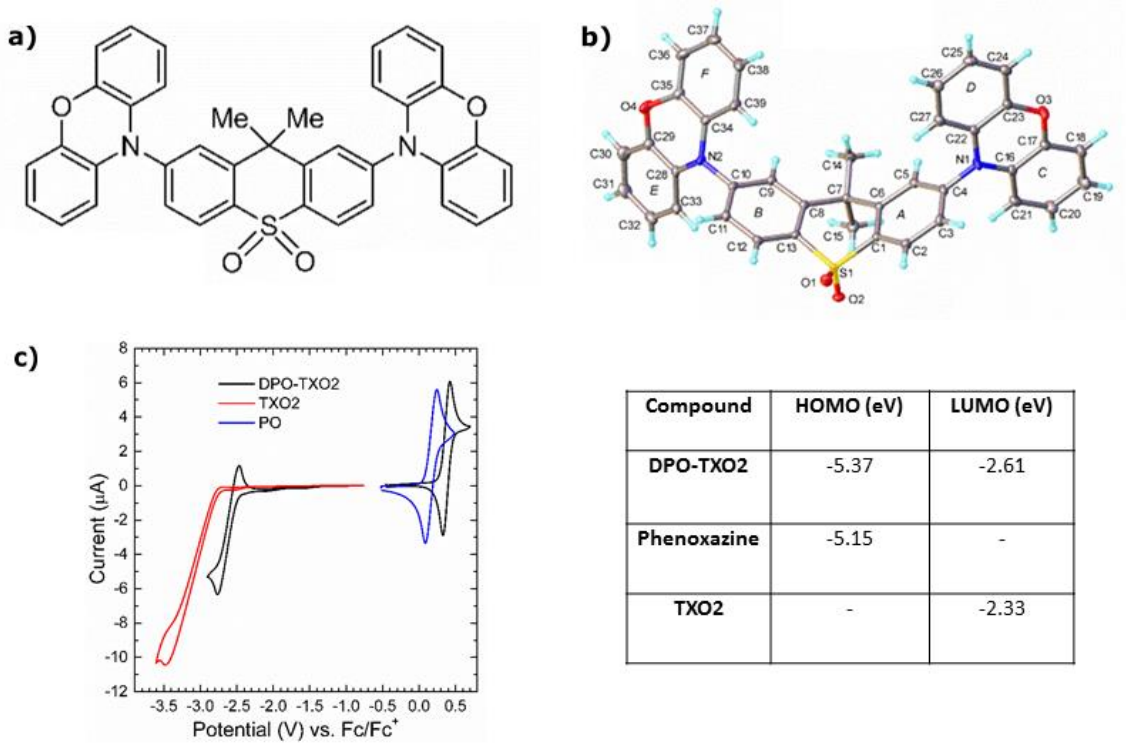

Compound	HOMO (eV)	LUMO (eV)
DPO-TXO2	-5.37	-2.61
Phenoxazine	-5.15	-
TXO2	-	-2.33

Figure 16 a) Chemical structure and b) X-ray molecular structure of DPO-TXO2. c) Cyclic voltammetry (CV) analysis by the estimation of the electron affinity and the ionization potentials for DPO-TXO2 (black), TXO2 acceptor unit (red) and phenoxazine (PO) (blue).

The HOMO-LUMO levels of DPO-TXO2 and its donor and acceptor units were investigated by cyclic voltammetry (CV) analyses (Figure 16c) and found to be at $HOMO_{DPO\text{-}TXO2}$= -5.37 eV, $LUMO_{DPO\text{-}TXO2}$= -2.61 eV, $HOMO_D$= -5.15 eV, $LUMO_A$= -2.33 eV. Consistent with the extensive twisting around the N(1)-C(4) and N(2)-C(10) bonds in the X-ray molecular structure, the CV data confirms that the HOMO and LUMO levels are largely localized on the donor and acceptor units respectively, as observed in other D-A-D type molecules[5,10,11]. This feature identifies DPO-TXO2 as a promising molecule for TADF; the near orthogonality of the

D and A components results in very small exchange energy and optical singlet-triplet energy gap. This feature should facilitate efficient rISC and TADF if the CT level is degenerate with the triplet states.

4.2.2 Solution State Photophysical Properties

Figure 17a shows the normalized optical absorption spectra of the acceptor (A) and donor (D) units as well as DPO-TXO2 molecule, measured in dilute methyl cyclohexane (MCH) solvent. The inset of Figure 17a shows the absorption peak around 390 nm in different solvents. In the DPO-TXO2 absorption spectrum, the first two absorption peaks (higher energy) also exist in the absorption spectra region of A and D molecules. The third peak, around 390 nm, does not appear neither in the D nor the A absorption spectra, and thus was assigned to the CT absorption in the D-A-D molecule. It shows a slight red shift by increasing the polarity of the solvent, which is associated with a predominantly $\pi \rightarrow \pi^*$ transitions. Figure 17b shows the normalized photoluminescence (PL) spectra of DPO-TXO2, and of the D and A single units, all in MCH solution with excitation around their absorption peak. Also in Figure 17b the inset graph shows the PL spectra of DPO-TXO2 in solvents of increasing polarity, showing a strong positive solvatochromism. Both the emission peak and full width at half maximum (FWHM) increase dramatically with solvent polarity. The DPO-TXO2 molecule emits blue light in MCH and green/yellow in dichlorobenzene. In the three solvents studied, the DPO-TXO2 PL spectra show clear and strong CT emission, evidenced by their Gaussian band shape and red-shift compared to the individual D and A spectra. In the less polar solvent (MCH), a blue shifted emission peaking around 370 nm is also observed and is assigned to residual donor emission (^1LE_D). This result shows that in MCH the radiative recombination from ^1LE_D can compete with electron transfer that populates the ^1CT state, indicating the weak electronic coupling between the donor ^1LE_D state and the molecular CT state. When DPO-TXO2 is excited at any of its three distinct absorption regions, the emission always arises from the CT state, indicating that the charge transfer occurs by excitation of the donor and the acceptor units or the direct CT transition. In other words, there is symmetry in the charge transfer process for hole and electron transfer, giving rise to the same CT emission.

After showing that the DF contribution in DPO-TXO2 is strongly dependent on the polarity of the medium (inset graph Figure 17b) within which the emitter is dispersed, I proceeded to investigate the causes of this strong influence by studying different environments. As the DPO-TXO2 excited state will be a linear combination of the all possible excited states in the system,

i.e., charge transfer and local excited states ($\psi = c_1 \, |D^*A\rangle_{Local} + c_2 \, |DA^*\rangle_{Local} + c_3 \, |D^+A^-\rangle_{CT}$), the delayed fluorescence in low and high polarity environments were studied. MCH solution was studied with the aim to investigate an environment where the DPO-TXO2 has weaker ion pair character in the CT state, i.e. the excited state retains strong local excited state character; and toluene where a strong CT character is observed.

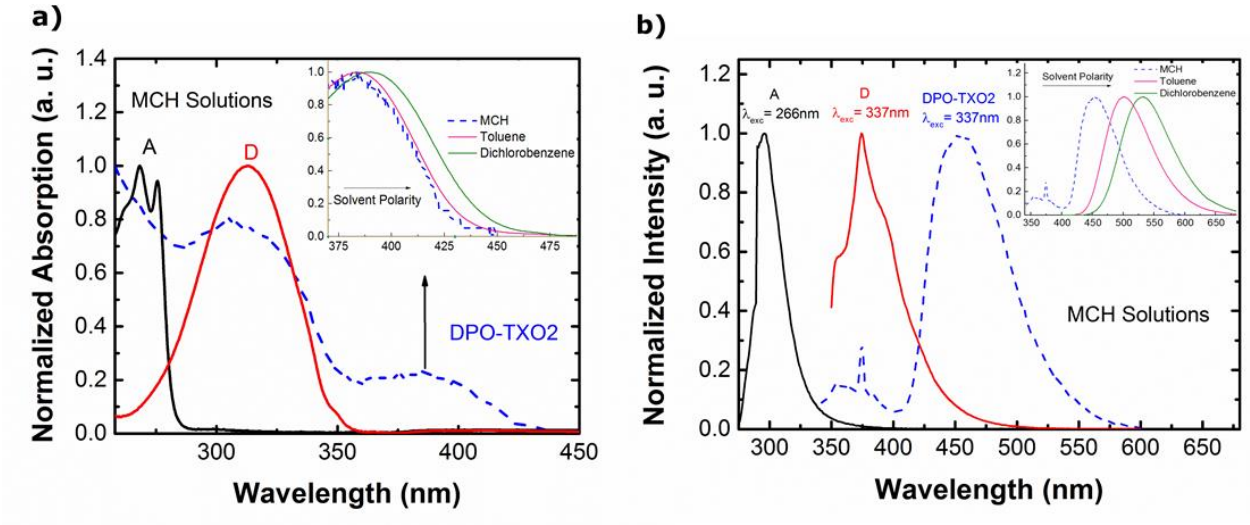

Figure 17 a) Optical absorption spectra of the acceptor (A), donor (D), and DPO-TXO2 molecules, all diluted in methyl cyclohexane (MCH) solvent. Inset graph - absorption spectra peak around 390 nm of DPO-TXO2 in different solvents. b) Normalized photoluminescence (PL) spectra of A, D and DPO-TXO2 molecules, all diluted in MCH solvent. Inset graph - PL of DPO-TXO2 in different solvents.

The contribution of triplet excited states to the overall emission was determined by comparing the emission intensity in non-degassed (aerated) and degassed solutions. The emission spectra obtained in degassed and non-degassed solutions match each other, showing that DF and prompt fluorescence come from the same ^{1}CT state. The CT emission increases by a factor of 3.10 when oxygen is removed, thus the contribution of DF is 52% (see Figure 18a), considering that just the triplet states are quenched by oxygen.

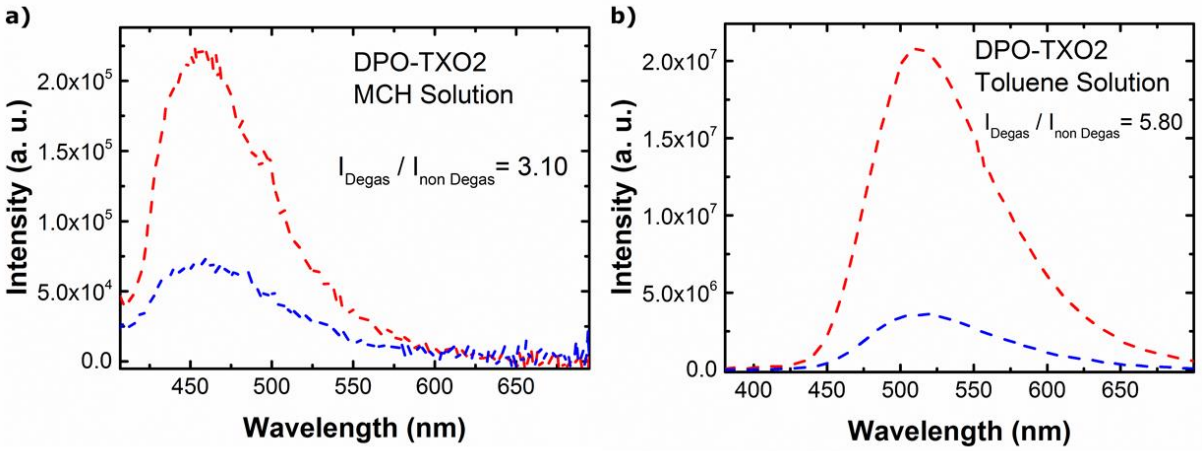

Figure 18 Photoluminescence spectra (PL) of DPO-TXO2 in degassed (red curves) and non-degassed (blue curves) in a) MCH and b) toluene solutions.

Figure 19a shows the decay curve of DPO-TXO2 in MCH solution from the early prompt emission (TD = 1.1 ns) to the end of the DF (TD = 0.14 ms), at different temperatures. The curves were obtained with 355 nm excitation. The decay curves are complex, prompt and delayed emission regions are not well defined, but the DF emission has clearly higher intensity at high temperatures, indicating the TADF mechanism. The analyses of the spectra (Figure 19b) in the entire region of study shows that at early times the emission spectra observed match the ^1LE_D emission of the donor. It is possible to identify the two regimes of the donor emission, a peak around 375 nm identified in the steady state measurements, and a dimer emission, peak around 450 nm, that can be seen just in the iCCD measurements (see Figure 20). Increasing the time delay, the emission spectra progressively shifts to longer wavelengths, moving from the ^1LE_D emission to stabilized ^{1}CT emission, passing through a region where both, ^{1}LED and CT emission, are observed, indicating very slow electron transfer, due to the decoupling between D and A units caused by near orthogonality between them even in the ground state (due to the N-C bridging bond). At TD = 14.9 ns the CT emission is clearly observed and has onset at (2.94 ± 0.02) eV. However, the emission shows a slight red-shift at very late times, indicating a contribution on the red edge from donor phosphorescence (PH). After TD = 0.8 μs, the PH emission is stabilized with onset at (2.78 ± 0.02) eV, and was collected until 0.14 ms.

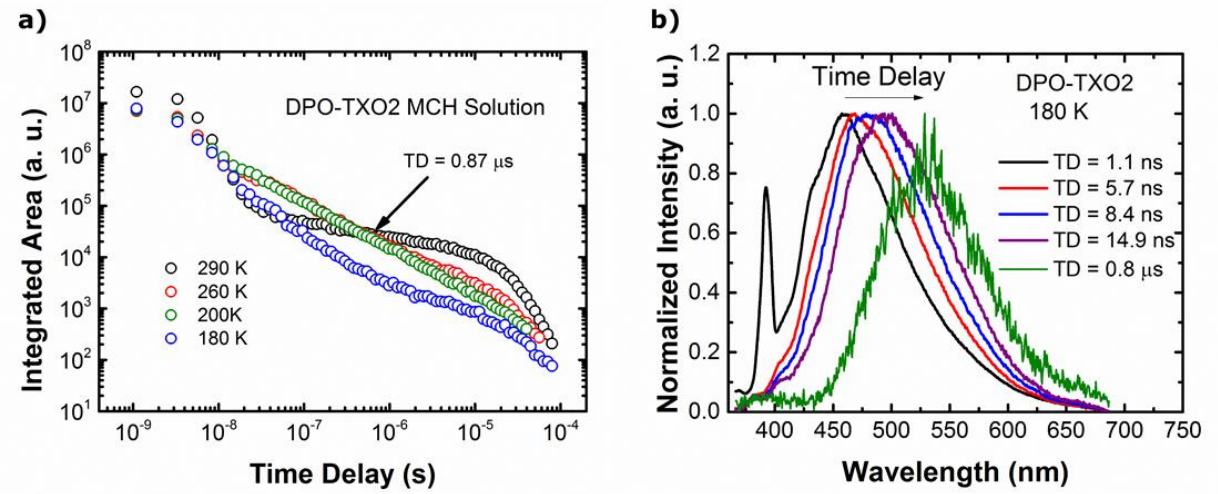

Figure 19 a) Time resolved fluorescence decay curves of DPO-TXO2 in MCH solution. The curves were obtained with 355 nm excitation. b) Time resolved normalized emission spectra in the entire region of analyses at 180 K.

The observed triplet emission comes from the local triplet state of the donor or/and the acceptor. Thus, the local triplet states (^{3}LE) of the donor and acceptor was investigated, studying these units separately. The ^3LE_D phosphorescence of the donor was found to have onset at (2.79 ± 0.02) eV in toluene solution, corroborating with the PH spectra obtained for DPO-TXO2, and also, with the triplet levels of phenoxazine reported previously in other solvents[12]. The PH spectra of the acceptor unit was found to have onset at (3.39 ± 0.02) eV, higher energy than the PH of DPO-TXO2. Thus, the triplet emission observed in DPO-TXO2 clearly comes from the donor units. Thus, the ^{1}CT state and the ^3LE_D state were identified in a MCH solution, and the splitting between these states was found to be ΔE_{ST} = (0.16 ± 0.03) eV.

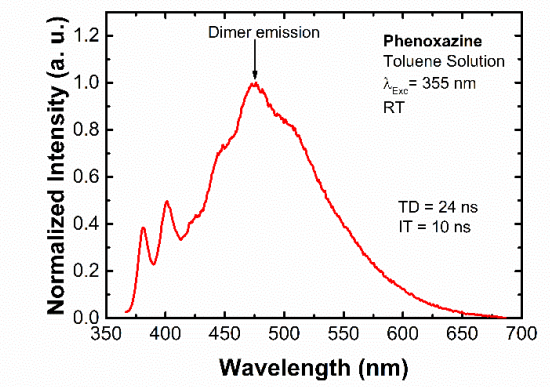

Figure 20 Time resolved emission spectra of Phenoxazine in toluene solution. The emission around 450 nm is observed just in the iCCD. The steady stady emission of Phenoxazine shows emission with peak around 375 nm as shown in figure Figure 17b.

The delayed fluorescence in toluene solution was also studied as it demonstrated to be a more stable environment for the CT state of DPO-TXO2. The contribution of DF to the overall emission in DPO-TXO2 was found to be 4.8 or 82% (see Figure 18b) indicating a much strong ion pair character to the CT state. Figure 21a shows the decay curve of DPO-TXO2 in toluene solution. There is a clear bi-exponential decay with a fast component of τ_{PF} =24.8 ns, assigned to the prompt fluorescence component (^{1}CT), and a longer decay of τ_{DF} = 4.61 μs, assigned to the delayed fluorescence component. The curve was obtained with 355 nm excitation. Also the ratio between I_{DF} and I_{PF}, the integral of the DF and PF regions respectively, was calculated and found to be $\bar{n}$ = 4.81, where $\bar{n}$ is emission contribution of TADF, in excellent agreement with the value calculated by the degassing test in toluene solution ($\bar{n}$= 4.80). From this, the reverse intersystem crossing rate constant was determined using equation 4.1 and shown to be 1.04 x10^6 s^{-1} [8].

$$k_{rISC} = \frac{\int I_{DF}(t)dt}{\int I_{PF}(t)dt} \cdot \frac{1}{\tau_{DF}} \qquad (4.1)$$

Figure 21b shows the decay curve of DPO-TXO2 toluene solution at different temperatures. The curves were obtained with 337 nm excitation. The decay curves of the DPO-TXO2 show four clear distinct regions, delineated by three well-defined crossing points: 51 ns, 5.6 μs and 63 μs. The decay below 51 ns, is dominated by ^{1}CT→S_0 prompt fluorescence. Between 51 ns and 63 μs the ^{1}CT→S_0 delayed fluorescence dominates, and ^3LE_D→S_0 phosphorescence is also clearly observed in the region from 63 μs to 1 ms. The decay curves at different temperatures show that the prompt region increases in emission intensity on cooling down the system, and at 180 K the onset of DF occurs at later times. In region A, the DF emission increases in intensity with increasing temperature, in accordance with the TADF mechanism, because of the increase in the available thermal activation energy. The intensity dependence of the DF emission in this region was analysed as a function of the laser excitation dose, and a linear gradient of 1.045 ± 0.005 was found (Figure 22a and b). This result confirms the thermally assisted mechanism as opposed to TTA. Region B however has an inverse temperature dependence; the intensity of the emission increases as the system temperature drops.

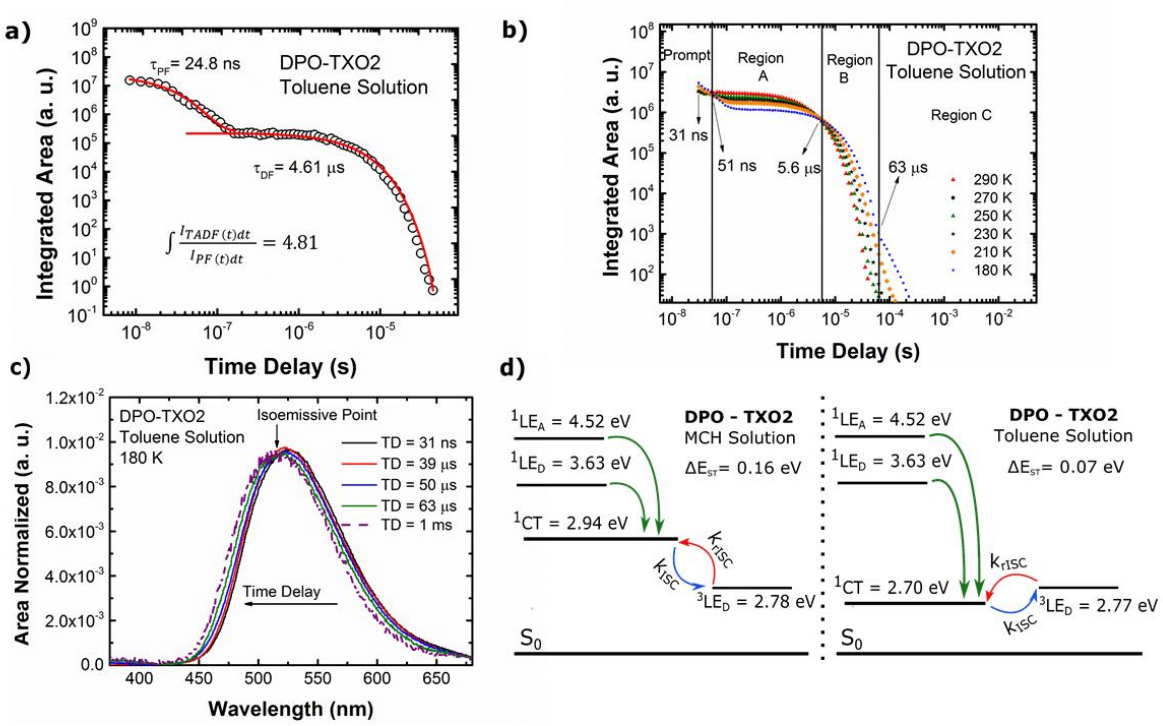

Figure 21 a) Time resolved fluorescence decay curves of DPO-TXO2 molecules in toluene solution at RT with 355 nm excitation b) at different temperatures with 337 nm excitation. c) Time resolved area normalized emission spectra in the entire region of analyses at 180 K. d) Energy level diagram describing the excited dynamics of DPO-TXO2 in toluene and MCH solutions, evidencing the local and charge transfer states.

The DF intensity dependence as a function of excitation dose in region B also shows a linear gradient (1.025 ± 0.004) (Figure 22c and d), confirming a monomolecular process. The behaviour of the temperature dependence in this region is unexpected and can be understood by analyses of the triplet lifetime (τ_T), given by equation 4.2:

$$\tau_T = \frac{1}{k_{rISC} + k_T} \qquad (4.2)$$

where k_{rISC} is the rate constant of rISC process and k_T is the sum of non-radiative and radiative triplet decays. At high temperature, $k_{rISC} >> k_T$, and the triplet lifetime is τ_T. At low temperature, k_{rISC} and k_T decrease, due to their temperature dependence, and consequently, τ_T increases, making the decay curve of DPO-TXO2 longer lived so phosphorescence occurs with higher efficiency at longer times where TADF no longer occurs. Hence, a crossing point at TD = 56 µs in the decay curves at different temperatures indicating the turning point in this TADF/phosphorescence competition is observed. Also, it should be mentioned that the dielectric constant of toluene slightly increases with decreasing

temperature[13]. Hence, at lower temperature, the CT state is slightly lower energetically, leading to an increased ΔE_{ST}, and consequently, weaker rISC and longer triplet lifetime. Region C shows the longest lived component of the decay curve. This appears just at low temperatures, vanishing at room temperature, and is assigned to the long lived ^3LE_D phosphorescence (PH).

Figure 21c shows the time evolution of the area normalized emission spectra at 180 K in toluene, giving the peak position of each spectrum. From TD = 31 ns to 39 µs, all the spectra have the same position, onset at (2.70 ± 0.02) eV, and same spectral shape. From TD = 39 µs to 63 µs a very slight and continuous blue shift is observed, due to the growing contribution of the ^3LE_D phosphorescence. The prompt and DF emission, until TD = 63 µs, have almost identical spectral line shape, showing that both originate from the same singlet excited state. Finally, after 63 µs the spectra achieve onset at (2.77 ± 0.02) eV and the same emission was collected until TD = 1 ms. The isoemissive point (identified in Figure 21c) gives a clear indication for the presence of two excited state species, firstly the ^{1}CT state and then a triplet state. The PH emission has onset very close to that found in MCH solution (2.78 ± 0.02) eV, showing that the phosphorescence of the donor does not change in different solvents. Thus, the ^{1}CT state and the ^3LE_D states were identified in a DPO-TXO2 toluene solution, and the optical splitting between these states was found to be ΔE_{ST} = (0.07 ± 0.03) eV. Additionally, the activation energy (E_A) required for the DF process was calculated from an Arrhenius fit of the temperature dependent DF emission intensity and found to be E_A = (0.031 ± 0.005) eV. As discussed in chapter 2, E_A is not exactly equal to the optical ΔE_{ST}, because it describes the thermal gap between ^{1}CT-^{3}CT. Comparing both environments, the contribution of delayed fluorescence is higher in toluene than in MCH solution, 82% and 52%, respectively. This is a direct consequence of the larger ΔE_{ST} in MCH solution. Also, the lifetime of the DF in MCH is clearly longer than in toluene, due to the larger $\Delta E_{ST,}$ corroborating observations in other TADF emitters[14]. It is important to notice that the ^3LE_D energy level in MCH and in toluene solutions differs by just (0.01± 0.02) eV, and the ^{1}CT energy levels change considerably with solvent polarity, causing a big difference in the energy splitting according to the environment. Therefore, the environment has a strong influence on the ΔE_{ST} energy value.

Figure 21d shows the full decay pathways available in DPO-TXO2 molecules dispersed in two different environments, MCH and toluene solutions. All the energy levels were taken from the onset of the spectra at 180 K in degassed solutions. Upon optical excitation of the donor or acceptor units, the population of ^{1}CT states are formed by electron or hole transfer. Intersystem crossing (direct and reverse) occurs between ^{1}CT and ^3LE_D (apart from ISC between local

states, i.e. $^1LE \rightarrow {}^3LE$), and the energy splitting between them is strongly dependent of the polarity of the system, mainly because of the strong solvatochromism experienced by the ^1CT state. The mechanism responsible for the delayed fluorescence in both cases is TADF. In MCH solution, ^3LE_D is located below ^1CT, excitons in the triplet levels must gain energy to match the singlet levels and then crossing the states, considering that rISC/ISC processes are adiabatic transitions. On the other hand, in toluene solution, ^3LE_D is located above the ^1CT, this is an unusual situation, but not forbidden as they are different states. This configuration does not prevent ISC/rISC to occur, the singlet and triplet states are very close to each other, and this is the important feature to promote these process.

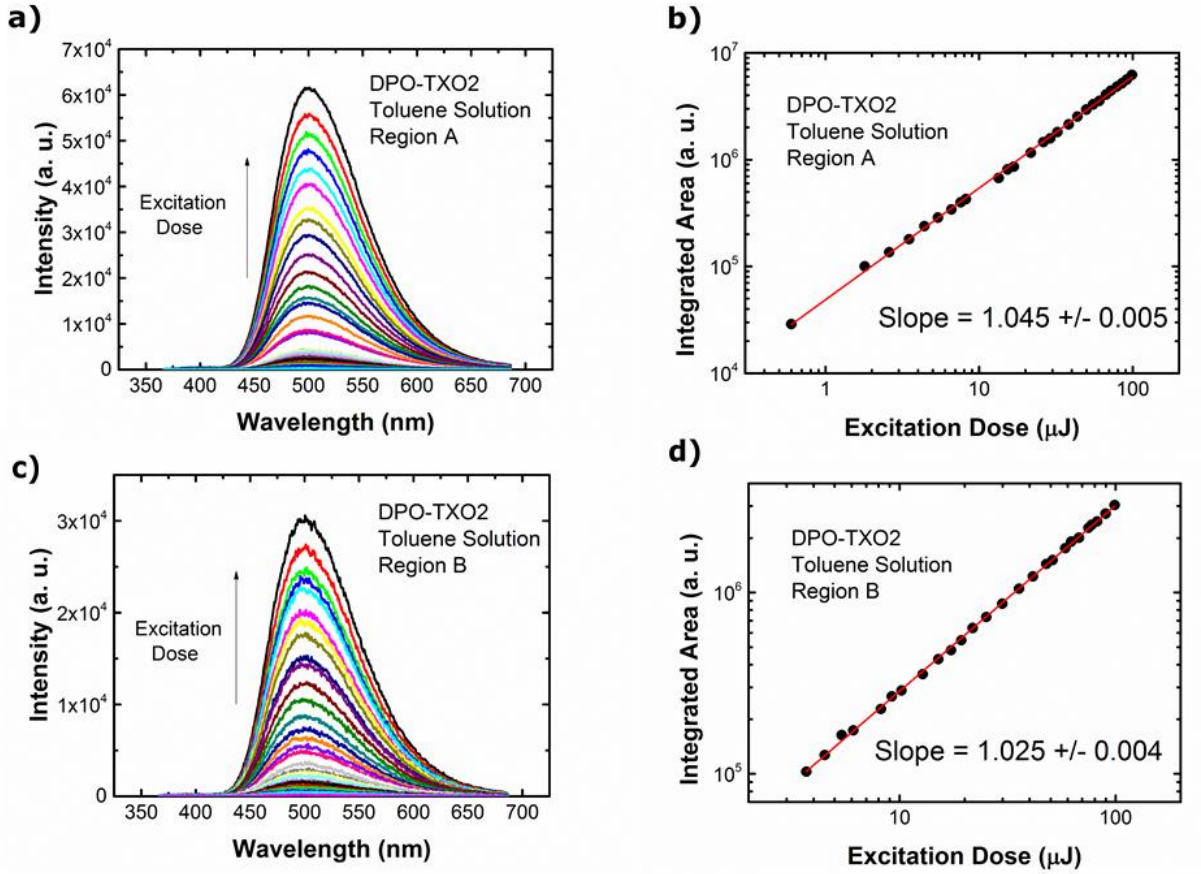

Figure 22 a) Delayed fluorescence spectra of DPO-TXO2 in different laser excitation doses for region a and b) the integrated area of each spectrum as a function of excitation dose. c) and d) the same analyses for region b. Region a and b are shown in Figure 21b.

4.2.3 Solid State Photophysical Properties

The TADF mechanism of DPO-TXO2 in solid-state was then studied. Figure 23a shows the PL of the acceptor and donor units as well as DPO-TXO2, all as films dispersed in zeonex

matrix. The PL spectrum of the acceptor shows the main emission of the unit, peak at 300 nm, and also a weak emission around 475 nm, which may be associated with a dimer emission. From time resolved spectroscopy the dimer emission was accentuated and identified to have onset at (2.98 ± 0.02) eV (see Figure 23b). The PL of DPO-TXO2 molecule shows a clear CT emission, as well as a small contribution from donor emission. This is similar behaviour to that observed in the steady state spectra of DPO-TXO2 in MCH solution (Figure 17b). The similarity of the optical behaviour between these two samples is expected, as both are nonpolar environments.

Figure 23c shows the decay curves of DPO-TXO2 in zeonex matrix. The well-defined separation between prompt and delayed emission is observed just at 290 K, whereas at lower temperature these two distinct emissions are unclear. Emission spectra detected in the long time delay region (ms) were observed just at low temperature, indicating that, in this region, the emission comes from triplet states. Figure 23d shows the normalized spectra collected in the whole region of analyses. At early times, from TD = 1.1 ns to 18 ns, the spectra show the same emission of the donor unit dispersed in zeonex film, which continuously red shifts to higher wavelengths until it achieves the CT state emission, onset at (2.83 ± 0.02) eV. The initial donor emission is weak, only being detected with the iCCD measurements. From TD = 70 µs to 89 ms the phosphorescence spectrum is observed to have an onset at (2.84 ± 0.02) eV. The PH spectrum is undoubtedly the ^{3}LE state from the donor, matching with the PH spectrum identified from the donor units in zeonex matrix, onset at (2.83 ± 0.02) eV. Also, the intensity dependence of the DF spectra (TD = 30 µs) was analysed as a function of the laser excitation dose and a linear gradient of (0.99 ± 0.03) was found, confirming the thermally assisted mechanism not TTA. Therefore, the ^{1}CT state and the ^3LE_D state were identified in a DPO-TXO2 zeonex film, and the optical energy splitting between these states was found to be ΔE_{ST} = (0.01 ± 0.03) eV. Additionally, the activation energy required for the DF process, calculated from an Arrhenius fit, was found to be E_A = (0.031 ± 0.004) eV, which shows again a different value compared to the optical ΔE_{ST} value obtained.

The second solid state environment chosen was 4,4′-bis(*N*-carbazolyl)-1,1′-biphenyl (CBP), because CBP is a host material with relatively high triplet level (2.66 eV) used in OLED emitter layers. However, often host–guest interactions give rise to complex photophysics, such as emissive exciplex states or quenching of excitons by the host[15]. Figure 24a shows the decay curves of the DPO-TXO2 in CPB matrix at two different temperatures. The well-defined

separation between prompt and delayed emission is observed just at 290 K, at low temperature, these two distinct emissions are unclear, as observed in the zeonex film (Figure 23c). Figure 24b shows the normalized emission spectra recorded at different time delays, from the early prompt emission (TD = 5.7 ns) to the phosphorescence emission (TD = 89 ms). From TD = 5.7 ns to TD = 72.5 ns, the spectra show a slight and continuous red shift, due to a growing contribution from a phosphorescence component. After TD = 72 ns, the spectra remain at 2.66 eV (onset) and this emission was collected until 89 ms. The PH spectra identified at long TD is clearly the PH of the host, CBP, having three well defined peaks (at 491 nm, 518 nm and 557 nm) with increasing emission intensity on cooling down the system[16,17]. In this thin film, the excited states were not confined on the DPO-TXO2 molecules, and a quenching of fluorescence was observed by the host.

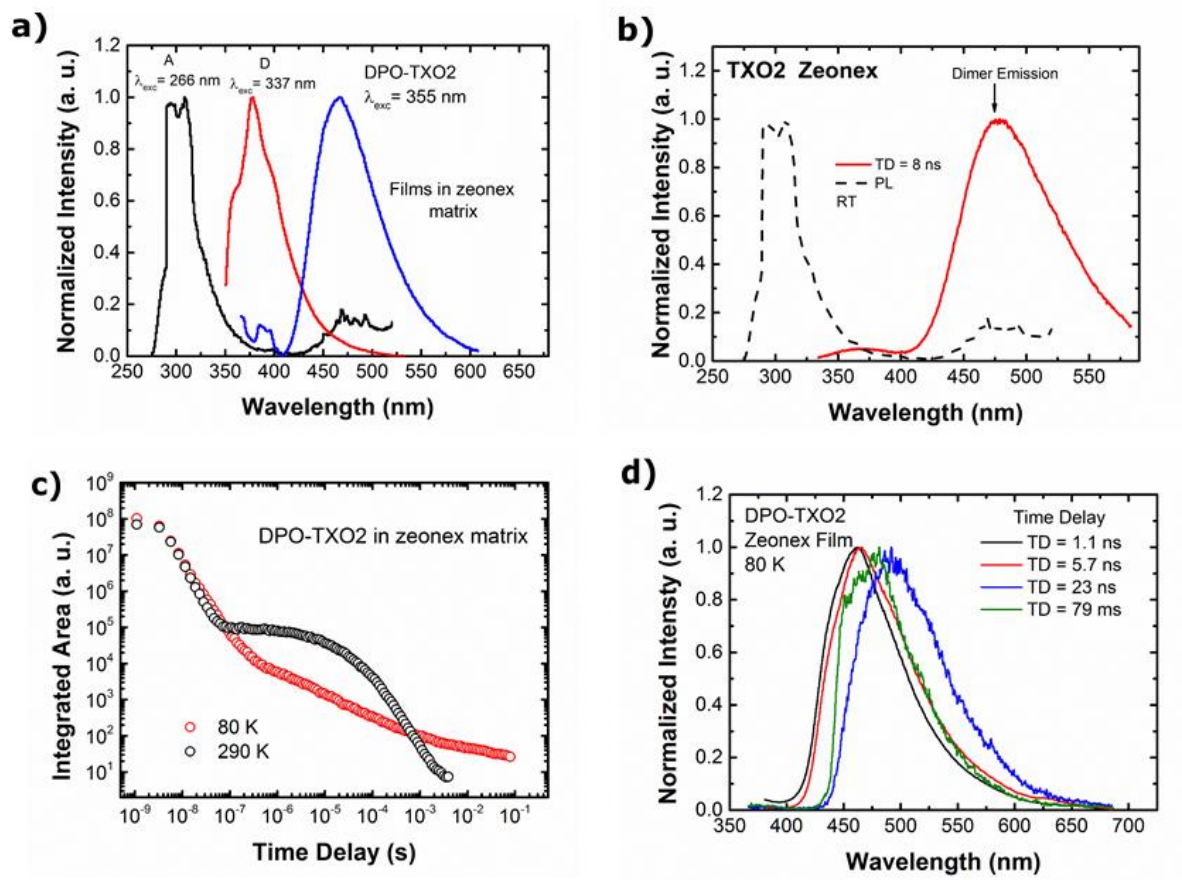

Figure 23 a) Normalized photoluminescence (PL) spectra of acceptor (A), donor (D), and DPO-TXO2 molecules, all dispersed in zeonex matrix. b) Time resolved fluorescence emission of A together with its PL spectrum. c) Time resolved fluorescence decay of DPO-TXO2 in zeonex matrix. The curves were obtained with 355 nm excitation. d) Time resolved normalized emission spectra in the entire region of analyses at 80K.

Therefore, the ^{1}CT was identified to be at 2.82 eV but the ^3LE_D level was not identified. Obviously, the ^3LE_D level must have energy higher than 2.66 eV in this environment, otherwise the phosphorescence of the CBP would not be a favourable pathway of decay and the ^3LE_D level would be identified. Also, the ^3LE_D in this film should be close to the one found in zeonex matrix, as the observed triplet energy difference in toluene and MCH solutions is negligible. Therefore, the ^3LE_D is likely to be located at 2.84 eV so at high temperature rISC out competes triplet transfer from guest to host whereas at 80 K the rISC rate is much lower and triplet energy transfer out competes the TADF. Hence, this would suggest a ΔE_{ST} = 0.05 eV.

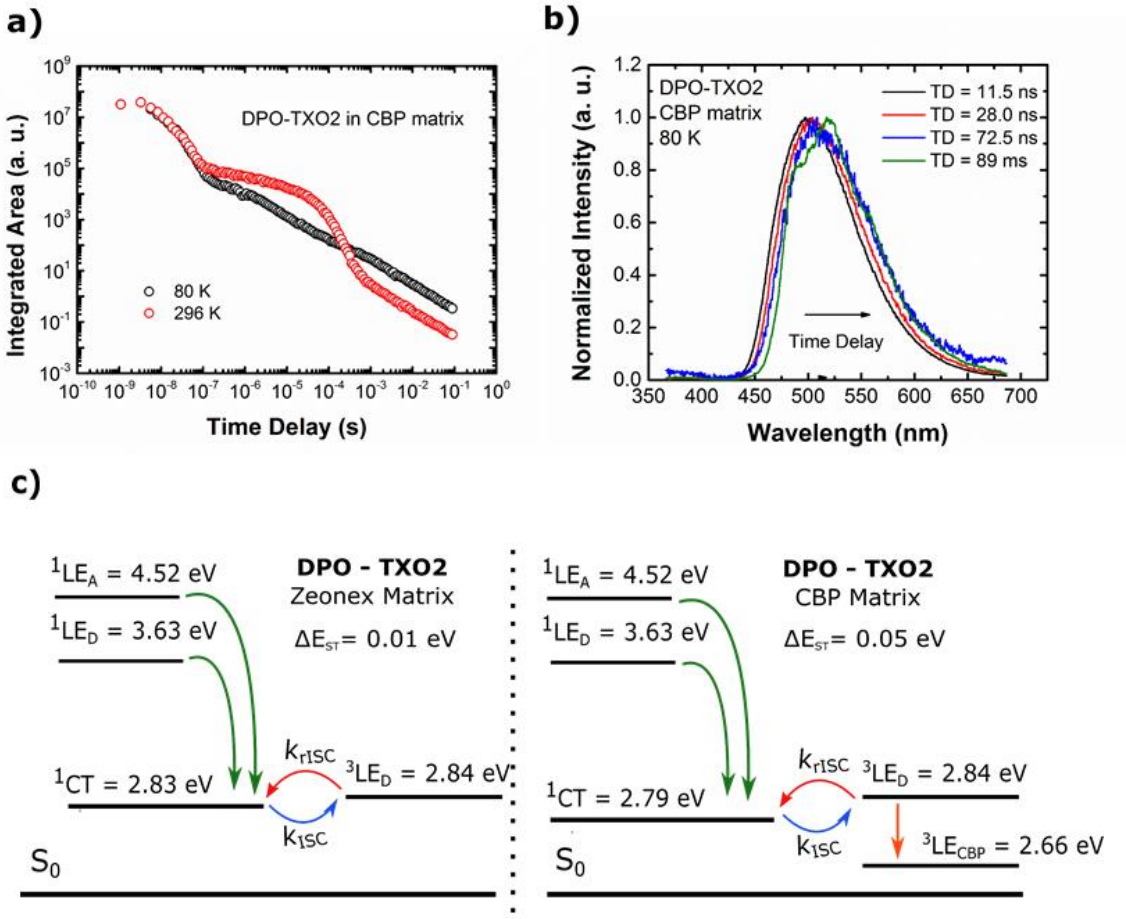

Figure 24 a) Time resolved fluorescence decay of DPO-TXO2 in CBP matrix. The curves were obtained with 355 nm excitation. b) Time resolved normalized emission spectra in the entire region of analyses. c) Energy levels diagram describing the excited dynamics of DPO-TXO2 in zeonex and CBP matrix, evidencing the local and charge transfer states.

Figure 24c shows the full decay pathways available in molecules dispersed in the two different environments in solid state, CBP and zeonex matrix. All the energy levels were taken from the onset of the spectra at 80 K apart from the ^3LE_D in CBP matrix. The mechanism responsible for the delayed fluorescence in both cases is TADF. In zeonex, ^3LE_D is located (slightly) above

^{1}CT, an unusual configuration. In the CBP matrix, ^3LE_D excitons are quenched by the triplet level of CBP and the radiative transition $^3LE_{CBP} \rightarrow S_0$ was observed strongly. In these two cases, the ^{1}CT level shows a strong energy shift (as in toluene compared to MCH solutions), leading to a difference of energy splitting between ^{1}CT and ^3LE_D. The host CBP is more polar than zeonex, a characteristic confirmed by the lower ^{1}CT level in this matrix.

4.2.4 Device Performance

The photophysical analyses of DPO-TXO2:CBP thin film showed a strong quenching of excitons by the CBP host, due to its triplet level being the lowest energy pathway available in the system. Thus, CBP is not an appropriate host for DPO-TXO2. To evaluate the potential of DPO-TXO2 in OLEDs, devices in bis[2-(di- (phenyl)phosphino)-phenyl]ether oxide (DPEPO) host were fabricated. This host has a reported higher triplet level (2.99 eV)[18] than CBP. The architecture of the device was: NPB(40nm)/TCBPA(10nm)/ 10%DPO-TXO2:DPEPO(30nm)/TPBi(60nm)/LiF/Al. NPB is *N*,*N*′-bis(naphthalene-1-yl)-*N*,*N*′-bis(phenyl)-benzidine, TPBi is 1,3,5-tris(*N*-phenylbenzimidazol-2-yl)benzene) and TCBPA is 4,4 – (diphenymethylene)bis(*N*,*N*-diphenylaniline).

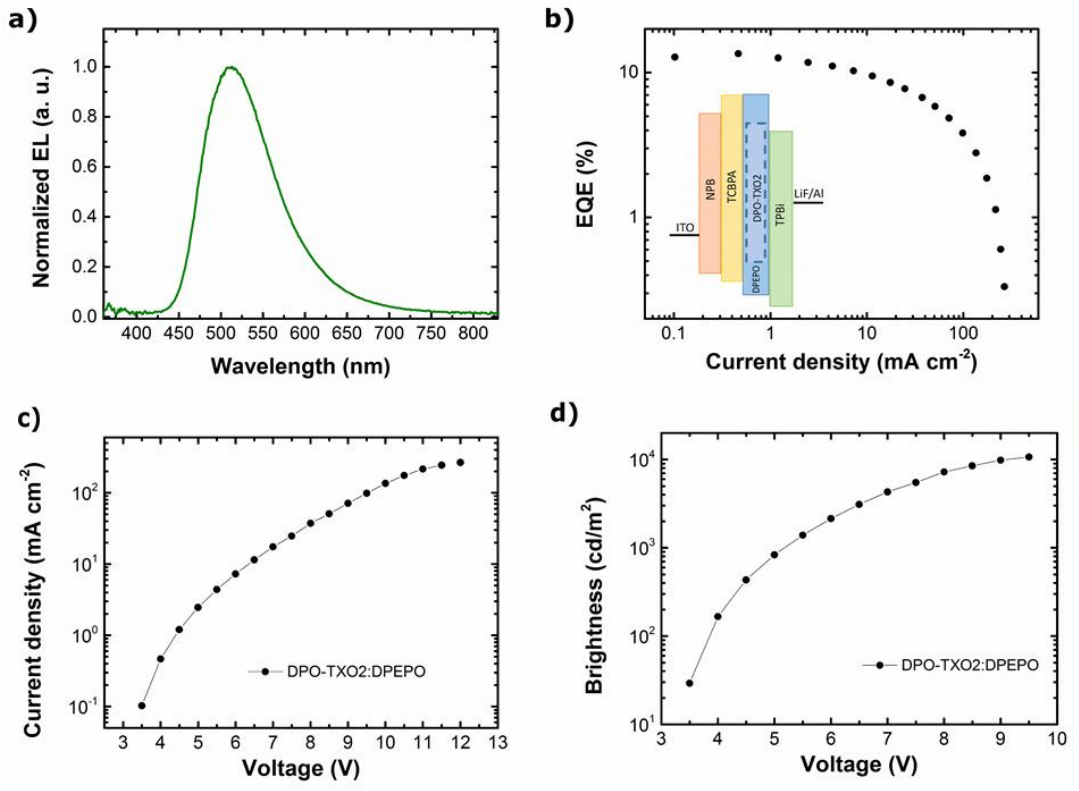

Figure 25 a) Electroluminescence spectrum b) EQE versus Current density c) Current density versus Voltage and d) Brightness versus Voltage curves of DPO-TXO2:DPEPO OLED.

Figure 25 (a-d) shows the full characterization of the DPO-TXO2:DPEPO device. The EL spectrum shows peak emission at 511 nm. EQE *versus* current density curve is shown in Figure 25c together with a scheme of the device structure. The device showed a maximum external quantum efficiency (EQE) of 13.5% at 166 cd/m^2 and good resistance to roll- off up to 11 mA/cm^2. Figure 25c shows the Current density *versus* Voltage curve, which shows low turn on voltage value, around 3.5 V. Brightness *versus* Voltage curve is shown in Figure 25d with brightness levels >10,000 cd/m^2. The device performance clearly exceeds the upper limits of the EQE (5%) in conventional fluorescent OLEDs, demonstrating the TADF contribution.

4.3 Conclusions

In summary, this chapter reports the design, photophysical properties and device performance of the TADF emitter molecule DPO-TXO2, dispersed in four different environments, along with the photophysics of the constituent D and A. The DPO-TXO2 shows a strong and clear CT state, and the TADF was readily identified in solution and in solid state, giving rise to strong delayed emission.

In less polar environments (i.e. MCH solution and zeonex film) similar photophysics is observed. Both showed a small contribution of ^1LE_D (donor singlet) emission in steady state measurements, as well as the ^1CT emission. Furthermore, they show a slow charge transfer step in the time resolved measurements indicative of weak electronic coupling between the donor and molecular CT state. The ^1LE_D was observed at early times followed by stabilisation of ^1CT emission. In more polar environments, (i.e. toluene solution and CBP matrix) only the ^1CT emission was identified in the steady state measurements and at early times in the time resolved measurements indicating much faster electron transfer (or more probably stabilisation of the charge separated character of the excited state). Also, a quenching of ^3LE_D excitons by the CBP host was identified, due to its triplet level being the lowest energy state of the system. In a higher triplet host, DPEPO, a good device performance was achieved, showing maximum EQE value of 13.5%, high brightness levels >10,000 cd/m^2 and good resistance to roll-off up to 11 mA/cm^2.

In polar and nonpolar environments, it was shown that ^3LE_D plays an important role in the ISC/rISC processes. The optical ΔE_{ST} in MCH solution, toluene solution, zeonex matrix and CBP matrix were identified to be: (0.16 ± 0.03) eV, (-0.07 ± 0.03) eV, (-0.01 ± 0.03) eV and (-0.05 ± 0.03) eV, respectively, showing the same TADF emitter displays distinct optical

energy splitting between singlet and triplet states. Negative energy splitting means that ^{1}CT is located below ^{3}LE. It is shown that the environmental stabilisation of the ^{1}CT energy is responsible for the changing in the optical ΔE_{ST}, since the ^3LE_D remains almost unchanged. Even in solid state, where the polarity difference was small, the host brought a change in the ^{1}CT level, showing that the ^{1}CT state is strongly depend on the environment. Thus, it is possible to control the optical ΔE_{ST} by changing the host, and consequently, maximize the TADF mechanism. Therefore, efficient TADF can occur either in polar or in nonpolar environments, because one of the crucial features is where the ^{1}CT energy level lies with respect to the ^{3}LE (donor or acceptor) level. This explains why some TADF materials show stronger TADF in nonpolar and others in polar environment. The polarity of the environment will clearly interfere in the stabilization of the CT formation. It was also demonstrated here that the ISC/rISC processes occur if the singlet state is localized at lower energy than the local triplet state (^{3}LE), as the most important feature is to have a small energy gap between singlets and triplets states.

Therefore, this study was crucial in forming the current model of the TADF vibronic coupling mechanism, that highlights the need for three excited states (^{1}CT, ^{3}CT and ^{3}LE) to come into resonance to achieve high TADF efficiency.

4.4 Sample Preparation Details

Three types of samples were studied in this work: solutions in different solvents (10^{-3} to 10^{-5} M), film produced in zeonex matrix (organic material 5 mg/mL : zeonex 180 mg/mL 1:1 *v/v*) and thin film produced in CBP matrix (10% DPO-TXO2:CBP). The solutions were degassed to remove all the oxygen dissolved by 4 freeze-thaw cycles to perform the degas test and delayed fluorescence measurements. The films in zeonex matrix were fabricated by spin-coating on quartz substrates at 500 rpm during 60 seconds. The thin film in CBP matrix was made by co-evaporation deposition onto transparent sapphire substrates using a Kurt J. Lesker Spectros II deposition system under vacuum, 10^{-6} mbar, at a steady evaporation rate of ~ 2.3 Å/ s and ~ 0.22 Å/ s for host and guest materials, respectively.

4.5 References Chapter 4

1. dos Santos, P. L. *et al.* Engineering the singlet-triplet energy splitting in a TADF molecule. *J. Mater. Chem. C* **4,** 3815–3824 (2016).
2. Kulkarni, A. P., Zhu, Y., Babel, A., Wu, P. T. & Jenekhe, S. A. New ambipolar organic semiconductors. 2. Effects of electron acceptor strength on intramolecular charge transfer

photophysics, highly efficient electroluminescence, and field-effect charge transport of phenoxazine-based donor-acceptor materials. *Chem. Mater.* **20,** 4212–4223 (2008).

3. Nowakowska-Oleksy, A., Sołoducho, J. & Cabaj, J. Phenoxazine Based Units- Synthesis, Photophysics and Electrochemistry. *J. Fluoresc.* **21,** 169–178 (2011).

4. Okamoto, T. *et al.* 1,4-Benzoxazino[2,3-b]phenoxazine and Its Sulfur Analogues: Synthesis, Properties, and Application to Organic Light-Emitting Diodes. *Chem. Mater.* **17,** 5504–5511 (2005).

5. Tanaka, H., Shizu, K., Miyazaki, H. & Adachi, C. Efficient green thermally activated delayed fluorescence (TADF) from a phenoxazine–triphenyltriazine (PXZ–TRZ) derivative. *Chem. Commun.* **48,** 11392 (2012).

6. Ogiwara, T., Wakikawa, Y. & Ikoma, T. Mechanism of Intersystem Crossing of Thermally Activated Delayed Fluorescence Molecules. *J. Phys. Chem. A* **119,** 3415–3418 (2015).

7. Zhang, Q. *et al.* Design of efficient thermally activated delayed fluorescence materials for pure blue organic light emitting diodes. *J. Am. Chem. Soc.* **134,** 14706–9 (2012).

8. Dias, F. B. *et al.* Triplet harvesting with 100% efficiency by way of thermally activated delayed fluorescence in charge transfer OLED emitters. *Adv. Mater.* **25,** 3707–3714 (2013).

9. Dias, F. B. *et al.* The Role of Local Triplet Excited States in Thermally-Activated Delayed Fluorescence: Photophysics and Devices. *Adv. Sci.* **3,** 1–10 (2016).

10. Shizu, K. *et al.* Strategy for Designing Electron Donors for Thermally Activated Delayed Fluorescence Emitters. *J. Phys. Chem. C* **119,** 1291–1297 (2015).

11. Numata, M., Yasuda, T. & Adachi, C. High efficiency pure blue thermally activated delayed fluorescence molecules having 10H-phenoxaborin and acridan units. *Chem. Commun.* **51,** 9443–9446 (2015).

12. Huber, J. R. & Mantulin, W. W. Emission Properties of Aromatic Amines in Solution. Phenoxazine System'. *J. Am. Chem. Soc.* **94:11,** 3755–3760 (1972).

13. Mopsik, F. I. Dielectric Properties of Slightly Polar Organic Liquids as a Function of Pressure, Volume, and Temperature. *J. Chem. Phys.* **50,** 2559–2569 (1969).

14. Lee, J. *et al.* Controlled emission colors and singlet–triplet energy gaps of dihydrophenazine-based thermally activated delayed fluorescence emitters. *J. Mater. Chem. C* **3,** 2175–2181 (2015).

15. Jankus, V. *et al.* Highly Efficient TADF OLEDs: How the Emitter-Host Interaction Controls Both the Excited State Species and Electrical Properties of the Devices to Achieve Near 100% Triplet Harvesting and High Efficiency. *Adv. Funct. Mater.* **24,** 6178–6186 (2014).

16. Schrögel, P. *et al.* A series of CBP-derivatives as host materials for blue phosphorescent organic light-emitting diodes. *J. Mater. Chem.* **21,** 2266–2273 (2011).

17. Jankus, V., Winscom, C. & Monkman, A. P. The photophysics of singlet, triplet, and degradation trap states in 4,4-N,N′-dicarbazolyl-1,1′-biphenyl. *J. Chem. Phys.* **130,** 074501 (2009).

18. Xu, H. *et al.* Application of chelate phosphine oxide ligand in EuIII complex with mezzo triplet energy level, highly efficient photoluminescent, and electroluminescent performances. *J. Phys. Chem. B* **110,** 3023–9 (2006).

Chapter 5: Optical and Polarity Control of D–A Conformation in TADF Emitters

A more in-depth understanding about the correlation between molecular conformation and the TADF mechanism is presented in this chapter by studying two D–A–D molecules, 2,7-bis(phenothiazin-10-yl)-9,9-dimethylthioxanthene-*S*,*S*-dioxide (DPT-TXO2) and 2,7-bis(1-methylphenothiazin-10-yl)-9,9-dimethylthioxanthene-*S*,*S*-dioxide (DMePT-TXO2), where the latter differs by only a methyl group incorporated on each of the donor units. DMePT-TXO2 in solution and solid state shows dual charge transfer (CT) emission. The CT states come from two distinctive conformations between the D and A units. Experiments show that the emission contribution of each state can be controlled by the polarity of the environment and by the excitation energy. Further, how the different conformers can be used to control the TADF mechanism is analyzed in detail.

The work presented in this chapter is an adapted version of the manuscript published at *The Journal of Physical Chemstry C* (P. L. dos Santos, J. S. Ward, A. Batsanov, M. R. Bryce, A. P. Monkman, *J. Phys.. Chem. C* 2017, *121*, 16462). It was collaborative work between the OEM group and the chemistry department, both at Durham University. P. L. dos Santos performed all steady state and time resolved photophysics measurements. Dr. J. S. Ward devised and performed the synthesis, purification and chemical characterization. X-ray measurements and their analysis were performed by Dr. A. Batsanov.

5.1 Introduction

A further consideration in the TADF mechanism is the possibility of different conformations for the D-A structures. Different conformers have different emissive states, and consequently different ΔE_{ST} and one simple way of identifying the presence of two different conformations on the same molecule is the observation of dual emission. For the specific case of the phenothiazine donor, this emission dependence on conformation was first observed in 2001 by Daub *et al.*[1] in phenothiazine-pyrene dyads. Where the conformation of the phenothiazine was crucial to the energy level arrangement in the molecule thus allowing dual emission of both LE and CT states. This was followed by similar observations by Stockmann *et al.*[2] in 2002 and Acar *et al.*[3] in 2003, again in phenothiazine-pyrene dyads.

To understand the origin of this dual emission in these phenothiazine based molecules one must consider the conformational behaviour of the molecule itself. This was first discussed in the 1960s and early 1970s[4–6]. The fundamental aspect is that the phenothiazine is a distorted boat structure forming either H-intra or H-extra conformers, as shown in Figure 26. This leads to two different sets of electronic states; in the H-intra conformation the lone pairs of the nitrogen delocalise into the phenyl rings of the phenothiazine, which is not the case for the H-extra conformation. This ability to form H-intra and H-extra folded conformers allows formation of parallel quasi-axial and perpendicular quasi-equatorial conformations in D-A and D-A-D molecules. This behaviour can be directly linked to the dual LE and CT emission observed in the early 2000s and to a more recent discovery of dual CT emission in TADF molecules leading to different ΔE_{ST}[7,8].

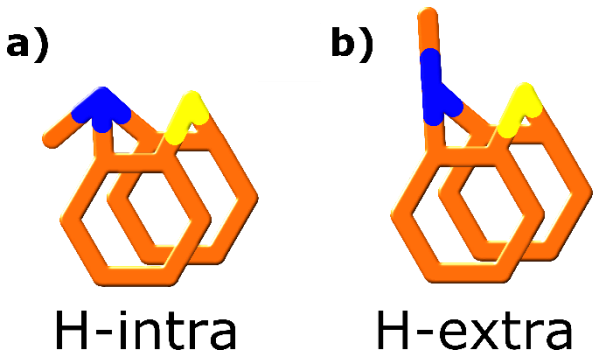

Figure 26 The two different conformers that can be obtained by phenothiazine. a) The H-intra conformation has greater delocalisation of the lone pair nitrogen's into the phenyl rings of the phenothiazine, whereas b) the H-extra conformation inhibits this. The blue bonds represent nitrogen and yellow bonds sulphur. Figure adapted from reference [4].

Adachi *et al.*[9] reported a D-A emitter that shows dual CT emission, PTZ-TRZ, which has phenothiazine as the donor unit and 2,4,6-triphenyl-1,3,5-triazine (TRZ) as the acceptor unit. Through density functional theory calculations, they identified the existence of two ground-state conformers that can exist with almost equal proportions in toluene solutions, i.e. the quasi-axial and quasi-equatorial. Calculations also gave estimates of two different singlet-triplet energy gaps, 1.14 and 0.18 eV, with the latter giving rise to DF via the TADF mechanism, as confirmed by temperature dependence analyses.

Taking this into consideration the choice of donor and acceptor can have a significant impact on the final performance of the TADF D-A-D molecule in a device. Choosing a molecule that has the ability to form two different conformers can lead to unwanted emission and other possible side effects. Thus, it is desirable to find solutions to control these conformations. Xiao-Hong Zhang *et al.*[10] showed this control using TADF molecules with donor units based on 9,9-dimethyl-9,10-dihydroacridine (DMAC), first reported by Adachi *et al.*[11]. The molecules have two possible conformations, which they entitled the planar and crooked forms. The dual conformations observed in 2-(9,9-dimethylacridin-10(9H)-yl) thianthrene-5,5,10,10-tetraoxide (DMAC-TTR) molecules resulted in low performance OLEDs (EQE of 13.9%), presenting a need in the development of solutions to supress the deleterious crooked form in these molecules. Thus, they presented two design strategies to address this problem: (1) increasing the rigidity of these groups to suppress the crooked form; (2) increasing the steric hindrance of the linked group to minimize the energy of the highly twisted form. Considering these two strategies, two modified TADF emitters were synthesized: (1) 2-(10H-spiro[acridine-9,9′-fluoren]-10-yl)thianthrene5,5,10,10 tetra-oxide (SADF-TTR), which has an additional fluorene group on the DMAC unit that retains a similar electron donating ability but increases the rigidity of the structure and (2) 2-(9,9-dimethylacridin-10(9H)-yl)-3-phenylthianthrene-5,5,10,10te-traoxide (DMAC-PTR), which has a phenyl group attached to the ortho-position of DMAC to increase the steric hindrance between the DMAC and TTR groups. OLEDs based on these new structures exhibited a single electroluminescence peak and increased performance (EQE values of 20.2% and 18.3%), confirming the success of the strategies in controlling the dual conformations and avoiding energy loss. However, substitution on the donor (or acceptor) also has more subtle changes, including the mixing of the n-π* and π-π* states giving rise to the direct CT transition. This affects the conjugation of the D and A, the PLQY of the CT fluorescence, but not the ΔE_{ST}[12] .

Another way of avoiding dual emission is the use of rigid units, e.g. phenoxazine, which appears only display single emission as demonstrated recently[12,13]. Apart from the molecules discussed above, there exists in literature warnings for other molecules such as acridan, xanthene, thioxanthene and isoalloxazin[14,15]. Any flexible molecule should be treated with caution regarding TADF.

In this chapter, two novel D–A–D type molecules, 2,7-bis(phenothiazin-10-yl)-9,9-dimethylthioxanthene-*S*,*S*-dioxide (DPT-TXO2) and 2,7-bis(1-methylphenothiazin-10-yl)-9,9-dimethylthioxanthene-*S*,*S*-dioxide (DMePT-TXO2) are studied. These two molecules differ only by a methyl group incorporated on each of the donor units. Phenothiazine was chosen as a donor unit since it is commonly used in efficient D-A-D TADF molecules[16], and adding a methyl group to it increases the steric restriction around the donor–acceptor bond, which can alter contributions from TADF and phosphorescence. Dramatic differences in the photophysical properties of these two molecules are observed. Particularly, it is shown that different molecular conformations give rise to different CT states, termed axial (CT_{ax}) and equatorial (CT_{eq}). Here, how the different conformers can be controlled by the polarity of the environment and by the excitation energy is shown. Moreover, it is discussed how the different conformers can be used to control the TADF mechanism.

5.2 Results and Discussion

5.2.1 Chemical Characterization

Figure 27 shows the X-ray molecular structure of DPT-TXO2 and DMePT-TXO2 in different viewing angles. DPT-TXO2 has no crystallographic symmetry but an approximate mirror plane through the S, O, C(7) and methyl carbon atoms. The TXO2 system (acceptor unit) is folded along the S(1)…C(7) vector, its arene rings *i* and *ii* forming a dihedral angle of 139.1º, cf. 137.8º in DPO-TXO2 and 133.9º in unsubstituted TXO2[17]. Both phenothiazine moieties are moderately folded along the N…S vectors, with inter-arene angles *iii/iv* 162.0º and *v/vi* 154.4º. The near-perpendicular twists around C(4)-N(1) and C(10)-N(2) bonds (86.0º and 80.1º, respectively) effectively preclude π-conjugation between donor and acceptor parts. These bonds are longer than N–C bonds within phenothiazine systems, average 1.438(1) vs 1.416(2) Å, indicating that the lone pairs of N interact predominantly with the phenothiazine arene rings. In DMePT-TXO2 the folding of the TXO2 unit is similar (dihedral angle *i/ii* 135.9º) but the

phenothiazine conformation is entirely different. The 1-methylphenothiazine substituent at C(4) is disordered between two orientations with methyl groups on opposite sides, with nearly equal probability, 0.482(2) to 0.518(2). The substituent at C(10), however, is ordered. The latter is folded (dihedral angle *v/vi* 134.0º) stronger than the (un-methylated) phenothiazine in DPT-TXO2, but similarly to mono- or di-methylated phenothiazine in DBT derivatives (128.7-135.5º)[18]. The twist around the C(10)-N(2) bond is negligible (0.9º) and this bond (1.408(3) Å) is considerably shorter than the other N(2)-C bonds (mean 1.434(3) Å). The geometry of the disordered phenothiazine is essentially similar (though less accurately determined), with the mean phenothiazine folding of ca. 135º and the twist around C(10)-N(2) bond of 16º (*A*) or 13º (*B*) (see reference [19] for details on X-ray study).

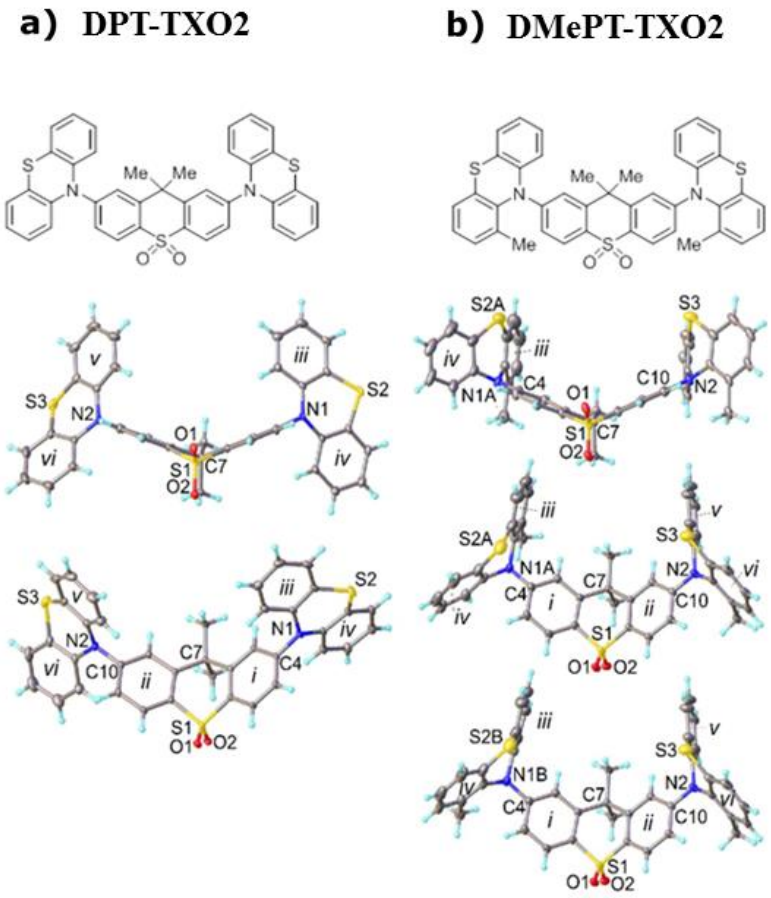

Figure 27 Chemical structures and X-ray molecular structures from different angles of a) DPT-TXO2 and b) DMePT-TXO2 (showing two conformers statistically mixed in the crystal).

Therefore, both molecules show a conformation with nearly perpendicular D–A orientation. The conformation shown by DPT-TXO2 is termed equatorial-equatorial (eq-eq) and DMePT-TXO2 axial-axial (ax-ax)[2,7]. Given that, in both conformations, the D and A units are

perpendicular, one could predict strong CT character leading to strong TADF in both systems. However, dramatic differences in the photophysical properties of these molecules are observed, showing that the nearly perpendicular orientation is not a sufficient design strategy of TADF emitters.

5.2.2 Solution State Photophysical Properties

Figure 28a shows the extinction coefficient (ε) spectra of DPT-TXO2 and DMePT-TXO2 and their individual D and A units, all in dichloromethane (CH_2Cl_2) solvent. Figure 28b, c and d show in detail how the values of ε were calculated for DPT-TXO2 (DMePT-TXO2, their D and A units, and all extinction coefficient results presented in this thesis were calculated using the same method). Initially, the absorption spectra of seven solutions with known concentration were measured (Figure 28b). Then, the values of the optical density (OD) for a chosen wavelength (317 nm particularly for DPT-TXO2) ranged from $0.1 < OD < 1.0$ was plotted *versus* their concentration. By fitting the straight line (Figure 28c), the value of ε at the chosen wavelength was obtained, considering the dependence between OD and ε (see equations 3.1 and 3.2 chapter 3). The calculated ε was then used to obtain the values covering the entire absorption spectrum (230 to 500 nm). Finally, all ε curves were plotted together (Figure 28d), to confirm that all spectra effectively match each other, as ε values do not depend on the solution' concentration.

DPT-TXO2 shows mainly the absorption band of the donor unit. DMePT-TXO2 shows a distinct absorption spectrum, at higher energies compared to DPT-TXO2. Figure 29 shows the absorption spectra of DPT-TXO2 (a) and DMePT-TXO2 (b) also in methylcyclohexane (MCH) and toluene solutions. The absorption peak at lower energy shows a slight red shift by increasing the polarity of the solvent, which can be associated with $\pi \rightarrow \pi^*$ character of the transitions. By comparison to the individual D and A units, the extinction coefficients of the low energy bands in both D–A–D molecules is greatly enhanced.

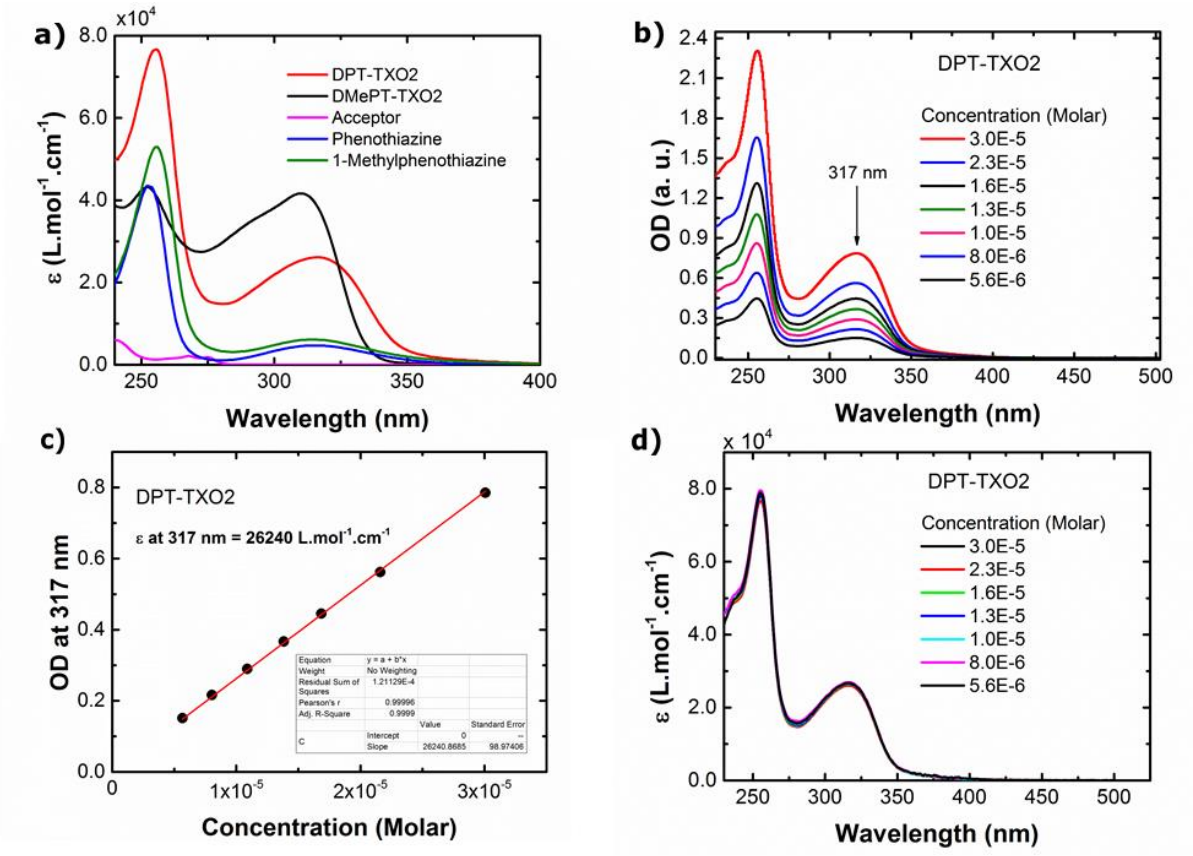

Figure 28 a) Extinction coefficient spectra of DPT-TXO2, DMePT-TXO2 and their acceptor and donor units, all diluted in dichloromethane (DCM). Figure taken from reference [19]. b) Absorption spectra of DPT-TXO2 in different CH_2Cl_2 concentrations. c) Optical density (OD) at 317 nm *versus* Concentration graph of DPT-TXO2. d) Extinction coefficient spectra of DPT-TXO2.

This increase in oscillator strength does not come from simple conjugation as the D–A units are orthogonal precluding such conjugation. Instead, this is a clear signature of state mixing, here the π-π* and n-π* states. The effect of state mixing has been described in detail by C. M. Marian[20] and T. J. Penfold[21]; of significance here is the effect of the methyl group on the donors of DMePT-TXO2. As these groups stabilise the H-extra (axial) conformation of the phenothiazine units[7] less of the bridging nitrogen lone pair couples into the donor increasing the π-π* character, and hence oscillator strength of the lowest energy transition, but at the expense of a blue shifted transition. Whereas in DPT-TXO2, the H-intra conformation of the phenothiazine is stabilized and more of the bridging nitrogen lone pair couples into the donor increasing the *n*-π* character, decreasing the oscillator strength of the lowest energy transition and giving a more red shift.

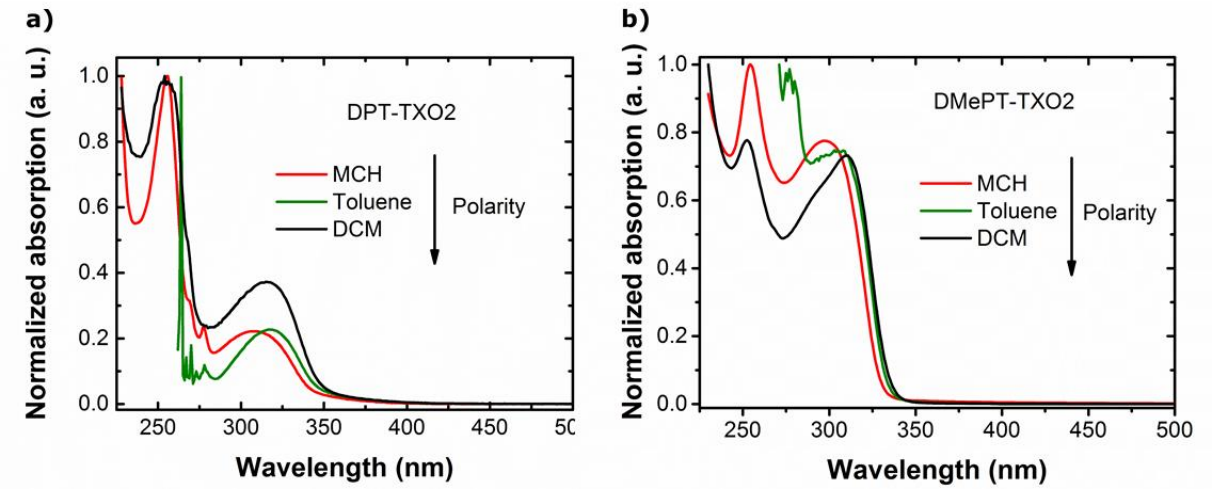

Figure 29 Absorption spectra in methylcyclohexane (MCH), toluene and dichloromethane (DCM) solutions for a) DPT-TXO2 and b) DMePT-TXO2.

Figure 30a shows the emission spectra of DPT-TXO2 in different solvents. The spectra show clear and strong CT emission having a Gaussian band shape and strong red shift compared to the individual D and A emission spectra. The photoluminescence (PL) spectra move to longer wavelength when increasing the solvent polarity, a typical strong positive solvatochromism, as observed before in other D–A–D type molecules[16,22–24]. A vestige of emission from the donor unit or weak axial CT state, around 400 nm, is observed in all solvents.

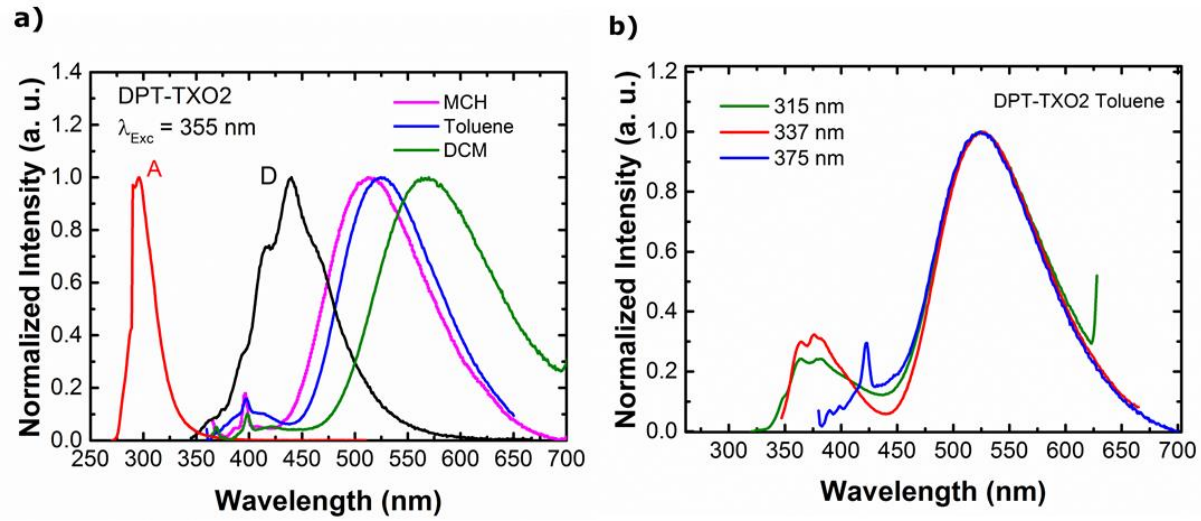

Figure 30 a) Normalized photoluminescence (PL) spectra of acceptor (A), donor (D) and DPT-TXO2 molecules. D and A units were diluted in methylcyclohexane (MCH) solvent and D–A–D in different solvents: MCH, toluene and dichloromethane (DCM). DPT-TXO2 molecules were excited at 355 nm. b) Normalized PL of DPT-TXO2 toluene solution at different excitation wavelengths.

Figure 30b shows the emission spectra of the toluene solution for different excitation energies. The ^{1}CT emission does not depend on the excitation energy; however, when excited at 375 nm, the edge of the absorption spectrum, the contribution from the ^{1}LE emission is weaker. The edge of the absorption spectrum, long tail, is assigned as direct absorption of CT states, such that when the molecules are excited in this region, less contribution of ^{1}LE is observed. The contribution of triplet excited states to the overall emission was determined by comparing the emission intensity in aerated and degassed solutions. The contributions of DF are 13%, 37% and 42% for MCH, toluene and DCB, respectively (Figure 31). The higher contribution of DF in DCB is due to the small CT-^{3}LE energy splitting (ΔE_{ST}) achieved in this polar environment, thus, an efficient repopulation of ^{1}CT state occurs via a reverse intersystem crossing (rISC) process from the ^{3}LE state. The phosphorescence (PH) spectrum of DPT-TXO2 was identified in the solid state (Figure 40), demonstrating that the PH onset is closest in energy to ^{1}CT in DCB solvent, confirming that the shift in the energy of triplet levels is small with the change in the polarity of the environment.

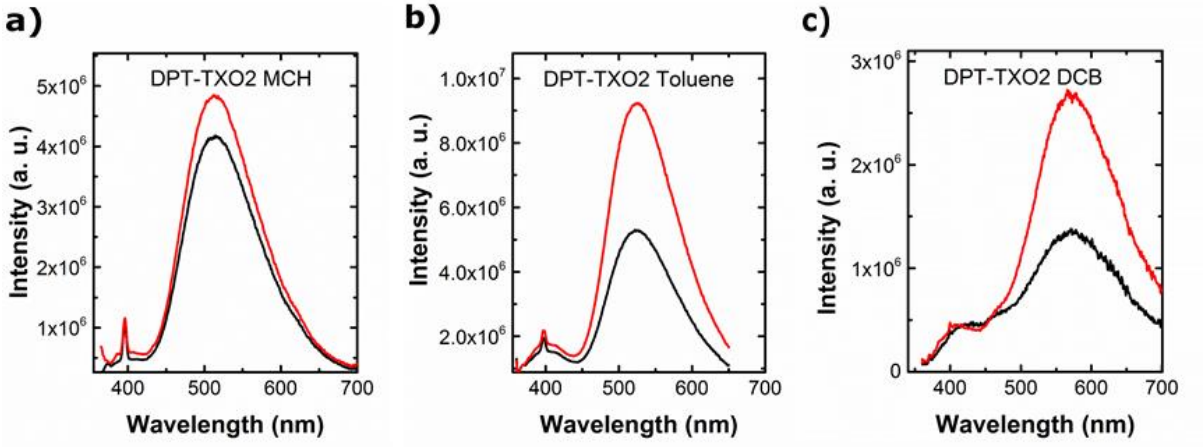

Figure 31 Degas test of DPT-TXO2 for different solvents a) methylcyclohexane (MCH) b) Toluene and c) 1,2-dichlorobenzene (DCB). Red curves refer to degassed solutions and black curves to aerated solutions. All solutions were excited at 355 nm.

DMePT-TXO2, on the other hand, shows a more complex emission spectra, with different emission bands in different polar environments and excitation energies. Figure 32a shows the emission spectra of all solutions (MCH, toluene and DCB) excited at 337 nm and also MCH solution excited at 316 nm. For the least polar solvent, MCH, the emission observed around 370 nm is associated with a weak CT state, coming from the axial-axial conformation (CT_{ax-ax}); which has strong local excited state character and consequently shows weak solvatochromism. At low excitation energy, 3.68 eV (337 nm), this emission is observed

together with another peak around 450 nm. This second CT emission comes from molecules with the axial-equatorial conformation, $CT_{ax\text{-}eq}$, and shows strong solvatochromism. For higher energy excitation, 3.93 eV (316 nm), $CT_{ax\text{-}eq}$ is enhanced and becomes the dominant emission. Figure 32b shows how the maximum intensity of each CT state in MCH solvent depends on the excitation energy. As can be seen, the emission that comes from the axial-axial conformation, $CT_{ax\text{-}ax}$, does not depend strongly on the excitation energy.

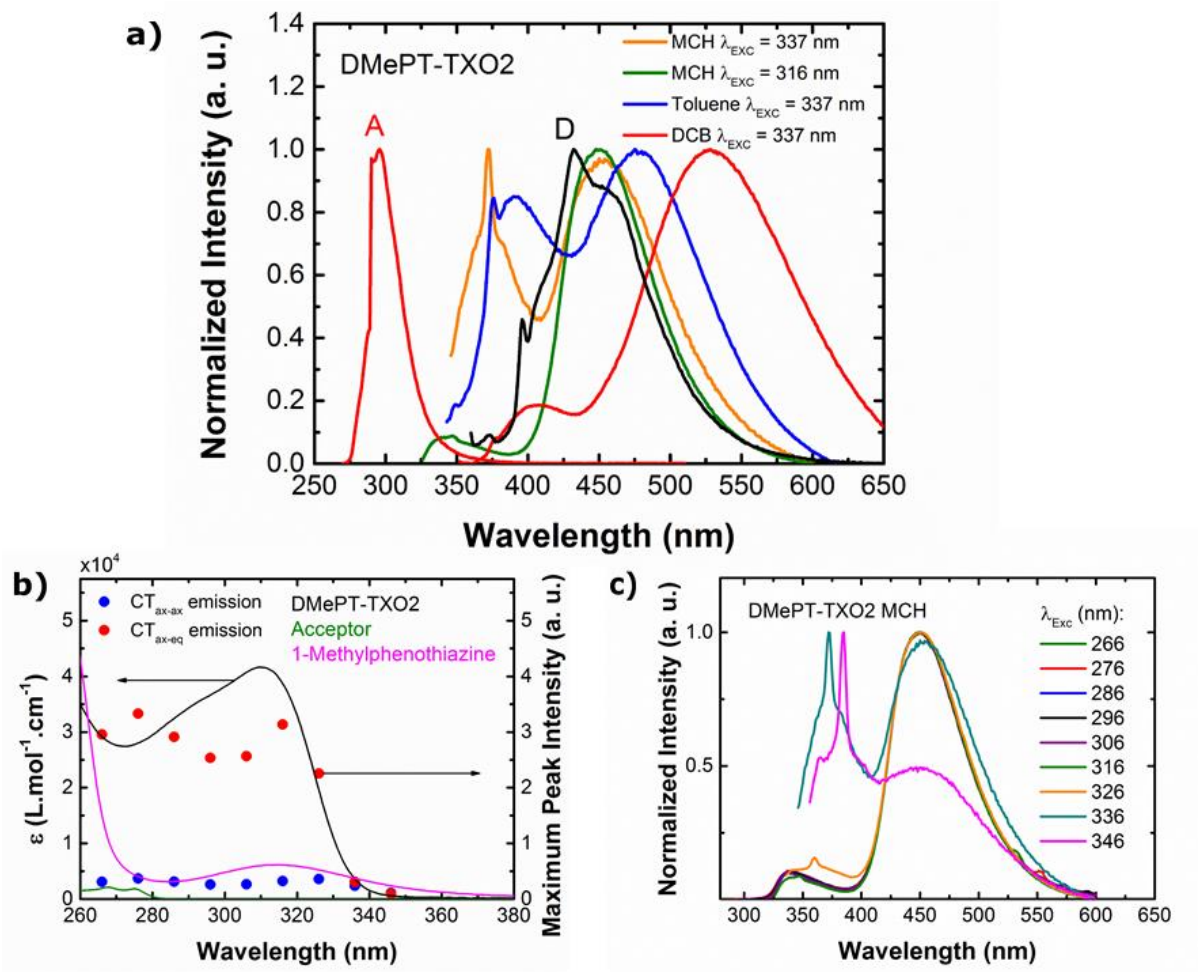

Figure 32 a) Normalized photoluminescence (PL) spectra of acceptor (A), donor (D) and DMePT-TXO2 molecules. D and A units were diluted in methylcyclohexane (MCH) solvent and D–A–D in different solvents: MCH, toluene and 1,2-dichlorobenzene (DCB). DMePT-TXO2 molecules were excited at 337/316 nm. b) Maximum peak intensity of CT axial-axial emission (blue dot) and CT axial-equatorial emission (red dot) of DMePT-TXO2 in MCH solution at different energy excitations. Full lines are the same extinction coefficient data shown in Figure 28a. c) PL spectra used to produce graphic shown in b.

However, the emission that comes from the axial-equatorial conformation, $CT_{ax\text{-}eq,}$ is enhanced when the excitation occurs in the absorption peak of the A and D units. When the molecules are excited at lower energy, i.e., at the edge of the absorption spectrum, both states emit equally and weakly. The emission spectra used to produce this data is shown in Figure 32c. Thus, higher excitation energy, with a high degree of excess energy, leads to the predominant formation of the $CT_{ax\text{-}eq}$ excited state, and it is proposed that the excess energy may enable molecular rearrangement from the ax-ax to the ax-eq conformation.

In toluene, the same behaviour is observed; the CT_{eq} and CT_{ex} emission have roughly the same relative contributions in the overall emission, but with a much smaller red shift of the CT_{ax} when compared with the CT_{eq}. However, when the toluene solution is excited at higher energy, 3.93 eV (315 nm), the CT_{eq} again dominates. Moving to even higher polarity, DCB solvent, the CT_{eq} emission is dominant (337 nm excitation) and just a vestige of CT_{ax} remains. This shows that the polarity of this environment is high enough to enable molecular rearrangement and hence strong stabilization of the $CT_{ax\text{-}eq}$ conformation, and high excitation energy is no longer needed. Thus, the contributions between the CT_{eq} and CT_{ax} emission can be controlled by increasing the excitation energy (excess energy), i.e., the $CT_{ax\text{-}eq}$ state has an energy barrier to formation/stabilization. However, in a high polarity environment (DCB solution) the ax-eq conformation is strongly stabilized even at low excitation energies so that predominantly CT_{eq} emission is observed.

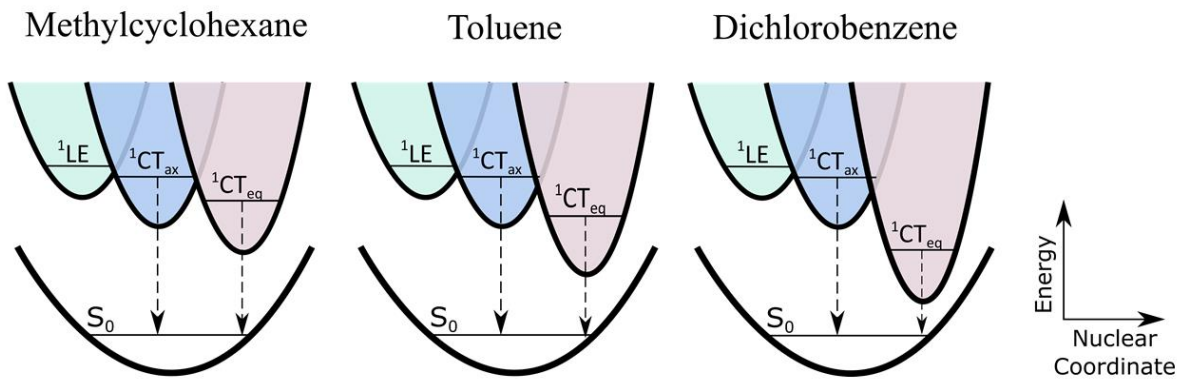

Figure 33 Schematic energy level diagram of DMePT-TXO2 in different solvents. ^1LE, CT_{ax}, CT_{eq} and S_0, refers to: local excited state, axial charge transfer state, equatorial charge transfer state and ground state, respectively.

The peak emission of CT_{ax} in MCH (337 nm excitation), toluene and DCB, are 371 nm, 391 nm and 407 nm, respectively. This leads to a red shift of 36 nm from the lowest to the highest-

polarity environments. The peak emission of CT_{eq} in MCH, toluene and DCB, are 450 nm, 479 nm and 528 nm, respectively, showing a large red-shift of 78 nm. These results enabled us to build a simple potential-well scheme of the excited states (^{1}LE and ^{1}CTs) in different solvent polarities (Figure 33). As the solvent polarity increases, the CT energy levels start to decrease, because of the large dipole moment of the charge transfer states leading to strong screening of the Coulomb term by the reorganization of the solvent shell. On the other hand, ^{1}LE remains nearly unchanged because its emission is not affected by the polarity of the solvent (see Figure 34a). In low-polarity solvents, the overall emission has strong LE character, and the energy difference between CT_{eq} and CT_{ax} is small. By increasing the solvent polarity, the CT states gradually red shift, resulting in less LE character and a higher energy difference between CT_{ax} and CT_{eq}. The contribution of triplet excited states to the overall emission was analyzed in DMePT-TXO2 (337 nm excitation) and it was 10% for toluene (see Figure 34b) and 16% for DCB (see Figure 34c).

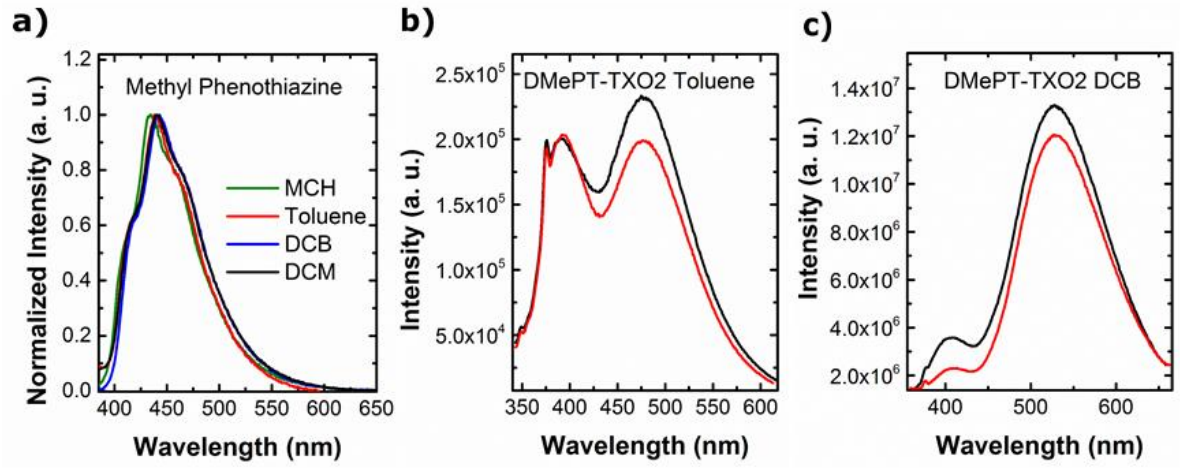

Figure 34 a) Normalized photoluminescence (PL) spectra of methyl phenothiazine in methylcyclohexane (MCH), toluene, 1,2-dichlorobenzene (DCB) and dichloromethane (DCM) solvents. Degas test of DMePT-TXO2 in b) toluene and c) DCB solutions. Black curves refer to degassed solutions and red curves to aerated solutions.

Figure 35a shows the decay curves of DPT-TXO2 in different solvents. The curves are normalized for better comparison. Two different regimes can be seen: a fast decay (early ns), associated to prompt CT emission (PF), and a slow decay (late ns, µs and ms), associated to the delayed fluorescence (DF). As expected, the DCB solution shows higher DF contribution because in this environment the DPT-TXO2 has the smallest CT-^{3}LE energy splitting (ΔE_{ST}). Figure 35b shows the same analysis for DMePT-TXO2. The decay curves are in agreement

with the degassing results, which show that the triplet contribution in DMePT-TXO2 is very low, with almost no DF emission. DMePT-TXO2 in MCH and toluene solvents show just prompt CT emission, no DF was observed. However, in DCB the DF emission was identified, but is much weaker than that observed from DPT-TXO2.

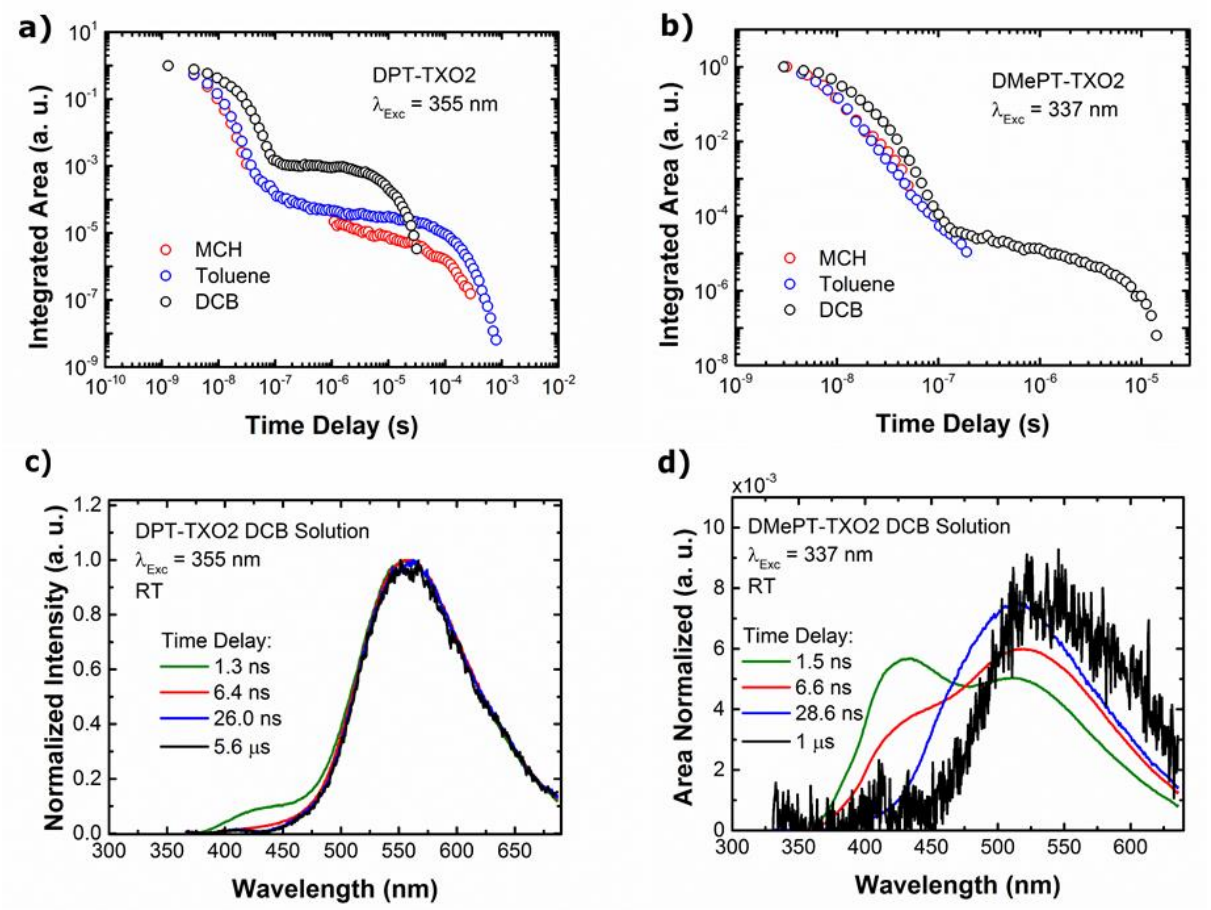

Figure 35 Time resolved fluorescence decay curves of a) DPT-TXO2 and b) DMePT-TXO2 molecules in different solvents: MCH, toluene and 1,2-dichlorobenzene (DCB). Time resolved emission spectra in different time delays of collection of c) DPT-TXO2 and d) DMePT-TXO2 molecules in DCB solvent. DPT-TXO2 molecules were excited at 355 nm and DMePT-TXO2 at 337 nm, all at RT.

DCB solutions show stabilized CT formation in both molecules, bringing CT closer to and in resonance with the ^{3}LE state; thus, the emission spectra in the PF and DF regions is analysed. Figure 35c shows that DPT-TXO2 has almost the same emission spectra (shape and position) in the entire region of analyses, apart from a vestige of emission around 425 nm in earliest times, which can be assigned to either donor emission or very weak CT_{ax}. The majority of the

emission in both regions (PF and DF) comes from the same transition, $^1CT \rightarrow S_0$. The latest emission was collected at TD = 35 µs.

Analogous experiments were performed with DMePT-TXO2 (Figure 35d). In the first 10 nanoseconds, strong CT_{ax} emission is observed competing with CT_{eq} emission, and at later times, pure CT_{eq} emission is detected. As both emissions are observed simultaneously and in these area normalized spectra an isoemissive point is observed, it is clear that they are independent states and that the CT_{ax} states are not quenched by CT_{eq}. In the µs range, the emission was very weak, as can be seen at TD = 1 µs, and the last DF spectrum detected was at TD = 15 µs. The emission spectra of DMePT-TXO2 in DCB solution at different time delays were also analysed for a lower excitation energy, 355 nm (Figure 36a). These results show that less CT_{eq} states are formed compared to the case shown in Figure 35d; this is because in the first few nanoseconds the spectra show a higher contribution of CT_{ax} than CT_{eq}.

Interestingly, in DCB, the CT_{ax} state still lives a few nanoseconds, making it possible to detect clearly its emission with the iCCD camera. However, for toluene (Figure 36b) and MCH (Figure 36c) solutions, the CT_{ax} emission is detected weakly, due to the very fast decay of this state in these less polar environments. Thus, it suggests that the high polarity environment stabilizes the $CT_{ax,}$ even though its contribution, in the overall emission (PL spectra), is much weaker than the CT_{eq} and the lifetime is much faster.

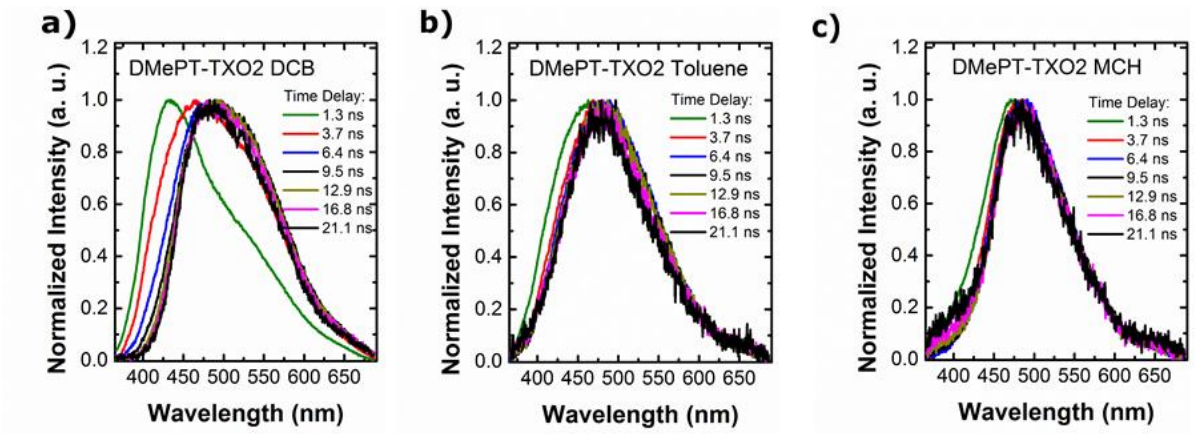

Figure 36 Time resolved emission spectra of DMePT-TXO2 in a) 1,2-dichlorobenzene (DCB) b) toluene and c) methylcyclohexane (MCH) solutions. The solutions was excited at 355 nm.

The intensity dependence of the DF emission in the DF region of both molecules was analysed as a function of the laser excitation dose. A linear gradient of 0.970 ± 0.005 was found for DPT-TXO2 and 1.19 ± 0.02 for DMePT-TXO2 (Figure 37). These results confirm the

thermally assisted mechanism as opposed to triplet-triplet annihilation (TTA) for DPT-TXO2 and DMePT-TXO2 in DCB solvent.

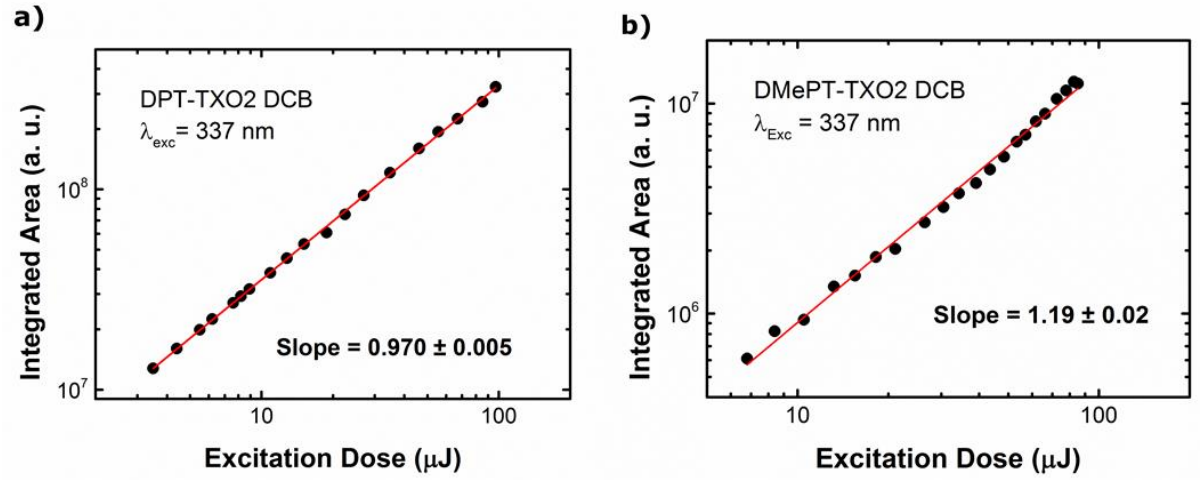

Figure 37 Integrated area of delayed fluorescence spectra as a function of excitation dose for a) DPT-TXO2 and b) DMePT-TXO2 1,2-dichlorobenzene (DCB) solutions.

Therefore, the analyses of the solution measurements show that the incorporation of a methyl group on the phenothiazine D units profoundly changes the photophysics of the D–A–D molecules. DMePT-TXO2 shows two clearly different CT states (337 nm excitation). These two CT states are correlated with two different conformations of the molecule. It is likely that, when the molecules are excited at higher energies (high excess energy) or are in a high polarity environment, the initial configuration between D and A units, namely $CT_{ax\text{-}ax}$, can re-orient to yield the $CT_{ax\text{-}eq}$ configuration. However, at low excitation energies or low polarity environments, the formation of the weak CT state, $CT_{ax\text{-}ax,}$ is also strongly observed. Recent research has also enabled the observation of two switchable conformations for D–A–D molecules with phenothiazine donor units, due to the intrinsic nature of this donor unit, and its ability to form H-intra and H-extra folded conformers that allow formation of parallel quasi-axial and perpendicular quasi-equatorial CT states in the DPTZ-DBTO2 molecule[7].

5.2.3 Solid State Photophysical Properties

The solid state properties of DPT-TXO2 and DMePT-TXO2 were analysed in a zeonex matrix (low polarity environment). Figure 38 shows the steady-steady emission of both molecules in air and under vaccum. DPT-TXO2 shows just ^{1}CT emission in air and a large contribution of phosphorescence (PH) when the oxygen is removed. PH emission at RT is not a common characteristic observed in highly efficient TADF emitters, because efficient rISC is observed,

up-converting the majority of the local triplet states back to the singlet CT state. However, as observed in MCH, the ΔE_{ST} of DPT-TXO2 is moderately large, and a proportion of the ^3LE_D states are not up-converted and remain as triplet states giving donor phosphorescence. DMePT-TXO2 in zeonex shows results similar to that observed in MCH solution: two different CT states are observed; $CT_{ax\text{-}ax}$ around 370 nm, and $CT_{ax\text{-}eq}$ around 450 nm. When the oxygen is removed, a large contribution of PH is also observed. Hence, three distinct emissions are observed simultaneously in DMePT-TXO2 zeonex film.

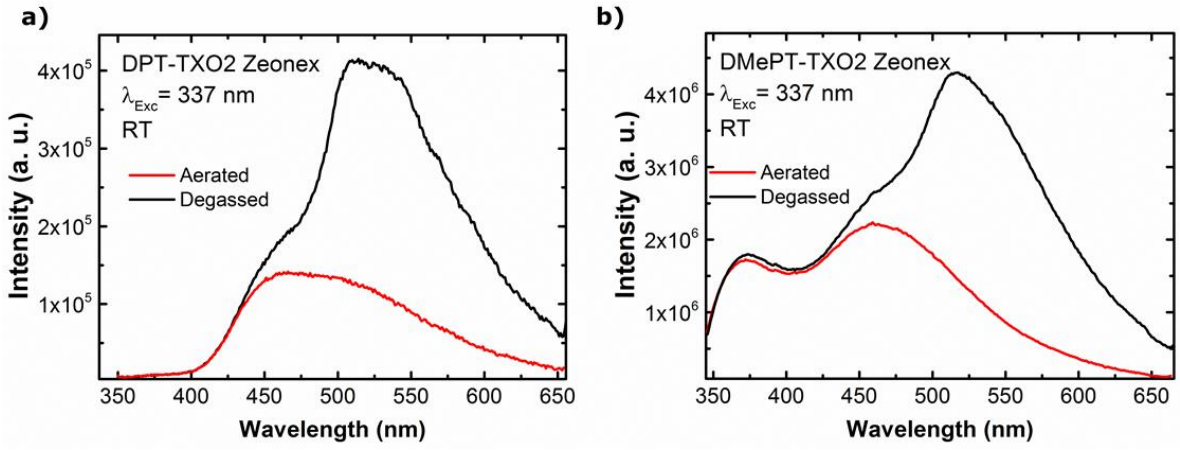

Figure 38 a) Normalized photoluminescence (PL) spectra of DPT-TXO2 and b) DMePT-TXO2. Black curves are taken with the film under vacuum (degassed) and red curves for aerated films.

Figure 39a shows how the maximum intensity of each CT state of DMePT-TXO2 zeonex film depends on the excitation energy. The emission spectra used to produce this data is shown in Figure 39b. Contrary to the result in MCH, the maximum peak intensity of the CT states does not change much by changing the excitation energy. This can be attributed to the fact that in solid state, the molecules are confined and are not free to re-orient as in solution.

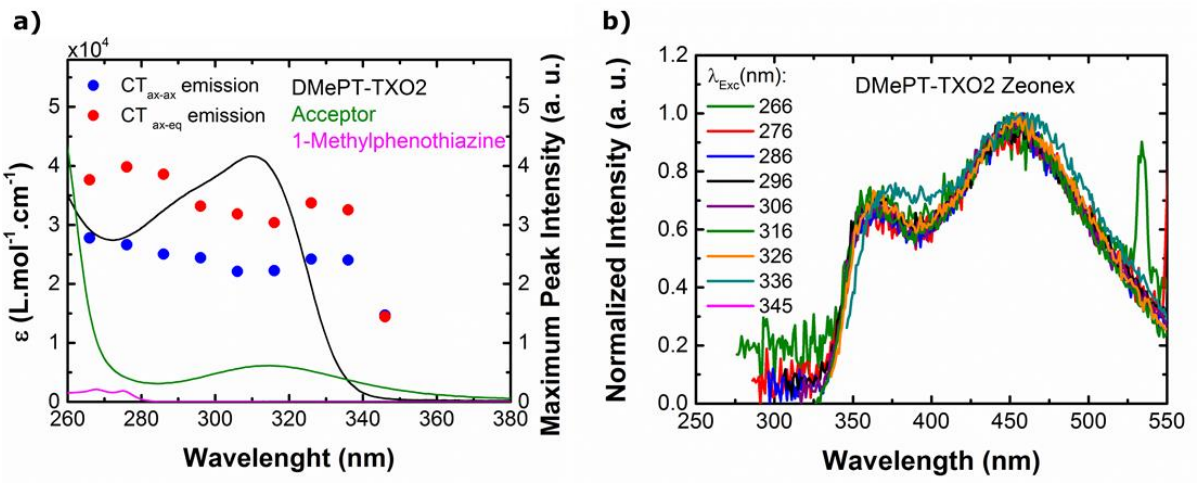

Figure 39 a) Maximum peak intensity of CT axial-axial emission (blue dot) and CT axial-equatorial emission (red dot) of DMePT-TXO2 in zeonex matrix at different energy excitations. Full lines are the same extinction coefficient data shown in Figure 28a. b) Photoluminescence (PL) spectra used to produce graphic shown in b.

Figure 40a shows the decay curve in different temperatures of DPT-TXO2 zeonex film. The PF emission does not show dependence with the temperature; however the DF emission shows higher intensity at higher temperatures, as expected for a TADF mechanism. Figure 40b shows the time resolved emission decay of DPT-TXO2 film at 80 K. In the first nanoseconds, DPT-TXO2 shows emission spectra that peaks around 450 nm. This emission is associated with the ^{1}CT state; however, some emission from ^{1}LE may occur because the ^{1}CT is very close in energy to the donor unit emission. Increasing the time delay, the emission spectrum progressively shifts to longer wavelengths, moving from ^1LE_D to ^{1}CT and then to ^3LE_D.

The observed triplet emission comes from the local triplet state of the donor unit, as seen by comparison of the PH spectra of DPT-TXO2 and pure phenothiazine taken with the same experimental conditions (Figure 40c). DPT-TXO2 PH emission has a relatively long lifetime, and it was easily detected even after 89 ms. The same spectral analyses were made at 290 K (Figure 40d). At higher temperature, the DF emission contribution, which comes from the ^{1}CT states, is stronger, and the PH weaker, as expected for TADF, due to the increased thermally activated energy for rISC.

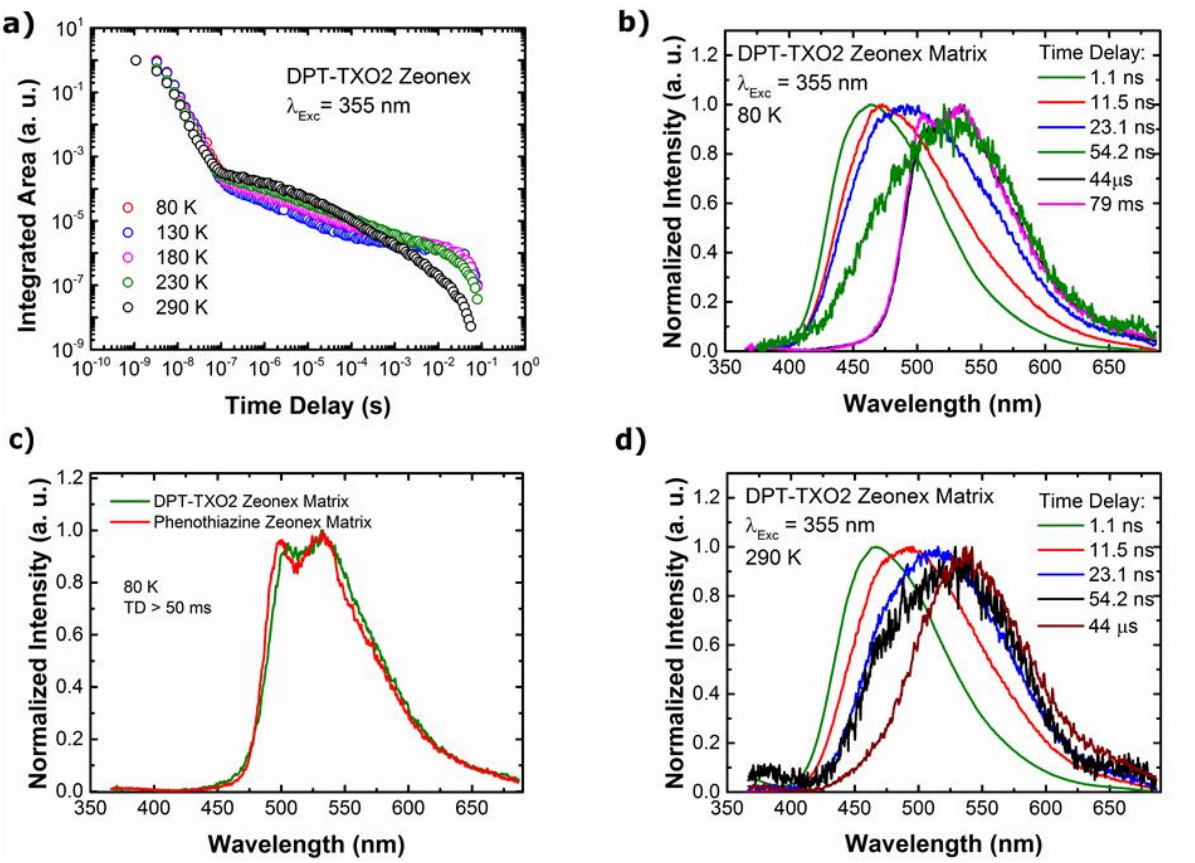

Figure 40 a) Decay curves of DPT-TXO2 in zeonex matrix. b) Time resolved normalized emission spectra of DPT-TXO2 in different time delays of collection at 80 K. c) Phosphorescence (PH) spectra of DPT-TXO2 and its donor unit, phenothiazine, both in zeonex matrix. The PH spectra were collected at 80 K with time delay (TD) longer than 50 ms. d) Time resolved normalized emission spectra of DPT-TXO2 in different time delays of collection at 290 K. All films were excited at 355 nm.

Figure 41a shows the decay curves for DMePT-TXO2 in zeonex matrix, under excitation at 337 nm. Initially, a fast decay, related to the prompt emission, is observed, followed by an interval during which no emission was above the detection noise floor of the iCCD camera (using the same TD and IT as used to collect the decay curve shown in figure 36a), and then, at longer time delays, phosphorescence appears. Figure 41b (left) shows the emission spectra in the PF region. At TD = 1.1 ns a shoulder around 375 nm is observed which may be associated with the $CT_{ax\text{-}ax}$ state, which has faster decay than $CT_{ax\text{-}eq}$. As the TD increases, the CT_{eq} emission shows a slight red shift to ca. 400 nm, and can be associated with the relaxation of this state, as also seen in the DPT-TXO2. The emission spectra in the PH region, Figure 41b (right), shows an interesting feature. As the TD increases, an emission on the blue edge of the spectra grows in. This PH emission on the blue edge is assigned as the PH from the axial

conformation, $^{3}LE_{ax}$, which acts as an effective loss pathway in the emission of this molecule. This higher energy triplet state cannot couple with the $^{1}CT_{eq}$ state identified in the prompt emission, thus the rISC is suppressed and any TADF is observed.

The photoluminescence quantum yields (PLQY) of each material also show strong dependence on the TADF mechanism. DPT-TXO2 in zeonex matrix has PLQY values of (10 ± 1)%, in nitrogen atmosphere and (4.2 ± 0.4)% in air. Whereas, DMePT-TXO2 has PLQY values of (4.5 ± 0.4)% in nitrogen atmosphere and (4.1 ± 0.4)% in air. The latter values are very close each other, due the fact that DMePT-TXO2 has no TADF contribution in zeonex matrix, therefore the PLQY value is not enhanced by removing the oxygen**.**

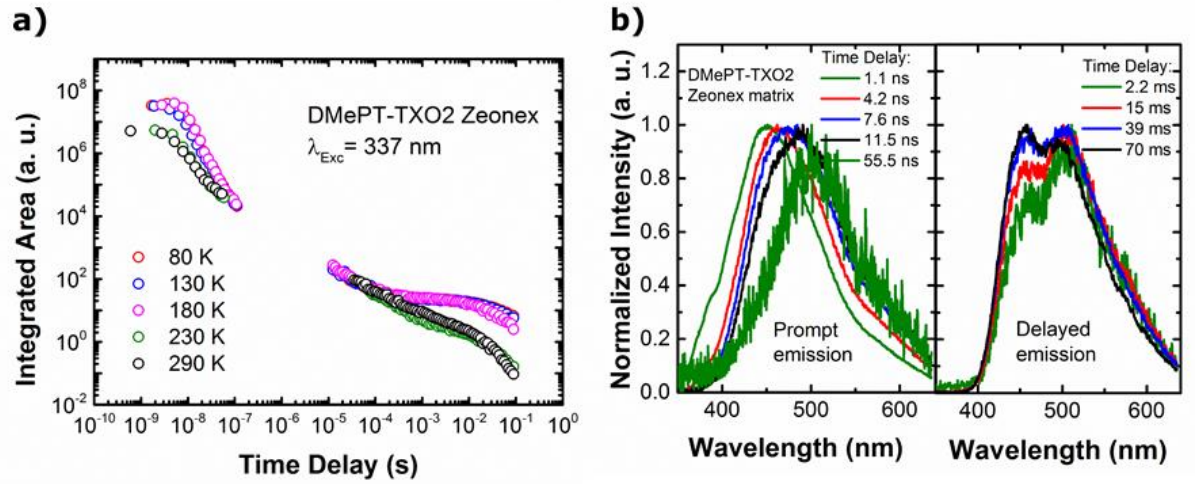

Figure 41 a) Decay curves of DMePT-TXO2 in zeonex matrix. b) Time resolved normalized emission spectra of DMePT-TXO2 in different time delays of collection at 80 K.

Figure 42 shows the DMePT-TXO2 PH time dependent spectra with different excitation energies, and longer integration time than the spectra showed in Figure 41b. The PH spectra of the donor and acceptor units in pristine film are also displayed, in dash-lines, for comparison. The PH spectrum of 1-methylphenothiazine is very similar to phenothiazine, and the PH spectrum of the acceptor unit have been previously reported [22].

With excitation at 355 nm, the earliest PH spectrum displayed in the graph (TD = 2 ms) shows just a shoulder due to the $^{3}LE_{ax}$ contribution, as described above. For excitation at 266 nm, the PH shows a different feature. A PH emission from the A units is also observed, which becomes the dominant triplet emission at later TD. This strong triplet emission arises from the strong

absorption of the A units at 266 nm (See Figure 28a). Both ^3LE_A and ^3LE_D, emit strongly until the end of the measurement (TD=89 ms).

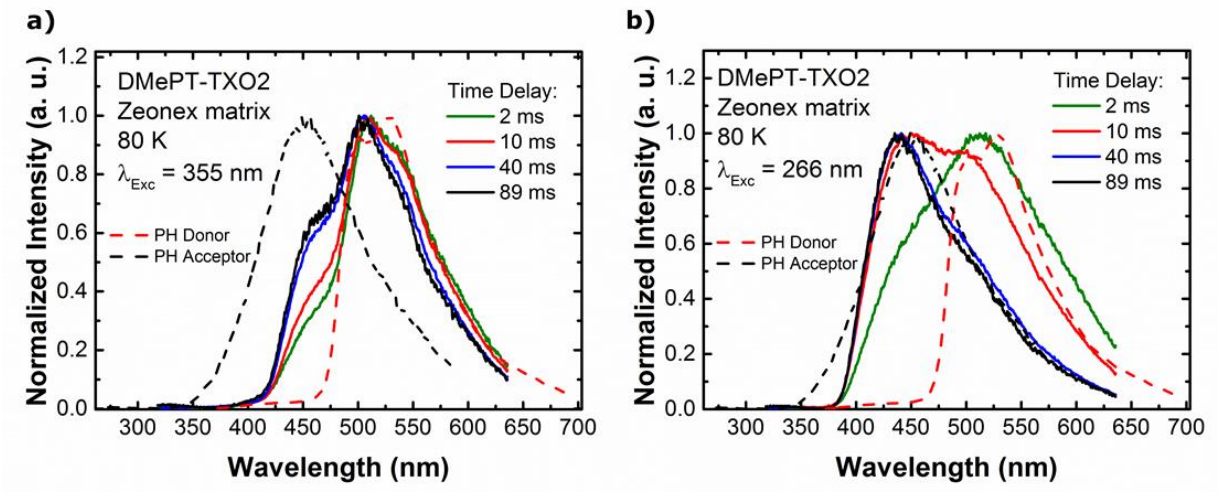

Figure 42 Time resolved normalized emission spectra of DMePT-TXO2 in the phosphorescence emission region for excitation at a) 355 nm and b) 266 nm at 80 K.

Therefore, the PH of DMePT-TXO2T in zeonex highlights different features at different excitations energies. Excitation at higher energy shows dual PH emission from the ^3LE states of both the donor and acceptor units, which behave as independent emitting species, showing that the D and A units of these molecules are totally electronically decoupled. The contribution from the acceptor is stronger at later times, indicating a longer triplet state lifetime. On the other hand, for DPT-TXO2 in zeonex matrix, the PH comes from the lowest triplet state, ^3LE_D which may imply some D–A conjugation within the molecules.

Regarding the ^1CT-^3LE energy splitting, ΔE_{ST}, DMePT-TXO2 should show more efficient TADF than DPT-TXO2. Both molecules have similar $^1CT_{eq}$ states, but DMePT-TXO2 has closer local triplet levels, due to the contribution of the $^3LE_{ax}$. However, $^3LE_{ax}$ cannot couple with $^1CT_{eq}$, and the $^1CT_{ax}$ has much higher energy, resulting in a huge energy gap between $^1CT_{ax}$ and $^3LE_{ax}$, suppressing any rISC process.

Therefore, the solid-state analysis reveals that the methyl group incorporated in the D units also gives rise to the formation of two distinct PH states, $^3LE_{eq}$ and $^3LE_{ax;}$ the latter one does not undergo rISC, preventing the TADF mechanism from occurring and giving rise to PH at RT. The $^3LE_{ax}$ state thus is an energy sink in the DMePT-TXO2 system, as has also been observed in other molecules where phenothiazine is in an axial conformation[7].

5.3 Conclusion

In summary, the photophyscial properties of DPT-TXO2 and DMePT-TXO2 in different solutions and solid state were investigated. DMePT-TXO2 molecules shows dual fluorescence clearly coming from two different CT states. These two CT states are correlated with two different conformations of the molecule. When the molecules are excited at higher energies (high excess energy) or are in a high polarity environment (polar solvents), it is likely that the initial configuration between D and A units $CT_{ax\text{-}ax}$ can re-orient to yield the $CT_{ax\text{-}eq}$ configuration. However, when molecular motion is suppressed, by dispersing the molecules in a solid state host, this re-orientation is not observed and strong phosphorescence at room temperature is detected, besides the fluorescence emission.

Additionally, the solid state analysis enables an in-depth study of the triplet states of these D–A–D molecules. Experiments identify that the PH of DMePT-TXO2 has a main contribution from $^3LE_{eq}$ but also shows $^3LE_{ax}$ emission. Regarding the TADF mechanism, DPT-TXO2 molecules show repopulation of the ^1CT state via a reverse intersystem crossing process in solutions and solid state. On the other hand, DMePT-TXO2 molecules show this characteristic only in polar solutions, that is in an environment where the molecules are free to rotate; in contrast, in the solid state, the rISC process is completely suppressed.

Therefore, the comparison between DPT-TXO2 and DMePT-TXO2 is important for gaining a better understanding about the subtle relationship between molecular conformation of the constituent units and the TADF mechanism, making easier the design of novel TADF materials in the future.

5.4 Sample Preparation Details

Two types of samples were studied in this chapter: solutions (10^{-3} to 10^{-5} M) and films produced in zeonex matrix (organic material 2.5 mg/mL:zeonex 180 mg/mL 1:1 *v/v*). The solutions were degassed to remove all the oxygen dissolved by four freeze-pump-thaw cycles to perform the degas test and delayed fluorescence measurements. The films in zeonex matrix were fabricated by drop casting onto quartz substrates.

5.5 References Chapter 5

1. Daub, J. *et al.* Competition between conformational relaxation and intramolecular electron transfer within phenothiazine-pyrene dyads. *J. Phys. Chem. A* **105,** 5655–5665 (2001).
2. Stockmann, A. *et al.* Conformational control of photoinduced charge separation within phenothiazine-pyrene dyads. *J. Phys. Chem. A* **106,** 7958–7970 (2002).
3. Acar, N. *et al.* Phenothiazine - Pyrene Dyads: Photoinduced Charge Separation and Structural Relaxation in the CT State. *J. Phys. Chem. A* **107,** 9530–9541 (2003).
4. Malrieu, J.-P. & Pullman, B. Sur les proprietes electroniques de la phenothiazine et de son radical. *Theor. Chim. Acta* **2,** 293–301 (1964).
5. Bodea, C. & Silberg, I. Recent Advances in the Chemistry of Phenothiazines. *Chim. Int. J. Chem.* **66,** 321–460 (1968).
6. Coubeils, J. L. & Pullman, B. Molecular orbital study of the conformational properties of phenothiazines. *Theor. Chim. Acta* **24,** 35–41 (1972).
7. Etherington, M. K. *et al.* Regio- and conformational isomerization critical to design of efficient thermally-activated delayed fluorescence emitters. *Nat. Commun.* **8,** 14987 (2017).
8. Okazaki, M. *et al.* Thermally Activated Delayed Fluorescent Phenothiazine-Dibenzo[a,j]phenazine-Phenothiazine Triads Exhibiting Tricolor-Changing Mechanochromic Luminescence. *Chem. Sci.* **8,** 2677–2686 (2017).
9. Tanaka, H., Shizu, K., Nakanotani, H. & Adachi, C. Dual intramolecular charge-transfer fluorescence derived from a phenothiazine-triphenyltriazine derivative. *J. Phys. Chem. C* **118,** 15985–15994 (2014).
10. Wang, K. *et al.* Avoiding Energy Loss on TADF Emitters: Controlling the Dual Conformations of D–A Structure Molecules Based on the Pseudoplanar Segments. *Adv. Mater.* **29,** 1–9 (2017).
11. Zhang, Q. *et al.* Efficient blue organic light-emitting diodes employing thermally activated delayed fluorescence. *Nat. Photonics* **8,** 1–7 (2014).
12. Higginbotham, H. F., Yi, C.-L., Monkman, A. P. & Wong, K.-T. Effects of Ortho-Phenyl Substitution on the rISC Rate of D–A Type TADF Molecules. *J. Phys. Chem. C* **122,** 7627–7634 (2018).
13. dos Santos, P. L. *et al.* Engineering the singlet-triplet energy splitting in a TADF molecule. *J. Mater. Chem. C* **4,** 3815–3824 (2016).
14. Malrieu, J.-P. & Pullman, B. Configuration spatiale et proprietes electroniques du noyau d'isoalloxazine. *Theor. Chim. Acta* **2,** 302–314 (1964).
15. Aizenshtat, Z., Klein, E., Weiler-Feilchenfeld, H. & Bergmann, E. D. Conformational Studies on Xanthene, Thioxanthene and Acridan. *Isr. J. Chem.* **10,** 753–763 (1972).
16. Dias, F. B. *et al.* The Role of Local Triplet Excited States in Thermally-Activated Delayed Fluorescence: Photophysics and Devices. *Adv. Sci.* **3,** 1–10 (2016).

17. Chu, S. S. C. & Chung, B. J ; *Acta Cryst.* **571,** 1616–1618 (1974).

18. Ward, J. S. *et al.* The interplay of thermally activated delayed fluorescence (TADF) and room temperature organic phosphorescence in sterically-constrained donor–acceptor charge-transfer molecules. *Chem. Commun.* **52,** 3–6 (2016).

19. dos Santos, P. L., Ward, J. S., Batsanov, A. S., Bryce, M. R. & Monkman, A. P. Optical and Polarity Control of Donor-Acceptor Conformation and Their Charge-Transfer States in Thermally Activated Delayed-Fluorescence Molecules. *J. Phys. Chem. C* **121,** 16462–16469 (2017).

20. Marian, C. M. Spin-orbit coupling and intersystem crossing in molecules. *Wiley Interdiscip. Rev. Comput. Mol. Sci.* **2,** 187–203 (2012).

21. Penfold, T. J. On Predicting the Excited-State Properties of Thermally Activated Delayed Fluorescence Emitters. *J. Phys. Chem. C* **119,** 13535–13544 (2015).

22. Santos, P. L. *et al.* Engineering the singlet–triplet energy splitting in a TADF molecule. *J. Mater. Chem. C* **4,** 3815–3824 (2016).

23. dos Santos, P. L., Ward, J. S., Bryce, M. R. & Monkman, A. P. Using Guest–Host Interactions To Optimize the Efficiency of TADF OLEDs. *J. Phys. Chem. Lett.* 3341–3346 (2016).

24. Youn Lee, S., Yasuda, T., Nomura, H. & Adachi, C. High-efficiency organic light-emitting diodes utilizing thermally activated delayed fluorescence from triazine-based donor-acceptor hybrid molecules. *Appl. Phys. Lett.* **101,** 1–5 (2012).

Chapter 6: Using Guest Host Interactions to Optimize Blue TADF OLEDs

This chapter shows that the emitter and host combination must be optimized to minimize the reverse intersystem crossing (rISC) barrier and maximize TADF. The blue TADF emitter, 2,7-bis(9,9-dimethyl-acridin-10-yl)-9,9-dimethylthioxanthene-*S*,*S*-dioxide (DDMA-TXO2), has strong TADF character due to efficient charge transfer state formation. By combining DDMA-TXO2 with a host of the correct polarity (DPEPO) that relaxes the CT manifolds energy to become resonant with the lowest energy local triplet state of DDMA-TXO2, the emitter and host combination produce a minimum rISC barrier (ΔE_{ST}), which maximises TADF efficiency. It is shown that the sensitivity of this splitting is highly dependent on emitter environment and must be carefully tuned to optimised device performance. Devices utilising DDMA-TXO2 in DPEPO host show blue EL, CIE (0.16, 0.24) with maximum external quantum efficiency of 22.4 %. This high device performance is a direct consequence of optimising the TADF efficiency by this 'host tuning'.

The work presented in this chapter is an adapted version of the manuscript published at *Journal of Physical Chemistry Letters* (P. L. dos Santos, J. S. Ward, M. R. Bryce and A. P. Monkman, *J. Phys. Chem. Letters* 2016, *7*, 3341). It was a collaborative work between the OEM group and the chemistry department, both at Durham University. P. L. dos Santos performed all steady state and time resolved photophysics measurements, the device fabrication, and device testing. Dr. J. S. Ward devised and performed the synthesis, purification and chemical characterization.

6.1 Introduction

Whereas the CT states are very sensitive to the local environment, the local triplet states are not, as discussed in chapter 4[1,2]. Therefore, the host choice effects the energy gaps that directly changes the rate of reverse intersystem crossing (rISC). Thus, to achieve very small optical ΔE_{ST} the host environment must be taken into account and tuned to optimise device efficiency.

In this chapter, the photophysical properties of 2,7-bis(9,9-dimethyl-acridin-10-yl)-9,9-dimethylthioxanthene-*S*,*S*-dioxide (DDMA-TXO2) in different hosts along with the photophysical properties of the acceptor (A) and donor (D) units are studied (see reference [3] for details on synthesis). 9,9-dimethyl-10H-acridine was chosen as the donor unit due its weaker donor character if compared to phenoxazine (Chapter 4) and phenothiazine (Chapter 5), thus the D-A-D emitter was expected to have higher singlet and triplet energies, and consequently emit in the blue region. TADF mechanism and blue emission was identified in DDMA-TXO2 molecules dispersed in nonpolar and polar hosts. Moreover, strong CT relaxation dynamics was observed and used to determine the correct CT energy that should be used to calculate correctly the optical ΔE_{ST}. After device optimization, efficient blue OLEDs were fabricated in DPEPO host showing maximum EQE of 22.4 % at 127 cd/m^2, high brightness levels (>2,500 cd/m^2), excellent resistance to roll-off up to 10 mA/cm^2 and low turn on voltage ≈ 3 V.

6.2 Results and Discussion

6.2.1 Solution State Photophysical Properties

Figure 43 shows the normalized absorption (a) and emission (b) spectra of the A and D units as well as the DDMA-TXO2 molecule. The donor unit is diluted in toluene solvent, the acceptor unit in methylcyclohexane (MCH) solvent and DDMA-TXO2 in both solvents. The chemical structure of DDMA-TXO2 is also shown in the inset of Figure 43a. The absorption spectrum of DDMA-TXO2 shows two peaks. The peak around 290 nm is the same as that observed in the donor unit spectrum; however, the second peak, around 360 nm, does not appear in either the D or the A absorption spectra and it was assigned as 'direct' CT absorption[4,5]. The DDMA-TXO2 emission spectra show clear and strong CT emission evidenced by its Gaussian band shape and red shift compared to the individual D and A

emission spectra. The PL spectra move to longer wavelength with increasing solvent polarity, showing a strong positive solvatochromism, as observed before in other D-A-D type molecules[2,6–9].

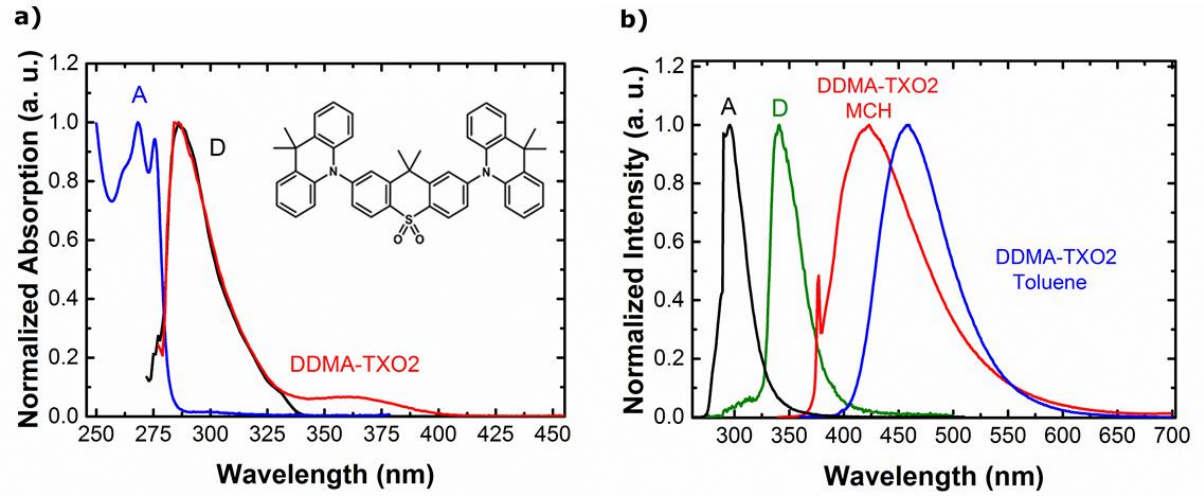

Figure 43 a) Normalized absorption and b) emission spectra of acceptor (A), donor (D), and D-A-D (DDMA-TXO2) molecules. D unit is diluted in toluene solvent, A unit in methylcyclohexane (MCH) solvent and D-A-D in both solvents. The acceptor and donor units were excited at 266 nm and the D-A-D at 337 nm. Inset graph shows the chemical structure of DDMA-TXO2.

6.2.2 Solid State Photophysical Properties

The first solid state matrix studied was zeonex, a nonpolar inert matrix. Figure 44a shows the time dependent emission decay curves at various temperatures of DDMA-TXO2 in zeonex matrix from the early prompt emission (ns) to the end of the DF (ms). The curves were obtained with 355 nm excitation (>200 μJ) giving direct CT photo creation. The decay curves at higher temperatures show clear double exponential decays, assigned as prompt and delayed emission regions (of the same species, having an effective longer life time due to rate of slow rISC). The DF emission has clearly higher intensity at high temperatures, indicative of a TADF contribution. At low temperatures, the curves show prompt emission, followed by an interval during which any emission was below the detection noise floor of the iCCD, and then, at longer time delays, phosphorescence emission appears. The emission at very long time delays, shows higher intensity at low temperatures, as expected for triplet emission.

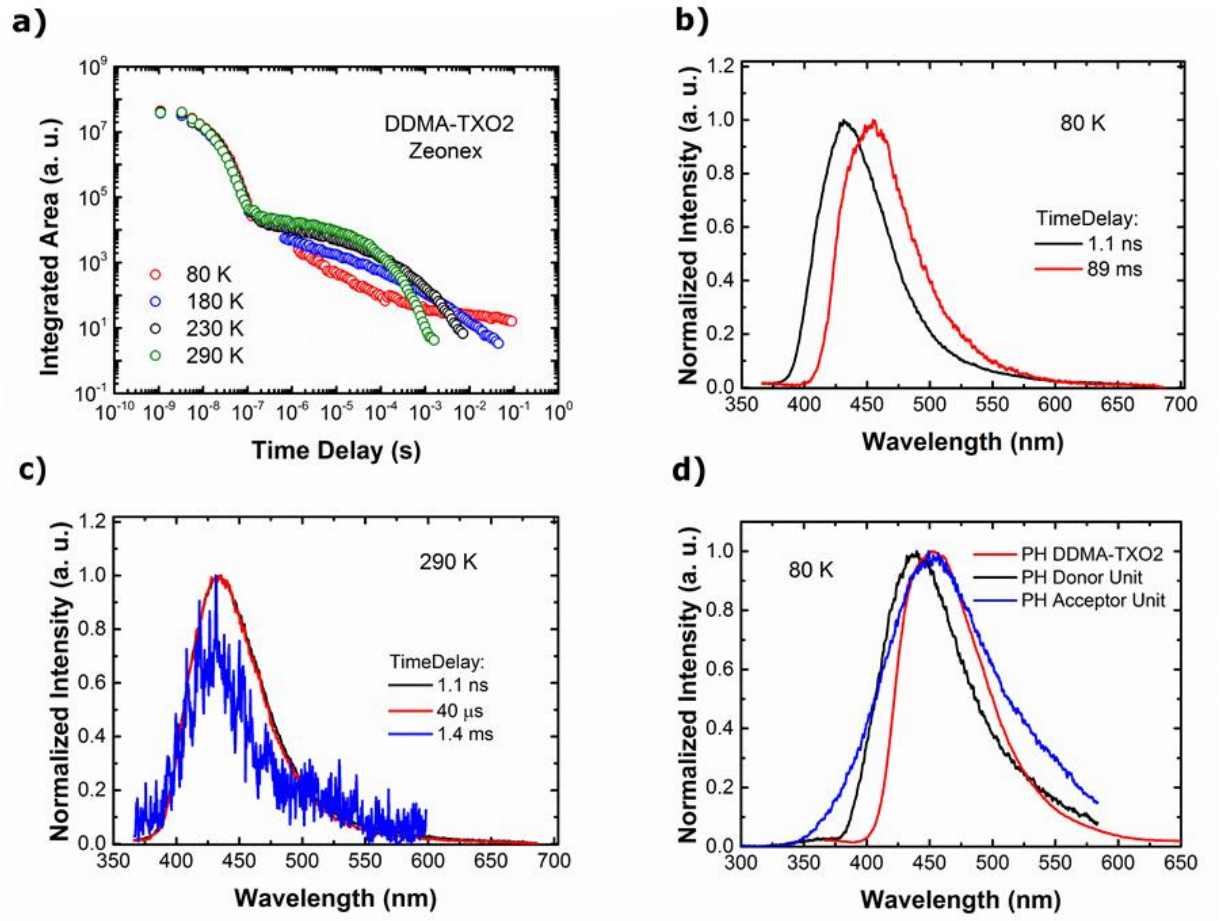

Figure 44 a) Time resolved fluorescence decay of DDMA-TXO2 in zeonex matrix in different temperatures. b) Time resolved normalized emission spectra of DDMA-TXO2 at 80 K and c) at 290 K. d) Phosphorescence spectra of donor and acceptor units and DDMA-TXO2, all in zeonex matrix at 80 K.

Figure 44 also shows the analyses of the normalized spectra in the entire region of study at 80 K (b) and 290 K (c). At 80 K, from TD=1.1 to TD = 124 ns, the transition $^1CT \rightarrow S_0$ is observed, and has onset at (3.17 ± 0.02) eV. At longer time delays, a very weak emission is observed, having negligible intensity. From TD = 1.3 µs to TD = 90 ms, a red shifted emission is observed, onset at (3.02 ± 0.02) eV which is assigned as phosphorescence emission (PH). The PH spectrum detected in the DDMA-TXO2 molecules was compared with the PH spectra of the individual donor and acceptor units (Figure 44d). Most likely, the DDMA-TXO2 triplet level is a mix of both local triplet (^{3}LE) states of the donor and acceptor unit, as seen in other similar D-A-D TADF molecules[10]. Therefore, the energy splitting between ^1CT and ^3LE was found to be ΔE_{ST} = (0.15 ± 0.03) eV. At 290 K, the emission spectra of DDMA-TXO2 showed a different behaviour. In the entire region of analyses, from TD = 1 ns to TD = 1.4 ms, only the transition $^1CT \rightarrow S_0$ is observed with onset at (3.17 ± 0.02) eV. This can be explained by the

fact that at high temperature, the rISC process is favourable and delayed fluorescence is efficiently observed. At low temperatures, triplet states do not have enough thermal energy to cross the activation barrier to the ^{1}CT manifold and PH is favoured over the rISC process.

After showing the strong TADF mechanism of DDMA-TXO2 in zeonex matrix, I proceed to investigate how the mechanism depends on the polarity of the medium in which the emitter is dispersed. Small molecules that are commonly used as potential hosts in TADF emitters, such as CBP and mCP, have triplet state much lower in energy than that observed in DDMA-TXO2, thus strong exciton quenching is expected. Bis[2-(di- (phenyl)phosphino)-phenyl]ether oxide (DPEPO) was then chosen as a potential host for DDMA-TXO2 as it has a triplet level comparable to DDMA-TXO2. The PH onset of DPEPO was found to be at (3.05 ± 0.02) eV **(**Figure 45), which is close to, but energetically above, the PH onset of DDMA-TXO2 in zeonex matrix, (3.02 ± 0.02) eV.

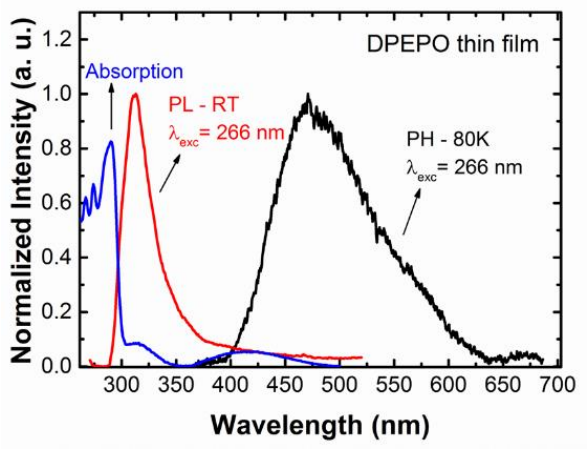

Figure 45 Absorption, photoluminescence (PL) and phosphorescence (PH) spectra of DPEPO thin film.

Figure 46a shows the time dependent emission decay curves at various temperatures of DDMA-TXO2 in DPEPO matrix from the early prompt emission (TD = 1.1 ns) to the end of the DF (TD = 89 ms). The curves were obtained with 355 nm excitation (>200 µJ). The decay curves at higher temperatures show clear double exponential decays, assigned as prompt and delayed emission regions (of the same species). At the beginning of the DF emission, the curves show clearly higher intensity at high temperatures, indicative of a TADF contribution. However, after ~ 44 µs (see Figure 46a) the temperature behaviour changes and the emission drops as the system temperature increases. The latter temperature behaviour is unexpected for

a TADF mechanism, and it will be explained later by analyses of ^{1}CT energy levels at 80 and 290 K.

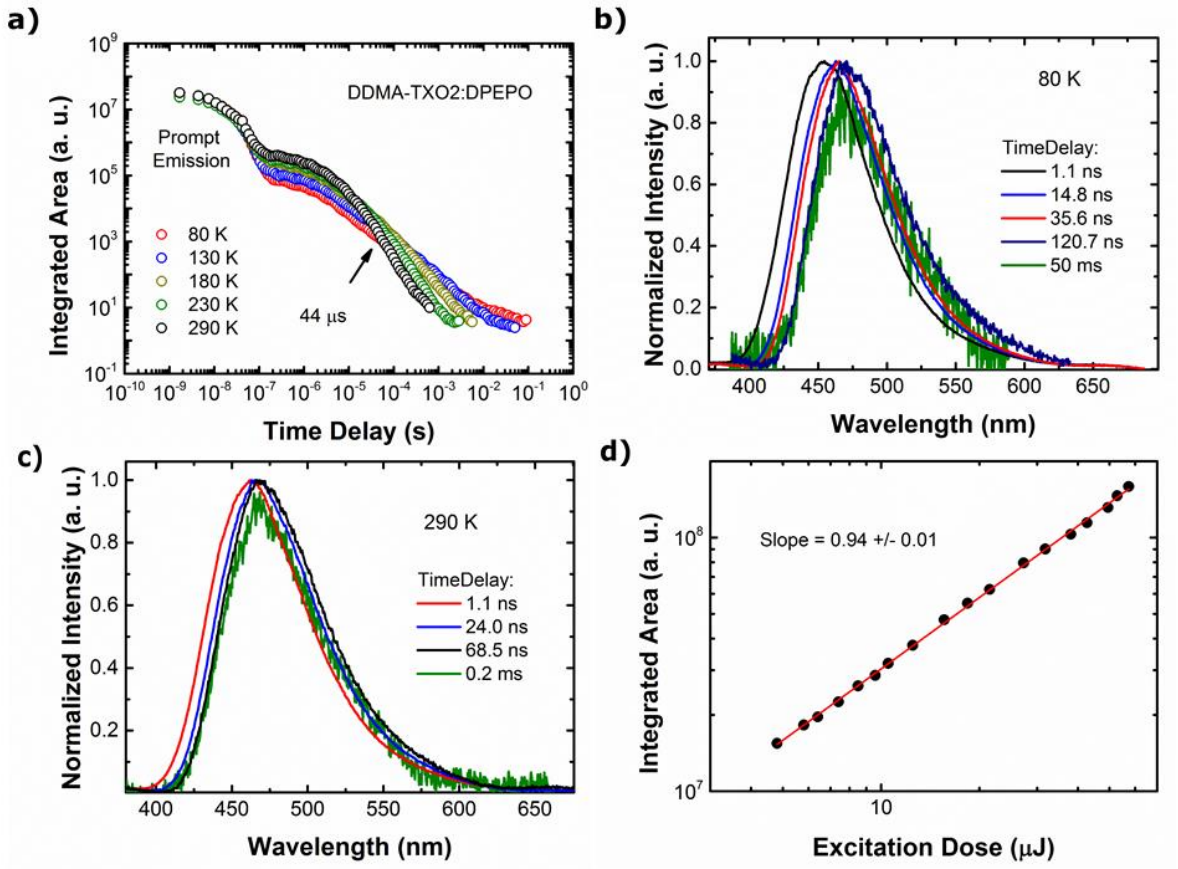

Figure 46 a) Time resolved fluorescence decay of DDMA-TXO2 in DPEPO matrix in different temperatures. b) Time resolved normalized emission spectra of DDMA-TXO2:DPEPO at 80 K and c) at 290 K. d) Integrated area of delayed fluorescence spectra as a function of excitation doses for DDMA-TXO2:DPEPO.

Figure 46 also shows the analyses of the normalized spectra in the entire region of study at 80 K (b) and 290 K (c). At 80 K, during the prompt emission, a continuous dynamic redshift is observed from TD = 1.1 to TD = 120.7 ns. This red shift is associated with the energetic relaxation of the CT state, which stabilizes after TD = 120.7 ns. The spectra have onset at (3.08 ± 0.02) eV and (2.93 ± 0.02) eV for TD = 1.1 ns and TD = 120.7 ns, respectively. After this time the spectra show no further shift until TD = 50 ms. Thus, only the transition ^{1}CT $\rightarrow S_0$ is observed in DDMA-TXO2:DPEPO at 80 K. At 290 K, the continuous redshift with increasing time delay is also observed during the prompt fluorescence region. However, at high temperatures the prompt emission region is shorter, and the stabilization of ^{1}CT occurs after TD = 68.5 ns. The spectra have onset at (3.03 ± 0.02) eV and (2.95 ± 0.02) eV for TD = 1.1 ns

and TD = 68.5 ns respectively. After this time no further relaxation is observed until TD = 0.2 ms. Furthermore, the intensity dependence of the DF emission (TD = 500 ns, Ti= 5000 ns) was analysed as a function of the laser excitation dose, and a linear gradient of 0.94 ± 0.01 was found (Figure 46d), confirming the thermally assisted mechanism.

Considering that the local triplet states, ^{3}LE, will be unaffected by the polarity of the host environment, the triplet levels of DDMA-TXO2 in DPEPO should also have onset close to (3.02 ± 0.02) eV (Figure 44b). Therefore, to evaluate the optical ΔE_{ST} barrier for rISC, the observed dynamic relaxation of the CT state should be taken into account. The energy of the unrelaxed ^{1}CT level (in DPEPO) should be taken because the relaxation of the CT state only begins after the CT state has formed, i.e. the energy of the ^{1}CT state transferred to from the ^{3}LE triplet state during rISC. Consequently, the energy splitting between ^{1}CT and ^{3}LE states at 80 and 290 K are ΔE_{ST} = (0.06 ± 0.03) eV and ΔE_{ST} = (0.01 ± 0.03) eV, respectively in DPEPO host. Also, comparing the energy of the ^{1}CT state in zeonex and DPEPO there is a static red shift of the CT state (seen at 1 ns) of ca. 140 meV because of the higher polarity of the DPEPO host matrix. It is very important to understand and take into consideration these effects of environment and relaxation on the energetics of the CT state, as in these D-A-D molecules the rate of rISC depends exponentially on the magnitude of the energy barrier. Thus, decreasing ΔE_{ST} from 0.15 eV to 0.01 eV has a very profound effect on the rISC rate and even changing from 0.06 eV to 0.01 eV will cause significant changes to the rISC rate, especially at low temperatures. Hence, at 290 K the ΔE_{ST} of DDMA-TXO2 is very small in magnitude and the rISC process is thus fast, leading to a more rapidly decaying DF component. On the other hand, at 80 K, the ΔE_{ST} is larger, and the rISC process is slower, leading to a longer lived DF component. This explains the unexpected temperature behaviour of the DF after TD = 44 µs (Figure 46a). This analysis also explains why the prompt emission is faster at 290 K, because at this temperature, the rISC has a higher rate, decreasing the time over which 'pure' prompt emission is observed. Moreover, it is also observed that as the optical ΔE_{ST} is so small, rISC is maximized and the transition ^{3}LE→S_0 is not observed in DPEPO host because all triplets are harvested by rISC which strongly out competes phosphorescence decay. Therefore, it is clear that for DDMA-TXO2 in DPEPO host, the initial ^{1}CT state energy lies very close to the triplet states, as compared to in zeonex host, yielding a very small optical ΔE_{ST}, and consequently, high efficient TADF mechanism.

The photoluminescence quantum yields (PLQY) also show strong consequences of the ΔE_{ST} values in different environments. DDMA-TXO2 in zeonex matrix shows PLQY values of (30

± 3) % in nitrogen atmosphere and (18 ± 3) % in air. Whereas, the film in DPEPO matrix shows PLQY values of (95 ± 3) % in nitrogen atmosphere and (92 ± 3) % in air. The later values are much higher than those found in zeonex matrix because the high-lying CT states yields a slow rISC rate (by at least an order of magnitude). Thus the residence time in the low lying ^{3}LE state decays by non-radiative processes in direct competition with rISC, leads to a lower PLQY values. However, in DPEPO matrix, the ΔE_{ST} is much smaller and an efficient repopulation of ^{1}CT state via rISC process occurs, leading to very high PLQY values. These results clearly show how a solid host still plays a major role in optimising the TADF efficiency and provides a unique way to tune the efficiency of an OLED.

6.2.3 Device Performance

To evaluate the potential of DDMA-TXO2:DPEPO in OLEDs, devices with different structure were fabricated. The first devices produced (Figure 47a, OLED 1) showed an extra green peak at 625 nm apart from the DDMA-TXO2 blue emission. As a tentative approach to achieve pure blue emission, a 5 nm layer of undoped DPEPO was included in the structure of the device (Figure 47b, OLED 2). As can be seen, the relative intensity of green peak in comparison to the blue peak has decreased. Thus, the undoped DPEPO layer was increased to 10 nm (Figure 47c, OLED 3) and dominant blue emission was achieved. OLED 3 was then considered to have the optimised device structure. The green peak ~625 nm was assigned as an exciplex formation between the emissive layer DDMA-TXO2 and the transport layer TPBi. Figure 47d shows the OLEDs structures in detail.

As OLED 3 was demonstrated to be the optimised device, Figure 47c compare its EL spectrum with the PH spectra of DDMA-TXO2 in zeonex matrix and the unrelaxed ^{1}CT state in DPEPO host. As can be seen, the onset of the unrelaxed ^{1}CT and EL are isoenergetic, supporting the proposal that the unrelaxed energy of the CT state is the energy 'seen' at the rISC step. The small peak shift of the EL compared to the PL is due to a residual exciplex contribution on the red side of the EL band. The onset of EL and PH spectra are very close to each other, yielding highly efficient TADF and hence efficient devices.

Figure 48 shows the electrical and optical properties of OLED 3: (a) EQE *versus* Brightness, (b) EQE *versus* Current density, (c) Brightness *versus* Current density and (d) Current density *versus* Voltage curves. OLED 3 shows a maximum EQE of 22.4% at 127 cd/m^2 with commission internationale de l'éclairage (CIE) chromaticity coordinates of (0.16, 0.24), peak

emission wavelength at 465 nm, all devices tested with this structure show an initial increase in efficiency of about 10%, before stabilizing (see Figure 48a). The device also shows good EQE value, 17.3 %, at high brightness, 913 cd/m^2, which demonstrates good resistance to roll-off up to 10 mA/cm^2. The brightness levels of the device are high >2,500 cd/m^2 and the turn on voltage very low ~ 3 V. By the date these devices were reported (2016), just few blue OLEDs exceeded 20% maximum EQE[11], which demonstrates the excellent performance of DDMA-TXO2 as blue emitter.

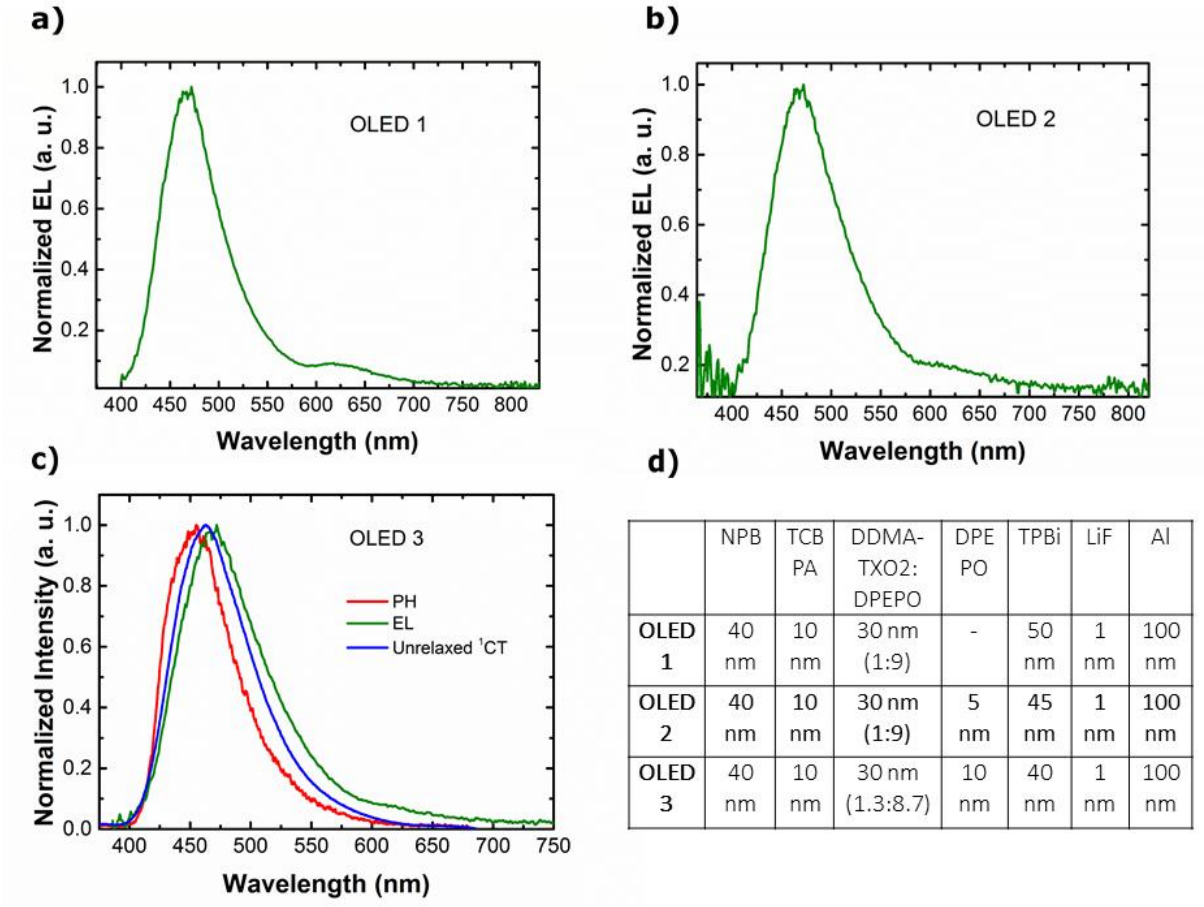

	NPB	TCBPA	DDMA-TXO2: DPEPO	DPEPO	TPBi	LiF	Al
OLED 1	40 nm	10 nm	30 nm (1:9)	-	50 nm	1 nm	100 nm
OLED 2	40 nm	10 nm	30 nm (1:9)	5 nm	45 nm	1 nm	100 nm
OLED 3	40 nm	10 nm	30 nm (1.3:8.7)	10 nm	40 nm	1 nm	100 nm

Figure 47 Normalized electroluminescence spectra of DDMA-TXO2:DPEPO devices collect at 12 V for a) OLED 1 b) OLED 2 and c) OLED 3. d) Device structures of all OLEDs. NPB is *N*,*N*′-bis(naphthalene-1-yl)-*N*,*N*′-bis(phenyl)-benzidine, TCBPA is 4,4-(diphenymethylene)bis(*N*,*N*-diphenylaniline), TPBi is 1,3,5-tris(*N*-phenylbenzimidazol-2-yl)benzene, LiF is lithium fluoride and Al is Aluminium.

The excellent performance of OLED 3 is due to a very small energy splitting between ^{1}CT and the local triplet states (^{3}LE) as confirmed by the photophysical analyses. These very promising device results clearly show that the host tuning to maximise TADF efficiency directly translates

in enhancement of OLED performance. Importantly, the high performance of OLED 3 was achieved just after purification of all the organic layers in the device, mainly the emitter and host, which were purified just before the device production[12].

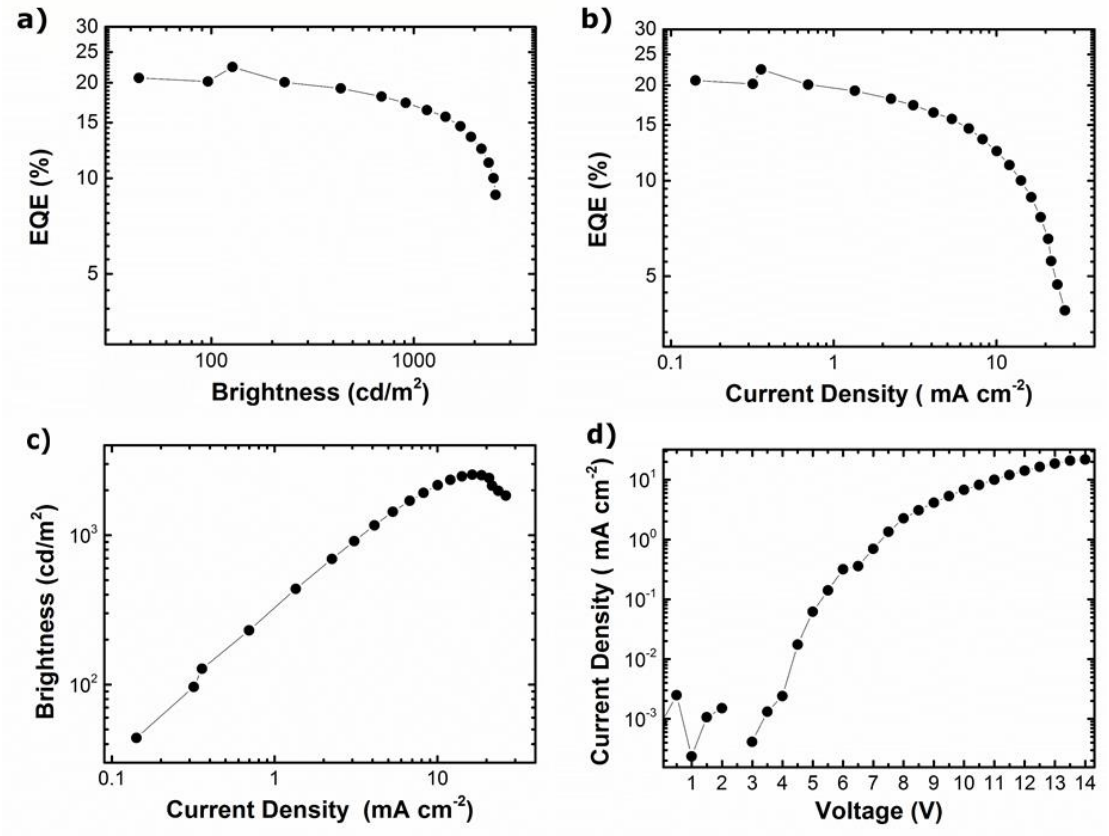

Figure 48 a) EQE versus Brightness b) EQE versus Current density c) Brightness versus Current density d) Current density versus Voltage curves for DDMA-TXO2:DPEPO OLED 3 device.

6.3 Conclusion

In summary, the photophysical properties of an efficient blue TADF emitter molecule, DDMA-TXO2, along with the photophysics of its constituent D and A units were presented. DDMA-TXO2 shows a strong and clear CT state in solution and solid state. The TADF mechanism was readily identified in solid state in different hosts. An in-depth photophysical study reveals the ^{1}CT state is lowered in energy within the polar host DPEPO, relaxed through the high polarity of the DPEPO compared to nonpolar host material zeonex, and becomes very close in energy to the triplet states of DDMA-TXO2, giving rise to a very small optical ΔE_{ST}. Moreover, the strong dynamic relaxation of the CT state, over the first 100 ns, was analysed and, when

calculating the optical energy gap for the rISC step one must use the unrelaxed (earliest time) energy of the CT state to correctly estimate the ^{1}CT ^{3}LE gap 'seen' at the rISC step.

The enhanced TADF efficiency observed in DPEPO host was directly translated into device performance. Optimized devices show a maximum external quantum efficiency of 22.4 % at 127.4 cd/m^2 luminance, high brightness levels >2,500 cd/m^2, excellent resistance to roll- off up to 10 mA/cm^2 and low turn on voltage ~ 3 V. Therefore, it is clear that both emitter and host combination must be designed and optimised together to produce a minimum rISC barrier in order to achieve highly efficient TADF OLEDs and also how sensitive the rISC rate is to the host and how carefully this tuning needs to be made.

6.4 Sample Preparation Details

Three types of samples were studied in this work: solutions in toluene and in methylcyclohexane (MCH) solvents (10^{-3} to 10^{-5} M), films produced in zeonex matrix (organic material 2.5 mg/mL :zeonex 180 mg/mL 1:1 *v/v*) and thin film produced in DPEPO host (11% DDMA-TXO2:DPEPO). The solutions were stirred for 24 hours and they were also degassed to remove all the oxygen dissolved in the solutions by 4 freeze-thaw cycles to measure the effect of oxygen quenching. Films in zeonex matrix were fabricated by spin-coating on quartz substrates at 500 rpm during 60 seconds. Thin film in a DPEPO host was made by co-evaporation deposition onto transparent sapphire substrates using a Kurt J. Lesker Spectros II deposition system under vacuum, 10^{-6} mbar, at a steady evaporation rate of ~ 1.2 Å/ s and ~ 0.12 Å/ s for host and guest materials, respectively.

6.5 References Chapter 6

1. dos Santos, P. L. *et al.* Engineering the singlet-triplet energy splitting in a TADF molecule. *J. Mater. Chem. C* **4,** 3815–3824 (2016).
2. Haseyama, S. *et al.* Control of the Singlet–Triplet Energy Gap in a Thermally Activated Delayed Fluorescence Emitter by Using a Polar Host Matrix. *Nanoscale Res. Lett.* **12,** 1–5 (2017).
3. dos Santos, P. L., Ward, J. S., Bryce, M. R. & Monkman, A. P. Using Guest–Host Interactions To Optimize the Efficiency of TADF OLEDs. *J. Phys. Chem. Lett.* **7,** 3341–3346 (2016).
4. Dias, F. B. *et al.* The Crucial Role of Donor and Acceptor Local Triplet States in Mediating Reverse Intersystem Crossing in the TADF. 1–24
5. Higginbotham, H. F., Yi, C.-L., Monkman, A. P. & Wong, K.-T. Effects of Ortho-

Phenyl Substitution on the rISC Rate of D–A Type TADF Molecules. *J. Phys. Chem. C* **122,** 7627–7634 (2018).

6. Dias, F. B. *et al.* Triplet harvesting with 100% efficiency by way of thermally activated delayed fluorescence in charge transfer OLED emitters. *Adv. Mater.* **25,** 3707–3714 (2013).

7. Dias, F. B. *et al.* Intramolecular Charge Transfer Assisted by Conformational Changes in the Excited State of Fluorene-dibenzothiophene- S,S -dioxide Co-oligomers. *J. Phys. Chem. B* **110,** 19329–19339 (2006).

8. Youn Lee, S., Yasuda, T., Nomura, H. & Adachi, C. High-efficiency organic light-emitting diodes utilizing thermally activated delayed fluorescence from triazine-based donor-acceptor hybrid molecules. *Appl. Phys. Lett.* **101,** 1–5 (2012).

9. Lee, I. & Lee, J. Y. Molecular design of deep blue fluorescent emitters with 20% external quantum efficiency and narrow emission spectrum. *Org. Electron. physics, Mater. Appl.* **29,** 160–164 (2016).

10. Nobuyasu, R. S. *et al.* Rational Design of TADF Polymers Using a Donor-Acceptor Monomer with Enhanced TADF Efficiency Induced by the Energy Alignment of Charge Transfer and Local Triplet Excited States. *Adv. Opt. Mater.* **4,** 597–607 (2016).

11. Chen, W.-C., Lee, C.-S. & Tong, Q.-X. Blue-emitting organic electrofluorescence materials: progress and prospective. *J. Mater. Chem. C* **3,** 10957–10963 (2015).

12. Drechsel, J. *et al.* Influence of Material Purification by Vacuum Sublimation on Organic Optoelectronic Device Performance. *SID Symp. Dig. Tech. Pap.* **37,** 1692 (2006).

Chapter 7: New Design of TADF Emitter to Combine Fast rISC Rates and Unity Quantum Yield

By inverting the common structural motif of TADF materials to a rigid donor core and multiple peripheral acceptors it was demonstrated reverse intersystem crossing (rISC) rates in an organic material that enables utilisation of triplet excited states at faster rates than Ir based phosphorescent materials. A combination of the inverted structure and multiple donor–acceptor interactions yields up to 30 vibronically coupled singlet and triplet states within 0.2 eV that are involved in rISC. This gives a significant enhancement to the rISC rate leading to delayed fluorescence (DF) decay times as low as 103.9 ns. This new material also has an emission quantum yield ≈1 and a very small singlet-triplet gap. This work shows it is possible to achieve both high PLQY and fast rISC in the same molecule. Green OLED devices with EQE >30% are demonstrated with low roll-off.

The work presented in this chapter is an adapted version of the manuscript published at *Advance Science* (P. L. dos Santos, J. S. Ward, D. G. Congrave, A. S. Batsanov, J. Eng, J. E. Stacey, T. J. Penfold, A. P. Monkman, M. R. Bryce, *Adv. Science.*, 5, 1700989, 2018). It was a collaborative work between the OEM group and the chemistry departament in Durham and Newcastle Universities. J. S. Ward and D. G. Congrave designed the molecule, performed the synthesis and chemical characterization. P. L. dos Santos performed the photophysics, device fabrication and device testing. D. G. Congrave performed the photoluminescence quantum yield (PLQY). J. Eng and J. E. Stacey performed calculations and the X-ray crystallography was performed by A. S. Batsanov.

7.1 Introduction

Currently, the main challenges facing the TADF community are the long overall residence times of emitter molecules in triplet excited states, and the low oscillator strengths of the ^{1}CT radiative transitions. Here, it is shown a new TADF molecular design, incorporating a rigid, planar, central donor unit with multiple acceptor units bound via C–N bridges. This new design gives a key step forwards in TADF efficiency through multiple coupled singlet-triplet states. The resulting fast rISC rates lead to DF emission lifetimes shorter than the phosphorescence lifetimes of most Ir complexes currently used in OLEDs[1]. Critically, a unity photoluminescence quantum yield (PLQY) is also maintained.

Specific molecular vibrations promote mixing between a manifold of singlet and triplet states driving efficient rISC. Other vibrational modes can contribute more to non-radiative decay, requiring careful molecular design[2,3]. Previously synthesized, 1-substituted phenothiazine (D) D–A–D TADF candidates show molecular restriction with several conformers in solution on the ^{1}H NMR timescale[4]. As well as the phenothiazine donor being tilted, it is clear that there is some rotational restriction around the C–N bond in these systems, which switches off TADF due to a lack of vibronic coupling. The conformation of the phenothiazine with respect to the acceptor is also important in these molecules[5,6]. All of the above factors must be taken into account when considering new molecular designs. Another key challenge in the design of TADF molecules is to balance the rates of rISC (and intersystem crossing, ISC)[2] with the fluorescence quantum yield (Φ_F). Ideally, the desired molecule should have a Φ_F close to 1 with a short emissive state lifetime. This requires strong coupling of the ^{1}CT to the ground state. However, to ensure near degenerate ^{1}CT, ^{3}CT and ^{3}LE states (which is a requirement for efficient rISC), D–A orthogonality is required. This effectively decouples the ^{1}CT states from the ground state. Therefore, either a compromise is required, or non-radiative quenching to the ground state i.e. internal conversion, must be dramatically curtailed. The new TADF molecule based on a triazatruxene central donor functionalized with three peripheral acceptors, TAT-3DBTO$_2$ is now shown to overcome many of the issues faced when designing an efficient TADF emitter.

7.2 Results and Discussion

7.2.1 Chemical Characterization

The design of TAT-3DBTO$_2$ (Figure 49) is based upon the reversal of the donor and acceptor motif typically found in current TADF emitters[7]. Tree dibenzothiophene-*S*,*S*-dioxide units are attached *via* the nitrogen atoms of a central triazatruxene core (TAT). Dibenzothiophene-*S*,*S*-dioxide was selected as the acceptor in an attempt to match the energy of the ^{3}LE triplet level of the donor to the ^{1}CT energy level. This takes into account that triazatruxene is more electron rich than carbazole due to the central 1,3,5-trinitrogen substituted benzene core, and is also more conjugated giving a smaller ΔE_{ST} and faster rISC rate with dibenzothiophene-*S*,*S*-dioxide acceptors (See reference [8] for details on synthesis).

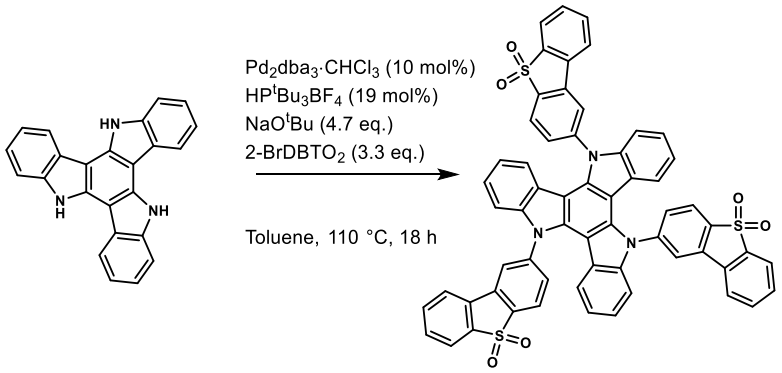

Figure 49. The synthesis of TAT-3DBTO2 via Buchwald–Hartwig coupling conditions.

The ^{1}H NMR spectrum of TAT-3DBTO$_2$ at room temperature (298 K) shows a mixture of broad and sharp peaks, suggesting that parts of the molecule are rotating slowly on the NMR timescale giving rise to multiple environments for the same protons. This has been shown to be the case by using variable temperature (VT) ^{1}H NMR, see Figure 50. Thus, there are different conformers of TAT-3DBTO$_2$ in solution. The VT ^{1}H NMR data indicate that there is an energy barrier to rotation around the D–A bridging bond and that increasing the temperature to 353 K overcomes this barrier. It is suggested that these conformers relate to the orientation of the three acceptor units with respect to each other and the triazatruxene core, in line with the chemical studies presented in section 7.2.2 (see reference [8] for details on NMR study).

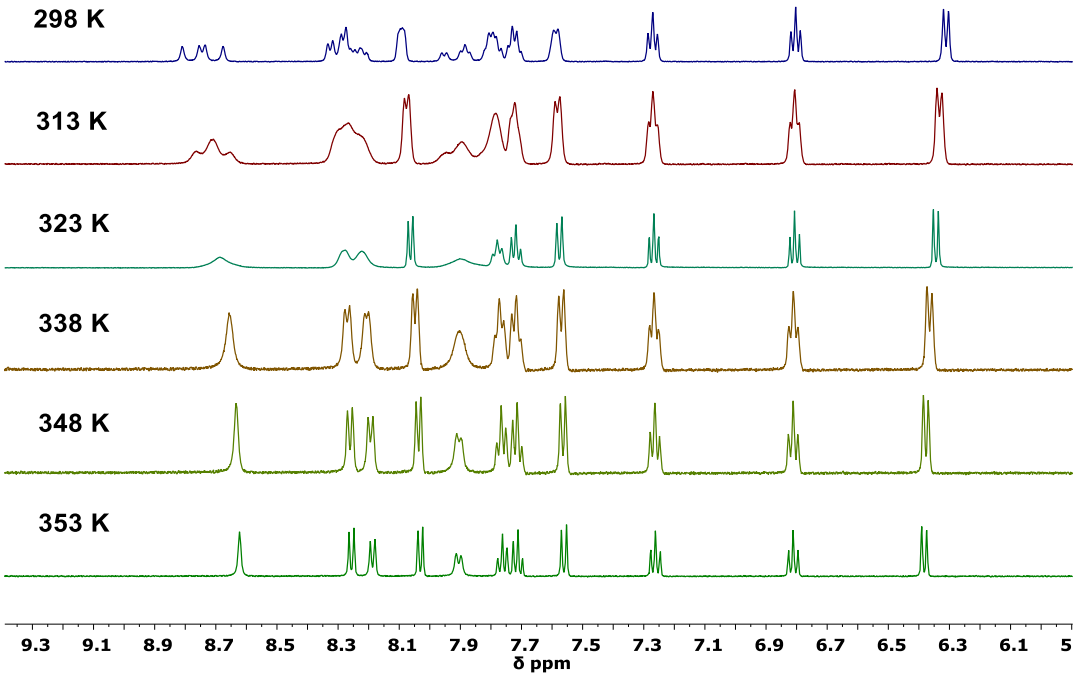

Figure 50 Temperature dependent solution state VT ^{1}H NMR of TAT-3DBTO$_2$ in DMSO-d$_6$.

The HOMO and LUMO energies for TAT-3DBTO$_2$ were estimated by cyclic voltammetry (CV) and differential pulse voltammetry (DPV) (Figure 51) at −5.60 and −3.00 eV, respectively. Within the respective solvent windows, as well as a reversible single-electron reduction, TAT-3DBTO$_2$ displays three reversible well-resolved single-electron oxidations ($\Delta E_{1/2}$ $E^{ox(1)}$/ $E^{ox(2)}$ = 487 mV, $\Delta E_{1/2}$ $E^{ox(2)}$/ $E^{ox(3)}$ = 603 mV). These correspond to sequential oxidations of the TAT core unit.

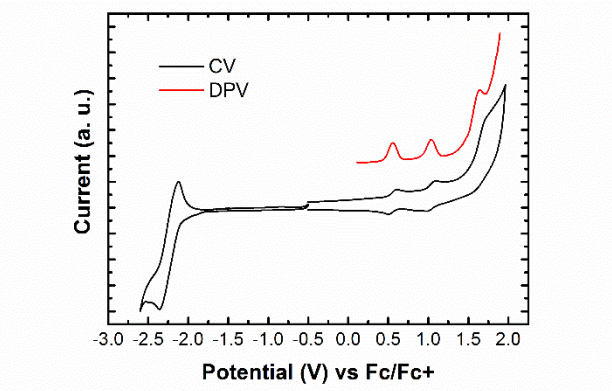

Figure 51 Cyclic and differential pulse voltammograms showing the oxidation (0.1 M n-Bu4NPF6/ CH_2Cl_2) and reduction (0.1 M n-Bu4NBF4/ THF) processes for TAT-3DBTO2.

Figure 52 shows the X-ray analyses of TAT-3DBTO$_2$. The ground state D–A dihedral angles range from 58° to 62°, significantly less than 90°, which is very much in line with one of the

current most efficient TADF materials for green OLEDs, 4CzIPN[9,10] (See reference [8] for details on X-ray study).

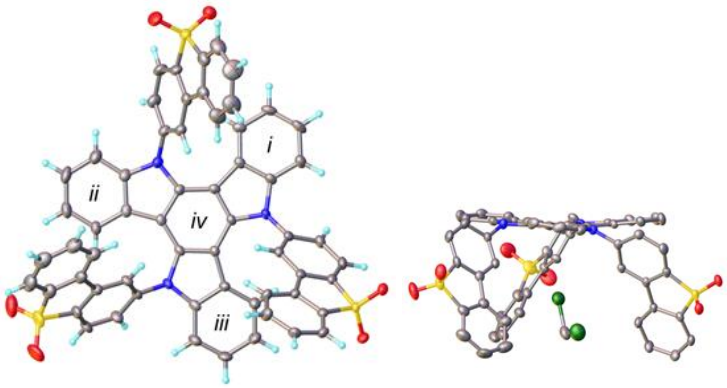

Figure 52 X-ray crystal structure of TAT-3DBTO2. Two views (perpendicular and side-on to the donor core) are shown. Displacement ellipsoids are drawn at the 50% probability level. CH_2Cl_2 solvent molecules are trapped in molecular clefts/cavities or disordered in intermolecular voids of the host.

7.2.2 Quantum Chemistry Studies

Figure 53 shows the ten possible conformers of TAT-3DBTO$_2$, all of which are within 0.03 eV of each other, reflecting the results from variable temperature ^{1}H NMR studies (Figure 50). The different conformations consist of different combination of acceptor orientations with respect to the donor moiety (See reference [8] for details on quantum chemistry studies).

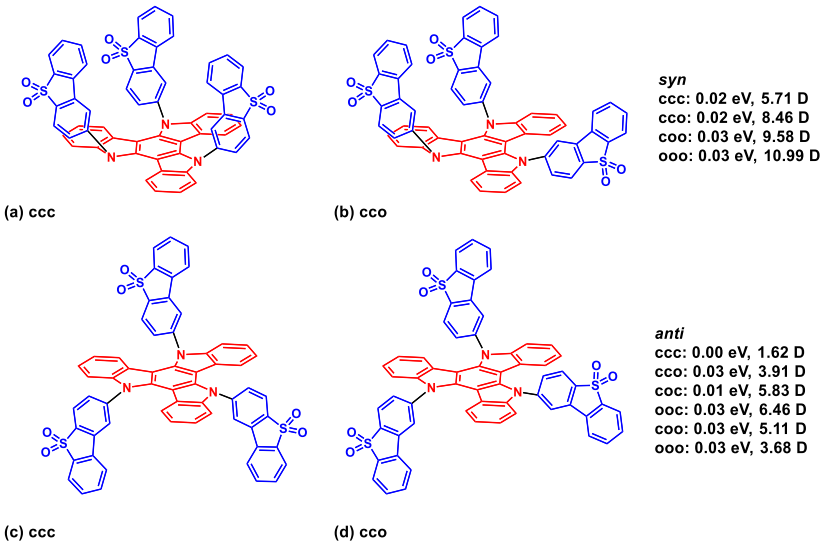

Figure 53 Different possible conformations of the TAT-3DBTO2 molecule. The stable conformations of the donor (red) and three acceptor units (blue) found by DFT(PBE0)

structural investigations, in line with the measured solution state NMR spectra. Syn represents conformations with all the acceptors pointing in the same direction, and anti represents conformations for which one acceptor points in a different direction. c=closed, o=open as illustrated in (a) ccc, (b) cco, (c) ccc and (d) cco.

7.2.2.1 Electronic Structure: Absorption

The absorption spectrum of TAT-3DBTO$_2$ **(**Figure 54**)** has been computed in the gas phase including the twenty lowest singlet and triplet states. The absorption spectrum exhibits three dominant peaks at 410 nm, 350 nm and 290 nm. The intensity of each peak increases with higher energy and there is a reasonable agreement with the experimental spectrum shown in Figure 55a. The molecular conformation has negligible effect on the position, intensity or character of the transitions and all of the excited states computed exhibit charge transfer character from the donor core to the acceptor moieties. The first absorption peak is composed of six pairs of singlet and triplet states of the same character all lying within a 0.3 eV of each other. Because of the C_3 symmetry at this geometry, the states T_2 and T_3 (S_2 and S_3) as well as states T_5 and T_6 (S_5 and S_6) are degenerate. At the ground state equilibrium geometry, the molecular dipole moment is found to be between 1–11 D depending on the conformer.

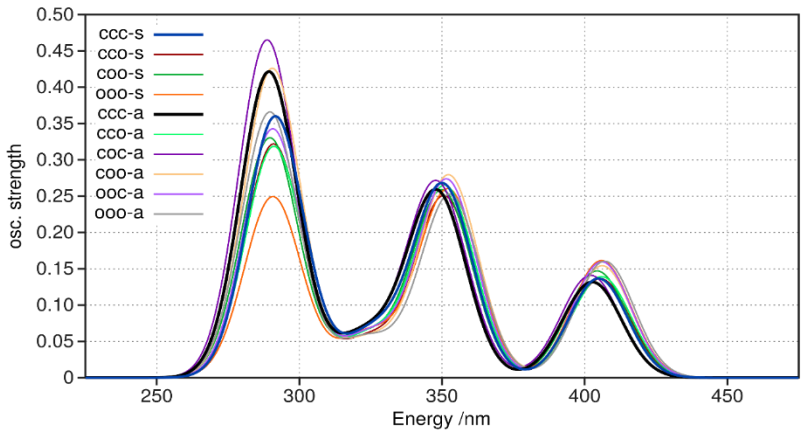

Figure 54 Calculated absorption spectrum for all conformers.

7.2.2.2 Electronic Structure: Emission/relaxation

The emission energy for each conformer is simulated by optimising the lowest singlet and triplet states. In each case a rotation of one acceptor moiety to become nearly orthogonal with respect to the donor core is observed. This motion allows minimization of the overlap between the orbitals involved in the excitation and therefore decreases the singlet-triplet energy gap ($\Delta E^{T1/S1}$=0.01 eV). The minimum energy geometry of both S_1 and T_1 is very similar as both

states are pure charge transfer states from the donor core to one of the acceptor moieties. The Stokes shift of the S_1 and T_1 states (difference between the energy at ground state and excited state optimized geometries) is 0.46 eV and 0.29 eV, respectively.

TAT-3DBTO$_2$ has three acceptors, which are quasi equivalent. Consequently, one can expect three energy minima in S_1 corresponding to a charge transfer from the donor core to each of the different acceptor moieties. It was thus found that within 0.2 eV of the T_1 state there are 12 excited states, all of which are likely to be vibrationally coupled. If one considers all of the angular momentum components (i.e. all M_s levels of the triplets), then TAT-3DBTO$_2$ has potentially 30 coupled states involved in rISC. This will give significant enhancement to the rISC rate.

The oscillator strength of TAT-3DBTO$_2$ is very similar (0.001) to a literature TADF material DPTZ-DBTO$_2$[11] (0.0007), as expected by the similar lifetime of the prompt emission in both molecules. Consequently, from the quantum chemistry simulations it would appear that the enhanced performance of TAT-3DBTO$_2$ is primarily associated with the enhanced rISC rate derived from the higher density of states (See reference [8] for details on chemical calculations).

7.2.3 Photophysical Properties

7.2.3.1 Solution Properties

Figure 55a shows the extinction coefficient spectra of TAT-3DBTO$_2$ and the individual D and A units in dichloromethane (CH_2Cl_2). By comparison to the individual D and A units, the extinction coefficient at all wavelengths is greatly enhanced in TAT-3DBTO$_2$. This increase in absorption intensity strongly reflects the higher density of states predicted from the quantum chemical calculations described above. Particularly, the absorption band at lower energy (350 nm to 425 nm), which is not observed in the D or A units, and is ascribed to a direct absorption from the CT states, is very strong in this new material. Figure 55c shows a slight red shift on the right edge of the spectra by increasing the polarity of the solvent, which is associated with a strongly mixed $n \rightarrow \pi^* / \pi \rightarrow \pi^*$ character transition[12], also confirmed by its relatively strong transition. Excitation into this band directly populates ^{1}CT excited states, as shown in the analogous D–A–D system DPTZ-DBTO$_2$[11].

Figure 55b shows the photoluminescence (PL) spectra of TAT-3DBTO$_2$ in different solvents together with the separated D and A units in toluene solution. The spectra show clear and strong CT emission, displaying a Gaussian band shape and strong red shift compared to the individual

D and A emission spectra. The PL spectra shift to longer wavelengths upon increasing the solvent polarity. This indicates strong positive solvatochromism, as observed in D–A–D-type molecules[11,14].

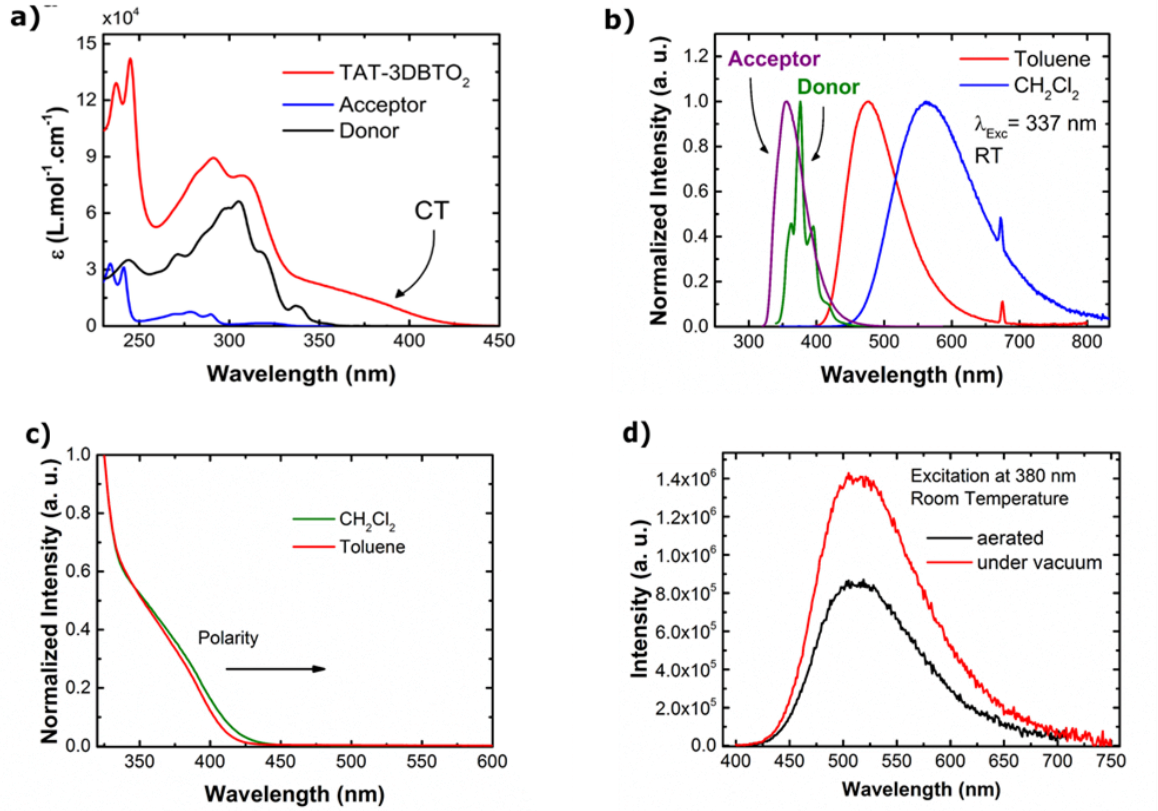

Figure 55 a) Extinction coefficient spectra of the acceptor (A), donor (D), and TAT-3DBTO2 molecules, all diluted in dichloromethane (CH_2Cl_2) solvent. b) Normalized photoluminescence (PL) spectra of acceptor (data taken from ref [13]), donor, and TAT-3DBTO2 molecules. D and A are diluted in toluene solvent, TAT-3DBTO2 diluted in toluene and CH2Cl2.c) Absorption spectra of TAT-3DBTO2 in CH_2Cl_2 and toluene. d) PL spectra of TAT-3DBTO2:BCPO film under vacuum and in air.

7.2.3.2 Solid State Properties

BCPO, (*bis*-4-(*N*-carbazolyl)phenyl)phenylphosphine oxide)[15] was used as a host for TAT-$3DBTO_2$ to maintain the low energy splitting between ^{1}CT and ^{3}LE with correct host polarity. The photoluminescence quantum yield (PLQY) of TAT-$3DBTO_2$:BCPO were recorded on a Horiba Jobin Yvon SPEX Fluorolog 3 using a calibrated Quanta-Φ integrating sphere and were calculated according to the literature method[16]. Solid state PLQY data were obtained in duplicate on two separate films which were prepared in parallel. The PLQY of the film was

evaluated under air at an excitation wavelength of 380 nm and it was found to be $PLQY_{PF}$ = (63 ± 10)%. This value includes mainly the contribution of the prompt fluorescence (PF). To estimate the PLQY with the incorporation of delayed fluorescence (DF), i.e. including the contribution from the triplet states, the PL spectrum of the TAT-3DBTO$_2$:BCPO film was collected both under air and vacuum (Figure 55d). The red curve refers to the PL spectrum under vacuum and the black curve to the aerated PL. Both PL spectra match each other, showing that DF and PF come from the same ^{1}CT state.

The ratio between the area of the red spectrum ($Area_{PF+DF}$) and the black spectrum ($Area_{PF}$) was found to be 1.69. Thus, the $PLQY_{PF+DF} \approx 100\%$ as shown below:

$$\frac{Area_{PF+DF}}{Area_{PF}} = \frac{\Phi_{PF+DF}}{\Phi_{PF}} = 1.69 \tag{7.1}$$

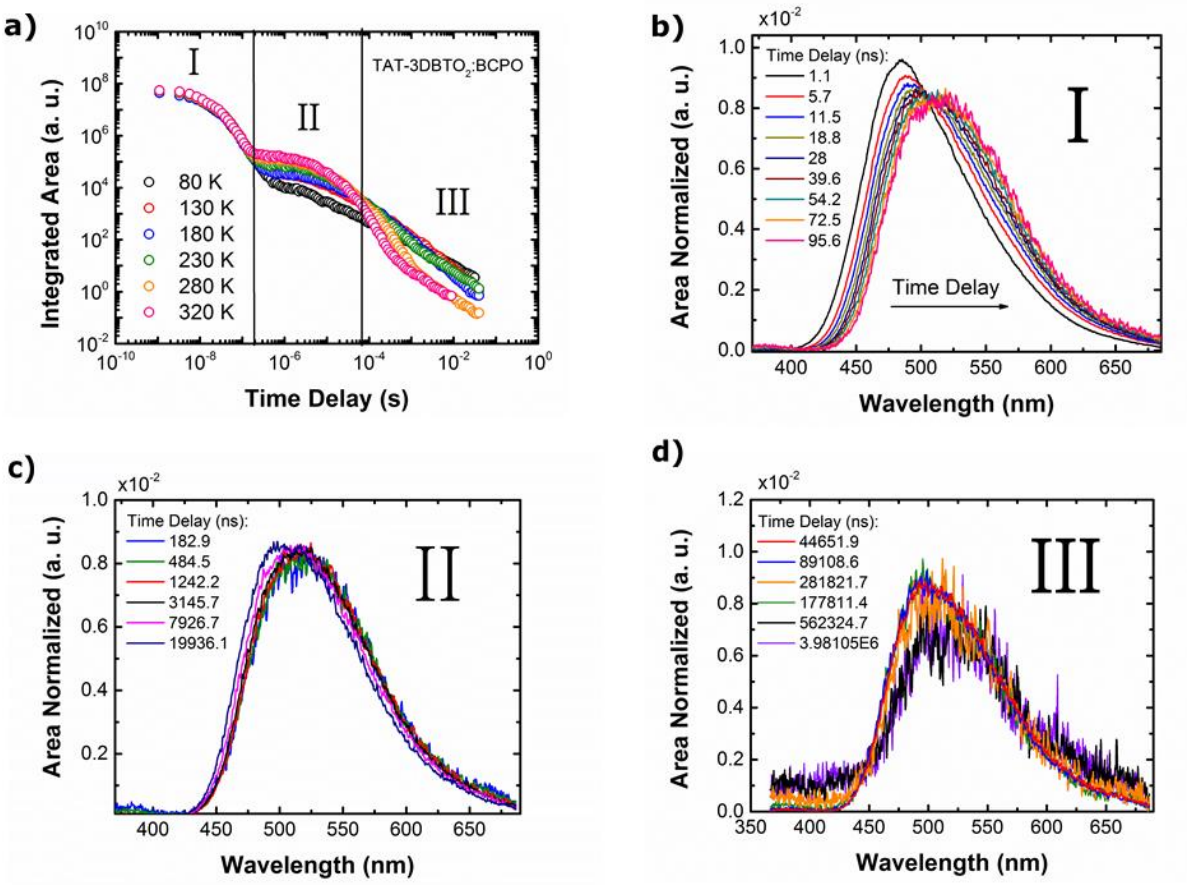

Figure 56 a) Decay curves of TAT-3DBTO2:BCPO film in different temperatures b,c,d) Time resolved normalized emission spectra in region I, II and III, respectively at 320 K. All spectra were obtained with 355 nm excitation.

The decay curves of TAT-3DBTO$_2$:BCPO were analysed in different temperatures. Three different emission decay regimes are observed, Figure 56a: region I is fast decay, associated with prompt CT emission (PF); region II is early times of delayed fluorescence (DF) and region III is long-lived DF. The PF decay curves show no temperature or oxygen dependence, indicating negligible migration of the singlet ^{1}CT excited state. The decay curve at 320 K was fitted using a bi-exponential function: $\boldsymbol{\tau}_1$ = 10 ns (I_1= 4.4) and $\boldsymbol{\tau}_2$ = 35 ns (I_2= 1.2), giving $\boldsymbol{\tau}_{average}$ = 22.4 ns for region I. Region II shows strong TADF, the DF emission increasing in intensity with increasing temperature. The decay times related to region II are $\boldsymbol{\tau}_1$ = 103.9 ns (I_1 = 42777) $\boldsymbol{\tau}_2$ = 3.2 µs (I_2 = 112006) and $\boldsymbol{\tau}_3$ = 15.1 µs (I_3 = 61040) (see fitting details on Figure 57), giving $\boldsymbol{\tau}_{average}$ = 11.7 µs for region II.

Usually, DF lifetimes of TADF emitters are in the µs timeframe, whereas TAT-3DBTO$_2$ has a DF component with a lifetime on the order of 100 ns, which is a result of fast rISC. As the PLQY for TAT-3DBTO$_2$ in BCPO is ca. 1, this is not a *quenched* component, and from its fit weighting it represents ≈ 20% of all delayed emission. This complex multi-component DF decay is ascribed directly to the multiple conformations possible in TAT-3DBTO$_2$. Region III has an inverse temperature dependence: the intensity of the emission increases as the system temperature drops. This has been observed before in highly efficient TADF molecules, and is associated with longer lived DF components and phosphorescence (PH) at low temperatures[17].

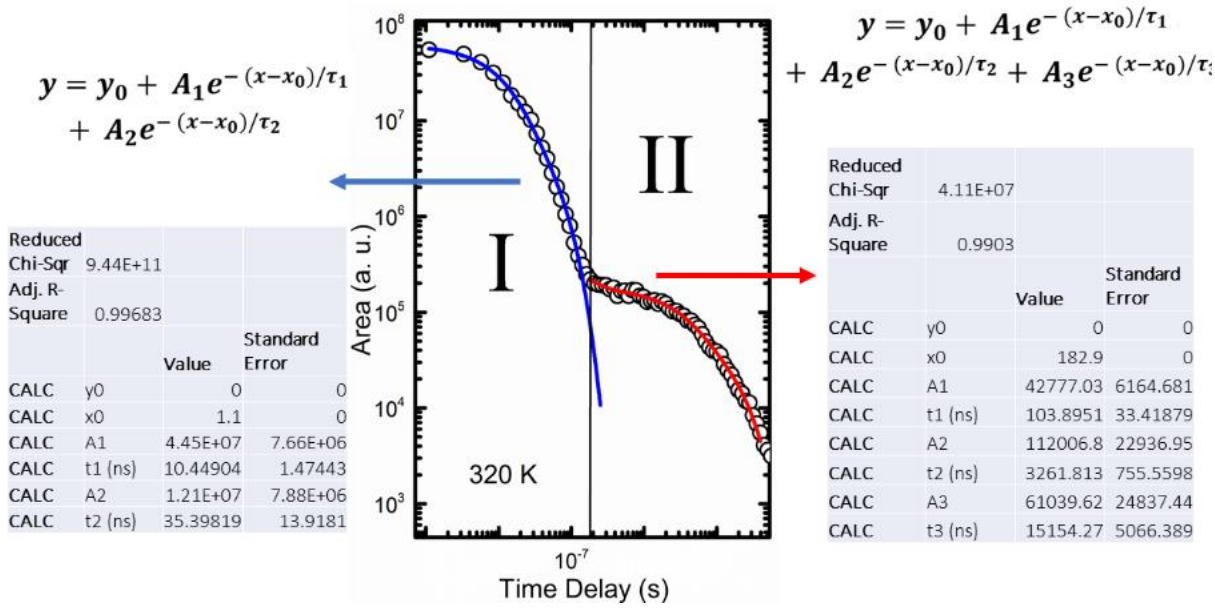

Figure 57 Decay curve of TAT-3DBTO$_2$:BCPO film at 320 K. The PF decay was fitted with two exponentials and the DF with three exponentials (Curve fitting - OriginPro 9.0). PF was

fitted in region I and DF was fitted in region II, which is the timeframe of strong TADF mechanism.

The reverse intersystem crossing rates (k_{rISC}) of TAT-3DBTO$_2$:BCPO film (320 K) were calculated using two different approaches (see table 2). Three different values of k_{rISC} were calculated, each value is associated with a distinct lifetime of DF in a TAT-3DBTO$_2$:BCPO film. The fastest lifetime of the DF emission ($\boldsymbol{\tau}_1$ in region II) gives very high $k_{rISC} > 10^7$ s^{-1}. Both k_{rISC} calculation methods show good agreement.

Decay component	$k_{rISC}^{a} = \frac{1}{\tau_{DF}} \cdot \frac{1}{(1-\Phi_{ISC})}$	$k_{rISC}^{b} = \frac{\int I_{DF}(t)dt}{\int I_{PF}(t)dt} \cdot \frac{1}{\tau_{DF}}$
$\boldsymbol{\tau}_1$ = 103.9 ns	1.5×10^7 s^{-1}	1.3×10^7 s^{-1}
$\boldsymbol{\tau}_2$ = 3.2 µs	4.9×10^5 s^{-1}	4.3×10^5 s^{-1}
$\boldsymbol{\tau}_3$ = 15.1 µs	1.0×10^5 s^{-1}	9.2×10^4 s^{-1}

Table 2 rISC rates determined from the three exponential decays from TAT–3DBTO$_2$:BCPO film. a) using k_{rISC}^{a} and b) k_{rISC}^{b} for comparison.

Figure 56b shows the area-normalized emission spectra in region I at 320 K. The PF emission shows a continuous dynamic red shift. This red shift is most likely associated with the energetic relaxation of the ^{1}CT state, primarily due to rotation about the D–A bond. Calculations and experiments suggest the D and A units twist towards a more orthogonal geometry, and stabilize in around 70 ns. Region II (Figure 56c) shows stabilized ^{1}CT emission at 320 K: the onset of each spectrum collected in this region is at (2.78 ± 0.02) eV. The intensity dependence of the DF emission in this region as a function of the laser excitation dose was found to be linear with a gradient of 1, indicative of TADF (Figure 58a). Figure 56d shows late time decay (weak emission). Between 70 to 400 µs (still exponential decay) emission as in region II is observed. From 400 µs to 10 ms (power law decay) very weak emission is detected. Likely, this region includes DF emission from additional conformers, and weak PH emission.

Spectral analysis at 80 K was performed to identify the PH emission. The harvesting of triplet states to singlet states in BCPO host is so rapid that obtaining a clear PH spectrum is problematic. This is due to residual ^{1}CT emission masking the very weak PH emission. Therefore, the PH spectrum was measured in mCP. In this host the ΔE_{ST} is larger, (0.21±0.03

eV), allowing the PH spectrum to be clearly identified at low temperature (80 K). The TAT-3DBTO$_2$:mCP PH spectrum was also compared to the PH spectrum collected in polyethylene oxide matrix, and both spectra show the same onset energy (Figure 58b).

Figure 58c shows the PH spectra of TAT-3DBTO$_2$:mCP film and the A and D units. The PH spectrum of TAT-3DBTO$_2$ shows mostly ^{3}LE character from the acceptor units, while a peak around 550 nm is strongly enhanced. Comparison of the phosphorescence vibronic intensities may indicate a perturbed geometry for the LE triplet state in TAT-3DBTO$_2$ compared to the isolated acceptor unit. Considering that the ^{3}LE states are almost unaffected by the polarity of the host environment, the triplet levels of TAT-3DBTO$_2$ doped into BCPO will have onsets very close to those observed in mCP and polyethylene oxide.

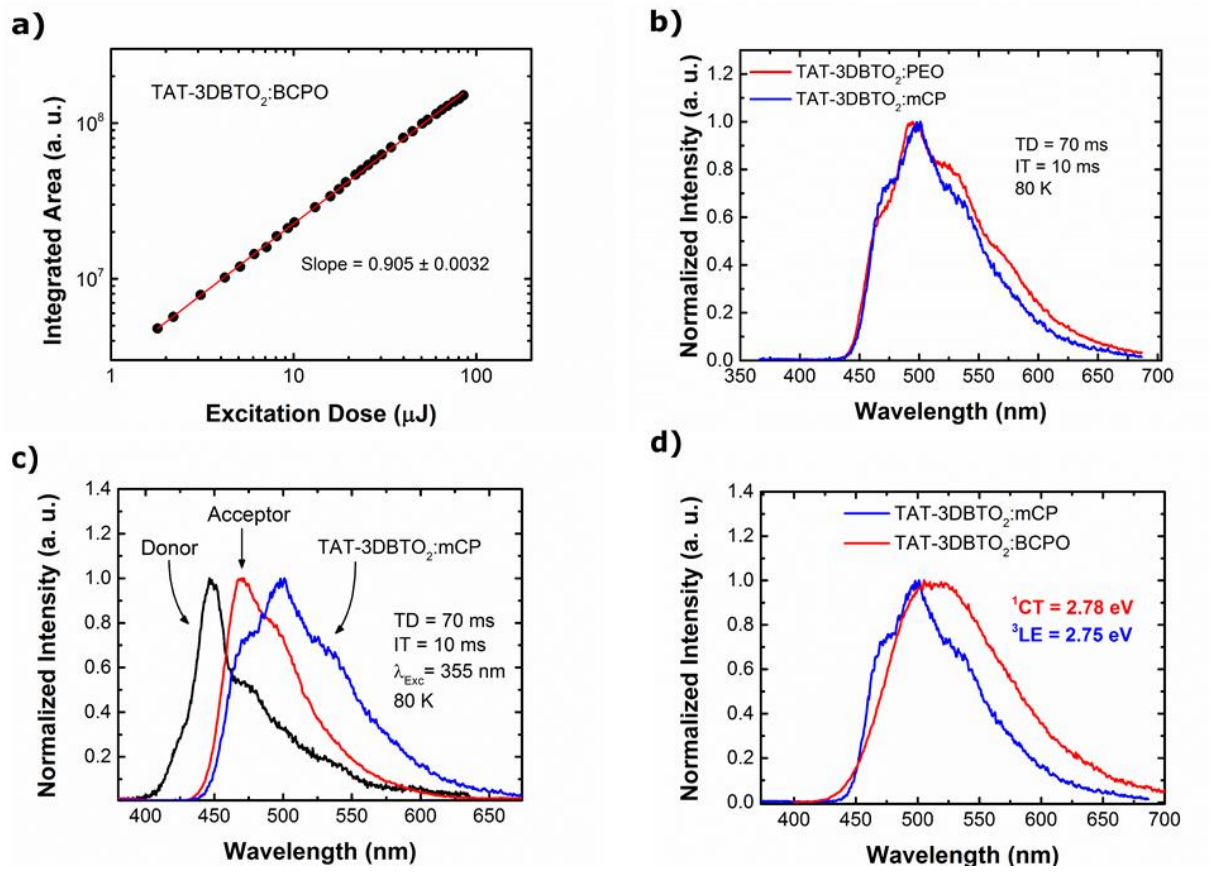

Figure 58 a) Integrated area of delayed fluorescence spectra as a function of excitation dose for TAT-3DBTO$_2$:BCPO b) Normalized phosphorescence (PH) spectra of TAT-3DBTO$_2$ in mCP and PEO hosts. c) PH of acceptor (data taken from ref 13), donor, and TAT-3DBTO2:mCP, all collected at 80 K. d) Normalized photoluminescence (PL) spectra of TAT-3DBTO$_2$:BCPO and PH of TAT-3DBTO2:mCP. All spectra were obtained with 355 nm excitation.

Figure 58d shows the PH spectrum together with the PL spectrum of TAT-3DBTO$_2$:BCPO film, for better comparison. The ^{1}CT and ^{3}LE states have onset energies of 2.78 ± 0.02 and 2.75 ± 0.02 eV respectively, leading to ΔE_{ST} = 0.03 ± 0.03 eV. Therefore, it is clear that for TAT-3DBTO$_2$ in BCPO host, the ^{1}CT state energy lies very close to the triplet states, as required for fast rISC and highly efficient TADF. However, it was also noted that there are twelve states very close in energy (described above), which would also couple to mediate rISC.

7.2.4 Device Performance

BCPO is an ideal ambipolar host for TAT-3DBTO$_2$, yielding the minimal ΔE_{ST} and a PLQY of ca. 100%. The second step of the optimization studies concerned finding the best guest:host (x:y) ratios. Therefore, two different device architectures were used: one designed for optimization of maximum external quantum efficiency (EQE) values (OLED 1) and another aiming for low roll-off (OLED 2). For optimization of maximum EQE, a lower amount of TAT-3DBTO$_2$ was co-evaporated with BCPO host (1:9 *v/v*), and for optimization of roll-off the ratio of TAT-3DBTO$_2$ was higher (1.7:8.3). The architecture of the optimized devices was: ITO/NPB(40nm)/TCTA(10nm)/TAT-3DBTO$_2$:BCPO(x:y,30nm) /TPBi(40nm)/LiF(1nm)/Al 100nm). NPB (*N*,*N*′-bis(naphthalen-1-yl)-*N*,*N*′-bis(phenyl)-benzidine) and TCTA (tris(4-carbazol-9-ylphenyl)amine)) were used as commercial hole transport layers, TPBi (1,3,5-tris(*N*-phenylbenzimidazol-2-yl)benzene) as electron transport layer, LiF (lithium fluoride) as electron injection layer and Al (aluminium) was used as cathode.

Figure 59a shows the green electroluminescence (EL) spectra of both devices collected at 10 V. The Commission Internationale de L'Éclairage (CIE_{xy}) chromaticity coordinates for these EL spectra are (0.26, 0.46) and (0.29, 0.50) for OLED 1 and OLED 2, respectively. The emission from OLED 2 is slightly red shifted, which is likely associated with the increase in the overall polarity of the emissive layer induced by the increased TAT-3DBTO$_2$ concentration.

Figure 59b shows representative EQE *versus* brightness curves. OLED 1 shows a maximum EQE value of 30.9% (76 cd/m^2). The EQE of an OLED is described by the equation 7.2 as the product between the charge balance factor, γ, the fraction of spin-allowed excitons, $\eta_{ST,}$ the photoluminescence quantum yield, Φ_{PL} and the outcoupling efficiency, $\eta_{out,}$ which is usually estimated 20 - 30%[18].

$$EQE = \gamma \cdot \eta_{ST} \cdot \Phi_{PL} \cdot \eta_{out} \quad (7.2)$$

For OLED 1, Φ_{PL} =1 and the high EQE values, it can be concluded that the device has a charge balance close to unity (γ =1); all the excitons are harvested from the triplet to the singlet states, i.e., 100% TADF efficiency (η_{ST} =1); under the assumption that η_{out} ~ 0.3. At 1,000 cd/m^2 OLED 1 shows an EQE above 15%, exhibiting good resistance to roll-off with maximum brightness values up to 10,000 cd/m^2 (EQE = 4.4%). By increasing the concentration of TAT-3DBTO$_2$ molecules in the emissive layer (OLED 2), the maximum EQE value drops to 20.2% (74 cd/m^2), but significantly lower efficiency roll-off is observed. At 10,000 cd/m^2, OLED2 shows an EQE of 8.8%, with brightness levels reaching 18,410 cd/m^2 (EQE = 3.9%).

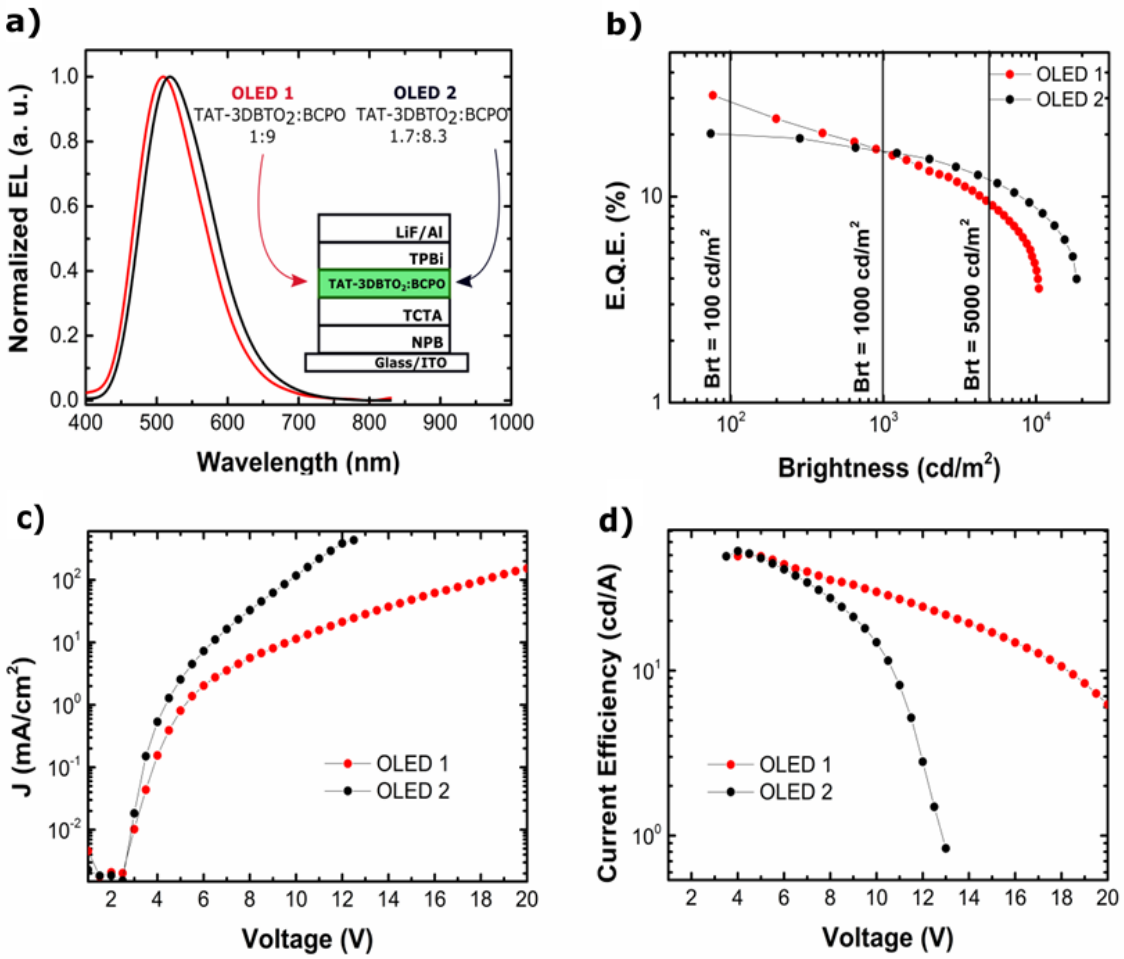

Figure 59 a) Eletroluminescencd (EL) spectra of OLED 1 and OLED 2 and a schematic of the OLED architectures. b) Measured external quantum efficiencies as a function of brightness. c) Current voltage curves and d) Current efficiency as a function of drive voltage, all graphs for both structures, OLED 1 and OLED 2.

Figure 59c shows the current density *versus* voltage curves. Both OLEDs show very low turn-on voltages of ca. 2.5 V. However, in OLED 1, this value is slightly lower, which may be

associated with the fact that TAT-3DBTO$_2$ molecules are not as ambipolar as BCPO, so by decreasing its concentration, a better JV curve (lower turn-on voltage) is observed. The same explanation holds for the current efficiency (η_c) *versus* voltage curves (Figure 6d) up to 8 V: both devices show similar current efficiency ($\eta_{c1,\ MAX}$ = 50.8 cd/A, $\eta_{c2,\ MAX}$ = 52.9 cd/A), although at higher voltages OLED 1 exhibits much better resistance to high current efficiency levels. Table 3 highlights all the electrical properties of these devices and the values of each efficiency at 100 and 1,000 cd/m^2 showing its electrical stability.

The reproducibility of these devices with such high EQEs and low roll-offs was studied in more detail. Several other sets of devices with slightly distinct device structures also show EQE values around 30%. Therefore, the data presented in above are the most representative among the OLEDs tested. Figure 60 shows the EQE *versus* brightness of eight devices (four distinct structures). The structures of the devices and EQE values are presented in the table 4. The device optimization aiming at low roll-off was studied previously (OLED A1, A2 and OLED 2), and in here, the optimization of maximum EQE values is demonstrated. Intending to increase the EQE values, a much smaller amount of TAT-3DBTO$_2$ was co-evaporated with BCPO, 4% (OLED B1 and B2). However, together with a strong increase in the maximum EQE values, a big increase in the roll-off was also observed. To retain the high EQE values without significantly sacrificing the roll-off, devices with 10% TAT-3DBTO$_2$ were produced (OLED C1, C2 and OLED 1). As the ratio ~ 10% *guest:host* was observed to be the best for maximum EQE values, devices were also fabricated with buffer layers of BCPO aiming at more balanced carrier density in the emissive layer. However, no significant increase in the performance was observed.

Device	V_{on}	$\eta_{ext,max}$ (%)	Brt $_{max}$ (cd/m^2)	$\eta_{c,max}$ (cd/A)	$\eta_{P,max}$ (lm/W)	$\eta_{ext,100}$ (%)	$\eta_{c,100}$ (cd/A)	$\eta_{P,100}$ (lm/W)	$\eta_{ext,1000}$ (%)	$\eta_{c,1000}$ (cd/A)	$\eta_{P,1000}$ (lm/W)
OLED1	2.3	30.9[a]	10,420	50.8	38.7	29	49.8	38.0	16.5	42.9	21.8
OLED2	2.5	20.2[b]	18,410	52.9	44.1	19	49.5	43.8	16.6	49.1	32.4

[a] At 76 cd /m^2 and [b] At 74 cd /m^2.

Table 3 Electrical properties of OLED 1 and OLED 2. V_{on} = Turn on voltage; η_{ext} = External quantum efficiency; Brt = brightness; η_c = Current efficiency and η_P = Power efficiency. Subscript 100 and 1000 refers to values taken at 100 cd/m^2 and at 1,000 cd/m^2, respectively.

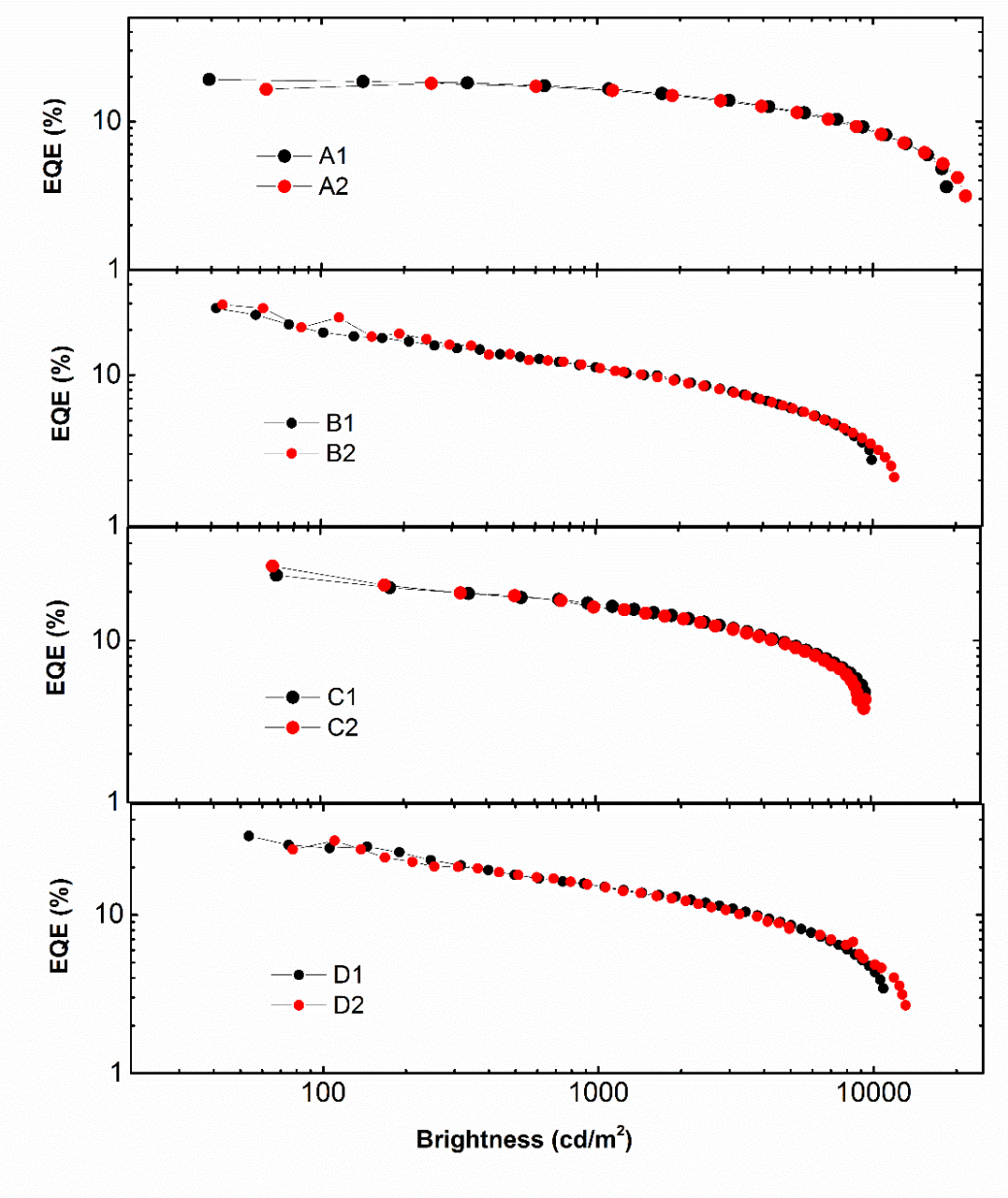

Figure 60 EQE *versus* brightness curves for OLEDs A1, A2, B1, B2, C1, C2 D1 and D2. Their structures are described in table 4.

OLED	Hole Transport	Layers	Emissive Layer	Electron Transport Layer	$\eta_{ext,\ max}$	$\eta_{ext,1000}$
A1	NPB (40 nm)	TCTA (10nm)	TAT-3DBTO$_2$:BCPO (1.7:8.3)	TPBi (50 nm)	19.2% 39 cd/m^2	16.7%
A2	NPB (40 nm)	TCTA (10nm)	TAT-3DBTO$_2$:BCPO (1.7:8.3)	TPBi (50 nm)	18.3% 250 cd/m^2	16.4%
B1	NPB (40 nm)	TCTA (10nm)	TAT-3DBTO$_2$:BCPO (0.4:9.6)	TPBi (50 nm)	27.9% 42 cd/m^2	11.2%
B2	NPB (40 nm)	TCTA (10nm)	TAT-3DBTO$_2$:BCPO (0.4:9.6)	TPBi (50 nm)	29.4% 44 cd/m^2	11.3%
C1	NPB (40 nm)	TCTA (10nm)	TAT-3DBTO$_2$:BCPO (1:9)	TPBi (50 nm)	25.4% 69 cd/m^2	16.7%
C2	NPB (40 nm)	TCTA (10nm)	TAT-3DBTO$_2$:BCPO (1:9)	TPBi (50 nm)	28.9% 67 cd/m^2	16%
D1	NPB (40 nm)	TCTA (10nm)	BCPO(5nm)/ TAT3DBTO$_2$:BCPO (0.8:9.2)/ BCPO (5nm)	TPBi (50 nm)	31.5% 53 cd/m^2	15.2%
D2	NPB (40 nm)	TCTA (10nm)	BCPO(5nm)/ TAT3DBTO$_2$:BCPO (0.8:9.2)/ BCPO (5nm)	TPBi (50 nm)	29.4% 110 cd/m^2	15.2%

Table 4 Structure and electrical properties of eight different TAT-3DBTO$_2$.:BCPO OLEDs. $\eta_{ext,\ max}$ = External quantum efficiency and $\eta_{ext,\ 1,000}$ the value collect at 1,000 cd/m^2.

7.3 Conclusion

In summary, this chapter reports the design, chemical properties, photophysical properties and device performance of TAT-3DBTO$_2$. TAT-3DBTO$_2$ introduces a new design for TADF emitters. The multi-acceptor single-donor motif imparts a large number of resonant energy states which gives a short prompt ^{1}CT lifetime and unitary PLQY. Moreover, it was found 12 singlet triplet resonances within 0.2 eV of each other that gives rise to a DF component with a very fast rISC rate, on the order of 1×10^7 s^{-1}. This shows that it is possible to achieve both a unitary PLQY and a sub-microsecond TADF lifetime in the same molecule. The conformational complexity of the molecule, however, gives rise to different rISC rates as observed in the emission decays. Nevertheless, in devices these optimal photophysical properties translate into an EQE which exceeds 30% and low efficiency roll-off. Therefore, this new TADF molecular design opens up a new dimension for achieving truly high performance TADF OLEDs and provides a solution to overcome the main concerns of current TADF molecular designs.

7.4 Sample Preparation Details

Three types of samples were studied in this work: TAT-3DBTO$_2$ solutions (10^{-3} to 10^{-5} M) in methylcyclohexane (MCH), toluene and dichloromethane (CH_2Cl_2) solvents; drop-casted blend film of TAT-3DBTO$_2$:mCP 1:9 molar ratio and evaporated doped films of TAT-3DBTO$_2$:BCPO 1:9 *v/v*. All the solutions were stirred for several hours to ensure complete dissolution. Thin film in a BCPO host was made by co-evaporation deposition onto transparent sapphire substrates using a Kurt J. Lesker Spectros II deposition system under vacuum, 10^{-6} mbar, at a steady evaporation rate of ~ 1.2 Å/ s and ~ 0.12 Å/ s for host and guest materials, respectively.

OLED devices were fabricated using pre-cleaned indium-tin-oxide (ITO) coated glass substrates purchased from Ossila with a sheet resistance of 20 Ω/cm2 and ITO thickness of 100 nm. The OLED devices had a pixel size of 4 mm × 2 mm or 4 mm × 4 mm. The small molecule and cathode layers were thermally evaporated using the Kurt J. Lesker Spectros II deposition chamber at 10^{-6} mbar. All commercial organic compounds were previously purified by vacuum sublimation.

7.5 References Chapter 7

1. Hofbeck, T. & Yersin, H. The Triplet State of fac -Ir(ppy) 3. *Inorg. Chem.* **49,** 9290–9299 (2010).
2. Gibson, J. & Penfold, T. J. Nonadiabatic coupling reduces the activation energy in thermally activated delayed fluorescence. *Phys. Chem. Chem. Phys.* **19,** 8428–8434 (2017).
3. Gibson, J., Monkman, A. & Penfold, T. The Importance of Vibronic Coupling for Efficient Reverse Intersystem Crossing. *ChemPhysChem* **17,** 2956–2961 (2016).
4. Ward, J. S. *et al.* The interplay of thermally activated delayed fluorescence (TADF) and room temperature organic phosphorescence in sterically-constrained donor–acceptor charge-transfer molecules. *Chem. Commun.* **52,** 3–6 (2016).
5. Tanaka, H., Shizu, K., Nakanotani, H. & Adachi, C. Dual intramolecular charge-transfer fluorescence derived from a phenothiazine-triphenyltriazine derivative. *J. Phys. Chem. C* **118,** 15985–15994 (2014).
6. Etherington, M. K. *et al.* Regio- and conformational isomerization critical to design of efficient thermally-activated delayed fluorescence emitters. *Nat. Commun.* **8,** 14987 (2017).
7. Tanaka, H., Shizu, K., Nakanotani, H. & Adachi, C. Twisted Intramolecular Charge Transfer State for Long-Wavelength Thermally Activated Delayed Fluorescence. *Chem. Mater.* **25,** 3766–3771 (2013).
8. dos Santos, P. L. *et al.* Triazatruxene: A Rigid Central Donor Unit for a D-A 3 Thermally Activated Delayed Fluorescence Material Exhibiting Sub-Microsecond Reverse Intersystem Crossing and Unity Quantum Yield via Multiple Singlet-Triplet State Pairs. *Adv. Sci.* **5,** 1700989 (2018).
9. Uoyama, H., Goushi, K., Shizu, K., Nomura, H. & Adachi, C. Highly efficient organic light-emitting diodes from delayed fluorescence. *Nature* **492,** 234–8 (2012).
10. Wang, S. *et al.* Achieving high power efficiency and low roll-off OLEDs based on energy transfer from thermally activated delayed excitons to fluorescent dopants. *Chem. Commun.* **51,** 11972–11975 (2015).
11. Dias, F. B. *et al.* The Role of Local Triplet Excited States in Thermally-Activated Delayed Fluorescence: Photophysics and Devices. *Adv. Sci.* **3,** 1–10 (2016).
12. Marian, C. M. Spin-orbit coupling and intersystem crossing in molecules. *Wiley Interdiscip. Rev. Comput. Mol. Sci.* **2,** 187–203 (2012).
13. Nobuyasu, R. S. *et al.* Rational Design of TADF Polymers Using a Donor-Acceptor Monomer with Enhanced TADF Efficiency Induced by the Energy Alignment of Charge Transfer and Local Triplet Excited States. *Adv. Opt. Mater.* **4,** 597–607 (2016).
14. dos Santos, P. L., Ward, J. S., Bryce, M. R. & Monkman, A. P. Using Guest–Host Interactions To Optimize the Efficiency of TADF OLEDs. *J. Phys. Chem. Lett.* **7,** 3341–3346 (2016).
15. Chou, H.-H. & Cheng, C.-H. A Highly Efficient Universal Bipolar Host for Blue, Green,

and Red Phosphorescent OLEDs. *Adv. Mater.* **22,** 2468–2471 (2010).

16. Pålsson, B. L. & Monkman, A. P. Measurements of Solid-State Photoluminescence Quantum Yields of Films Using a Fluorimeter. *Adv. Mater.* **14,** 933–935 (2002).

17. Santos, P. L. *et al.* Engineering the singlet–triplet energy splitting in a TADF molecule. *J. Mater. Chem. C* **4,** 3815–3824 (2016).

18. Higginbotham, H. F., Etherington, M. K. & Monkman, A. P. Fluorescence and Phosphorescence Anisotropy from Oriented Films of Thermally Activated Delayed Fluorescence Emitters. *J. Phys. Chem. Lett.* **8,** 2930–2935 (2017).

Chapter 8: TADF Mechanism in Bimolecular Systems

This chapter demonstrates new design rules for exciplex systems showing dominant delayed fluorescence due to rISC for devices based on TADF. The donor:acceptor systems studied in this chapter have been demonstrated to show strong exciplex formation by their red shifted emission spectra when compared to the individual donor and acceptor molecules, and all give rise to delayed fluorescence. In all cases, the channels by which this delayed fluorescence is generated, along with the energy levels involved in rISC have not previously been identified. Here, the intermolecular charge transfer states (iMCT) formed in the donor acceptor molecular pairs are studied. It is demonstrated that the local triplet excited state (^{3}LE) is crucial to couple to the singlet iMCT state to give rise to rISC and hence TADF in exciplex systems. Moreover, in most systems there is a competition between delayed fluorescence mechanisms, triplet triplet annihilation (TTA) and thermally activated delayed fluorescence (TADF), and this is analyzed in detail.

The work presented in this chapter is an adapted version of the manuscript published at *The Journal of Physical Chemistry C* (P. L. dos Santos, F. B. Dias, A. P. Monkman, *J. Phys. Chem. C*, 2016, 120, 18259−18267). P. L. dos Santos performed all steady state and time resolved photophysics measurements.

8.1 Introduction

Exciplex formation in organic materials is an excited state complex between donor (D) and acceptor (A) molecules, and their application in organic light emitting diodes (OLEDs) have attracted significant attention due to the observation of TADF mechanism in some examples[1–4]. Exciplex formation has for a long time been regarded as a negative effect in OLEDs due to reduced device performances and damaged colour purity, especially when they form interfacial states between the transport and the emissive layers in devices[5,6]. However, when exciplex emitters are used as emissive layers in devices, they can show great performance because of the capability they offer to harvest dark lower energy triplet excitons into emissive singlet states of higher energy.

Differently from the D-A molecules studied in previous chapters, the exciplex systems can have small exchange energy because electrons and holes are located on two different molecules, leading to very small spatial wavefunction overlap and hence small exchange energy. However, as the current exciplex-OLEDs have not achieved high performance as the OLEDs based on D-A molecules, they have not attracted as much attention as the monomolecular TADF emitters[7,8]. Therefore, the number of available exciplex emitters showing a true TADF mechanism is still limited and strategies for designing exciplexes with this character are greatly desirable.

In the case of an exciplex, the comparison between their intermolecular charge transfer state (iMCT) and the intramolecular CT systems seems difficult. However, one needs to consider that two different factors control spin-orbit coupling (SOC): i) the overlap of the wavefunctions of the two electrons in the exciplex state and ii) the electronic coupling between them, which falls off as $1/r^3$ [9,10]. One way to view SOC is the spin interaction of 1 electron's angular momentum in the magnetic field of the other orbiting electron, which quantum mechanically follows the exchange interaction between the two electrons and falls off very quickly with increasing electron separation, typically at 1.5 nm separation, the SOC rate $< 10^0$ s^{-1} [11]. Thus, the exact orientation of D and A molecules in an exciplex does not affect SOC rates as it does in CT systems, because the exchange interaction is already very small since the electron separation distance is already > 1 nm, therefore SOC is totally dominated by the electron separation spatial term. In an intermolecular exciplex system, the electron separation is large[12] showing exciplex separations in the range 2-3 nm, with the separation and intensity controlled by external electric field. Thus, no SOC will occur between ^{1}iMCT and ^{3}iMCT irrespective of

relative orientation of D and A in an exciplex, it is totally overwhelmed by the large electron separation, and a different mechanism is responsible for singlet triplet interconversion.

This chapter shows that the same mechanism for SOC proposed in CT systems[13] is valid in bimolecular exciplex emitters. By studying different blends made of well-known electron D and A materials by time resolved spectroscopy it is shown that the local triplet states (^{3}LE) play an important role to mediate ISC/rISC processes. Consequently, to obtain efficient TADF exciplex emitters the ^{3}LE state from the D or A molecules should be close enough in energy to the ^{1}iMCT state to minimize the thermal activation barrier between them. Competition between TTA and TADF mechanisms in exciplex blends are analyzed and, for those systems with small energy splitting between ^{1}iMCT and ^{3}LE, the TADF mechanism dominates, in contrast, TTA dominates for larger ΔE_{ST} because the residence time in ^{3}LE is long and TTA outcompetes rISC. Moreover, the role of HOMO/LUMO energies levels between the electron D and A molecules in the exciplex are analyzed, by combining the results of a large number of exciplex systems. No direct correlation between HOMO or LUMO energy offsets and TADF was observed because of the dominance of the ^{1}iMCT and ^{3}LE energy difference on rISC and thus TADF.

8.2 Results and Discussion

8.2.1 Solid State Photophysical Properties

Figure 61a shows the chemical structure of *m*-MTDATA, TPBi, TPD and OXD-7. Figure 61b-d shows the normalized absorption (dashed lines) and emission spectra (full line) for the following blends: b) *m*-MTADATA:TPBi, c) TPD:TPBi, and d) TPD:OXD-7, as well as the spectra of the pristine films of donor and acceptor molecules. The films were excited by 337 nm or 355 nm, at room temperature.

The absorption spectra of the blends shows features that are nearly identical to the combination of those pristine D and A films. This result proves that the formation of a new ground state transition does not occur in the blended films or is very weak. However, their emission spectra are broader and significantly red shifted when compared to either the D and A pristine emission spectra. These observations confirm the formation of new excited state in the blend films, i.e., exciplex formation. Unambiguous exciplex emission spectra are assigned in all cases.

The exciplex formation between *m*-MTADATA:TPBi, TPD:TPBi and TPD:OXD-7 blends have been reported before[14–17]. However, the exciplex formation was only identified and the blends were either applied in OLEDs or considered as a negative effect that reduce the quality of devices, without further investigation. Thus, time resolved spectroscopy was used to investigate these systems.

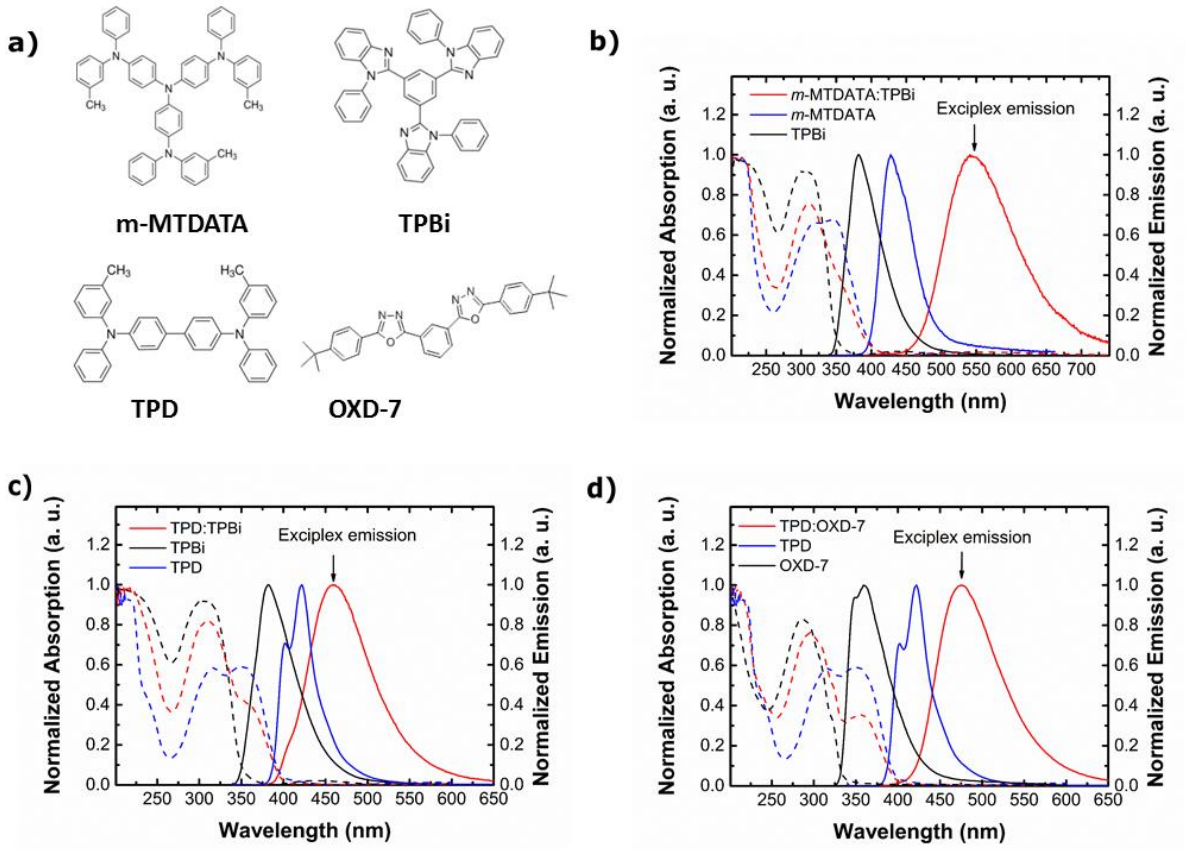

Figure 61 a) Chemical structure of m-MTDATA, TPBi, TPD and OXD-7, b) Normalized photoluminescence (PL) and absorption spectra of m-MTDATA:TPBi, c) TPD:TPBi and d) TPD:OXD-7, as well as their pristine acceptor and donor molecules.

8.2.1.1 *m*-MTDATA:TPBi Blend: TADF mechanism

Figure 62a shows the decay curves of *m*-MTDATA:TPBi from the early prompt emission (Time delay (TD) = 1.1 ns) to the end of delayed fluorescence emission (TD = 89 ms), at different temperatures. The curves were obtained with 355 nm excitation (> 200 µJ). The decay curves show first a rapid decay, associated to prompt emission, and later a long lived emission, associated to delayed fluorescence emission. The delayed fluorescence region can be subdivided and analyzed in two different time windows, region A and B. Initially, region A shows a temperature dependence which is typical of a TADF mechanism, i.e. higher intensities

at higher temperatures, because of the increase in thermal activation energy. Region B, on the other hand, shows a behavior that is not typical of a TADF mechanism - the intensity is higher at low temperatures. This behavior can be understood by means analyses of the rISC rate (k_{rISC}), equations (8.1 and 8.2)[18]:

$$k_{rISC} = k_{ISC}^{-T} e^{\frac{-\Delta E_{ST}}{RT}} \quad (8.1)$$

$$k_{rISC} = \frac{1}{\tau_{TADF}} \frac{\int I_{TADF}(t)dt}{\int I_{PF}(t)dt} \quad (8.2)$$

where k_{rISC} is the rISC rate from triplet level to singlet, k_{ISC}^{-T} is the maximum rISC rate, ΔE_{ST} is the energy splitting between singlet and triplet levels, R is the gas constant, τ_{TADF} is the lifetime of the TADF component, I_{TADF} is the delayed fluorescence component and I_{PF} the prompt fluorescence component. At high temperature, k_{rISC} is maximized (Equation 8.1), which leads to a short τ_{TADF} (Equation 8.2) giving rise to a short decay curve. On the other hand, at low temperature, k_{rISC} and internal conversion are minimized and the triplet state will live longer, leading to a longer lived decay curve, as it is observed. Thus, the decay lifetime increases with decreasing temperature, as demonstrated in Figure 62a.

Figure 62b shows the analyses of the emission spectra in the entire region of the study at 80 K. At earlier times, TD = 1.1 ns, a first peak at 425 nm together with the ^{1}iMCT state emission are observed. This first peak is associated to a vestige of the donor emission (^1LE_D), *m*-MTDATA. As the time delay increases, this peak emission disappears, showing that the process of electron transfer from the donor to the acceptor molecules takes about 4.6 ns, giving a rate for the electron transfer process estimated at ca. 2x 10^8 s^{-1}. During the prompt emission and region A, a continuous red shift is observed, which is associated with the energetic relaxation of the iMCT state. Around TD = 31 µs, the ^{1}iMCT state stabilizes and the same emission is observed until TD = 89 ms. The same analyses was made at 290 K, the temperature at which TADF mechanism is maximized (Figure 62c). The main difference from those spectra measured at 80 K is that the ^{1}iMCT is slightly further red shifted at longer time delays. This shows that the ^{1}iMCT state suffers more relaxation at higher temperatures, due to the increased vibrational energy.

As can be seen in Figure 2b and c, no phosphorescence emission was detected from *m*-MTDATA:TPBi blend. Most probably, all the excitons in the triplet states are efficiently converted back to ^{1}iMCT due to the small energy splitting between singlet and triplet states.

Second order (vibrationally coupled)[13,19] spin-orbital coupling (SOC) allows intersystem crossing, both direct and reverse (ISC/rISC processes) to occur between the states ^{1}iMCT $\leftrightarrow{}^3LE_A$ and ^{1}iMCT $\leftrightarrow{}^3LE_D$, where ^3LE_A and ^3LE_D refers to a local triplet state of the acceptor and donor molecules, respectively. *m*-MTDATA:TPBi blend shows ^{1}iMCT energy level of (2.64 ± 0.02) eV, which was determined by the onset of the PL emission at 290 K. The phosphorescence of the pristine donor and acceptor molecules were identified and the spectra are shown in Figure 62c. The ^3LE_D has onset at (2.65 ± 0.02) eV and ^3LE_A at (2.66 ± 0.02) eV, leading to very small values of $\Delta E_{ST,}$ (-0.01 ± 0.03) eV and (-0.02 ± 0.03) eV, maximizing the ISC/rISC processes. The negative values means that the ^{3}LE is located above the ^{1}iMCT.

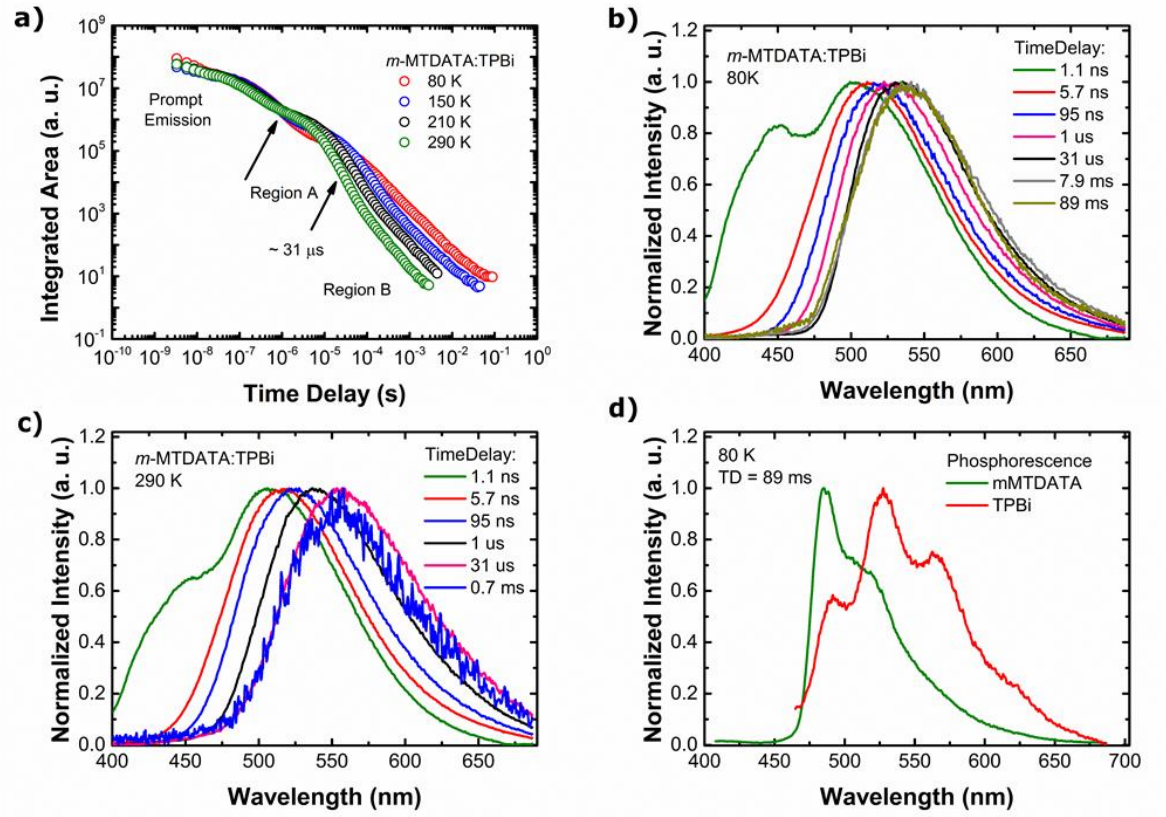

Figure 62 a) Time resolved fluorescence decay curves at different temperatures b) Time resolved normalized emission spectra at 80 K c) at 290 K of *m*-MTDATA:TPBi blend d) Phosphorescence spectra of neat m-MTDATA and TPBi at 80 K.

The intensity dependence of the DF emission in region A (Time delay TD= 2µs , Integration time IT= 5 µs) was analyzed also as a function of the laser excitation dose to certify the DF was due to a TADF mechanism and not TTA. A linear gradient of 0.82 ± 0.02 was found (Figure 63), confirming the thermally assisted mechanism as opposed to triplet-triplet

annihilation (TTA). Generally, TADF complexes show slope close to 1 at low and high excitation doses while TTA complexes show slop close to 2 at low excitation doses turning to slop close to 1 at high excitation doses.

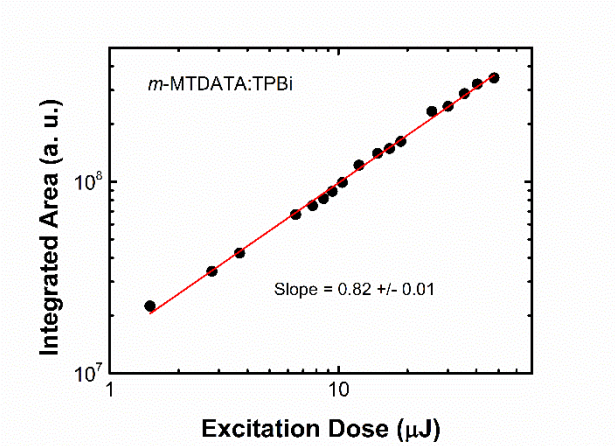

Figure 63 d) Integrated area as a function of the laser excitation (337 nm) of *m*-MTDATA:TPBi film.

8.2.1.2 TPD:TPBi Blend: TTA Mechanism

Figure 64a shows the decay curve of TPD:TPBi from the early prompt emission (TD = 1.1 ns) to the end of the PH emission (TD = 89 ms), at different temperatures (excitation at 355 nm, > 200 μJ). The decay curves show first a rapid decay, associated with prompt emission, and a long lived emission, associated to delayed fluorescence emission. Also, a very long lived emission at low temperatures is observed associated to phosphorescence emission. There is no strong temperature dependence anywhere between 80 K to 210 K, but a slight increase of the intensity of the assigned DF region is observed at higher temperatures. However, it is clear that at low temperature, the emission detected lives longer.

Figure 64b shows the analyses of the emission spectra in the entire region of the study at 80 K. Initially, at early TD, the ^1LE_D emission of the D, TPD, is detected, and then, the ^{1}iMCT emission spectra grows in. At TD= 5.7 ns pure ^{1}iMCT emission is observed with onset at (3.05 ± 0.02) eV. The rate of electron transfer in the TPD:TPBi was estimated at ca. $2x10^8$ s^{-1}. Very interestingly, at 5.7 ns only ^{1}iMCT emission is observed, no high energy shoulder coming from ^1LE_D emission is seen as at earlier times, but at 1.1 ms one observes a small contribution from ^1LE_D emission again. This very delayed ^1LE_D emission must hints at a TTA mechanism as it is the only mechanism that can regenerate a ^1LE_D state. Given that films are made by co-evaporation it is very unlikely that there are large regions of segregated D hence the ^1LE_D

emission most likely comes from ^1LE_D states formed by TTA which decay radiatively before electron transfer to the ^{1}iMCT manifold occurs. At later times, the ^{1}iMCT emission starts to compete with PH emission, and the result is that both emissions are observed at TD = 1.1 ms. The PH is the dominant emission at TD = 89 ms, but vestige of ^{1}iMCT emission around 450 nm is also detected. The phosphorescence emission is well structured and show two peaks, at 523 nm and 564 nm, and a shoulder, at 615 nm, which matches the local triplet state emission of the donor, TPD (^3LE_D has onset at (2.44 ± 0.02) eV).

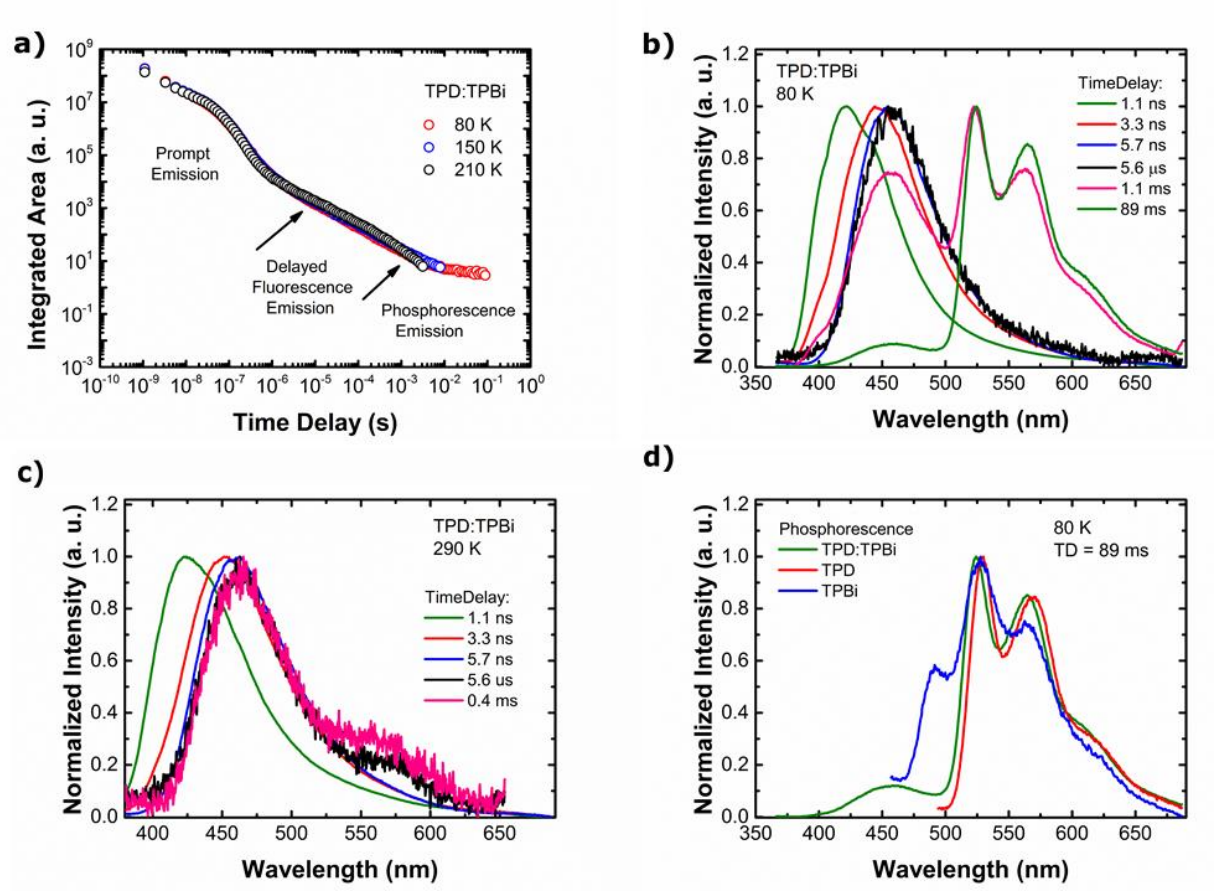

Figure 64 a) Time resolved fluorescence decay curves at different temperatures b) Time resolved normalized emission spectra at 80 K c) at 290 K of TPD:TPBi blend d) Phosphorescence spectra of TPD:TPBi blend and TPD and TPBi neat films.

However, the PH of TPBi, acceptor molecules, also emits in this wavelength region (onset at ^3LE_A= (2.66 ± 0.02) eV), but has different peak positions. For better comparison, the spectra of the blend TPD:TPBi and the pristine TPD and TPBi at TD=89 ms are shown in Figure 64d. Thus, the energy splitting between ^{1}iMCT and ^3LE_D was found to be ΔE_{ST} = (0.61 ± 0.03) eV, and between ^{1}iMCT and ^3LE_A , ΔE_{ST} = (0.39 ± 0.03) eV. Both ΔE_{ST} are large and TADF is

unlikely. The spectra analyses at 290 K (Figure 64c), show that the phosphorescence from the ^3LE_D is very weak, and just a shoulder is observed around 550 nm. This clearly indicates that the TTA mechanism is dominating at high temperatures, and the excitons no long populate the triplet states, explaining why no emission is detected after TD = 0.4 ms.

Figure 65 shows the integrated area as a function of the laser excitation dose (337 nm), collected in the delayed fluorescence region (TD = 2 µs and IT = 20 µs). The intensity dependence shows a slope of 1.60 ± 0.03 at low excitation dose (< 11 µJ), which turns to slop of 1.08 ± 0.02 at high excitation doses. This behavior strongly indicates a dominant TTA mechanism.

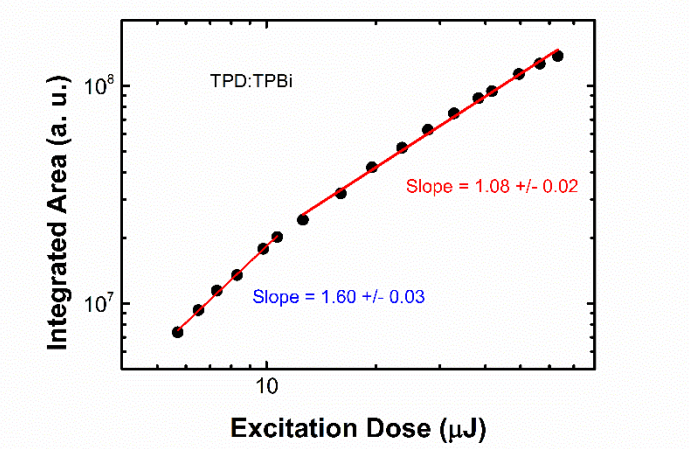

Figure 65 Integrated area as a function of the laser excitation (337 nm) of TPD:TPBi film.

8.2.1.3 TPD:OXD-7 Blend: TADF and TTA Mechanisms

Figure 66a shows the decay curves of TPD:OXD-7 from the early prompt emission (TD = 1.1 ns) to the end of the phosphorescence emission (TD = 89 ms), at different temperatures (excitation at 355 nm, > 200 µJ). There is a clear separation between prompt emission and delayed fluorescence (DF) emission around TD = 2 µs. The prompt emission does not show temperature dependence, exhibiting the same intensity from 80 K to room temperature, whilst, the DF and PH regions show clear temperature dependence. DF emission shows higher intensity at higher temperatures, in accordance with a TADF mechanism. PH emission shows higher intensity at low temperatures, as expected from triplet emission with reduction in the non-radiative decay channels.

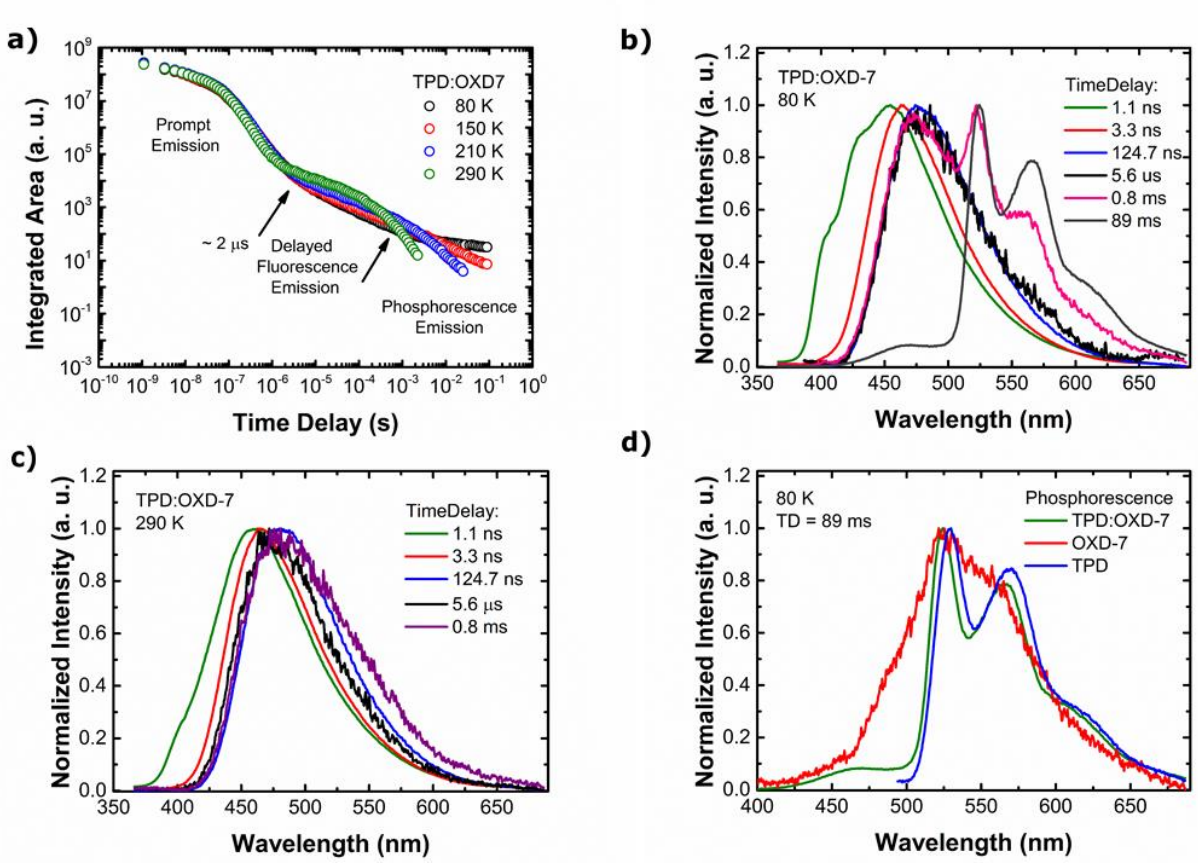

Figure 66 a) Time resolved fluorescence decay curves at different temperatures b) Time resolved normalized emission spectra at 80 K c) at 290 K of TPD:OXD-7 d) Phosphorescence spectra of TPD:OXD-7 and OXD-7 and TPD neat films.

Figure 66b shows the analyses of the emission spectra in the entire region of the study at 80 K. At earlier times, the emission spectra has two shoulders, at 403 nm and 426 nm, which matches that of local singlet state (^1LE_D) of the donor, TPD. As the time delay increases, the emission spectra shift to longer wavelengths, moving from ^1LE_D to ^{1}iMCT emission, clearly showing that the process of electron transfer from the D to the A molecules over about 2 ns at a rate of $K_{ET} \sim 5x10^8$ s^{-1}, faster than those estimated for *m*-MTDATA:TPBi and TPD:TPBi. From formation until ca. TD = 124.7 ns the ^{1}iMCT emission relaxes and further red shifts to an onset of about (2.95 ± 0.02) eV. At later time, the ^{1}iMCT emission starts to compete with phosphorescence emission, and both emissions are observed at TD=0.8 ms for example. The phosphorescence outcompetes the ^{1}iMCT emission being the dominant emission at TD=89 ms, but a vestige of ^{1}iMCT emission around 475 nm is still detected. The PH emission is well structured and shows two peaks, at 526 nm and 569 nm, and a shoulder at 615 nm. This triplet emission originates from the local triplet state of the donor, TPD. For better comparison, the

spectra of the blend TPD:OXD-7 and the pristine TPD and OXD-7 at TD = 89 ms are shown in Figure 66d. The ^3LE_D has onset at (2.44 ± 0.02) eV. Thus, the ^{1}iMCT and the ^1LE_D (lowest energy excited states) were identified in the TPD:OXD-7 blend, and the energy splitting between these two states was found to be ΔE_{ST} = (0.51 ± 0.03) eV. The ΔE_{ST} between ^{1}iMCT and ^3LE_D is relatively large and indicating that TADF is unlikely to be efficient, as shown by the rISC rate equations (Equation 1). However, the ^3LE_A from the acceptor molecules, OXD-7, was identified to have onset at (2.72 ± 0.02) eV. Thus, the energy splitting between ^{1}iMCT and ^3LE_A is ΔE_{ST} = (0.23 ± 0.03) eV and rISC involving these two state would have much higher probability. Therefore, there could well be a complex competition between TTA (process involving ^1LE_D and ^3LE_D energy states) and TADF (process involving ^{1}iMCT and ^3LE_A energy states) depending on the relative lifetime of each process.

Figure 66c shows the normalized spectra at different time delays at 290 K. As can be seen, the contribution of the donor emission at TD = 1.1 ns is higher at 80 K than at 290 K, because at low temperature the non radiative decays are minimized. Also, the ^{1}iMCT is slightly red shifted at longer time delays, because high temperatures promote more vibrational transitions, leading to a higher relaxation of ^{1}iMCT state.

The integrated area, collected over the delayed fluorescence region (TD =5 µs and IT = 50 µs), was analyzed as a function of the laser excitation (337 nm) dose (Figure 67). The intensity dependence shows a slope of 1.33 ± 0.03 at low excitation dose (< 11 µJ), which turns to a linear dependence with slope of 1.00 ± 0.02, at high excitation doses. This suggests that the delayed fluorescence of this blend has some contribution from TTA, but it is not entirely, otherwise the behavior at low excitation doses would show a slope much closer to 2. Most probably, the TTA mechanism is not a pure process because the excitons in ^{3}LE need to collide with excitons in other A/D molecules to up-convert them to a ^{1}LE state, which is a slow process due to its' bimolecular character. Therefore, from the power dependence of the DF it can be deduced that there must also be a contribution coming from TADF. Thus, the delayed fluorescence mechanism in TPD:OXD-7 is most probably a mixture of TADF and TTA.

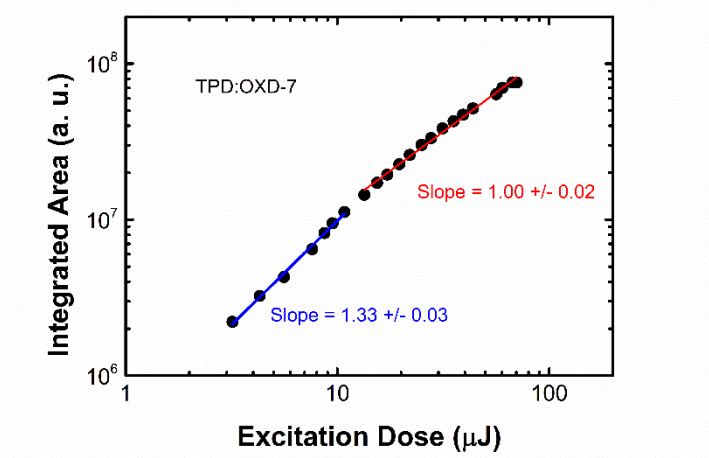

Figure 67 Integrated area as a function of the laser excitation (337 nm) of TPD:OXD-7 film.

In summary, *m*-MTDATA:TPBi blend shows two energy splitting between ^{1}iMCT and ^{3}LE for the donor and acceptor molecules of ΔE_{ST} = (-0.01 ± 0.03) eV and ΔE_{ST} = (-0.02 ± 0.03) eV, respectively, which are very small, giving rise to TADF mechanism. TPD:TPBi blend shows the values of ΔE_{ST} = (0.61 ± 0.03) eV and ΔE_{ST} = (0.39 ± 0.03) eV, resulting in TTA dominating because the triplet states are far below the ^{1}iMCT state. TPD:OXD-7 blend shows ΔE_{ST} = (0.51 ± 0.03) eV and ΔE_{ST} = (0.23 ± 0.03) eV, respectively. The results for this blend show that the DF mechanism is mixed TTA and TADF, because one energy splitting favors TADF while and the other one TTA.

After systematically analyzing the delayed fluorescence mechanisms in these different exciplex blends, a collective energy diagram showing the full decay pathways available in these systems was derived (Figure 68). Green dashed arrows represent the internal non-radiative transitions and purple full ones the radiative transitions, which were detected by time dependence spectroscopy. Upon optical excitation of the donor or acceptor molecules, a population of iMCT states is formed, relatively slowly, $k_{ET} \sim 10^8$ s^{-1}, via electron or hole transfer. At early times, ^{1}iMCT $\rightarrow S_0$ and $^1LE_D \rightarrow S_0$ transitions are detected. As the acceptor molecules studied absorb very weakly at 355 nm, the transition $^1LE_A \rightarrow S_0$ is not detected. It is also highly likely that internal non-radiative transitions $^1LE_A \rightarrow {}^1LE_D$ will occur as potentially would $^1LE_A \rightarrow {}^1$iMCT. As intersystem crossing between ^{1}iMCT and ^{3}iMCT states potential can only occur by hyperfine coupling (HFC) if the energy difference between the singlet and triplet CT states is very small, of order 10^{-3} meV, i.e. when the electronic coupling between ^{1}iMCT $\leftrightarrow {}^3$iMCT is effectively zero, this channel is extremely inefficient compared to that between the ^{1}iMCT state and a local excited triplet state (^{3}LE)[20]. Therefore, the transition ^{1}iMCT $\leftrightarrow {}^3$iMCT is very unlikely to occur. The energy splitting between ^{1}iMCT $\leftrightarrow {}^3LE_D$ and ^{1}iMCT $\leftrightarrow {}^3LE_A$

depends on which molecules are chosen as donor and acceptor. If these energies splitting are small, excitons in the local triplet levels gain enough thermal energy to match the ^{1}iMCT level and then cross, considering that rISC/ISC processes are adiabatic transitions. Hence, the transition ^{1}iMCT→S_0 is detected also at longer times and assigned as delayed fluorescence emission. If, however these energy splittings are large, this mechanism is unlikely to occur. In this case another delayed fluorescence mechanism, triplet-triplet annihilation TTA dominates, which occurs between $^1LE_A \leftrightarrow {}^3LE_A$, $^1LE_D \leftrightarrow {}^3LE_D$, or $^3LE_A \leftrightarrow$, ^1LE_D converting two triplet excitons into one singlet exciton in ^{1}LE state and one in the ground state. If TTA occurs in the acceptor molecules, the exciton converted to ^1LE_A can go back to ^3LE_A or compete with the transitions $^1LE_A \rightarrow {}^1LE_D$ and $^1LE_A \rightarrow {}^1$iMCT. Finally, at very late times and at low temperature, the emission from the transition $^3LE_D \rightarrow S_0$ is detected, assigned as phosphorescence. The transition $^3LE_A \rightarrow S_0$ is not detected because the Dexter energy transfer from ^3LE_A to ^3LE_D may occur.

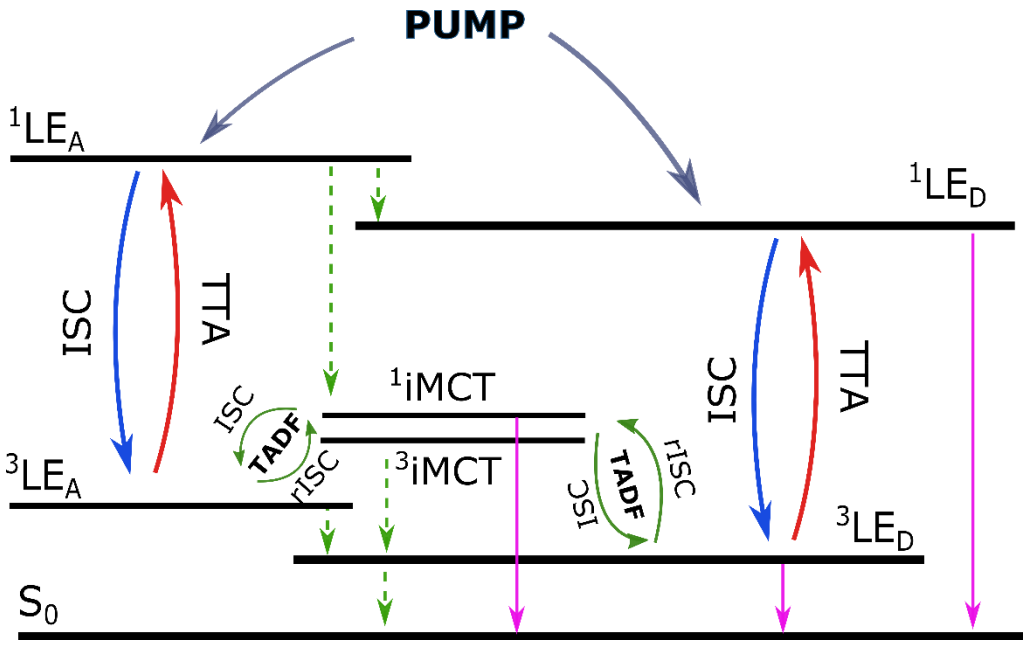

Figure 68 Energy diagram showing all the radiative and non-radiative available pathways of decay in an exciplex blend.

From power dependencies it is clear that TADF and TTA compete with each other. When the singlet-triplet gap between ^{1}iMCT and ^{3}LE is small and also one triplet state is not far below the ^{1}iMCT state, then TADF dominates. In all three cases the D A separation must be about the same at around 3-4 nm, thus the ^{1}iMCT ^{3}iMCT separation would be expected to be very small

in all cases. Thus, as in CT D-A molecules, the LE CT gap is very important to control rISC and thus TADF efficiency in exciplexes as it does in the CT molecules[21,22].

These findings are essential for the design of exciplex blends. It means, in order to produce an exciplex blend showing efficient TADF, it is crucial to analyze the position of ^{3}LE of the donor and acceptor molecules in respect to the ^{1}iMCT emission. To date, the exciplex blends were designed to have the ^{1}iMCT state close to ^{3}iMCT, which can lie below both ^3LE_D and ^3LE_A but here it is shown that this is not the only energy splitting that should be considered. Also, it is shown that to achieve pure TADF both ^{3}LE state should be very close in energy to ^{1}iMCT, or at least one very close lying and one above ^{1}iMCT.

8.2.1.4 Other Blends Made of D and A Commercial Materials

In the attempts to fully elucidate the underlying mechanism of exciplex systems, a set of 17 blends (chemical structure of all compounds are shown in chapter 3), which show clear exciplex formation (emission) were selected, and the correlation between their HOMO/LUMO energy levels as well as their ^{1}iMCT /^{3}LE energy levels (Table 5) was determined. The HOMO/LUMO energy levels for the individual donor and acceptor molecules were taken from literature, and used as an estimation, because these values are sensitive to experimental conditions and vary considerably in the literature[4,23–26]. The ^{3}LE onset values of TCTA, mCP and NPB also were taken from literature from phosphorescence spectra[4,27,28], the other ^{3}LE spectra are shown in Figure 69**.**

Material	HOMO (eV)	LUMO (eV)	H-H (eV)	L-L (eV)	^{1}iMCT Onset (±0.02eV)	Triplet Onset (±0.02eV)	ΔE_{ST} (±0.03eV)
m-MTDATA	5.1	2.0	-1.2	-0.8	2.64	2.65	-0.01
TPBi	6.3	2.8			2.64	2.66	-0.02
TPD	5.3	2.2	-1.0	-0.6	3.05	2.44	0.61
TPBi	6.3	2.8			3.05	2.66	0.39
TPD	5.3	2.2	-1.2	-0.6	2.95	2.44	0.51
OXD-7	6.5	2.8			2.95	2.72	0.23
TPD	5.3	2.2	-0.8	-0.6	3.06	2.44	0.62
BCP	6.1	2.8			3.06	2.56	0.50
TCTA	5.7	2.3	-0.8	-0.5	3.10	2.93	0.17

OXD-7	6.5	2.8			3.10	2.72	0.38
TCTA	5.7	2.3	-0.4	-0.5	3.24	2.93	0.31
BCP	6.1	2.8			3.24	2.56	0.68
TCTA	5.7	2.3	-0.6	-0.5	3.08	2.93	0.15
TPBi	6.3	2.8			3.08	2.66	0.42
TAPC	5.5	2.0	-0.6	-0.5	3.04	2.85	0.19
PBD	6.1	2.5			3.04	2.60	0.44
TAPC	5.5	2.0	-0.8	-0.8	3.13	2.85	0.28
TPBi	6.3	2.8			3.13	2.66	0.47
TAPC	5.5	2.0	-1.0	-0.8	3.07	2.85	0.22
OXD-7	6.5	2.8			3.07	2.72	0.35
m-MTDATA	5.1	2.0	-1.0	-0.5	2.62	2.65	-0.03
PBD	6.1	2.5			2.62	2.60	0.02
m-MTDATA	5.1	2.0	-1.4	-0.8	2.62	2.65	-0.03
OXD-7	6.5	2.8			2.62	2.72	-0.10
m-MTDATA	5.1	2.0	-1.0	-0.8	2.71	2.65	0.06
BCP	6.1	2.8			2.71	2.56	0.15
mCP	6.1	2.4	-0.4	-0.4	3.44	2.87	0.57
OXD-7	6.5	2.8			3.44	2.72	0.72
TAPC	5.5	2.0	-0.5	-1.0	2.78	2.85	-0.07
DPTPCz	6.0	3.0			2.78	2.91	-0.13
TCTA	5.7	2.3	-0.3	-0.7	2.81	2.93	-0.12
DPTPCz	6.0	3.0			2.81	2.91	-0.10
NPB	5.4	2.8	-0.6	-0.2	2.95	2.40	0.55
DPTPCz	6.0	3.0			2.95	2.91	0.04

Table 5 Energy levels of different blends that show exciplex formation. The energy values labeled as L-L in the table means the energy difference between the LUMO of the donor and acceptor molecules. The same analyses was carried out for the HOMO energy levels.

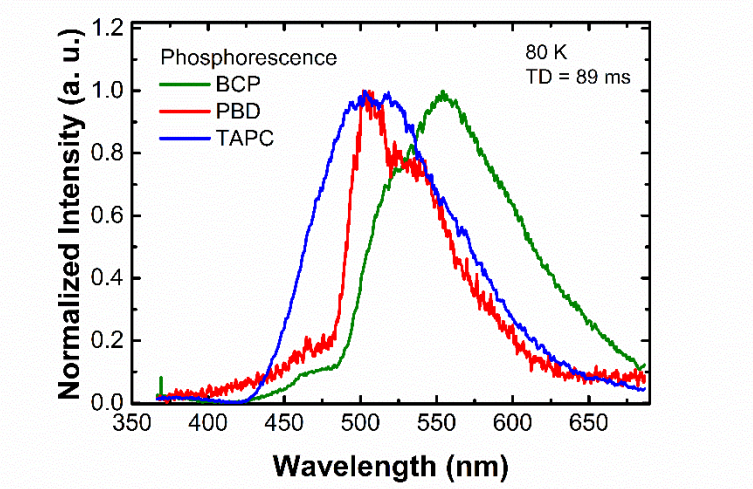

Figure 69 Phosphorescence spectra of TAPC, PBD and BCP neat films. The spectra were taken at 80 K with TD= 89 ms and excitation at 355 or 266 nm.

^{1}iMCT onset values of the first 13 blends were taken from PL spectra (Figure 70) and ^{1}iMCT onset values of the last 3 blends were estimated from PL spectra from reference 4. The energy values labeled as L-L in the table means the energy difference between the LUMO of the donor and acceptor molecules. The same analyses were carried out for the HOMO energy levels.

There is no obvious correlation among L-L or H-H values and exciplex formation (evidenced by CT emission); the exciplex is formed for low and high energy offset values. These values may influence the efficiency of charge transferred from donor to acceptor molecules, i.e., the charge transfer rates, but certainly the exciplex formation can occur for a large range of distinctive values of H-H and L-L. By the analyses of ΔE_{ST}, i.e. the difference between ^{1}iMCT and ^{3}LE, it is possible to estimate which pairs of molecules are likely to yield TADF. The negative values mean that the ^{3}LE is located above the ^{1}iMCT, a preferable characteristic for the designing of efficient exciplex emitters, because it prevents quenching of the excited states to a low lying local triplet state, as reported before,[7] but it is not essential for TADF to occur. *m*-MTDATA:PBD blend shows both ΔE_{ST} values to be very small, very promising for TADF mechanism. This blend was demonstrated to have strong TADF,[2,29] and, the analysis provided here gives a better understanding of the good performance of its TADF mechanism. *m*-MTDATA:OXD-7 also shows both ΔE_{ST} values likely for TADF, which was also confirmed by time resolved optical spectroscopy (Figure 71a,b). TPD:BCP blend shows both ΔE_{ST} values large, which have the TTA mechanism confirmed by time resolved optical spectroscopy (Figure 71c,d). TAPC:PBD shows energy splitting values close to those of TPD:OXD-7, one ΔE_{ST} likely for TADF and another for TTA. The mix of the delayed fluorescence mechanisms

was confirmed in this blend (Figure 71e,f). Ping Chen *et al.* have compared the performance of the OLEDs produced with emissive layers of *m*-MTDATA: TPBi and *m*-MTDATA:BCP, with measurements carried out under the same conditions[30]. The first one has shown better performance, which was associated to the largest exciplex bandgap (energy difference between the LUMO of the donor and the HOMO of the acceptor). Thus, it is possible to associate the better performance of *m*-MTDATA:TPBi with the smaller values of both ΔE_{ST}. These smaller energy values leads to a stronger TADF characteristic, and consequently, a better performance if compared to *m*-MTDATA:BCP device. Liu *et al.*[4] have compared three exciplex blends, TAPC:DPTPCz, TCTA:DPTPCz and NPB:DPTPCz. The TADF mechanism was identified in the first two blends. These results are in agreement with the analyses shown here, because TAPC:DPTPCz and TCTA:DPTPCz blends have ^{1}iMCT and ^{3}LE very close in energy, on the other hand, NPB:DPTPCz blend shows one ^{3}LE level located far below the ^{1}iMCT, preventing efficient rISC.

The cases where TADF dominates are rare and correlate to the absence of a low lying quenching local triplet state. However, in all cases showing at least a contribution from TADF, a ^{3}LE state lies very close in energy to ^{1}iMCT even if the other ^{3}LE state lies well below the CT states causing quenching. The rISC rates depend on the energy gap and electronic coupling, thus, only in specially cases, the 'pure' TADF will be observed, this will be a very resonant effect. Hence, only (partially) mono exponential decay from ^{1}iMCT showing a unique species in *m*-MTDATA:TPBi is shown. If the ^{1}iMCT and ^{3}iMCT orbitals were not very close to degenerate the exchange energy would be large, i.e. bigger than 50 -100 meV. This might 'allow' some direct SOC between them, but then the gap between ^{1}iMCT and ^{3}iMCT would be too large to yield efficient TADF, and TADF is clearly observed. The clear observation of TADF indicates that ^{1}iMCT, ^{3}iMCT and ^{3}LE are *all* close to isoenergetic allowing efficient TADF and no quenching to a low lying triplet state yielding TTA. However, when mixed TADF and TTA is observed, the case when ^{1}iMCT, ^{3}iMCT and ^{3}LE are *all* near isoenergetic but the other local triplet lies below them, then a competition between rISC and ^{1}iMCT emission with quenching to the low lying ^{3}LE state has to be fairly equal such that both mechanisms compete. A low lying local triplet state does not always lead to full quenching of TADF.

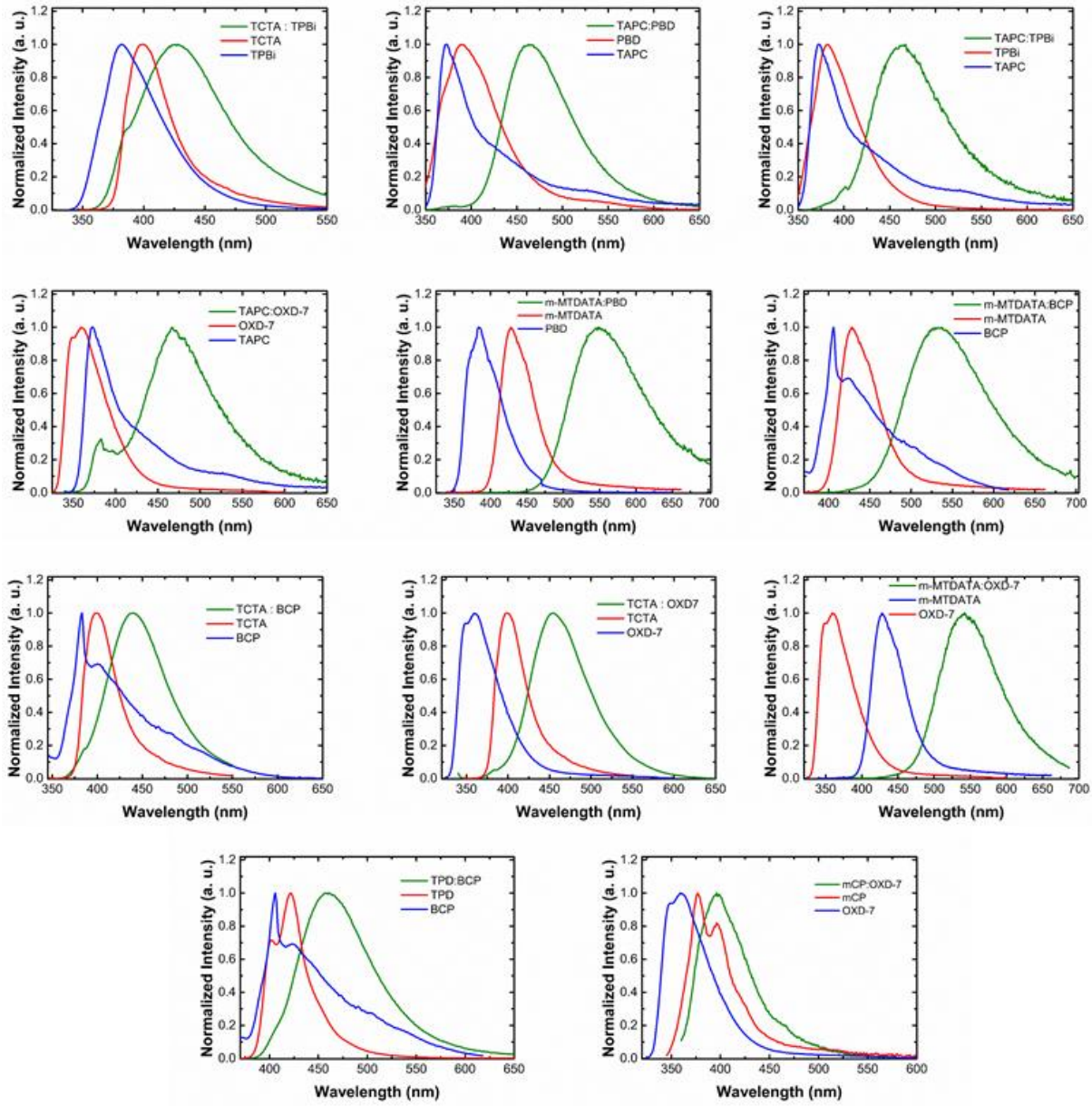

Figure 70 Photoluminescence (PL) spectra of different blend films together with the PL spectra of the neat films.

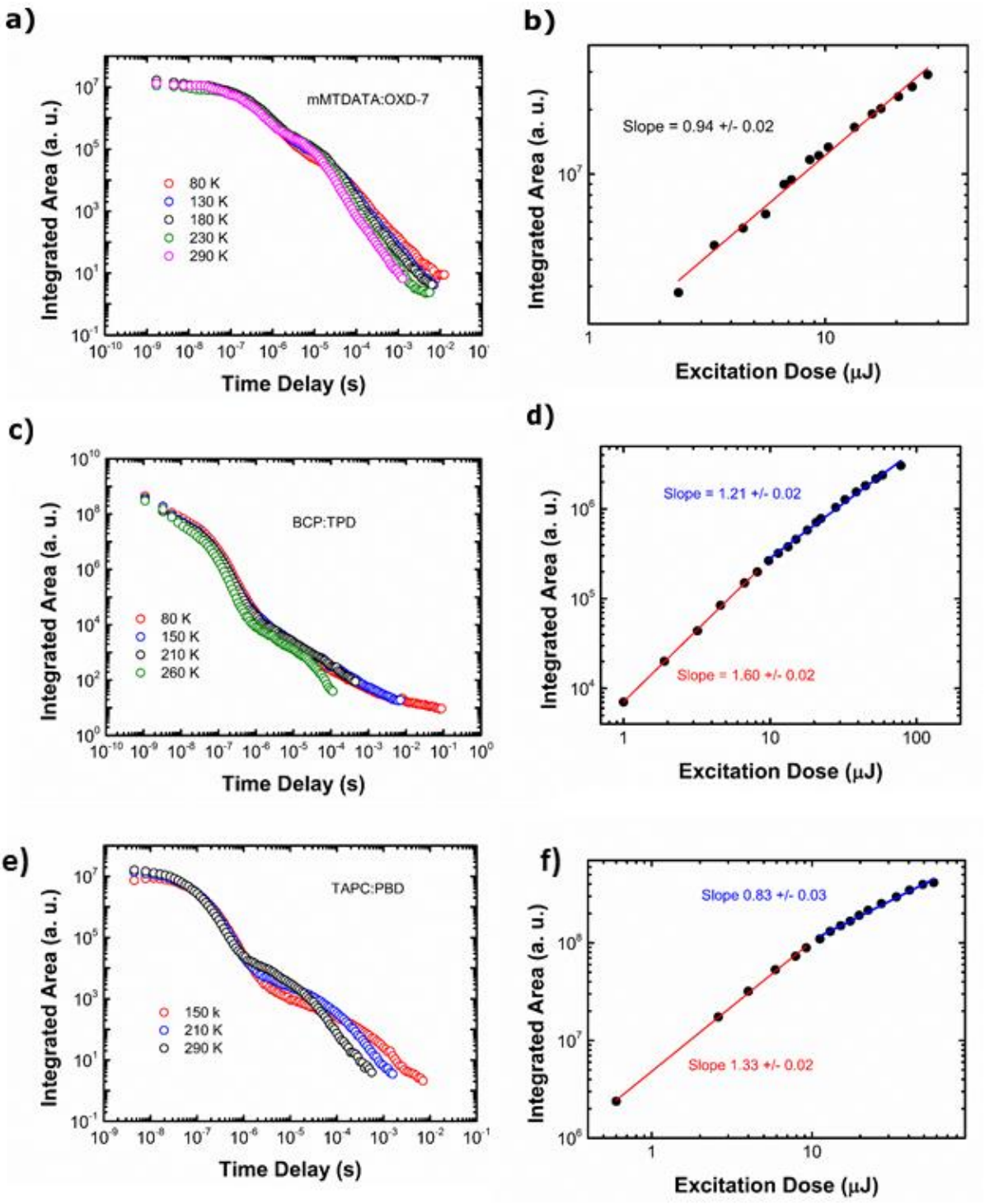

Figure 71 a) Time resolved fluorescence decay curves at different temperatures and b) Integrated area as a function of the laser excitation (337 nm) of m-MTDATA:OXD-7 film. c) Time resolved fluorescence decay curves at different temperatures and d) Integrated area as a function of the laser excitation (337 nm) of BCP:TPD film. e) Time resolved fluorescence decay curves at different temperatures and f) Integrated area as a function of the laser excitation (337 nm) of TAPC:PBD film.

8.3 Conclusion

In summary, the photophysical properties of 17 exciplex systems were studied in this chapter, focusing on three blends made of well-known electron donor and acceptor materials (*m*-MTDATA:TPBi, TPD:OXD-7 and TPD:OXD-7). It is shown that the ISC/rISC processes between ^{1}iMCT and ^{3}iMCT is mediated by a local triplet state (^{3}LE) following a similar mechanism shown for CT TADF molecules (previous chapters). Consequently, to obtain TADF emission, a ^{3}LE state from the donor or acceptor molecules must be close enough in energy to the CT states to minimize the thermal activation barrier i.e. achieving vibronic coupling between ^{3}LE and ^{3}CT. However, for many systems (studied here as well as taken from the literature) mixed TADF and TTA is observed. By analyzing the competition between TTA and TADF it is found that for those systems with an energetically close lying ^{1}iMCT and ^{3}LE, the TADF mechanism dominates, in contrast, TTA dominates for larger ΔE_{ST} because the residence time in the triplet state is long and TTA outcompetes rISC. In the case of one close lying and one lower energy LE state then mixed TTA and TADF can be observed showing that the two processes compete fairly equally. In this case the low lying LE state does not completely quench the TADF. Moreover, the role of the highest occupied and lowest unoccupied molecular orbitals (HOMO/LUMO) energies levels between the electron donor and acceptor molecules in the exciplex formation is analyzed. No obvious correlation between energy offset and TADF to these values because the ^{1}iMCT and ^{3}LE energy difference dominates this property was observed. Therefore, this study opens a new development route for the design of new materials selection for delayed fluorescence device based on TADF mechanism.

8.4 Sample Preparation Details

The films were prepared by thermal evaporation. Pure evaporated thin films and blend films (co-evaporation) were deposited onto transparent sapphire substrates using a Kurt J. Lesker Spectros II deposition system under vacuum, 10^{-6} mbar at a steady evaporation rate of ~ 1.0 Å/ s. The thickness of the evaporated thin films are ~ 200 nm. All blends were mixed in the ratio D:A 1:1.

8.5 References Chapter 8

1. Hung, W. *et al.* Highly E ffi cient Bilayer Interface Exciplex For Yellow Organic Light-Emitting Diode. *ACS Appl. Mater. Interfaces* **5,** 6826–6831 (2013).
2. Graves, D., Jankus, V., Dias, F. B. & Monkman, A. Photophysical Investigation of the Thermally Activated Delayed Emission from Films of m-MTDATA: PBD Exciplex. *Adv. Funct. Mater.* **24,** 2343–2351 (2014).
3. Zhang, T. *et al.* Blue exciplex emission and its role as a host of phosphorescent emitter. *Org. Electron.* **24,** 1–6 (2015).
4. Liu, X.-K. *et al.* Prediction and Design of Efficient Exciplex Emitters for High-Efficiency, Thermally Activated Delayed-Fluorescence Organic Light-Emitting Diodes. *Adv. Mater.* **27,** 2378–2383 (2015).
5. Chen, B. *et al.* Improved color purity and efficiency of blue organic light-emitting diodes via suppression of exciplex formation. *Synth. Met.* **118,** 193–196 (2001).
6. Chan, L. H., Lee, R. H., Hsieh, C. F., Yeh, H. C. & Chen, C. T. Optimization of high-performance blue organic light-emitting diodes containing tetraphenylsilane molecular glass materials. *J. Am. Chem. Soc.* **124,** 6469–6479 (2002).
7. Jankus, V., Chiang, C. J., Dias, F. & Monkman, A. P. Deep blue exciplex organic light-emitting diodes with enhanced efficiency; P-type or E-type triplet conversion to singlet excitons? *Adv. Mater.* **25,** 1455–1459 (2013).
8. Tao, Y. *et al.* Thermally Activated Delayed Fluorescence Materials Towards the Breakthrough of Organoelectronics. *Adv. Mater.* 7931–7958 (2014). doi:10.1002/adma.201402532
9. Marian, C. M. Spin-orbit coupling and intersystem crossing in molecules. *Wiley Interdiscip. Rev. Comput. Mol. Sci.* **2,** 187–203 (2012).
10. Masmanidis, C. A., Jaffe, H. H. & Ellis, R. L. Spin-orbit coupling in organic molecules. *J. Phys. Chem.* **79,** 2052–2061 (1975).
11. Turro, N. J., Ramammurthy, V. & Scaiano, J. C. *Principles of Molecular Photochemistry*. (2009).
12. Al Attar, H. A. & Monkman, A. P. Electric Field Induce Blue Shift and Intensity Enhancement in 2D Exciplex Organic Light Emitting Diodes; Controlling Electron-Hole Separation. *Adv. Mater.* **28,** 8014–8020 (2016).
13. Gibson, J., Monkman, A. & Penfold, T. The Importance of Vibronic Coupling for Efficient Reverse Intersystem Crossing. *ChemPhysChem* **17,** 2956–2961 (2016).
14. Imaizumi, K., Mori, T. & Mizutani, T. Injection and transport of carriers at organic interfaces in organic light-emitting-diode with oxadiazole derivatives. *IEEE 1997 Annu. Rep. Conf. Electr. Insul. Dielectr. Phenom.* **2,** 459–462 (1997).
15. Haverinen, H. M. *et al.* Inkjet printing of light emitting quantum dots Inkjet printing of light emitting quantum dots. *Appl. Phys. Lett.* **94,** 073108-1 (2009).
16. Zhang, G. *et al.* Highly efficient photovoltaic diode based organic ultraviolet

photodetector and the strong electroluminescence resulting from pure exciplex emission. *Org. Electron.* **10,** 352–356 (2009).

17. Chen, S. *et al.* Efficient organic light-emitting device from exciplex emission between 4,4′,4″-tris[3-methylphenyl(phenyl)amino]triphenylamine and 2,2′,2″-(1,3,5-benzenetriyl)tris-[1-phenyl-1H-benzimidazole]. *Org. Electron.* **6,** 111–117 (2005).

18. Dias, F. B. Kinetics of thermal-assisted delayed fluorescence in blue organic emitters with large singlet-triplet energy gap. *Philos. Trans. R. Soc. A Math. Phys. Eng. Sci.* **373,** 20140447–20140447 (2015).

19. Gibson, J. & Penfold, T. J. Nonadiabatic coupling reduces the activation energy in thermally activated delayed fluorescence. *Phys. Chem. Chem. Phys.* **19,** 8428–8434 (2017).

20. Lim, B. T., Okajima, S., Chandra, A. K. & Lim, E. C. Radiationless transitions in electron donor-acceptor complexes: selection rules for S1 → T intersystem crossing and efficiency of S1 → S0 internal conversion. *Chem. Phys. Lett.* **79,** 22–27 (1981).

21. Santos, P. L. *et al.* Engineering the singlet–triplet energy splitting in a TADF molecule. *J. Mater. Chem. C* **4,** 3815–3824 (2016).

22. Data, P. *et al.* Dibenzo[a,j]phenazine-Cored Donor-Acceptor-Donor Compounds as Green-to-Red/NIR Thermally Activated Delayed Fluorescence Organic Light Emitters. *Angew. Chemie Int. Ed.* **55,** 5739–5744 (2016).

23. Etori, H. *et al.* Design of multilayer structure for UV organic light-emitting diodes based on 2-(2-naphthyl)-9,9'-spirobifluorene. *Japanese J. Appl. Physics, Part 1 Regul. Pap. Short Notes Rev. Pap.* **46,** 5071–5075 (2007).

24. Jeon, S. O., Yook, K. S., Joo, C. W. & Lee, J. Y. A phosphine oxide derivative as a universal electron transport material for organic light-emitting diodes. *J. Mater. Chem.* **19,** 5940–5944 (2009).

25. Mohd Sarjidan, M. A. *et al.* Blending effect on small molecule based OLED. *Optoelectron. Adv. Mater. Rapid Commun.* **7,** 498–501 (2013).

26. Yang, Y. *et al.* Blue-violet electroluminescence from a highly fluorescent purine. *Chem. Mater.* **22,** 3580–3582 (2010).

27. Kim, J. W. *et al.* Study of Sequential Dexter Energy Transfer in High Efficient Phosphorescent White Organic Light-Emitting Diodes with Single Emissive Layer. *Sci. Rep.* **4,** 7009 (2014).

28. Reineke, S. *et al.* White organic light-emitting diodes with fluorescent tube efficiency. *Nature* **459,** 234–8 (2009).

29. Goushi, K., Yoshida, K., Sato, K. & Adachi, C. Organic light-emitting diodes employing efficient reverse intersystem crossing for triplet-to-singlet state conversion. *Nat. Photonics* **6,** 253–258 (2012).

30. Chen, P., Peng, Q., Yao, L., Gao, N. & Li, F. Identifying the efficient inter-conversion between singlet and triplet charge-transfer states by magneto-electroluminescence study. *Appl. Phys. Lett.* **102,** (2013).

Chapter 9: TADF Mechanism in an Excited State Intramolecular Proton Transfer Emitter

The previous chapters focus on combining donor and acceptor units to achieve efficient TADF. Here, the TADF mechanism was identified in a planar excited state intramolecular proton transfer (ESIPT) emitter, triquinolonobenzene (TQB). The singlet and triplet states involved in the optical energy gap of TQB molecules were identified to be at 2.71 eV and 2.53 eV, respectively, i.e., ΔE_{ST} = 0.18 eV. This small ΔE_{ST} gives rise to DF via the TADF mechanism. The advantages of this type of emitter to achieve TADF are discussed in this chapter.

The work presented in this chapter is a collaborative work between the OEM group and Center of Organic Photonics and Eletronics Research (OPERA) lead by Prof Chihaya Adachi. The compound was synthesised and purified by Prof Adachi's group. The steady state and time resolved photophysics measurements were performed by P. L. dos Santos and C. Menelaou.

9.1 Introduction

Excited state intramolecular proton transfer (ESIPT) molecules have attracted intense attention as the focus of both theoretical and experimental studies[1]. Typical ESIPT molecules exist in the ground state almost exclusively in the enol form, which is stabilized by intramolecular hydrogen bonding. On photoexcitation, redistribution of electronic charge occurs and fast proton transfer from the proton donor to the proton acceptor takes place. As very little structural change is required, this transformation from the enol to the keto tautomer in the excited state is an extremely fast process (picosecond timescale) and can proceed even at low temperatures[2]. One useful characteristic of the ESIPT process is its sensitivity to the environment. As it can be disrupted by interaction with the surrounding medium, ESIPT emitters can be used to design fluorescent probes for pH sensing, for example. Moreover, ESIPT has shown its merits in optoeletronic applications, including organic light-emitting diodes (OLEDs)[1,3,4]. Figure 72 shows a scheme of ESIPT process in the molecules studied in this chapter.

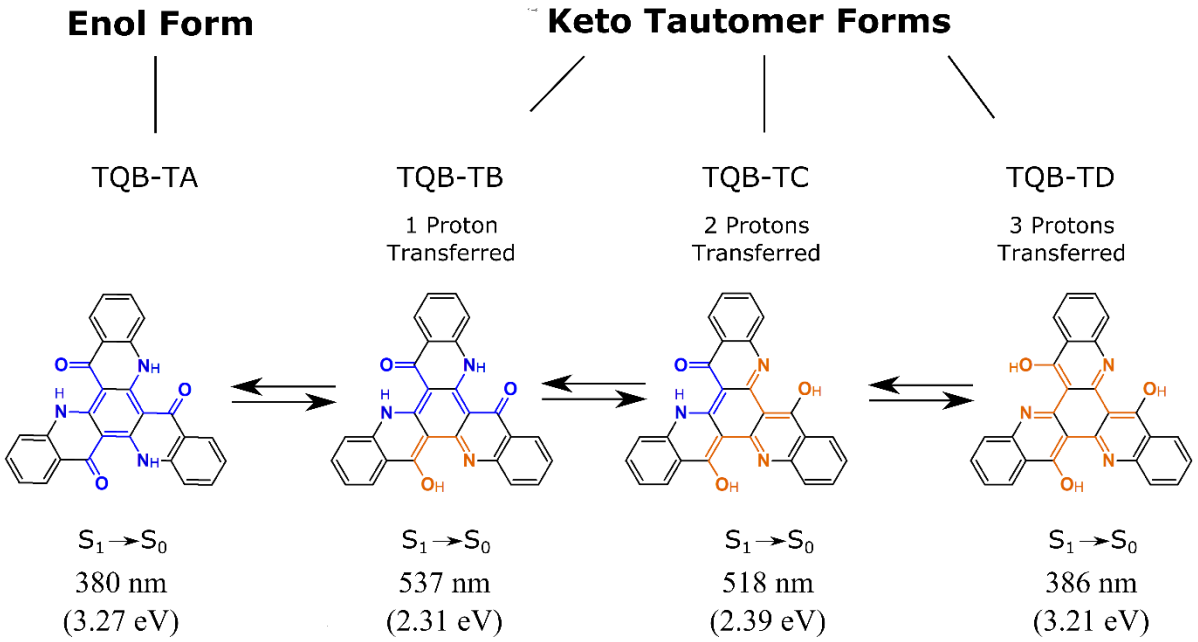

Figure 72 Excited state intramolecular proton transfer (ESIPT) process model in triquinolonobenzene molecule proposed by Adachi and co-authors[4]. The stationary points of both the ground S_0 and the first excited S_1 states were investigated for each tautomer by density functional theory (DFT) and time-dependent DFT (TD-DFT) methods.

The discovery of TADF in ESIPT emitters opens up new avenues for molecular design as noted by Park *et. al* in 2007[5]. They investigated a hydroxyl-substituted tetraphenyl imidazole

derivative (HPI-Ac) molecule using time resolved spectroscopic techniques and observed the TADF mechanism with estimated limiting rISC rate-constant of $1.3x10^7$ s^{-1}. Before this, rISC processes from higher triplet excited states to excited singlet states in ESIPT emitters had also been observed by Itoh *et al.*[6] and Oyama *et al.*[7] in their studies on 2',3',4',5',6'-pentamethyl-3-hydroxyflavone (PM3HF) and 2,2'-bipyridine-3,3'-diol, respectively.

Recently, Adachi and co-authors[4] demonstrated the use of ESIPT molecules in OLEDs by studying the planar triquinolonobenzene (TQB) emitter. The spatial separation of the HOMO and LUMO required for efficient TADF emitters is obtained by the ESIPT process in TQB molecules. In this process, a hydrogen atom covalently bonded to one atom and hydrogen bonded to a second in the same molecule switches to being covalently bonded to the second atom and hydrogen bonded to the first upon excitation. They have identified that a TADF mechanism gives rise to a delayed fluorescence component in TQB molecules, which directly translated to devices with external electroluminescence quantum efficiencies up to 14%. The devices, however, showed large roll-off that was attributed to the formation of excess triplet excitons. The slow rISC observed in TQB led to an increase in exciton quenching by triplet-triplet and singlet-triplet annihilation processes.

Here, the TQB emitter in different environments is further investigated. The choice of dispersing TQB molecules in a non-polar solid environment, zeonex, enabled the identification of its phosphorescence spectrum for the first time. Thus, the optical energy gap involved in the TADF mechanism for this molecule was found to be 0.18 eV, which is small enough to give rise to slow TADF.

9.2 Results and Discussion

Figure 73 shows the normalized absorption, photoluminescence (PL) and photoluminescence excitation (PLE) spectra of TQB and the chemical structures of its enol and tautomer species. The large Stokes shift observed (~200 nm) is evidence that excited-state intramolecular proton transfer (ESIPT) occurs in this molecule. Likely, features in the absorption spectrum come from the TQB-TA molecules (species without any proton transferred) and the PL comes from the tautomer species. Adachi and co-authors[4] have computationally calculated the emission energy of the tautomer after one, two and three protons have transferred to be: 2.31 eV (537 nm), 2.39 eV (518 nm) and 3.21 (386 nm), see Figure 72. TQB-TB was considered the main

fluorescent species, therefore the emission observed in Figure 73 is assigned to the species with one proton transferred.

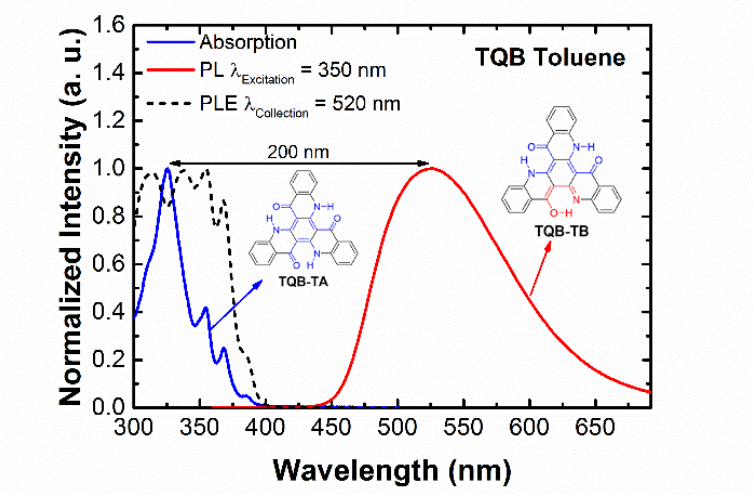

Figure 73 Normalized absorption, photoluminescence (PL) and photoluminescence excitation (PLE) spectra. Insets show the chemical structures of TQB-TA and TQB-TB.

The absorption and PLE spectra show different features, as, while the absorption spectrum shows contributions from all optically allowed transitions from the ground to excited states, the PLE spectrum shows preferentially those which form the state emitting at the detection wavelength. Thus, the peaks with increased absorption intensity (311, 336, 355, 369 and 384 nm) represent transitions that promote ESIPT and the formation of TQB-TB. The absence of a peak at 325 nm, which is strongly observed in the absorption spectrum, suggests that this is an absorption transition unique to TQB-TA.

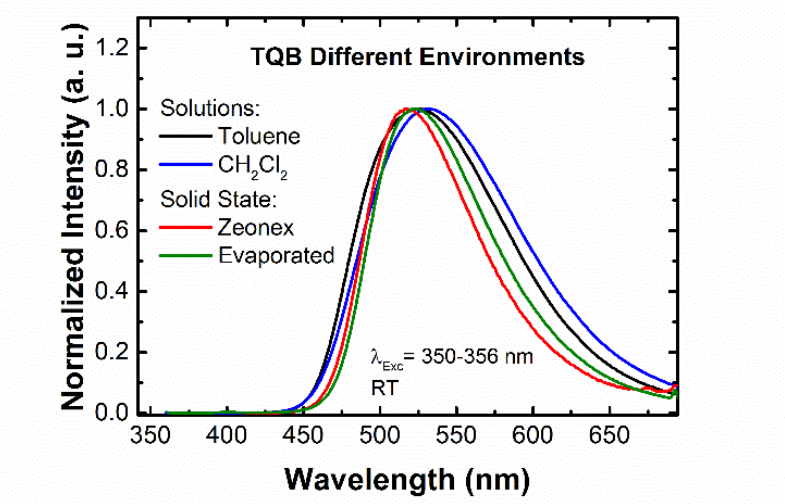

Figure 74 Photoluminescence spectra of TQB solutions (toluene and dichloromethane (CH_2Cl_2)) and solid state (zeonex matrix and neat evaporated thin film).

Figure 74 shows the PL spectra of TQB in solutions (toluene and dichloromethane (CH_2Cl_2) solvents) and solid state (zeonex matrix and neat evaporated film). The main difference among all spectra is the red edge of the spectra, as all of them show similar onset energy (~2.67 eV). The increase in the FWHM with the polarity can may be associated to inhomogeneity in the degree of proton transfer with increasing environment polarity.

The contribution of triplet excited states to the overall emission was determined by comparing the emission intensity in aerated and degassed toluene solutions. The emission spectra obtained in degassed and non-degassed solutions match each other, showing that DF and PF come from the same singlet state. The emission area increases by 20% when oxygen is removed, confirming that the TQB emission has a contribution from delayed fluorescence.

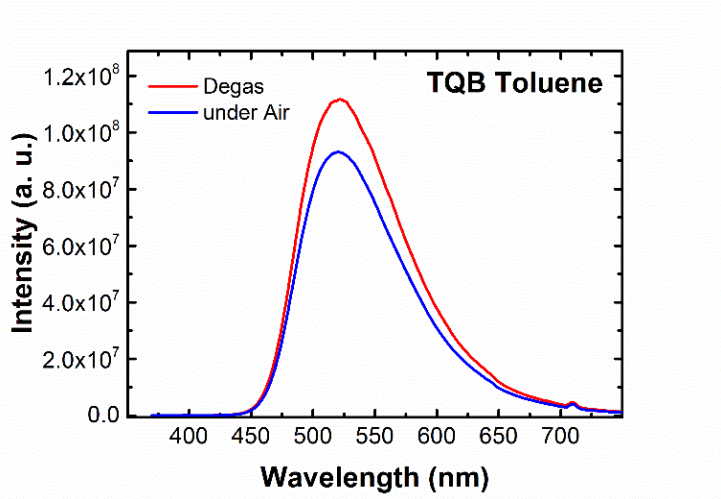

Figure 75 Photoluminescence spectra of TQB in toluene in air and after degassing the solution.

TCSPC measurements were conducted in TQB CH_2Cl_2 solutions and in TQB evaporated films to investigate if any emission around 400 nm (TQB-TA) could be identified (see Figure 76a). The time resolved emission of TQB in CH_2Cl_2 solution is shown at multiple wavelengths following excitation at 288 nm. In all cases above 460 nm, there is strong emission corresponding to that of the TQB-TB species in which transfer has already taken place. The emission is long lived relative to the 13 ns detection window available with the Ti:Sapphire laser used to excite the sample. This is shown by the presence of a high background signal before the initial step-up in PL intensity, and is due to residual emission from molecules excited by the previous pulse. The decay dynamics are mono-exponential ($\tau = 0.194 \pm 0.001$ ns) with no variation in emission lifetime across the entire spectrum of the TQB-TB emission, indicating a homogenous sample with radiative decay from a single excited state. No emission from the

TQB-TA (pre-proton transfer) could be resolved with our system (instrument response function ~27 ps). In HPI-Ac ESIPT material measured by Park *et. al*[5], emission from the excited enol form (pre-proton transfer) could be resolved as a weak shoulder at the blue end of the spectrum, which had a fast (≤5 ps) lifetime. Here, however, no such shoulder is seen in the steady state emission, and no fast component at wavelengths below the onset of the TQB-TB emission could be seen. Likely, as TQB has a bigger energy difference between enol-keto forms than HPI-Ac[5], proton transfer process are favorable, making it more efficient in TQB molecules if compared to HPI-Ac.

In Figure 76b the decay transients of fluorescence from evaporated TQB films at four wavelengths are shown. Unlike in solution, there is a strong wavelength dependence on the initial decay, with increased contribution from fast decay (of approximately 1-1.5 ns) at shorter wavelengths, and a slower decay of 12.5 ns which is common to the decay transients measured at all emission wavelengths. As can be clearly seen, the contribution of the faster component decreases with increasing the wavelength and it is negligible beyond 500 nm. This only occurs in solid state and since is not observed in solution, it is probably due to an excited state relaxation of the tautomer form.

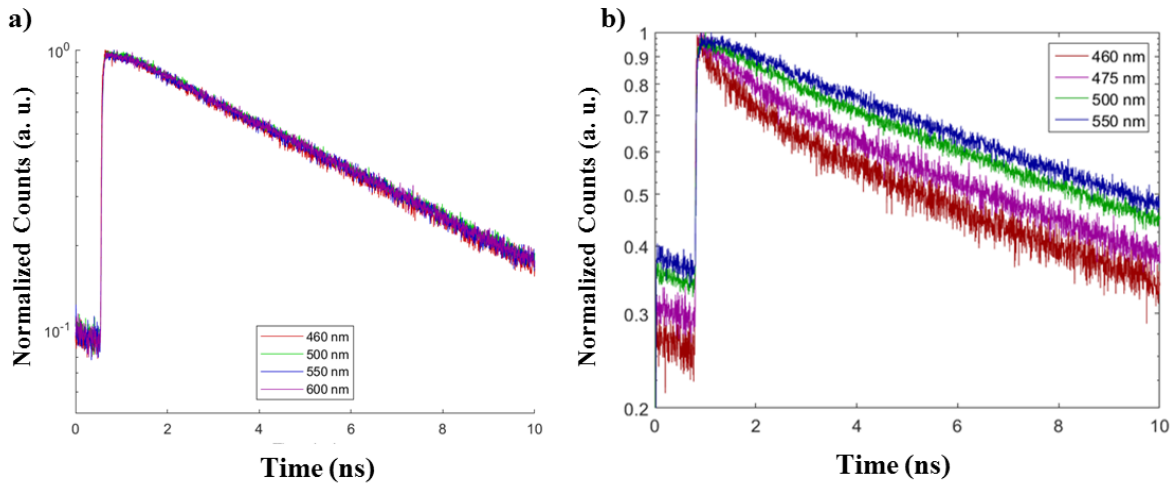

Figure 76 Decay curves of TQB in dichloromethane solution (a) and in neat film (b) at different collection wavelengths with 288 nm (solution) and 278 nm (neat film) excitation.

Figure 77a shows the decay curves of TQB in zeonex matrix at 300 K and 80K. Three different emission decay regimes are observed: Prompt fluorescence (PF) region, which shows a fast decay observed at high and low temperatures; a delayed fluorescence (DF) region (hundreds of *ns* to few *ms*) observed at 300 K; and the phosphorescence (PH) region, longest-lived region (*ms*) observed only after cooling down the system.

At 300 K, a fast decay (PF) is observed, followed by DF emission generated by the TADF mechanism. The spectra observed in the PF and DF region come from the same electronic transition, $S_1 \rightarrow S_0$, as observed by perfect overlap of the spectra (Figure 77b). Moreover, the fact that the DF is not detected at 80 K, shows the strong temperature dependence of the emission, supporting the TADF mechanism. Adachi and co-authors[4] have shown the intensity dependence of the DF emission as a function of the laser excitation dose varies linearly with a gradient of 1, confirming the TADF mechanism as opposed to TTA.

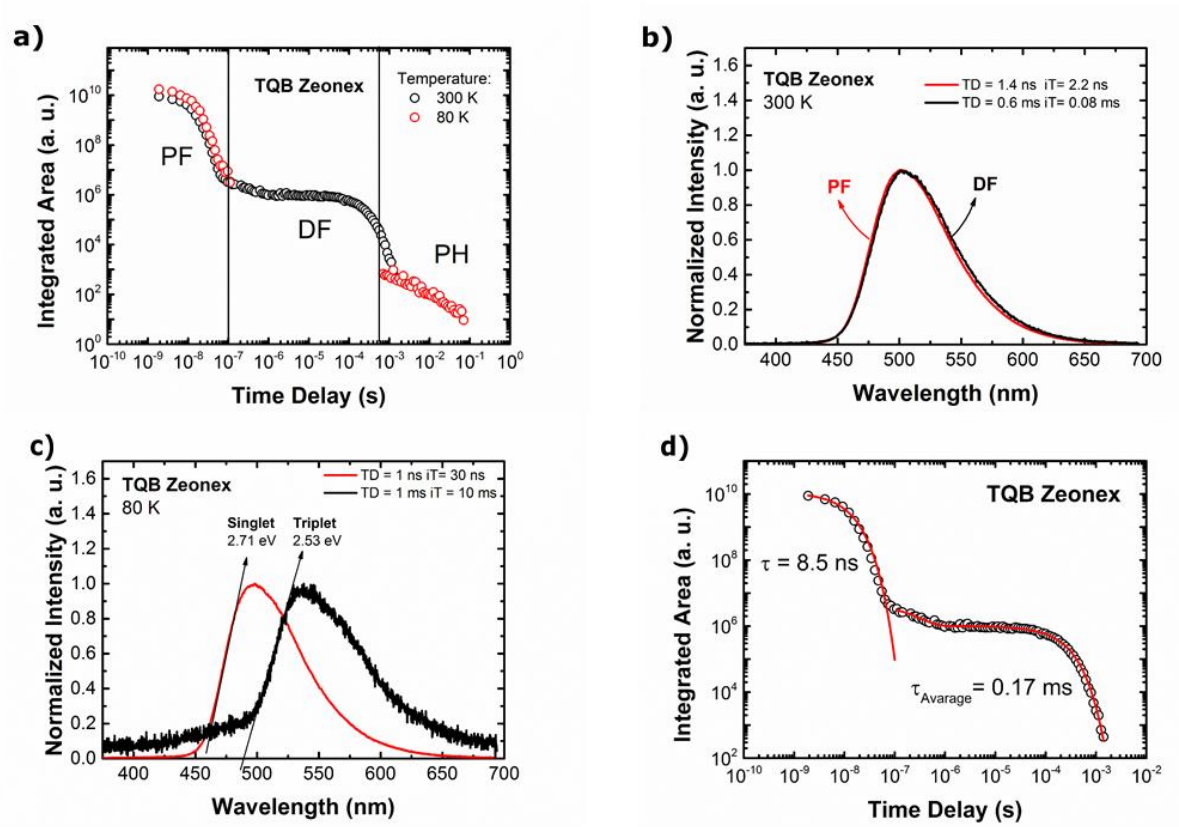

Figure 77 a) Decay curves at 300 and 80 K b) time resolved emission spectra collect in the PF and DF region at 300 K and c) at 80 K d) decay curve at 300 K of TQB in zeonex matrix.

At 80 K, PF is observed, followed by an interval during which no emission was seen above the detection noise floor of the iCCD camera. As the time delay is further increased, PH emission appears. Figure 77c shows the spectra collected in the PF and PH regions with onset energies at (2.71 ± 0.02) eV and (2.53± 0.02) eV, respectively. Thus, the optical gap between singlet and triplet states was found to be (0.18 ± 0.03) eV. The detection of the PH spectrum was not an easy task, as this emission is very weak if compared to the emission from the singlet states even when the non-radiative transitions are suppressed by cooling down the system. Likely,

this is the reason why the PH spectrum was not identified in previous work. Adachi *et al*[4] have calculated the S-T gap by Arrhenius plot and found to be 0.19 eV, much in line with the optical gap found here.

The PF and DF lifetimes were investigated in zeonex matrix at 300 K (see Figure 77d). The PF emission shows a very short lifetime of 8.5 ns, as expected. However, the DF average lifetime (0.17 ms) is much longer than those observed in efficient TADF emitters with few microsecond timeframe[8,9], resulting in very slow k_{rISC} rates. Reference [4] shows DF average lifetime in DPEPO to be 0.1 ms, which is very close to the one found in zeonex, showing that the environment plays no role in this emitter.

Interestingly, molecules that show emission via the TADF mechanism usually show large shifts to longer wavelengths upon increasing the solvent polarity. For example, when changing the solvent from toluene to CH_2Cl_2 or the solid state host from zeonex to DPEPO, a strong, positive solvatochromism is observed due to the strong charge transfer character of the emissive states[10]. This feature is not observed in TQB molecules however showing it has little or no CT character in the excited state. The solvatochromism generally observed in TADF emitters makes the OLED optimization more complicated, as the emitter and host must be optimized together. This means that a molecule can be tuned from a poor TADF emitter into a good TADF emitter simply through changing the polarity of its host. Commonly, the solvatochromism considerably changes the optical energy gap (^{1}CT-^{3}LE) between singlet and triplet states (ΔE_{ST}), as it strongly affects the singlet state energy (^{1}CT), while the energy of the triplet state (^{3}LE) remains almost unchanged. In the case of this ESIPT molecule, the ΔE_{ST} varies only slightly with the host. This property of the molecule will lead to simpler design of OLEDs structures, as the same photophysics will be observed regardless of the host selected.

As the optical ΔE_{ST} remains almost unchanged in different host materials, the triplet harvesting (spin-statistic factor on the EQE equation) will remain close to 100%. Differences in OLED performance described by Mamada *et al*[4] are therefore likely related to other parameters such as the charge balance. Hence, planar ESIPT emitters are indeed an alternative to standard orthogonal D-A-D systems in which TADF can be used. However, caution should be taken in the OLED design, as due to directly injection of electron and holes, both species (enol and tautomer) are populated[11,12]. Thus, if the lowest triplet states of the enol species is lower than that of the host, triplet quenching by the host may occur. This, however, is not the case of TQB, as the proton transfer process is very efficient.

9.3 Conclusions

This chapter presents a planar TADF emitter with small optical ΔE_{ST} resulting from the redistribution of the HOMO and LUMO after excited state intramolecular proton transfer (ESIPT). TQB clearly shows ESIPT due the large stoke shift observed in different environments in solutions and solid state but no solvatochromism ruling out a CT state. The DF via TADF was identified in zeonex matrix, and showed to have similar photophysical properties as observed in DPEPO host by Adachi *et al*.[4] The fact that TQB does not form CT states, can be an advantage in the design of OLEDs, as a large number of different hosts can results in spin-statistic factor close to 100%. Hence, planar ESIPT emitters are an alternative class of molecules which can be used to obtain emission via TADF mechanism. The long lifetime of the DF found in TQB, however, directly translated to poor roll-off efficiency in devices.

9.4 Sample Preparation Details

Three types of samples were studied in this work: solutions in different solvents (the solutions were filtered to ensure completely dilution and thus their concentration could not be determined), film produced in zeonex matrix (using the filtered solutions) and thin neat film produced by evaporation deposition onto transparent sapphire substrates using a Kurt J. Lesker Spectros II deposition system under vacuum, 10^{-6} mbar.

9.5 References Chapter 9

1. Kwon, J. E. & Park, S. Y. Advanced Organic Optoelectronic Materials: Harnessing Excited-State Intramolecular Proton Transfer (ESIPT) Process. *Adv. Mater.* **23,** 3615–3642 (2011).

2. Ernsting, N. P., Mordzinski, A. & Dick, B. Excited-state intramolecular proton transfer in jet-cooled 2,5-bis(2-benzothiazolyl)hydroquinone. *J. Phys. Chem.* **91,** 1404–1407 (1987).

3. Tang, C. W. & VanSlyke, S. A. Organic electroluminescent diodes. *Appl. Phys. Lett.* **51,** 913–915 (1987).

4. Mamada, M. *et al.* Highly Efficient Thermally Activated Delayed Fluorescence from an

Excited-State Intramolecular Proton Transfer System. *ACS Cent. Sci.* **3,** 769–777 (2017).

5. Park, S., Kwon, O. H., Lee, Y. S., Jang, D. J. & Park, S. Y. Imidazole-based excited-state intramolecular proton-transfer (ESIPT) materials: Observation of thermally activated delayed fluorescence (TDF). *J. Phys. Chem. A* **111,** 9649–9653 (2007).

6. Tokumura, K., Yagata, N., Fujiwara, Y. & Itoh, M. Two-step laser-induced-fluorescence study of 2',3',4',5',6'-pentamethyl-3-hydroxyflavone in solution at room temperature: contribution of triplet states and confirmation of ground-state tautomer. *J. Phys. Chem.* **97,** 6656–6663 (1993).

7. Tokumura, K., Kurauchi, M. & Oyama, O. Reverse intersystem crossing from higher triplet to excited singlet in 2,2′-bipyridine-3,3′-diol phototautomer. *J. Photochem. Photobiol. A Chem.* **81,** 151–158 (1994).

8. dos Santos, P. L. *et al.* Triazatruxene: A Rigid Central Donor Unit for a D-A 3 Thermally Activated Delayed Fluorescence Material Exhibiting Sub-Microsecond Reverse Intersystem Crossing and Unity Quantum Yield via Multiple Singlet-Triplet State Pairs. *Adv. Sci.* **5,** 4842–4853 (2018).

9. Dias, F. B. *et al.* The Role of Local Triplet Excited States in Thermally-Activated Delayed Fluorescence: Photophysics and Devices. *Adv. Sci.* **3,** 1–10 (2016).

10. dos Santos, P. L., Ward, J. S., Bryce, M. R. & Monkman, A. P. Using Guest–Host Interactions To Optimize the Efficiency of TADF OLEDs. *J. Phys. Chem. Lett.* 3341–3346 (2016). doi:10.1021/acs.jpclett.6b01542

11. Tarkka, R. M., Zhang, X. & Jenekhe, S. A. Electrically Generated Intramolecular Proton Transfer: Electroluminescence and Stimulated Emission from Polymers. *J. Am. Chem. Soc.* **118,** 9438–9439 (1996).

12. Tang, K.-C. *et al.* Fine Tuning the Energetics of Excited-State Intramolecular Proton Transfer (ESIPT): White Light Generation in A Single ESIPT System. *J. Am. Chem. Soc.* **133,** 17738–17745 (2011).

Chapter 10: Concluding Remarks

Throughout the course of this thesis, the origin of delayed fluorescence (DF) was investigated in a variety of organic molecules including: D-A-D, D-A_3, bimolecular exciplex blends and excited state intramolecular proton transfer (ESIPT). Each of the molecules was particularly chosen for the purpose of developing new perspectives on the underlying mechanism of thermally activated delayed fluorescence (TADF) aiming a reduction in time and cost in the design of new emitter materials for efficient TADF based organic light emitting diodes (OLEDs). Important new contributions towards the full elucidation of the TADF mechanism were presented by showing the experimental characterization of the physical and chemical aspects that are relevant in the development of new TADF molecules. In particular, this thesis focused on how to maximize the TADF contribution in different types of emitters, considering the singlet-triplet energy gaps (ΔE_{ST}) that must be overcomed by in the reverse intersystem crossing process (rISC) and the different external factors and design principles that can influence these ΔE_{ST}.

Major challenges concerning the full understanding of the TADF mechanism still persist, mainly regarding the rISC process, which clearly involves three different states (^{1}CT, ^{3}CT and ^{3}LE). Therefore, more computational studies on the vibronic coupling dynamics[1,2] are fundamental, so that better understanding can be developed for the relation of the different energy gaps (^{1}CT↔^{3}CT and ^{1}CT↔^{3}LE) and also the coupling mechanisms that promote population transfer between the triplet states (nonadiabatic coupling ^{3}CT↔^{3}LE)[3], giving bigger insights into the dynamical mechanisms for highly efficient TADF, complementing the current model.

Regarding the design strategies of these emitters, the desired TADF molecule should have a photoluminescence quantum yield (PLQY) close to 1 with a short emissive state lifetime; this is to ensure that the harvested triplets do not cycle back to the triplet state avoiding decay by non-radiative pathways. Solving this seemingly paradoxical situation is not yet fully understood but, with TAT-3DBTO_2 emitter[4] (work presented in chapter 7), a rISC rate > 10^7 s^{-1} whilst retaining a PLQY ~ 1 through near degenerate multiple excited states arising from the multi D-A structure was achieved. However, this fast rISC rate was achieved for only one of the many conformations that the emitter can access, and therefore represents just a parcel (20%)

of the DF emission observed via TADF. The ideal TADF emitter should show similar characteristics as TAT-3DBTO$_2$ but with only one conformation active, the one that gives rise to the fast rISC rate.

Regarding the performance of TADF emitters in devices, a wide variety of TADF-based OLEDs were shown throughout this thesis with satisfactory maximum external quantum efficiencies (EQE), higher than 20% (chapters 6 and 7). However, the best roll-offs and EQEs reported so far are still on devices based on phosphorescence emission (PH-OLEDs)[5] and thus, they are the commercially available in displays and lighting applications. Still recent improvements in the EQEs and roll-offs of TADF OLEDs show that they are becoming competitive, meaning it is a matter of time until these become commercially available for the industry[4,6,7]. To enhance further the roll-off of the TADF OLEDs, the degradation mechanisms require clarification. Therefore, more research is needed to evaluate the degradation pathways observed in the emitter and host, such as polaron/exciton and exciton/excitons annihilation[8].

Moreover, research is needed in the direction of the development of stable emitters and hosts materials as the instability of the molecules can generate degradation products that act as exciton quenchers and non-radiative carrier recombination centers[9]. In this matter, it is worth mentioning that, a great deal of interest has been recently devoted to the elaboration of TADF emitters exhibiting blue colour[10]. To get full-colour displays or white-light OLEDs, the balanced combination of the three primary colours (red, green and blue) is essential. The challenges with the blue emitters start with their weak stability due to the lack of conjugation that can rapidly degrade during device operation. Also, due to their large bandgaps, charge injection from the adjacent layers is difficult and devices are required to be operated at high voltages. Finally, as blue emitters have high triplet states, finding suitable hosts that combine higher triplet and good electrical mobility for blue emitters is currently challenging.

Therefore, the TADF emitters have truly demonstrated promising properties for OLED applications and promise to become commercially available soon. Though much work has been done in the TADF field, many possibilities still remain to be explored, and to solve the open questions that have been addressed above, joint efforts of synthetic chemistry, theoretical chemistry, photophysical characterization and device engineering are required.

10.1 References Chapter 10

1. Gibson, J., Monkman, A. P. & Penfold, T. J. The Importance of Vibronic Coupling for Efficient Reverse Intersystem Crossing in Thermally Activated Delayed Fluorescence Molecules. *ChemPhysChem* **17,** 2956–2961 (2016).

2. Etherington, M. K., Gibson, J., Higginbotham, H. F., Penfold, T. J. & Monkman, A. P. Revealing the spin–vibronic coupling mechanism of thermally activated delayed fluorescence. *Nat. Commun.* **7,** 13680 (2016).

3. Gibson, J. & Penfold, T. J. Nonadiabatic coupling reduces the activation energy in thermally activated delayed fluorescence. *Phys. Chem. Chem. Phys.* **19,** 8428–8434 (2017).

4. dos Santos, P. L. *et al.* Triazatruxene: A Rigid Central Donor Unit for a D-A 3 Thermally Activated Delayed Fluorescence Material Exhibiting Sub-Microsecond Reverse Intersystem Crossing and Unity Quantum Yield via Multiple Singlet-Triplet State Pairs. *Adv. Sci.* **5,** 1700989 (2018).

5. Minaev, B., Baryshnikov, G. & Agren, H. Principles of phosphorescent organic light emitting devices. *Phys. Chem. Chem. Phys.* **16,** 1719–1758 (2014).

6. Kim, K. J. *et al.* A new rigid diindolocarbazole donor moiety for high quantum efficiency thermally activated delayed fluorescence emitter. *J. Mater. Chem. C* **6,** 1343–1348 (2018).

7. Lin, T.-A. *et al.* Sky-Blue Organic Light Emitting Diode with 37% External Quantum Efficiency Using Thermally Activated Delayed Fluorescence from Spiroacridine-Triazine Hybrid. *Adv. Mater.* **28,** 6976–6983 (2016).

8. Murawski, C., Leo, K. & Gather, M. C. Efficiency Roll-Off in Organic Light-Emitting Diodes. *Adv. Mater.* **25,** 6801–6827 (2013).

9. Sandanayaka, A. S. D., Matsushima, T. & Adachi, C. Degradation Mechanisms of Organic Light-Emitting Diodes Based on Thermally Activated Delayed Fluorescence Molecules. *J. Phys. Chem. C* **119,** 23845–23851 (2015).

10. Bui, T.-T., Goubard, F., Ibrahim-Ouali, M., Gigmes, D. & Dumur, F. Recent advances on organic blue thermally activated delayed fluorescence (TADF) emitters for organic

light-emitting diodes (OLEDs). *Beilstein J. Org. Chem.* **14,** 282–308 (2018).